Free Surface Flow over Bottom Topography

Jack Samuel Keeler

April 23, 2018

Thesis submitted for the degree of
Doctor of Philosophy
in
Applied Mathematics
at
The University of East Anglia
School of Mathematics
and
The University of Adelaide
Faculty of Engineering, Computer and Mathematical Sciences
School of Mathematical Sciences

THE UNIVERSITY of ADELAIDE

UEA
University of East Anglia

Contents

List of Tables

List of Figures

Signed Statement

This work contains no material which has been accepted for the award of any other degree or diploma in any university or other tertiary institution and, to the best of my knowledge and belief, contains no material previously published or written by another person, except where due reference has been made in the text.

I consent to this copy of my thesis, when deposited in the University Library, being available for loan and photocopying.

Signed: ..... Date: .....

Acknowledgements

Many thanks to Mark and Ben for the belief, guidance and support. I hope I have repaid your faith in me. It's really been a privilege to work with you both.

Thanks also to Mum and Dad for all the fine dinners, Jo for always answering her phone, Sam for keeping me grounded, and Tess, Alice and Nancy for being such a light in this world.

Finally, so many thanks go to Marta, the most patient of them all.

"Let somebody know something" - Gilly

Abstract

This thesis explores flow in a channel over a bottom topography. In particular, the problem of finding the shape of the unknown free-surface if the bottom topography is prescribed forms the main problem of this thesis. In chapter 2 the forced Korteweg De-Vries equation is derived from first principles as a model partial differential equation that determines the shape of the unknown free-surface profile in terms of the topography. A discussion of the steady solution space when the forcing is highly localised is also presented. In chapter 3 flow over bottom topography at critical Froude number (when $F = 1$) is examined. For large amplitude negative Gaussian forcing, asymptotic solutions are constructed using boundary layer theory; one point of interest here is an internal layer away from the origin which mediates a change from exponential decay away from the central dip to algebraic decay in the far-field. Intriguingly, solutions with different numbers of waves trapped around the central dip are also found for large amplitude topography but these cannot be captured by the boundary-layer analysis. In fact a seemingly infinite sequence of solution branches is uncovered using numerical methods and a nonlinear multiple-scales technique, and in general the solution for any given topography amplitude is non-unique. In addition to these results the stability of the steady solutions is examined using numerical simulations, linear stability analysis and formal stability analysis. In chapter 4 the issue of existence of steady solutions is analysed for an algebraically decaying topography at critical flow speed. For this topography the analysis is subtle and numerical solutions have to be treated with care. In chapter 5 the solution space is studied for varying Froude number for flow over a corrugated topography where a rich solution space is discovered. Finally, preliminary work on the three-dimensional analogue of the fKdV equation, namely the fKP equation is presented, including a novel result regarding three-dimensional solitary waves that decay in all spatial directions.

Chapter 1

Introduction

A free boundary problem can broadly be described as finding the unknown interface between two different media. Free boundaries are ubiquitous in nature, for example studying the surface of a melting block of ice or the shape of a sail flapping in the wind. The study of free-boundaries has produced a wide range of interesting physical phenomena and the development of a wide range of mathematical techniques. There are many other different contexts in which the calculation of a free boundary is required. For example a study of the shape of the interface between the air and surface water-waves in the ocean can help us understand tsunamis, whilst a study of the interface between regions of different density in the atmosphere can help us understand weather patterns and other related phenomena. These are examples of *free-surface* problems where boundary conditions are implemented on an unknown free-surface that has to come as part of the solution. A common feature to these problems are that they are inherently nonlinear and analytic solutions, in general, are not available and numerical techniques are required. However, great insight can still be made by deriving approximate models that do have analytic solutions.

In this thesis, a two dimensional fluid flow in an infinite horizontal domain that is bounded above by a free-surface and below by a fixed bottom topography (see figure 1.0.1 for a diagram of the situation) is investigated. The broad question that this thesis attempts to answer is to what extent the shape of the topography affects the response of the free-surface. In particular the case where the topography is prescribed and the free-surface is found as part of the solution is investigated in this thesis. Steady solutions are the primary focus but solutions of the time-dependent initial-value problem will also be studied. If the fluid is considered inviscid, irrotational and incompressible Laplace's equation describes the velocity potential of the flow (see, for example, Acheson, 1990). On the unknown free-surface two conditions have to be satisfied. The kinematic condition states that if a fluid particle is initially on the free-surface then it stays there. The dynamic boundary condition represents a force balance on the free-surface between the fluid and the air. The dynamic boundary condition is highly nonlinear and is what makes this problem a challenge to solve. Laplace's equation, to-

gether with the two boundary conditions on the free-surface are known collectively as the *water-wave equations*. There is in general no analytic solution for these equations. On the assumption that the deviation of the free-surface from the mean level upstream and downstream is not too large progress can be made by an asymptotic analysis of these equations. By making certain modelling assumptions a number of different model equations (that importantly are simpler) can be derived that provide an asymptotic description of the water-wave equations. A common feature of these equations is a competition between nonlinear terms and dispersive terms. Small amplitude periodic waves, for which nonlinearity can be neglected, propagate at a speed dictated by their wavenumber according to an appropriately derived dispersion relation. In the absence of dispersive terms the nonlinearity means shock wave solutions are typically found (see, for example Whitham, 1974).

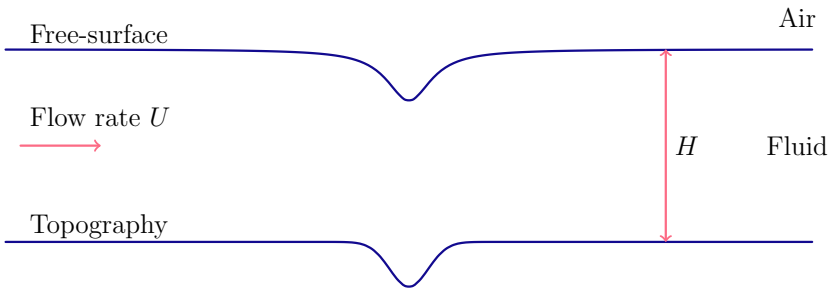

Figure 1.0.1: A diagram showing the physical set up of the problem

When the height of the fluid domain, H (see figure 1.0.1), is small and the topography is assumed flat, the *shallow water equations* can be derived (see, for example Whitham, 1974). These equations admit shock-wave solutions and can accurately describe dam-breaking and river-bores (Acheson, 1990). In the case of deep water, the *nonlinear Schrödinger equation* can be derived where nonlinear and dispersive effects are included (Whitham, 1974). When the nonlinear effects are balanced with dispersive effects the *Korteweg-de Vries equation* (KdV) can be derived when the flow depth is small compared to a typical wavelength on the free-surface and the amplitude of the waves are small and propagate in one direction only, (Whitham, 1974) (for waves propagating in both directions the *Boussinesq equation* is a more appropriate model equation). There is a trivial *uniform flow* solution of this equation which describes a flat free-surface. Additionally, the KdV equation is well known to admit *solitary wave* solutions of the form where the free-surface is given by

$$\eta(z) = 2V \operatorname{sech}^2\left(\sqrt{\frac{3}{2}V}z\right)$$

where z is a horizontal travelling wave coordinate and V is the speed of propagation.

Solitary waves decay exponentially upstream and downstream and are well studied (see, for example Billingham & King, 2000; Drazin & Johnson, 1989; Whitham, 1974, and others). When the flow is three-dimensional the *Kadomtsev-Petviashvili* is an appropriate model (see chapter 6 for a detailed discussion).

These are not the only examples of asymptotic approximations to the water-wave equations (see Lannes (2013) for a detailed description of the plethora of different models). However, the last four models described are all examples of *integrable* systems (see, for example Ablowitz & Clarkson, 1991). Briefly this means that they admit an infinite number of conserved quantities and can be solved by an inverse-scattering method developed in the mid-twentieth century. A large range of interesting phenomena have been described since this breakthrough. For a detailed discussion see, for example Whitham (1974) and Drazin & Johnson (1989). This area of nonlinear waves continues to be an active research area. A recent popular article (Champneys, 2017) stated that according to an internet search engine there are over 200 scientific papers each year with KdV in the title!

The introduction of a fixed, bottom topography results in a plethora of interesting and complex wave behaviour. In the case of fluid flow over topographic forcing the *forced Korteweg De-Vries equation* (fKdV equation) is a weakly nonlinear model partial differential equation (PDE) that describes the evolution of the surface when the maximum height of the topography and free-surface response is small (see, for example Akylas, 1984; Dias & Vanden-Broeck, 2002*a*; Grimshaw & Smyth, 1986; Iguchi, 2006; Shen, 1995). It will be derived from the water-wave equations in chapter 2. It is worth emphasising that the results presented for the fKdV equation have wider applicability than to free-surface flows. Indeed, the fKdV equation has been discussed in the context of a wide range of physical scenarios. One application of particular importance, and which is of direct relevance to the present work, concerns internal waves in a stratified flow when the pycnocline, that is the fluid layer over which the predominant variation in density occurs, is located close to the ground surface, as may occur in atmospheric flow over ground relief (Baines, 1977, 1984; Grimshaw & Smyth, 1986; Malanotte-Rizzoli, 1984).

The advantage of this model is that in certain situations an exact form can be written down for the steady free-surface by treating the steady fKdV equation as a dynamical system and analysing the trajectories in the phase space. For example it is well known that for a single localised bump or dip topography, which can be represented as a delta function, the solution space is non-unique and in each case an exact solution can be obtained (Dias & Vanden-Broeck, 2002*a*,*b*; Wade *et al.*, 2014). In fact the solution space for a delta forcing can be shown to be two-dimensional (Dias & Vanden-Broeck, 2002*a*); depending on the maximum height of the small bump, α and the non-dimensionalised flow rate given by the Froude number F. The Froude

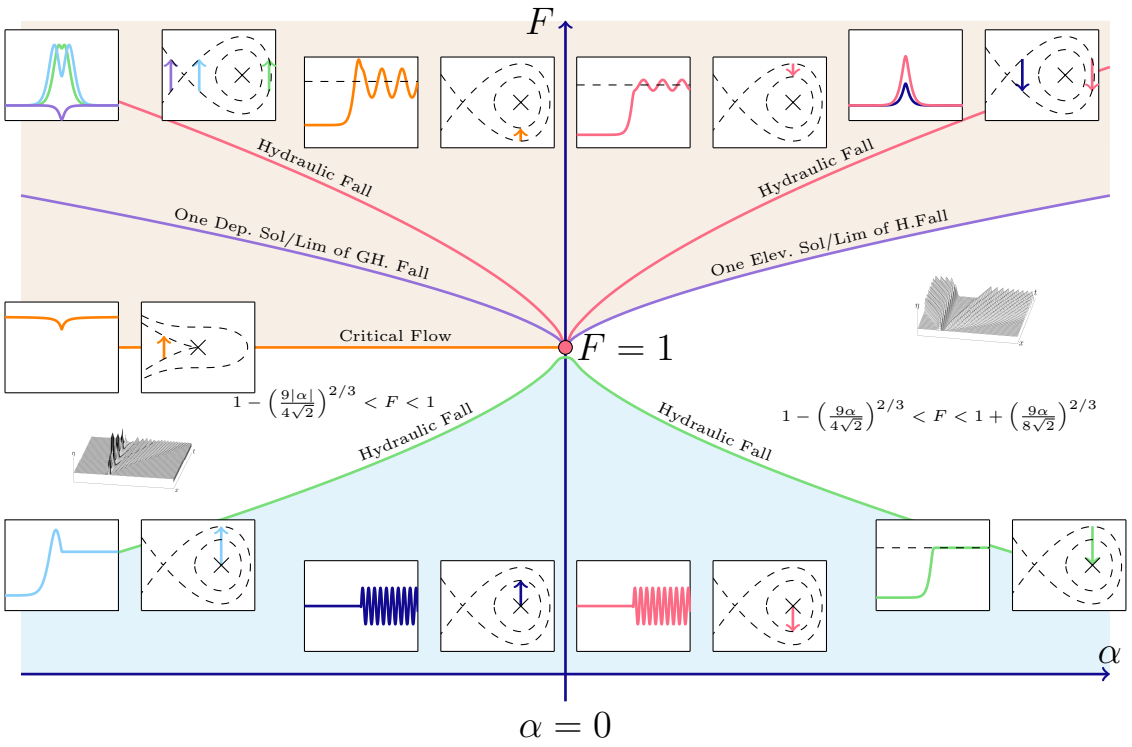

Figure 1.0.2: Point Forcing Solution Space. White areas correspond to *transcritical flow* parameter space, blue areas correspond to *cnoical wave* parameter space. Beige areas correspond to *forced solitary wave/generalised hydraulic falls* parameter space. The green curve is given by $F = 1 - \left(\frac{9|\alpha|}{4\sqrt{2}}\right)^{2/3}$ corresponding the one parameter family, (α), of *hydraulic fall* solutions. The orange curve is $F = 1$ corresponding to the one-parameter family, (α) of critical-flow solutions. The purple curve is given by $F = 1 + \left(\frac{9|\alpha|}{8\sqrt{2}}\right)^{2/3}$, corresponding to when there is only one non-uniqueness occurs. The red curve is given by $F = 1 + \left(\frac{9|\alpha|}{4\sqrt{2}}\right)^{2/3}$ when a unique one-parameter family of *hydraulic falls* can exist.

number is an important parameter throughout this work and is defined as

$$F = \frac{U}{\sqrt{gH}}, \tag{1.0.1}$$

where U is the speed of the uniform flow far upstream, g is the acceleration due to gravity and H is the uniform height of the flow upstream. This can be thought of as the Mach number for water-waves. It is the ratio of the speed of the flow to the speed of a small amplitude periodic gravity wave. The range of different steady free-surface responses in this situation are shown in figure 1.0.2. The analysis in chapter 2 will explain the form of this solution space in more detail, for now it is enough to say that for simple point forcing model there is a large number of different steady solutions with complex behaviour that depends on two parameters: the amplitude of the obstacle and the flow speed. The complete number of solution types for a general topography has been categorised by Binder *et al.* (2013). Following their work the following definitions are made to help characterise the free-surface flow. *Super-critical* flow is defined when $F > 1$, upstream and downstream, *sub-critical* flow when $F < 1$ upstream and down-

stream and *critical* flow when $F = 1$ upstream and downstream. *Generalised hydraulic falls* occur when the flow is super-critical upstream and oscillatory downstream and *hydraulic fall* solutions when the the flow is sub-critical upstream and super-critical downstream. Note this is not a complete description of the flow-types available but the interested reader is encouraged to read Binder *et al.* (2013) for a complete description. Finally, *transcritical flow* is defined in the range when $F \approx 1$ and steady solutions (for a delta forcing) do *not exist*. All of these terms will be explained in more detail in chapters 2 and 3 (NB: other authors define this differently but in this work it is defined as such).

By modelling the bottom topography as a delta function steady solutions exist for super-critical flow that decay exponentially both downstream and upstream of the topographic forcing (Dias & Vanden-Broeck, 2002a). These are called *forced solitary waves* and can be considered as a perturbation of a classical solitary wave over a flat surface. For sub-critical flow steady solutions exist that are flat far upstream but oscillate downstream of the localised topography. There has been extensive numerical investigations of super-critical and sub-critical flow in the past by a number of different authors. A semi-circular bump topography has been investigated by Dias & Vanden-Broeck (2002a) with an explanation of different steady solutions using a phase-plane analysis. Work by Binder *et al.* (2005) and Dias & Vanden-Broeck (2002b) looked at nonlinear solutions to waves past more than one submerged obstacle with reference to a weakly nonlinear analysis whilst Grimshaw *et al.* (2007), Zhang & Zhu (1997) and Donahue & Shen (2010) have completed similar work using a numerical approach for the weakly nonlinear case for unsteady flows. Dias & Vanden-Broeck (2002a) and Wade *et al.* (2014) were able to classify, with recourse to a phase-plane argument, five distinct types of solutions for super-critical flow; two for a positive point-forcing and three for a negative point-forcing. These solutions can be interpreted as either perturbations of a uniform flow over a flat topography or perturbations of a classical solitary wave over a flat topography. The complete solution space is shown in figure 1.0.2 and is explained in detail at the end of chapter 2. More recent work includes that by Binder *et al.* (2013) and Tam *et al.* (2015) who have worked on developing a so-called 'inverse' approach to find steady solutions using the fKdV and fully nonlinear models (see subsection 3.5.3 for a description of this approach). In chapter 2 the different types of steady solutions for point forcing that are discussed above are analysed in more detail.

For critical flow, a similar argument can be made to demonstrate that there is only a steady solution if the point-forcing is negative (i.e. small dip), and furthermore this solution is *unique*. Interestingly, the steady solution decays algebraically in the far-field, a point of departure from the super-critical case where they decay exponentially. Algebraically decaying solitary waves have been studied before by Sun (1997) in the case of gravity-capillary waves in an infinite two-layer fluid and Akylas (1984) in the

case of solitary waves in a fluid of infinite depth. For forced gravity waves there has not been an extensive study and this provides motivation to investigate further. Furthermore, the recent work of Binder *et al.* (2014) demonstrated that by employing a numerical technique non-uniqueness can be established when $F = 1$ for a smoothly varying topography. However a number of questions still remain: is it possible to quantify and understand the solution space when $F = 1$? When does non-uniqueness occur? How important is the algebraic decay of the wave profile? These questions will be discussed in detail in chapter 3.

The time-dependent initial-value problem is now discussed. To understand the stability properties of a given steady state the initial condition can be chosen to be a small perturbation away from the steady state. The super-critical time-dependent calculations show that the perturbed solitary wave solution is generally unstable whilst the perturbed uniform flow solution is generally stable (Chardard *et al.*, 2011; Grimshaw & Maleewong, 2013; Grimshaw *et al.*, 2007; Shen *et al.*, 2000; Wade *et al.*, 2014). There have been some analytic attempts to study the stability properties of the steady solutions by examining the time-dependent equation, namely Camassa & Wu (1991) and Shen *et al.* (1995), where nonlinear stability was established for waves of a certain type, but as noted by Shen *et al.* (2000) and Chardard *et al.* (2011) there still remains a fully rigorous proof for the stability of the forced steady solutions, especially with regard to the lower perturbed uniform flow solution. Additionally Choi *et al.* (2008) managed to prove that the unsteady fKdV equation for positive forcing with zero initial condition admitted a range of super-critical F where the solution would evolve to a steady state. Outside this range of F the solution is unstable and would emit solitons periodically as demonstrated numerically by Wade *et al.* (2014).

The unsteady response of the free surface for critical flow in the presence of topography has been discussed by Binder & Vanden-Broeck (2006); Ee *et al.* (2010); Grimshaw (2010); Grimshaw & Smyth (1986); Smyth (1988); Wu (1987). For a flat initial condition at critical flow speed, so-called *undular bores* are created (see figure 1.0.3) where solitons get emitted upstream and a periodic wave train exists downstream (Camassa & Wu, 1991; Grimshaw, 2010; Grimshaw & Smyth, 1986; Grimshaw *et al.*, 2007; Wu, 1987). An important observation is that no steady state is approached as time increases. For a positive topography Whitham's modulation theory can be exploited to describe the time-evolution of the free surface, but for a negative bump this is a difficult, and in the words of Grimshaw & Smyth (1986), a 'daunting' task. However although the initial-value problem has been well studied when the initial state is flat, less investigation has been made when the initial condition is a perturbation of a steady state. The possibility of non-unique steady solutions at critical flow speed open a fresh avenue of research in that the stability properties of the non-unique forced solitary waves at critical Froude number become of interest. In particular, do stable solutions exist?

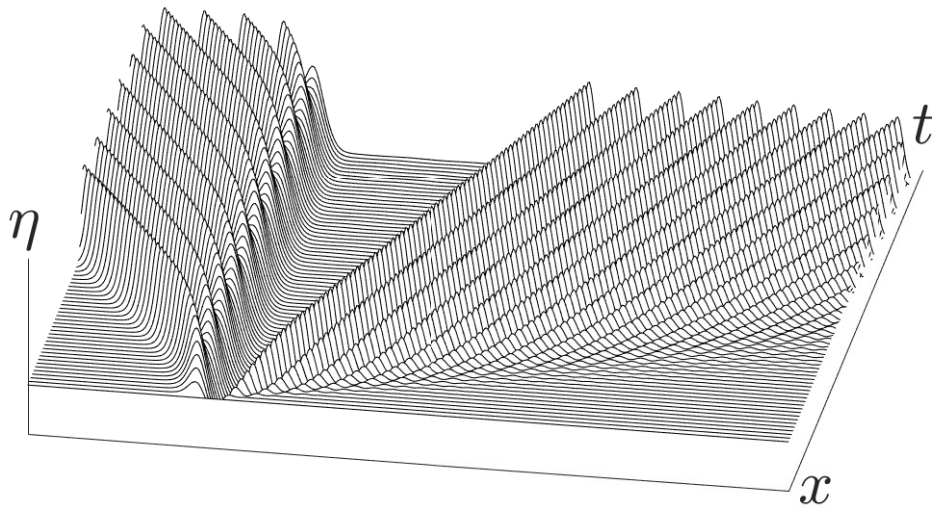

Figure 1.0.3: A sketch of the non steady free surface response when there is a positive bump topography and the initial condition is $\eta(x, 0) = 0$

In chapter 3 the problem of steady and time-dependent flow at critical flow speed is investigated. The non-uniqueness of the steady solutions is examined initially with a rectangular trench topography using phase-plane methods and exact solutions can be written down. The non-uniqueness is also examined for a smoothly varying Gaussian dip topography. In this case asymptotic methods are used to demonstrate non-uniqueness. It will be shown that a common feature of these critical flow solutions is that they decay algebraically in the far-field. As well as the fKdV model these solutions are shown to exist numerically in the fully nonlinear water-wave equations and it is also shown analytically that these decay algebraically in the far-field.

Additionally in chapter 3 the time-dependent unsteady problem is considered. The stability of the steady solutions discovered in chapter 3 for the Gaussian bump is established. The method of establishing stability is three-pronged: linear stability, formal stability and numerical simulations. The formal stability argument exploits the Hamiltonian nature of the fKdV equation to determine additional stability properties of the solutions. Finally these arguments are augmented by numerical simulations using a pseudo-spectral method. The resulting behaviour is compared to that of the intrinsically unsteady flow past a bump (see figure 1.0.3) and the stability of some inverse solutions discovered by Binder *et al.* (2014) are also considered.

Chapter 4 explores the problem when the shape of the topography decays algebraically, in particular if a 'Witch of Agnesi' topography is chosen. A simple asymptotic analysis reveals an expansion that satisfies the boundary conditions at all orders. Whilst it might seem reasonable to believe that the solution space will be similar to that of a Gaussian topography, the situation will be shown to be more subtle than that. In this problem exponentially small terms in the asymptotic expansion can cause difficulties in establishing a consistent expansion that satisfies the boundary conditions beyond all orders.

The other problem that this thesis will set out to solve is flow over a non-localised corrugated topography. As discussed previously when the topography is highly localised exact solutions can be found. Phase-plane methods are not well-suited to studying flow over a corrugated topography and the steady solution space is relatively unknown. For a damped steady fKdV equation, Grimshaw & Tian (1994) managed to show the presence of chaotic solutions using a Melnikov method. More recently it has been shown by Binder *et al.* (2015) that for an infinitely corrugated topography bounded periodic steady solutions exist and are described well using an asymptotic and Melnikov method. Using the Melnikov method they also showed that for the undamped fKdV equation the solutions can be chaotic.

In chapter 5 it will be shown using an asymptotic method that these solutions to an infinite corrugation are not in general periodic but are actually in general quasi-periodic. Additionally a numerical analysis of the cases when the corrugation is semi-infinite and finite shows that for super-critical flow the solutions approach a periodic wave far downstream of whilst for sub-critical flow they approach a quasi-periodic wavetrain far downstream. This behaviour will be augmented by Poincaré plots and power spectra which agree with the asymptotic theory. The solution space is analysed with the fKdV equation and the fully nonlinear boundary integral equations and are described in terms of the types of solutions for the delta function forcing discussed in chapter 2. There are also a wide range of hybrid solutions that also appear in the solution space, including so-called 'table-top solitons' (see Chardard *et al.* (2011)). In addition to the fKdV solutions the solutions are also discovered in the fully nonlinear water-wave equations numerically. A taxonomy of the steady solution space for corrugated topographies is a previously unknown result and is described in detail in this chapter.

The final chapter discusses future work and research avenues. Chapter 6 focuses on the three-dimensional problem. The *forced KP* equation will be analysed as a three-dimensional analogue to the fKdV equation. Using the previously mentioned 'inverse' approach steady solutions will be explored with the eventual aim of constructing solutions that are localised in space.

Chapter 2 contains mostly review material and is included to supplement the results of the later chapters and to provide a background to the original work in later chapters. The derivation of the fKdV in this chapter, although derived many times by many different authors, is included as to the author's knowledge it has not been derived in a manner similar to that of Whitham (1974). The two-parameter asymptotic analysis is a delicate procedure (see, for example Burde & Sergyeyev, 2013) and the analysis at each stage is justified carefully and thoroughly. The steady flow over a Gaussian bump and stability analysis in Chapter 3 is based on the work in the article Keeler *et al.* (2017), which is published in the Journal of Fluid Mechanics, with the exception of the analysis using Kuzmak's method. The third chapter is partly an analysis of

the fKdV equation when the topography decays algebraically. The fourth chapter is a novel analysis of the solution space over a corrugated topography using extensive numerical calculations and examples and an article on this is currently in preparation. The last chapter is a novel analysis of the KP equation to demonstrate for the first time (to the author's knowledge) that a localised free surface solution for a localised topography can be found.

Chapter 2

Background and Formulation

2.1 Derivation of fKdV equation

The approach to derive the fKdV equation is similar to the analysis of Whitham (1974) for a flat bottom. The equation has been derived before by Akylas (1984) for the case of a moving pressure distribution on the surface and by Grimshaw & Smyth (1986) for the case of forcing due to a bottom topography.

The diagram in figure 2.1.1 illustrates the physical situation. Let there be a uniform, inviscid, irrotational stream of fluid of height H bounded below by a bottom topography $\hat{\sigma}(\hat{x})$ with speed U far upstream. The coordinate axes are positioned central with the bottom topography $\hat{y} = \hat{\sigma}(\hat{x})$. The equation of the free surface is $\hat{y} = H + \hat{\eta}(\hat{x})$. Let a be a typical height scale for the free surface and L be a typical wavelength.

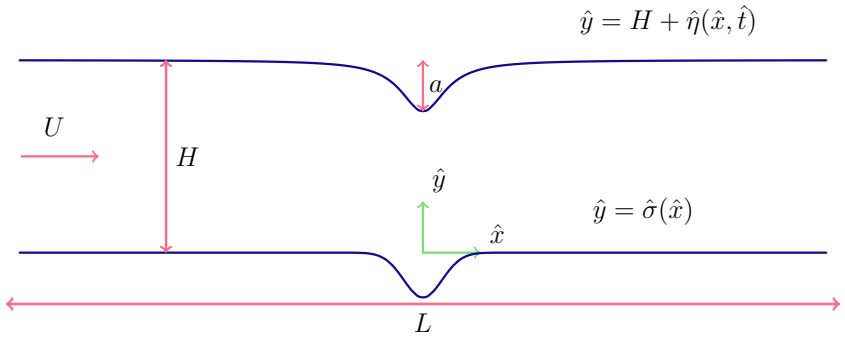

Figure 2.1.1: A diagram showing the physical set up of the problem

In this analysis the effects of surface tension are ignored. The physical situation is modelled by Euler's equations (see, for example Acheson (1990)) which describe the evolution of an inviscid fluid with velocity vector $\hat{\mathbf{u}}(\hat{x}, \hat{y}, \hat{t})$, pressure field $\hat{p}(\hat{x}, \hat{y}, \hat{t})$ and constant density ρ. These quantities satisfy

$$\frac{\partial \hat{\mathbf{u}}}{\partial \hat{t}} + (\hat{\mathbf{u}} \cdot \nabla)\hat{\mathbf{u}} = -\frac{1}{\rho}\nabla \hat{p} + \mathbf{F}, \tag{2.1.1a}$$

$$\nabla \cdot \hat{\mathbf{u}} = 0, \tag{2.1.1b}$$

where $\mathbf{F}$ is a body force which is assumed to be conservative, i.e. it can be written it as $\mathbf{F} = \nabla\chi$. In this particular instance, $\chi = -g\hat{y}$, with g as the gravitational acceleration. The first equation is a statement of Newton's second law whilst the second states the conservation of mass and is a consequence of the fluid's incompressibility. Additionally if the fluid is irrotational, i.e. $\nabla \times \hat{\mathbf{u}} = \mathbf{0}$, then a velocity potential $\hat{\mathbf{u}} = \nabla\hat{\Phi}$ can be introduced. By substituting this into (2.1.1b) it becomes Laplace's equation

$$\nabla^2\hat{\Phi} = 0. \tag{2.1.2}$$

By using vector identities and by integrating (2.1.1a) Bernoulli's condition can be stated as:

$$\frac{\partial\hat{\Phi}}{\partial\hat{t}} + \frac{1}{2}|\nabla\hat{\Phi}|^2 + g\hat{y} = -\frac{1}{\rho}\hat{p} + B(\hat{t}). \tag{2.1.3}$$

The 'so-called' Bernouilli constant $B(\hat{t})$ is constant on every streamline and since the fluid is irrotational it is also constant everywhere in the flow domain (for a given $\hat{t}$). There is a uniform horizontal flow from $\hat{x} \to -\infty$ of speed U. Let $\hat{\mathbf{u}} = (\hat{u}, \hat{v})$ represent the horizontal and vertical fluid velocities. By considering perturbations to this uniform stream the velocity is written as

$$(\hat{u}, \hat{v}) = (\hat{\Phi}_{\hat{x}}, \hat{\Phi}_{\hat{y}}) = (U + \hat{\varphi}_{\hat{x}}, \hat{\varphi}_{\hat{y}}), \tag{2.1.4}$$

where $\hat{\varphi}$ is the potential of the perturbed flow. Substituting (2.1.4) into (2.1.2) yields:

$$\hat{\varphi}_{\hat{x}\hat{x}} + \hat{\varphi}_{\hat{y}\hat{y}} = 0 \tag{2.1.5}$$

This equation describes the velocity potential for the entire flow domain. As discussed in the introduction a kinematic and dynamic boundary condition needs to be imposed on the free-surface. First, define $G = \hat{y} - (H + \hat{\eta}(\hat{x}, \hat{t}))$. Clearly if a particle is on the free surface it should remain there, hence

$$\frac{DG}{D\hat{t}} = 0$$

is the kinematic condition on the free surface[1]. The dynamic condition states that the pressure of the on the free-surface is equal to the atmospheric pressure $\hat{p} = \hat{p}_0$. By examining the flow far upstream, Bernoulli's constant, $B(\hat{t})$, can be determined in which case (2.1.3) becomes

$$\frac{\partial\hat{\Phi}}{\partial t} + \frac{1}{2}|\nabla\hat{\Phi}|^2 + gy = \frac{1}{2}U^2 + gH,$$

where $B(\hat{t}) = \frac{1}{2}U^2 + gH + \frac{\rho}{\hat{p}_0}$. On the bottom topography, $\hat{y} = \hat{\sigma}(\hat{x})$, the no normal flow condition must be imposed. This is written as $\hat{\mathbf{n}} \cdot \hat{\mathbf{u}} = 0$, at $\hat{y} = \hat{\sigma}$, where $\hat{\mathbf{n}}$ is the

[1] $D/D\hat{t}$ represents the usual material derivative

unit normal to the bottom. The unit normal is defined as

$$\hat{\mathbf{n}} = \frac{\nabla(\hat{y} - \hat{\sigma})}{|\nabla(\hat{y} - \hat{\sigma})|},$$

and therefore on the bump

$$(1 + \hat{\sigma}_{\hat{x}}^2)^{-1/2}(-\hat{\sigma}_{\hat{x}}, 1) \cdot (\hat{\Phi}_{\hat{x}}, \hat{\Phi}_{\hat{y}}) = 0. \tag{2.1.6}$$

Summarising, the boundary conditions for the physical problem on the free surface and bottom topography are

$$\left.\begin{aligned} &\hat{\eta}_{\hat{t}} + (U + \hat{\varphi}_{\hat{x}})\hat{\eta}_{\hat{x}} - \hat{\varphi}_{\hat{y}} = 0 \\ &\hat{\varphi}_{\hat{t}} + \tfrac{1}{2}(U + \hat{\varphi}_{\hat{x}})^2 + \tfrac{1}{2}\hat{\varphi}_{\hat{y}}^2 + g\hat{y} = \tfrac{1}{2}U^2 + gH \end{aligned}\right\} \quad \text{on } \hat{y} = H + \hat{\eta}(\hat{x}, \hat{t}), \tag{2.1.7a}$$

$$(1 + \hat{\sigma}_{\hat{x}}^2)^{-1/2}(-\hat{\sigma}_{\hat{x}}, 1) \cdot (U + \hat{\varphi}_{\hat{x}}, \hat{\varphi}_{\hat{y}}) = 0. \qquad \text{on } \hat{y} = \hat{\sigma}(\hat{x}). \tag{2.1.7b}$$

Equations (2.1.7), together with (2.1.5), form the water wave equations. It is convenient to non-dimensionalize the variables to reduce the number of parameters in the problem. This can be done by setting:

$$\bar{x} = \frac{\hat{x}}{L}, \quad \bar{y} = \frac{\hat{y}}{H}, \quad \bar{\varphi} = \frac{1}{a\sqrt{gH}}\hat{\varphi}, \quad \bar{t} = \frac{\sqrt{gH}}{L}\hat{t}, \quad \bar{\eta} = \frac{\hat{\eta}}{a}, \quad \bar{\sigma} = \frac{\hat{\sigma}}{H}. \tag{2.1.8}$$

Substituting these into (2.1.7) and (2.1.5) the non-dimensional version of the water wave equations are obtained:

$$\mu^2\bar{\varphi}_{\bar{x}\bar{x}} + \bar{\varphi}_{\bar{y}\bar{y}} = 0 \qquad \text{in } \Omega \tag{2.1.9a}$$

$$\left.\begin{aligned} &\mu\bar{\eta}_{\bar{t}} + (F + \epsilon\mu\bar{\varphi}_{\bar{x}})\mu\bar{\eta}_{\bar{x}} - \bar{\varphi}_{\bar{y}} = 0 \\ &\mu\bar{\varphi}_{\bar{t}} + F\mu\bar{\varphi}_{\bar{x}} + \tfrac{1}{2}\epsilon(\mu^2\bar{\varphi}_{\bar{x}}^2 + \bar{\varphi}_{\bar{y}}^2) + \bar{\eta} = 0 \end{aligned}\right\} \quad \text{on } \bar{y} = 1 + \epsilon\bar{\eta}(\bar{x}, \bar{t}) \tag{2.1.9b}$$

$$(1 + \mu^2\bar{\sigma}_{\bar{x}}^2)^{-1/2}(-\mu\bar{\sigma}_{\bar{x}}, 1) \cdot (F + \mu\epsilon\bar{\varphi}_{\bar{x}}, \epsilon\bar{\varphi}_{\bar{y}}) = 0. \qquad \text{on } \bar{y} = \bar{\sigma}(\bar{x}) \tag{2.1.9c}$$

where Ω is the flow domain defined by $-\infty < \bar{x} < \infty$, $\bar{\sigma} < \bar{y} < 1 + \epsilon\bar{\eta}$. The non-dimensional parameters introduced are defined as $\mu = \frac{H}{L}$, $\epsilon = \frac{a}{H}$ and the non-dimensional Froude number is defined in (1.0.1). Up to this point the equations are exact, but present a considerable challenge to solve as they are highly nonlinear. In the case of steady flow a boundary integral technique can transform the equations into a simpler system of integro-differential equations that can be solved numerically (see next section). To make progress the height of the channel is assumed small compared to the length so that $\mu \ll 1$. Initially a naive expansion of the form

$$\bar{\varphi} = \sum_0^\infty \mu^n\bar{y}^n\bar{\varphi}_n = \bar{\varphi}_0(\bar{x}, \bar{t}) + \mu\bar{y}\bar{\varphi}_1(\bar{x}, \bar{t}) + \mu^2\bar{y}^2\bar{\varphi}_2(\bar{x}, \bar{t}) + \cdots . \tag{2.1.10}$$

is considered. By inserting (2.1.10) into (2.1.9a), Laplace's equation becomes

$$\mu^2(\bar{\varphi}_{0,\bar{x}\bar{x}} + \mu\bar{y}\bar{\varphi}_{1,\bar{x}\bar{x}} + \mu^2\bar{y}^2\bar{\varphi}_{2,\bar{x}\bar{x}}\cdots) = -(2\mu^2\bar{\varphi}_2 + 6\mu^2\bar{y}\bar{\varphi}_3\cdots).$$

By equating coefficients of μ^n, the following recursive relations are obtained for $n < 5$

$$\begin{aligned} O(\mu^2): &\quad \bar{\varphi}_{0,\bar{x}\bar{x}} = -2\bar{\varphi}_2, \\ O(\mu^3): &\quad \bar{\varphi}_{1,\bar{x}\bar{x}} = -6\bar{\varphi}_3, \\ O(\mu^4): &\quad \bar{\varphi}_{2,\bar{x}\bar{x}} = -12\bar{\varphi}_4, \\ &\vdots \end{aligned}$$

The functions, $\bar{\varphi}_n$, can be expressed purely in terms of $\bar{\varphi}_0$, $\bar{\varphi}_1$ and their derivatives. The first few can be written as

$$\bar{\varphi}_2 = -\frac{1}{2}\bar{\varphi}_{0,\bar{x}\bar{x}}, \tag{2.1.11a}$$

$$\bar{\varphi}_3 = -\frac{1}{6}\bar{\varphi}_{1,\bar{x}\bar{x}}, \tag{2.1.11b}$$

$$\bar{\varphi}_4 = \frac{1}{24}\bar{\varphi}_{0,\bar{x}\bar{x}\bar{x}\bar{x}}, \tag{2.1.11c}$$

$$\vdots$$

The problem has been reduced to finding two unknown functions; $\bar{\varphi}_0$, the leading order term for the potential, and $\bar{\varphi}_1$, the first order term. The first order term $\bar{\varphi}_1$ can be written in terms of the topography using the boundary condition on $\bar{y} = \bar{\sigma}$. To see this, as $\mu \ll 1$, the condition in (2.1.9c) can be linearised to obtain

$$(F + \mu\epsilon\bar{\varphi}_{\bar{x}})\mu\bar{\sigma}_{\bar{x}} = \epsilon\bar{\varphi}_{\bar{y}}, \qquad \text{on } \bar{y} = \bar{\sigma}. \tag{2.1.12}$$

The expansion, (2.1.10), is substituted into (2.1.12). The leading order balance yields an expression for $\bar{\varphi}_1$ in the form

$$\epsilon\bar{\varphi}_1(\bar{x}, \hat{t}) = F\bar{\sigma}_{\bar{x}}. \tag{2.1.13}$$

By assuming that $\epsilon \ll 1$ means that there is no balance as the left hand side is $O(\epsilon)$ and the right hand side is $O(1)$. Therefore the topography is rescaled by $\bar{\sigma} \mapsto \epsilon\bar{\sigma}$. By performing this transformation the leading order balance yields an expression for $\bar{\varphi}_1$ in the form

$$\bar{\varphi}_1(\bar{x}, \hat{t}) = F\bar{\sigma}_{\bar{x}}. \tag{2.1.14}$$

which is independent of the small parameter ϵ. Now the relations in (2.1.11) can be written purely in terms of $\bar{\varphi}_0$ and $\bar{\sigma}$. The asymptotic expansion in (2.1.10) can be

written as

$$\bar{\varphi} = \bar{\varphi}_0 + \mu\bar{y}F\bar{\sigma}_{\bar{x}} - \frac{1}{2}\mu^2\bar{y}^2\bar{\varphi}_{0,xx} - \frac{1}{6}\mu^3\bar{y}^3F\bar{\sigma}_{\bar{x}\bar{x}\bar{x}} + \frac{1}{24}\mu^4\bar{y}^4\bar{\varphi}_{0,\bar{x}\bar{x}\bar{x}\bar{x}} + \cdots \tag{2.1.15}$$

It is noted that in the absence of a topography $\hat{\sigma} = 0$, and the expansion above only contains even powers of μ and $\hat{y}$, (see, also Whitham, 1974). It is also reiterated that to get to this point it has been assumed that μ and ϵ are both small and that $\bar{\sigma}$ has been rescaled by ϵ.

To proceed further the expression for $\bar{\varphi}$ from (2.1.15) is now substituted into the two boundary conditions on the free-surface. First (2.1.15) is substituted into the non-dimensionalized kinematic boundary condition, the first equation in (2.1.9b), to obtain

$$\begin{aligned}\bar{\eta}_{\bar{t}} + \Bigg[F + \epsilon\mu\Bigg(&\bar{\varphi}_0 + \mu(1+\epsilon\bar{\eta})F\bar{\sigma}_{\bar{x}} - \frac{1}{2}\mu^2(1+\epsilon\bar{\eta})^2\bar{\varphi}_{0,xx} \\ &-\frac{1}{6}\mu^3(1+\epsilon\bar{\eta})^3F\bar{\sigma}_{\bar{x}\bar{x}\bar{x}} + \frac{1}{24}\mu^4(1+\epsilon\bar{\eta})^4\bar{\varphi}_{0,\bar{x}\bar{x}\bar{x}\bar{x}} + \cdots\Bigg)\Bigg]\bar{\eta}_{\bar{x}} \\ = F\bar{\sigma}_{\bar{x}} - \mu(1+\epsilon\bar{\eta})\bar{\varphi}_{0,xx} &- \frac{1}{2}\mu^2(1+\epsilon\bar{\eta})^2F\bar{\sigma}_{\bar{x}\bar{x}\bar{x}} + \frac{1}{6}\mu^3(1+\epsilon\bar{\eta})^3\bar{\varphi}_{0,\bar{x}\bar{x}\bar{x}\bar{x}} + \cdots .\end{aligned} \tag{2.1.16}$$

Looking at the right hand side and the left hand side of (2.1.16) it can be seen there is a leading order balance at $O(1)$ but there is not a balance at $O(\mu)$. At $O(\mu)$, $\bar{\varphi}_{0,\bar{x}\bar{x}} = 0$ and therefore $\bar{\varphi}_0 = A\bar{x} + B$ for constants A and B. Examining the flow in the far-field requires that A and B are zero and hence $\bar{\varphi}_0 = 0$, resulting in all even power terms in (2.1.15) to vanish. This means that if there is no topography, there can be no flow disturbance, which on physical grounds is not permissible. To remedy this $\bar{\varphi}_0$ is rescaled by $\bar{\varphi}_0 \mapsto \frac{1}{\mu}\bar{\varphi}_0$. The rescaled equation in (2.1.16) becomes

$$\begin{aligned}\bar{\eta}_{\bar{t}} + \Bigg[F + \epsilon\Bigg(&\bar{\varphi}_0 + \mu^2(1+\epsilon\bar{\eta})F\bar{\sigma}_{\bar{x}} - \frac{1}{2}\mu^2(1+\epsilon\bar{\eta})^2\bar{\varphi}_{0,xx} \\ &-\frac{1}{6}\mu^3(1+\epsilon\bar{\eta})^3F\bar{\sigma}_{\bar{x}\bar{x}\bar{x}} + \frac{1}{24}\mu^3(1+\epsilon\bar{\eta})^4\bar{\varphi}_{0,\bar{x}\bar{x}\bar{x}\bar{x}} + \cdots\Bigg)\Bigg]\bar{\eta}_{\bar{x}} \\ = F\bar{\sigma}_{\bar{x}} - (1+\epsilon\bar{\eta})\bar{\varphi}_{0,xx} &- \frac{1}{2}\mu^2(1+\epsilon\bar{\eta})^2F\bar{\sigma}_{\bar{x}\bar{x}\bar{x}} + \frac{1}{6}\mu^2(1+\epsilon\bar{\eta})^3\bar{\varphi}_{0,\bar{x}\bar{x}\bar{x}\bar{x}} + \cdots .\end{aligned} \tag{2.1.17}$$

There are now balances at each order. At this stage the equation involves two small parameters, ϵ and μ and nothing has been remarked regarding their relative magnitude. The smallest powers of these parameters are ϵ and μ^2. Therefore it is assumed that $\epsilon \sim \mu^2$ so terms of order $O(\epsilon + \mu^2)$ can be safely neglected in (2.1.17). Proceeding in this way yields the weakly nonlinear approximation to (2.1.17) as

$$\bar{\eta}_{\bar{t}} + (F + \epsilon\bar{\varphi}_{0,\bar{x}})\bar{\eta}_{\bar{x}} + \bar{\varphi}_{0,\bar{x}\bar{x}} - F\bar{\sigma}_{\bar{x}} + \epsilon\bar{\varphi}_{0,\bar{x}\bar{x}}\bar{\eta} - \frac{1}{6}\mu^2\bar{\varphi}_{0,\bar{x}\bar{x}\bar{x}\bar{x}} + \frac{1}{2}\mu^2F\bar{\sigma}_{\bar{x}\bar{x}\bar{x}} = 0. \tag{2.1.18}$$

It is noted now that the correct expansion for the potential, $\bar{\varphi}$ takes the form

$$\bar{\varphi} = \frac{1}{\mu}\bar{\varphi}_0 + \mu(\bar{y}F\bar{\sigma}_{\bar{x}} - \frac{1}{2}\bar{y}^2\bar{\varphi}_{0,xx}) - \mu^3(\frac{1}{6}\bar{y}^3F\bar{\sigma}_{\bar{x}\bar{x}\bar{x}} + \frac{1}{24}\bar{y}^4\bar{\varphi}_{0,\bar{x}\bar{x}\bar{x}\bar{x}}) + \cdots . \tag{2.1.19}$$

This asymptotic expansion is substituted into the dynamic boundary condition, the second equation in (2.1.9b) which is restated for convenience

$$\mu\bar{\varphi}_{\bar{t}} + F\mu\bar{\varphi}_{\bar{x}} + \frac{1}{2}\epsilon\left(\mu^2\bar{\varphi}_{\bar{x}}^2 + \bar{\varphi}_{\bar{y}}^2\right) + \bar{\eta} = 0. \tag{2.1.20}$$

The expression (2.1.19) is substituted into (2.1.20) and then differentiated with respect to $\bar{x}$. Truncating at $o(\epsilon + \mu^2)$ the dynamic boundary condition becomes

$$\bar{\eta}_{\bar{x}} + F\bar{\varphi}_{0,\bar{x}\bar{x}} + \bar{\varphi}_{0,\bar{x}\bar{t}} + \epsilon\bar{\varphi}_{0,\bar{x}}\bar{\varphi}_{0,\bar{x}\bar{x}} - \frac{1}{2}\mu^2F\bar{\varphi}_{0,\bar{x}\bar{x}\bar{x}\bar{x}} - \frac{1}{2}\mu^2\bar{\varphi}_{0,\bar{x}\bar{x}\bar{x}\bar{t}} + \mu^2F^2\bar{\sigma}_{\bar{x}\bar{x}\bar{x}} = 0. \tag{2.1.21}$$

Two equations from the boundary conditions at the free-surface have been derived that determine the leading order potential $\bar{\varphi}_0$ and $\bar{\eta}$. For convenience, let $\bar{\varphi}_{0,\bar{x}} = w$, and the equations in (2.1.18) and (2.1.21) become

$$\bar{\eta}_{\bar{t}} + (F + \epsilon w)\bar{\eta}_{\bar{x}} + w_{\bar{x}} - F\bar{\sigma}_{\bar{x}} + \epsilon w_{\bar{x}}\bar{\eta} - \frac{1}{6}\mu^2w_{\bar{x}\bar{x}\bar{x}} + \frac{1}{2}\mu^2F\bar{\sigma}_{\bar{x}\bar{x}\bar{x}} = 0, \tag{2.1.22a}$$

$$\bar{\eta}_{\bar{x}} + Fw_{\bar{x}} + w_{\bar{t}} + \epsilon ww_{\bar{x}} - \frac{1}{2}\mu^2Fw_{\bar{x}\bar{x}\bar{x}} - \frac{1}{2}\mu^2w_{\bar{x}\bar{x}\bar{t}} + \mu^2F^2\bar{\sigma}_{\bar{x}\bar{x}\bar{x}} = 0. \tag{2.1.22b}$$

Before continuing to higher order systems it is worthwhile considering the equations in the limit $\epsilon \sim \mu^2 \to 0$. Insight can be gained by the linear case to help inform the higher order analysis. Equations (2.1.22a) and (2.1.22b) become:

$$\bar{\eta}_{\bar{t}} + F\bar{\eta}_{\bar{x}} + w_{\bar{x}} = F\bar{\sigma}_{\bar{x}}, \tag{2.1.23a}$$

$$w_{\bar{t}} + Fw_{\bar{x}} + \bar{\eta}_{\bar{x}} = 0. \tag{2.1.23b}$$

The free-surface, $\bar{\eta}$ can be eliminated and a PDE for w can be stated as

$$w_{\bar{t}\bar{t}} + 2Fw_{\bar{x}\bar{t}} + (F^2 - 1)w_{\bar{x}\bar{x}} = -F\bar{\sigma}_{\bar{x}\bar{x}}. \tag{2.1.24}$$

This is can be written in operator form as:

$$L_+L_-w = \left(\frac{\partial}{\partial\bar{t}} + (F+1)\frac{\partial}{\partial\bar{x}}\right)\left(\frac{\partial}{\partial\bar{t}} + (F-1)\frac{\partial}{\partial\bar{x}}\right)w = -F\bar{\sigma}_{\bar{x}\bar{x}}.$$

Each of the operators produces a travelling wave solution. The L_+ operator produces a wave travelling to the right with speed $F+1$ whilst the second bracket L_- represents produces a wave travelling to the right with speed $F-1$. If $F < 1$ there are waves travelling to the right with speed $F+1$ and to the left with speed $F-1$. For $F > 1$ there are waves travelling to the right only. Waves travelling in one direction, to the

right only, are considered. This equation has a solution of the form

$$w(\bar{x},\bar{t}) = G_1(\bar{x}-(F+1)\bar{t}) + G_2(\bar{x}-(F-1)\bar{t}) - \frac{F}{F^2-1}\bar{\sigma}(\bar{x}) \tag{2.1.25}$$

and the corresponding expression for $\bar{\eta}$ is

$$\bar{\eta}(\bar{x},\bar{t}) = G_1(\bar{x}-(F+1)\bar{t}) + G_2(\bar{x}-(F-1)\bar{t}) + \frac{F^2}{F^2-1}\bar{\sigma}(\bar{x}), \tag{2.1.26}$$

where G_1 and G_2 are arbitrary functions. For flow speeds close to $F=\pm 1$ the non-homogeneous part of the solution creates large free surface displacement which contradict the fact that the free-surface displacement is small (in fact of $O(\epsilon)$). In this case resonance occurs. To avoid this the bottom topography is rescaled so that $\bar{\sigma} \mapsto \epsilon\bar{\sigma}$. The linear equations are now written as:

$$\bar{\eta}_{\bar{t}} + F\bar{\eta}_{\bar{x}} + w_{\bar{x}} = 0, \tag{2.1.27a}$$

$$w_{\bar{t}} + Fw_{\bar{x}} + \bar{\eta}_{\bar{x}} = 0. \tag{2.1.27b}$$

Examining (2.1.27a) and (2.1.27b) suggests that $w = \pm\bar{\eta}$. Choosing $w = -\bar{\eta}$ means that from (2.1.27a) that $\bar{\eta}_{\bar{t}} = -(F-1)\bar{\eta}_{\bar{x}}$. This choice of sign restricts the waves to moving to the right with wavespeed $F-1$. The system of equations in (2.1.27) can be solved by

$$w = -\bar{\eta}, \tag{2.1.28a}$$

$$\bar{\eta}_{\bar{t}} = -(F-1)\bar{\eta}_{\bar{x}}. \tag{2.1.28b}$$

These relations eliminate the leading order velocity potential if $\epsilon, \mu = 0$. Now if terms of order $O(\epsilon+\mu^2)$ are retained then the weakly nonlinear equations in (2.1.22a) and (2.1.22b) have to be considered. The equations (2.1.22a) and (2.1.22b) are restated as

$$\bar{\eta}_{\bar{t}} + (F+\epsilon w)\bar{\eta}_{\bar{x}} + w_{\bar{x}} - F\bar{\sigma}_{\bar{x}} + \epsilon w_{\bar{x}}\bar{\eta} - \frac{1}{6}\mu^2 w_{\bar{x}\bar{x}\bar{x}} + \frac{1}{2}\mu^2 F\bar{\sigma}_{\bar{x}\bar{x}\bar{x}} = 0, \tag{2.1.29a}$$

$$\bar{\eta}_{\bar{x}} + Fw_{\bar{x}} + w_{\bar{t}} + \epsilon w w_{\bar{x}} - \frac{1}{2}\mu^2 F w_{\bar{x}\bar{x}\bar{x}} - \frac{1}{2}\mu^2 w_{\bar{x}\bar{x}\bar{t}} + \mu^2 F^2\bar{\sigma}_{\bar{x}\bar{x}\bar{x}} = 0. \tag{2.1.29b}$$

Recalling that in the linear theory the topography was rescaled, $\bar{\sigma} \mapsto \epsilon\bar{\sigma}$ is replaced in the (2.1.29b). Terms of order ϵ^2 are dropped and (2.1.29a) and (2.1.29b) become

$$\bar{\eta}_{\bar{t}} + (F+\epsilon w)\bar{\eta}_{\bar{x}} + w_{\bar{x}} - F\epsilon\bar{\sigma}_{\bar{x}} + \epsilon w_{\bar{x}}\bar{\eta} - \frac{1}{6}\mu^2 w_{\bar{x}\bar{x}\bar{x}} = 0, \tag{2.1.30a}$$

$$\bar{\eta}_{\bar{x}} + Fw_{\bar{x}} + w_{\bar{t}} + \epsilon w w_{\bar{x}} - \frac{1}{2}\mu^2 F w_{\bar{x}\bar{x}\bar{x}} - \frac{1}{2}\mu^2 w_{\bar{x}\bar{x}\bar{t}} = 0. \tag{2.1.30b}$$

Inspired by (2.1.28a), to eliminate the velocity potential w in (2.1.29a) and (2.1.29b) the form

$$w = -\bar{\eta} + \epsilon A + \mu^2 B, \tag{2.1.31}$$

is substituted into (2.1.30a) and (2.1.30b). A and B are functions of $\bar{\eta}$ and $\bar{\eta}$ derivatives. These are the small order corrections to the expression (2.1.28a). Using (2.1.28b), the fact that

$$\bar{\eta}_{\bar{t}} = -(F-1)\bar{\eta}_{\bar{x}}, \tag{2.1.32}$$

will transform time derivatives in w to spatial derivatives in w. To transform the time derivatives of A and B into spatial derivatives it is noted that

$$A_{\bar{t}} = \bar{\eta}_{\bar{t}} A_{\bar{\eta}} + \cdots = -(F-1)\bar{\eta}_{\bar{x}} A_{\bar{\eta}} + \cdots = -(F-1)A_{\bar{x}}.$$

Therefore the time derivatives can be completely eliminated by writing $A_{\bar{t}} \approx -(F-1)A_{\bar{x}}$ and $B_{\bar{t}} \approx -(F-1)B_{\bar{x}}$. To eliminate w, (2.1.31) and (2.1.32) are substituted into (2.1.30a) and (2.1.30b). These equations should be consistent at orders $O(\epsilon)$ and $O(\mu^2)$. By equating terms of $O(\epsilon)$ in (2.1.30a) and (2.1.30b) the following identity is established

$$\bar{\eta}\bar{\eta}_{\bar{x}} + A_{\bar{x}} \equiv F\bar{\sigma}_{\bar{x}} + 2\bar{\eta}\bar{\eta}_{\bar{x}} - A_{\bar{x}}, \tag{2.1.33}$$

which means that

$$A_{\bar{x}} \equiv \frac{1}{2}\bar{\eta}\bar{\eta}_{\bar{x}} + \frac{1}{2}F\bar{\sigma}_{\bar{x}}. \tag{2.1.34}$$

Similarly at $O(\mu^2)$ the identity

$$\frac{1}{2}\bar{\eta}_{\bar{x}\bar{x}\bar{x}} + B_{\bar{x}} \equiv -\frac{1}{6}\bar{\eta}_{\bar{x}\bar{x}\bar{x}} - B_{\bar{x}}, \tag{2.1.35}$$

is formed. This implies that

$$B_{\bar{x}} \equiv -\frac{1}{3}\bar{\eta}_{\bar{x}\bar{x}\bar{x}}. \tag{2.1.36}$$

Therefore w takes the form

$$w = -\bar{\eta} + \epsilon\left(\frac{1}{4}\bar{\eta}^2 + \frac{1}{2}F\bar{\sigma}\right) - \mu^2\left(\frac{1}{3}\bar{\eta}_{\bar{x}\bar{x}}\right). \tag{2.1.37}$$

Substituting (2.1.37) into either of (2.1.30a) or (2.1.30b) will eliminate w. To eliminate the the mixed time derivatives (2.1.31) and (2.1.32) are utilised. Therefore by performing this substitution both of the equations in (2.1.30a) and (2.1.30b) become a single equation for $\bar{\eta}$ written as

$$\bar{\eta}_{\bar{t}} + (F-1)\bar{\eta}_{\bar{x}} - \frac{3}{2}\epsilon\bar{\eta}\bar{\eta}_{\bar{x}} - \frac{1}{6}\mu^2\bar{\eta}_{\bar{x}\bar{x}\bar{x}} = \frac{1}{2}F\epsilon\bar{\sigma}_{\bar{x}}. \tag{2.1.38}$$

To balance this equation it is assumed that $F \approx 1$. Writing $F = 1 + \epsilon\lambda$, scaling $\bar{t}$ by writing $\bar{t} \mapsto \epsilon^{-1}\bar{t}$ and taking the distinguished limit; $\mu^2 \sim \epsilon$, the equation becomes (upon dropping terms of $O(\epsilon^2)$)

$$\bar{\eta}_t + \lambda\bar{\eta}_{\bar{x}} - \frac{3}{2}\bar{\eta}\bar{\eta}_{\bar{x}} - \frac{1}{6}\bar{\eta}_{\bar{x}\bar{x}\bar{x}} = \frac{1}{2}\bar{\sigma}_{\bar{x}}. \tag{2.1.39}$$

Physical Variables	Non-dimensional Variables	Long-wave Variables
$\hat{x}$	$\bar{x}L$	xH
$\hat{y}$	$\bar{y}H$	yH
$\hat{t}$	$\bar{t}\frac{L}{\sqrt{gH}}$	$t\frac{a}{\sqrt{gH}}$
$\hat{\eta}$	$\bar{\eta}a$	ηH
$\hat{\varphi}$	$\bar{\varphi}a\sqrt{gH}$	$\varphi H\sqrt{gH}$
$\hat{\sigma}$	$\bar{\sigma}H$	$\epsilon^2\sigma H$

Table 2.1: Scaling of the physical, non-dimensional and long-wave variables. Between columns read it as , i.e. $\hat{x} \sim L\bar{x} \sim Hx$, etc.

Finally the variables are scaled by

$$\bar{x} = \epsilon^{1/2}x, \;\; \bar{t} = \epsilon^{3/2}t, \;\; \bar{\eta} = \epsilon^{-1}\eta, \;\; \bar{\sigma} = \epsilon^{-2}\sigma. \tag{2.1.40}$$

Equation (2.1.39) becomes

$$\eta_t + (F-1)\eta_x - \frac{3}{2}\eta\eta_x - \frac{1}{6}\eta_{xxx} = \frac{1}{2}\sigma_x. \tag{2.1.41}$$

This is the *forced Korteweg de Vries equation* (fKdV). It is finally worth highlighting the scaling involved from going from the physical variables $(\hat{x}, \hat{y}, \hat{t}, \hat{\eta}, \hat{\sigma}, \hat{\varphi})$ to the non-dimensionalized variables, $(\bar{x}, \bar{y}, \bar{t}, \bar{\eta}, \bar{\sigma}, \bar{\varphi})$ to the long-wave variables, $(x, y, t, \eta, \sigma, \varphi)$. This is shown in table 2.1. The analysis can easily be extended for waves where surface tension is present. The tension strength T is defined and then the dynamic boundary condition becomes

$$\hat{\varphi}_{\hat{t}} + \frac{1}{2}(U + \hat{\varphi}_{\hat{x}})^2 + \frac{1}{2}\hat{\varphi}_{\hat{y}}^2 + g\hat{y} = \frac{1}{2}U^2 + \frac{T\hat{\eta}_{\hat{x}\hat{x}}}{(1+\hat{\eta}_{\hat{x}}^2)^{\frac{3}{2}}} \tag{2.1.42}$$

In the non-dimensional variables at leading order this becomes

$$\epsilon\mu\bar{\varphi}_{\bar{t}} + F\epsilon\mu\bar{\varphi}_{\bar{x}} + \epsilon^2\frac{1}{2}(\mu^2\bar{\varphi}_{\bar{x}}^2 + \bar{\varphi}_{\bar{y}}^2) + 1 + \epsilon\bar{\eta} - \tau\epsilon\mu^2\bar{\eta}_{\bar{x}\bar{x}} = 0 \tag{2.1.43}$$

where

$$\tau = \frac{T}{\rho g H^2} \tag{2.1.44}$$

is the non-dimensional *Bond number* describing the strength of the surface tension. The analysis afterwards is very similar and eventually the fKdV with surface tension is derived:

$$\eta_t + (F-1)\eta_x - \frac{3}{2}\eta\eta_x - \frac{1}{2}\left(\frac{1}{3} - \tau\right)\eta_{xxx} = \frac{1}{2}\sigma_x \tag{2.1.45}$$

If there is no surface tension then $\tau = 0$ and (2.1.41) is retained as before. Clearly the dispersive behaviour of the equation is determined by the coefficient of the η_{xxx} term. For $\tau < \frac{1}{3}$ the surface tension is weak but the sign of the term is the same as the one for no surface tension. For $\tau > \frac{1}{3}$ the dispersive behaviour changes sign. Therefore the regime $\tau < \frac{1}{3}$ is for *weak surface tension* where the fKdV (2.1.41) describes the waves and the regime $\tau > \frac{1}{3}$ is for *strong surface tension* where (2.1.45) is more appropriate. Note that this agrees with the results of Maleewong *et al.* (2005), Ablowitz & Clarkson (1991) , Meur (2015) and Lannes (2013).

2.1.1 Discussion

The properties of the fKdV equation are briefly discussed (for no surface tension, $\tau = 0$) . Each term in (2.1.41) holds physical relevance. The first term is simply a term governing whether the free surface is steady or not. If a topography is absent then travelling wave solutions can be obtained by transforming the equation to a moving frame of reference by a Galilean transformation of the independent variable. In the presence of a topography this is not possible as translation symmetry is broken. Hence steady solutions to the fKdV equation can be found by setting $\eta_t = 0$.

The second term is a linear transport term and is a direct consequence of translation symmetry being broken (in the case of no topography this term is usually omitted in the literature). The third term is nonlinear which in general is responsible for shock wave solutions and wave breaking (if the higher order derivatives are neglected then the water wave equations can be simplified to the shallow-water wave equations; a system of equations allowing shock wave solutions, (see, for example Acheson, 1990)). The fourth term is the dispersive term which is responsible for wave dispersion. The overall balance of these last two effects make KdV equations interesting to study as the dispersive effects interact with the nonlinear effects so that wave breaking does not occur and solitary waves can form. The final term on the right hand side is the effect due to the bottom topography; the forcing term.

As a model for long-wave theory the validity has been studied extensively especially by Shen (1995) and others. Shen (1995) stated that the amplitude of the bottom topography has to be of order $O(\epsilon^2)$ and the typical horizontal variation has to be at most half of the typical depth. Shen (1995) also found that in these cases the Dirac-delta function $\alpha\delta(x)$ can provide a reasonable estimate if α is the area underneath the bottom topography. This forms the basis of the analysis of the next section.

2.2 Steady flow over a point forcing

The forced KdV equation has been derived as an approximation to the fully nonlinear water wave equations. The aim of this section is to use the fKdV equation to characterise the known solution space when the topography is a narrow bump or dip. This

has been investigated thoroughly by Binder & Vanden-Broeck (2006), Binder *et al.* (2005), Dias & Vanden-Broeck (2002*b*), Lustri *et al.* (2006), Chapman & Vanden-Broeck (2006), Wade *et al.* (2014) and others but is included in detail here so as to provide motivation for analysis in further chapters.

The steady fKdV equation can be found by writing $\eta_t = 0$ in (2.1.41). After an initial integration this becomes

$$\eta_{xx} + \frac{9}{2}\eta^2 - 6(F-1)\eta + A = -3\sigma(x), \tag{2.2.1}$$

where A is a constant of integration. Solutions are sought that are wave-free far upstream, i.e.

$$\eta, \eta_x, \eta_{xx} \to 0, \qquad \text{as } x \to -\infty. \tag{2.2.2}$$

The topography, σ is chosen to model a narrow dip or bump. As $x \to -\infty$ all of the terms in (2.2.1) vanish due to (2.2.2) and hence A is chosen to be zero. To simplify the analysis σ is chosen to be $\hat{\alpha}\delta(x)$, where $\delta(x)$ is the Dirac delta function. The steady fKdV becomes

$$\eta_{xx} + \frac{9}{2}\eta^2 - 6(F-1)\eta = -3\hat{\alpha}\delta(x) \tag{2.2.3}$$

and a further integration of (2.2.3) (and setting the constant to zero using the same argument as before) yields the dynamical system

$$\eta_x = \rho, \tag{2.2.4a}$$

$$\rho_x = 6(F-1)\eta - \frac{9}{2}\eta^2, \tag{2.2.4b}$$

which is valid for $x \neq 0$. A 'jump' condition can also be derived across $x = 0$ as

$$\rho(0+) - \rho(0-) = -3\hat{\alpha}. \tag{2.2.5}$$

The equilibrium points (η_s, ρ_s) of (2.2.4) satisfy

$$\rho = 0 \tag{2.2.6}$$

$$6(F-1)\eta - \frac{9}{2}\eta^2 = 0. \tag{2.2.7}$$

The equilibrium points are therefore at $(\eta_s, \rho_s) = (0, 0)$ and $(\eta_s, \rho_s) = \left(\frac{4}{3}(F-1), 0\right)$. The system can be linearised by writing $\eta = \eta_s + \eta^*$ and $\rho = \rho_s + \rho^*$ where the starred quantities are small and hence close to the equilibrium points. The linearised system can be written in matrix form as

$$\begin{pmatrix} \eta^*_x \\ \rho^*_x \end{pmatrix} = \begin{pmatrix} 0 & 1 \\ 6(F-1) - \frac{9}{2}\eta_s & 0 \end{pmatrix} \begin{pmatrix} \eta^* \\ \rho^* \end{pmatrix}. \tag{2.2.8}$$

Near the stationary point $(0,0)$ the eigenvalues s satisfy:

$$s^2 = 6(F-1) \tag{2.2.9}$$

Hence there are two distinct cases. If $F > 1$, defined as *super-critical* flow, then the origin is a saddle node, whilst if $F < 1$, defined as *sub-critical* flow, then the origin becomes a centre due to the imaginary eigenvalues. On the other hand for the equilibrium point $(\frac{4}{3}(F-1),0)$ the eigenvalues satisfy:

$$s^2 = -6(F-1) \tag{2.2.10}$$

and the opposite occurs. When $F = 1$ the equilibrium point becomes degenerate and and this is defined as *critical* flow. The three cases are examined separately.

Super-Critical Flow

For $F > 1$ there are periodic orbits around the center $(\frac{4}{3}(F-1),0)$ of varying amplitudes. The amplitude of the periodic waves are limited by the homoclinic trajectory emanating from the saddle node at $(0,0)$ traversing around the centre and returning to the saddle node. This trajectory corresponds to a solitary wave solution. The phase planes are shown in figures 2.2.1(b) and (d). The amplitude of the solitary wave can be found by integrating (2.2.4b) to find

$$(\eta_x)^2 = 6(F-1)\eta^2 - 3\eta^3 + C, \tag{2.2.11}$$

where C is a constant. For the trajectory passing through $(\eta,\eta_x) = (0,0)$, in order to satisfy the boundary conditions, C has to be zero. By solving this equation for η when $\eta_x = 0$ gives the amplitude of the unforced solitary wave traversing the homoclinic orbit as

$$\eta_{max} = 2(F-1).$$

The jump condition (2.2.5) has to be invoked. It requires that the change in ρ is equal to $-3\hat{\alpha}$. This means for $\hat{\alpha} < 0$ (a dip) an 'upwards' jump occurs and for $\hat{\alpha} > 0$ (a bump) a 'downwards' jump occurs. For $F > 1$ there are two ways this is possible if $\hat{\alpha} > 0$, and three ways if $\hat{\alpha} < 0$. These solutions are classified by Wade *et al.* (2014) as solution types I to V. See figures 2.2.1(a) and (c) for the profiles for $F > 1$. All of these solutions are a two-parameter family depending on $\hat{\alpha}$ and F. Figure 2.2.4 shows the solution space for varying $\hat{\alpha}$ and F and is explained in more detail later.

The size of the jump is determined by $\hat{\alpha}$ and there are limits that can be imposed in order for a steady solution to exist. The maximum this can be is found by finding the length of line jumping from the one part of the homoclinic orbit to the other passing through the centre as shown in figures 2.2.1(b) and (d). So by substituting $\eta = \frac{4}{3}(F-1)$

in (2.2.11) a maximum value for $\hat{\alpha}$ can be derived

$$\hat{\alpha}_{max} = \frac{8\sqrt{2}}{9}(F-1)^{\frac{3}{2}}. \tag{2.2.12}$$

This value will help impose limits on the value of $\hat{\alpha}$ that give steady solutions.

Critical Flow

When $F = 1$ the equilibrium point is degenerate. There are unbounded trajectories with unique stable and unstable orbits intersecting the origin in the phase plane $(\eta, \eta_x) = (0, 0)$ as shown in figure 2.2.1(f). Solutions start at the origin and move in the lower-left half (η, η_x) plane. A steady solution only exists therefore if $\hat{\alpha} < 0$ as this corresponds to an upwards 'jump' in the phase plane on to the orbit in the upper-left plane which returns to the origin. The profile is shown in figure 2.2.1(e). Note when $F = 1$ the equation for $x \neq 0$,

$$\eta_{xx} + \frac{9}{2}\eta^2 = 0 \tag{2.2.13}$$

has the exact solution

$$\eta = -\frac{4}{3(x - C_1)^2} \tag{2.2.14}$$

where C_1 is a constant of integration which can be expressed in terms of the height of the bump. Trajectories in the phase plane therefore approach the origin with a zero slope and the far-field behaviour of the profile is algebraic as opposed to the super-critical solutions which decay exponentially in the far-field.

Sub-Critical Flow

When $F < 1$ a global bifurcation occurs in the phase plane. The centre is now at the origin and the saddle node is at $(\frac{4}{3}(F-1), 0)$. To satisfy the boundary conditions (2.2.2) solutions must start as the origin $(\eta, \eta_x) = (0, 0)$ far upstream. When these solutions 'jump' up (down) over the bump they will enter a periodic orbit and hence there will be a solution consisting of a flat-free surface upstream but periodic waves downstream. This is called a *cnoidal wave* solution as shown in figure 2.2.2(a) with corresponding phase plane in figure 2.2.2(b). This is a two parameter family depending on $\hat{\alpha}$ and F. The maximum possible jump for when $F < 1$ is given by

$$\hat{\alpha}_{max} = \frac{4\sqrt{2}}{9}(1-F)^{\frac{3}{2}} \tag{2.2.15}$$

Using (2.2.12) and (2.2.15) there is a range of possible values for F for which there is *no* steady flow

$$1 - \left(\frac{9\hat{\alpha}}{4\sqrt{2}}\right)^{\frac{2}{3}} < F < 1 + \left(\frac{9\hat{\alpha}}{8\sqrt{2}}\right)^{\frac{2}{3}} \tag{2.2.16}$$

It should be noted that these limits refer to the values of $\hat{\alpha}$ for which there are no steady solutions. This is defined as the *transcritical* range where typical *undular bores*

are formed in the time-dependent response from a flat initial state. The solution space in terms of $(\hat{\alpha}, F)$ is sketched out in figure 1.0.2 in the introduction. These limits verify the results of Binder *et al.* (2014) and Grimshaw *et al.* (2007).

Hydraulic Falls

The final type of steady solution occurs when the flow is flat and $F > 1$ far upstream. The solution starts at the saddle-node at the origin and then traverses the homoclinic orbit until the jump condition causes the trajectory to latch onto a periodic cnoidal wave solution oscillating around the value of $\eta = \frac{4}{3}(F-1)$ as seen in figures 2.2.3(a) and (b). This is called a *generalised hydraulic fall* (Dias & Vanden-Broeck, 2002*b*). This is a three-parameter family of solutions depending on $\hat{\alpha}$, F and the period of the cnoidal orbit that it jumps on to.

There is also a family of solutions where the size of the jump dictates that the trajectory can jump onto the centre at $(\eta, \eta_x) = \left(\frac{4}{3}(F-1), 0\right)$. The solution is therefore flat far downstream but at an elevated level. This is known as a *hydraulic fall* as shown in figure 2.2.3(c) with corresponding phase plane in figure 2.2.3(d). This solution is only achievable when $|\hat{\alpha}|^2 = \frac{32}{81}(F-1)^3$, and therefore it is a one-parameter family of solutions.

2.2.1 Solution Space for super-critical flow

When describing the solution space for super-critical flow it is useful to categorise the solutions in terms of $\eta(0)$ as the profiles are symmetric. If F is fixed and $\hat{\alpha}$ varied then the shape of the bifurcation curve takes the form

$$\hat{\alpha}^2 = \frac{4}{3}(2(F-1)\eta^2(0) - \eta^3(0)). \tag{2.2.17}$$

Additionally $\hat{\alpha}$ must be contained by the limits given in (2.2.16). This can can be seen in the solution space diagrams in the $(\hat{\alpha}, \eta(0)$ space as seen in figure 2.2.4(a) where the limits are represented as folds. In contrast if $\hat{\alpha}$ is fixed and F is varied the solution space in the $(F, \eta(0))$ solution space with $\hat{\alpha}$ fixed will also take the form of (2.2.17), but is restated in a more convenient form

$$F = 1 + \frac{3\hat{\alpha}^2 + 4\eta^3(0)}{8\eta^3(0)}. \tag{2.2.18}$$

The fold in the$(F, \eta(0))$ space will occur at

$$(F, \eta(0)) = \left(1 + \left(\frac{9\hat{\alpha}}{8\sqrt{2}}\right)^{\frac{2}{3}}, \sqrt{\frac{3}{2}}\hat{\alpha}\right). \tag{2.2.19}$$

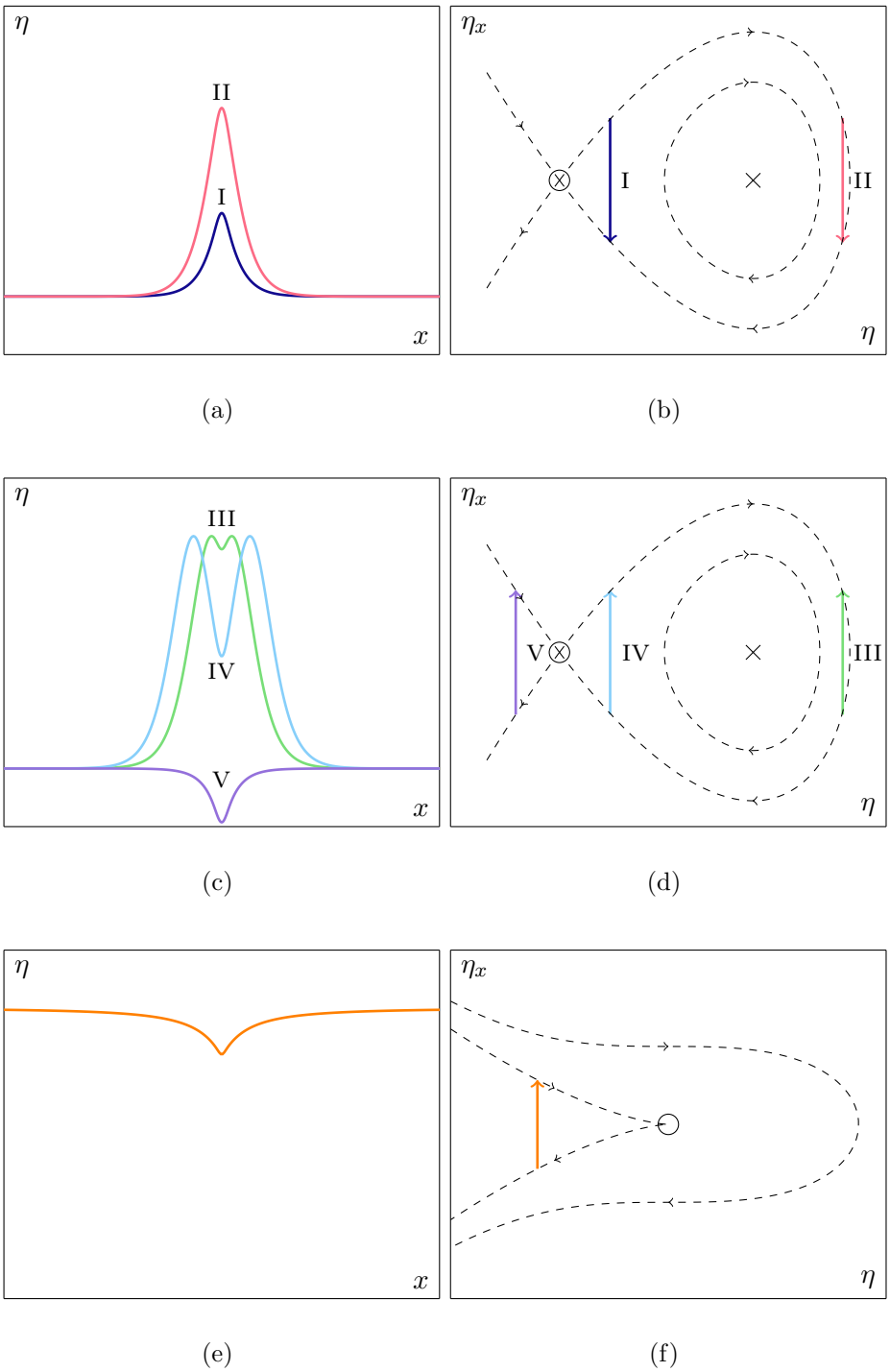

Figure 2.2.1: Sketch of super-critical ($F > 1$) and critical solution ($F = 1$) and phase planes for a Delta forcing. The colour of the profiles is matched to the colours of the arrows in the phase planes. In the figures on the right hand side a cross denotes the saddle at $(\eta, \eta_x) = (\frac{4}{3}(F-1), 0)$ and a circle denotes the origin. (a) $\hat{\alpha} > 0$. Type I solution in red, type II solution in blue. (b) Phase plane for $\hat{\alpha} > 0$. The solution starts at the origin goes up on the homoclinic orbit and has 2 options to 'jump' down to the bottom half of the orbit and return to the origin. (c) $\hat{\alpha} < 0$. Type III in green, type IV in light blue and type V in purple. (d) Phase plane for $\hat{\alpha} < 0$. The solution starts at the origin goes up on the homoclinic orbit and has two options to 'jump' up to the upper half of the orbit and return to the origin, resulting in a extra bump near $x = 0$. Additionally it can go in the lower left (η, η_x) plane and 'jumps' up to the upper half plane and then return to the origin. (e) Solution profile when $F = 1$. The solution decays algebraically in the far-field. (f) Phase plane for $F = 1$. There is a unique solution that goes in the lower left (η, η_x) plane and 'jumps' up to the upper half plane and then return to the origin.

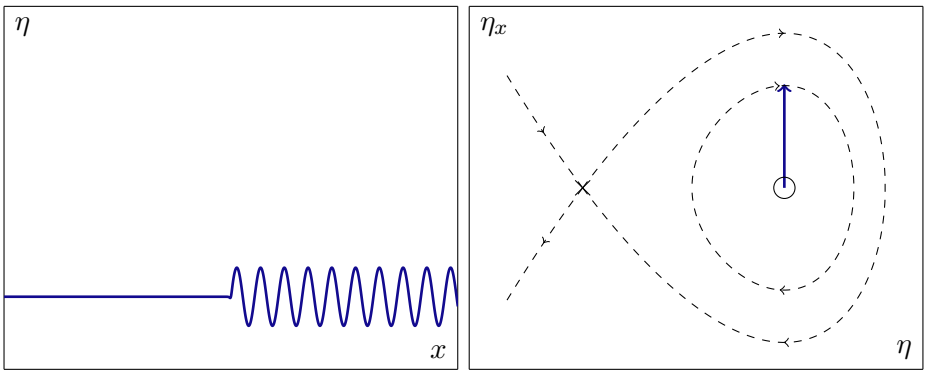

(a) (b)

Figure 2.2.2: Sketch of sub-critical ($F < 1$) solutions for a Delta forcing with $\hat{\alpha} < 0$. (a) Cnoidal wave solution. (b) Phase plane for cnoidal wave solution. The solution starts at $(0, 0)$ and jumps up (down for $\hat{\alpha} > 0$) onto a periodic cnoidal orbit. The cross denotes the saddle at $(\eta, \eta_x) = (\frac{4}{3}(F-1), 0)$ and the circle denotes the origin.

For large F, from (2.2.18), there are three possible behaviours given by

$$\eta(0) \sim 2(F-1), \tag{2.2.20a}$$

$$\eta(0) \sim +\left(\frac{3\hat{\alpha}^2}{8(F-1)}\right)^{1/2}, \tag{2.2.20b}$$

$$\eta(0) \sim -\left(\frac{3\hat{\alpha}^2}{8(F-1)}\right)^{1/2}. \tag{2.2.20c}$$

Note that the behaviour in (2.2.20c) can only occur in the case when $\hat{\alpha} < 0$. The solution space along with this behaviour is illustrated in figure 2.2.4(b).

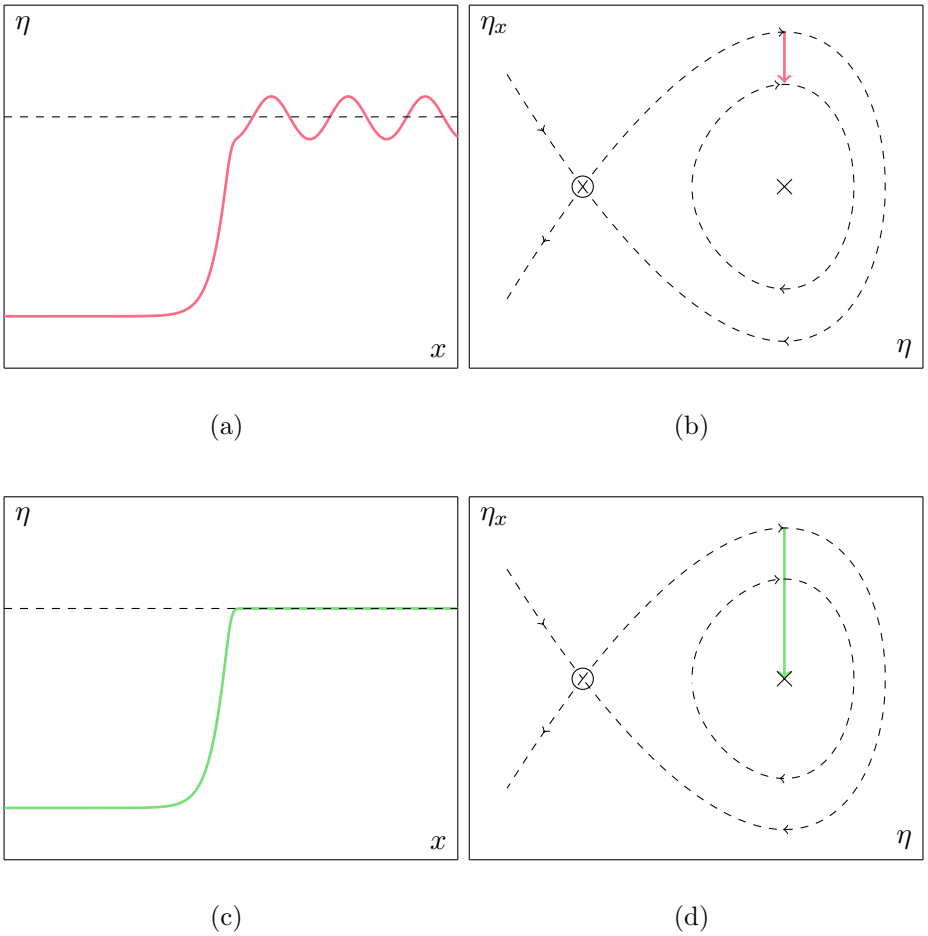

Figure 2.2.3: Sketch of generalised hydraulic fall solutions for a Delta forcing when $\hat{\alpha} > 0$. The flow is super-critical upstream, i.e. $F > 1$. The dotted line in figures (a) and (c) represents the level $\eta = 4/3(F-1)$. The cross in (b) and (d) denotes $(\eta, \eta_x) = (4/3(F-1), 0)$ and the circle denotes the origin.(a) Generalised Hydraulic Fall solution. (b) Phase plane for the generalised hydraulic fall. The solution starts at $(0, 0)$ goes up on the homoclinic orbit and jumps up (down) onto a periodic cnoidal orbit. (c) Hydraulic Fall solution. (d) Phase plane for the one parameter family of hydraulic falls.

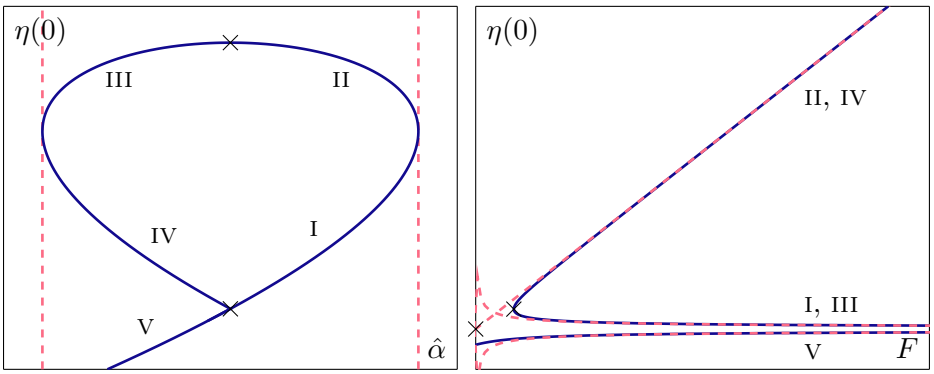

(a) (b)

Figure 2.2.4: Sketch of solution space for a Delta forcing and $F > 1$. The labels on the curves correspond to the solutions described in figure 2.2.1. (a) $F > 1$. The solution space as $\hat{\alpha}$ is varied. The lower marker denotes $(\hat{\alpha}, \eta(0)) = (0, 0)$ whilst the upper denotes $(\hat{\alpha}, \eta(0)) = (0, 2(F-1)$. The dashed lines are the limits given in (2.2.12). (b) The solution space as $F > 1$ is varied. The dashed lines in figure (b) represents the behaviour given in (2.2.20). The left most marker denotes $(F, \eta(0)) = (1, 0)$ whilst the right most marker denotes the coordinates given in (2.2.19).

2.3 Steady flow over a smooth obstacle

The point-forcing model, although useful in categorising the solution space, is rather limited in physical situations due to the discontinuity at $x = 0$. A good smooth approximation to the point forcing model is a Gaussian topography of the form

$$\sigma = \frac{\hat{\alpha}\hat{\beta}}{\sqrt{\pi}} \mathrm{e}^{-\hat{\beta}^2 x^2}. \tag{2.3.1}$$

The parameters, $\hat{\alpha}$ and $\hat{\beta}$ are parameters measuring the depth and width of the forcing and the $\sqrt{\pi}$ factor is added to ensure that the area under the curve has magnitude $|\hat{\alpha}|$. In the limit as $\hat{\beta} \to \infty$, the Gaussian in (2.3.1) becomes the Dirac delta function with amplitude $\hat{\alpha}$.

By a pseudo arclength numerical continuation technique (see Doedel, 2010, for details), the value of $\hat{\beta}$ is varied and the solution space in terms of $(\hat{\alpha}, \eta(0))$ is recorded. The value of $F > 1$ is kept constant. As $\beta \to \infty$ the solution space will tend to the space depicted in figure 2.2.4. As $\hat{\beta} \to 0$ something interesting occurs to the shape of the bifurcation curve in the $(\hat{\alpha}, \eta(0))$ solution space. As can be seen from figure 2.3.1(a) the location of the left most fold bifurcation moves further into the third quadrant in the $(\hat{\alpha}, \eta(0))$ space as $\beta \to 0$. Eventually for a sufficiently small β the the fold bifurcation disappears and the 'loop' breaks as can be seen from the green curve in figure 2.3.1(a).

Furthermore by choosing a sufficiently small $\hat{\beta}$ so the fold disappears the solution curve eventually 'breaks' into two disjoint branches as F is decreased from $F > 1$ to $F = 1$ as shown in figure 2.3.1(b).

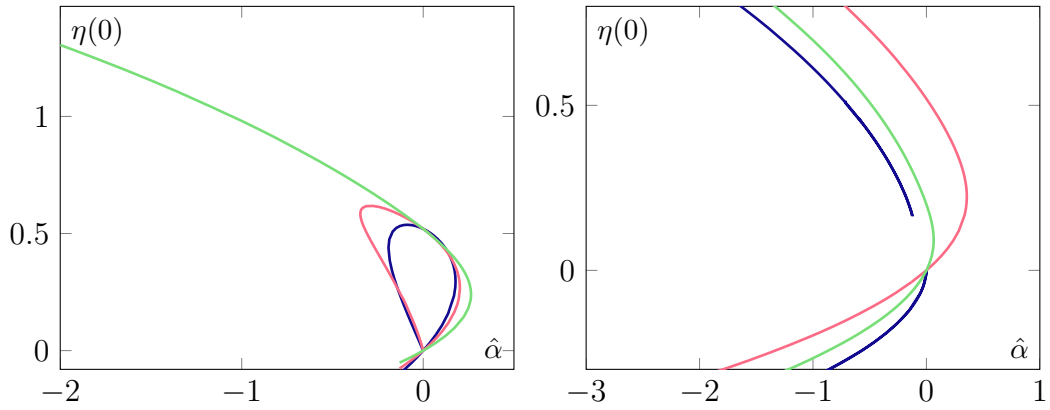

(a) (b)

Figure 2.3.1: (a) $F = 1.26$. The horizontal axis is $\hat{\alpha}$ and the vertical axis is $\eta(0)$. The green curve is for $\hat{\beta} = 0.5$, the red $\hat{\beta} = 1$ and the blue is $\hat{\beta} = 2$. (b) $\hat{\beta} = 0.3$. The x axis is for varying $\hat{\alpha}$ and the y axis is η_0. The blue curve is for $F = 1$, the green $F = 1.1$ and the red is $F = 1.5$

The delta function analysis predicts that the solution at critical Froude number is unique. The initial numerical investigation for a Gaussian forcing has revealed that actually if $\hat{\beta}$ is chosen small enough at $F = 1$ then this uniqueness disappears and another type of solution occurs. Steady solutions at $F = 1$ have been studied by Camassa & Wu (1991) but solutions which decay algebraically have not been thoroughly explored before. Furthermore in Camassa & Wu (1991), the solutions were obtained by an 'inverse' method so that the steady solutions were chosen to decay exponentially and then using the steady fKdV equation a topography was chosen to 'match' with their steady solution. Presently, if instead a Gaussian topography is prescribed then the steady solutions will be predicted to decay algebraically in the far-field as per the analysis of the delta function forcing. Steady solutions at critical flow speed which decay algebraically have not been studied before and the next chapter seeks to understand the steady solution space for $F = 1$ and the effects that algebraic decay in the far-field have on the structure of the solutions.

2.3.1 Numerical Method

The steady solutions are calculated and checked using a finite-difference code and a Runge-Kutta algorithm. For the finite difference code N grid points were generated along a truncated domain $x \in [-L/2, L/2]$ with grid spacing Δx. An initial guess for the solution is made at each of these points, u_i. The fKdV equation is then discretised using a finite difference method;

$$f_i(u_i) = \frac{u_{i+1} - 2u_i + u_{i-1}}{2\Delta x^2} + u_i^2, -\hat{\alpha} s_i \tag{2.3.2}$$

for $i = 1, N$. The equation for $f_i = 0$ is solved using Newton's method to machine accuracy.

These solutions are also complemented with a Runge-Kutta algorithm. For symmetric solutions the problem is changed to an initial-value problem on the half domain $x \in [0, L/2]$. The values of u and u_ξ are specified at $\xi = 0$ and then using a fourth order Runge-Kutta 4 algorithm the solution is found and checked with the finite-difference solution. These solutions are carefully checked by increasing L, the domain length, to check that the solutions are on a trajectory that enters the origin in the phase space (η, η_x) as L increases. To continue the solutions in the $\hat{\alpha}$ parameter space Keller's pseudo arclength algorithm is used.

2.4 Stability

Once steady solutions have been calculated it is of interest to understand the time-dependent behaviour of any steady solutions of the fKdV equation. The aim is to classify the steady solutions that have been computed as being *neutrally*, *spectrally*, *linearly* or *formally* stable. For a definition of these terms, (Holm *et al.*, 1985, see for example); however the reader will be reminded of their precise meaning as the analysis proceeds.

2.4.1 Linear stability

To investigate the stability of these solutions a perturbation of the form $\eta(x,t) = \eta_s(x) + \varepsilon\zeta(x,t)$ is written, where η_s is a steady solution of (2.1.41) and ζ is a time-dependent perturbation, and where $\varepsilon \ll 1$. The perturbation ζ is demanded to satisfy the same far-field conditions as η, namely equation (2.2.2). Substituting into (2.1.41) and retaining terms at $O(\varepsilon)$ yields

$$\zeta_t = \mathcal{M}\zeta = -\frac{\partial}{\partial x}(\mathcal{K}\zeta), \tag{2.4.1}$$

where the operator $\mathcal{K}$ is defined as

$$\mathcal{K} = -\frac{1}{6}\partial_{xx} - \left(\frac{3}{2} - 6(F-1)\right)\eta_s. \tag{2.4.2}$$

The general solution to (2.4.1) may be written in the form (see, for example Chang & Demekhin, 2002, section 7.3)

$$\zeta(x,t) = \sum_{k=1}^{N_p} a_k g_k(x)\,\mathrm{e}^{s_k t} + \int_\Gamma a(s)g(x,s)\,\mathrm{e}^{st}\,\mathrm{d}s, \tag{2.4.3}$$

where the a_k and $a(s)$ are expansion coefficients corresponding respectively to the N_p values of s in the point spectrum and to the continuous spectrum of the operator $\mathcal{M}$. These satisfy the relation

$$\mathcal{M}g = sg \tag{2.4.4}$$

(with k subscripts appended in the case of the point spectrum). The integral in the second term in (2.4.3) is taken over the contour Γ which delineates the continuous spectrum in the complex s plane. The eigenfunctions in the point spectrum, $g_k(x)$, reside in $L_2(-\infty, \infty)$.

If there is no eigenvalue in the spectrum in the right-half complex plane, that is with a positive real part, then $\eta_s(x)$ is *spectrally stable*. If the spectrum is contained along the imaginary axis, then the solution is *neutrally stable*. The solution is *linearly stable* if for every $\varepsilon > 0$ there exists a $\delta > 0$ such that if in a suitable norm $\|\zeta(x,0)\| < \delta$ then $\|\zeta(x,t)\| < \varepsilon$ for $t > 0$. While linear stability clearly implies spectral stability, the converse is not necessarily true (see Holm *et al.*, 1985, for some examples). As was pointed out by Camassa & Wu (1991), for a steady solution $\eta_s(x)$ which is even in x (resulting from an even topography), the operator $\mathcal{M}$ is odd in x, i.e. $\mathcal{M}g(-x) = -\mathcal{M}g(x)$, which means that for each eigenvalue s satisfying equation (2.4.4), $-s$, s^* and $-s^*$ are also eigenvalues, so that the spectrum has a four-fold symmetry in the complex plane. As a consequence, spectral stability can only occur if all of the eigenvalues lie on the imaginary axis, in which case the solution is neutrally stable. Therefore for the fKdV equation with even topography, neutral stability for even solutions is a necessary and sufficient condition for spectral stability.

If the spectrum of $\mathcal{M}$ is purely imaginary then linear instability is still not ruled out. It may be the case that there exist non-simple point-spectrum eigenvalues embedded in the continuous spectrum on the imaginary axis which may lead to algebraic growth in time (Holm *et al.*, 1985). For example, consider the simple one-dimensional system $\dot{x} = y$, $\dot{y} = 0$. This has an unbounded solution but the Jacobian has repeated eigenvalues which lie on the imaginary axis.

To proceed an alternative approach is adopted, suggested by Camassa & Wu (1991), Chardard *et al.* (2011) and others, which exploits the fact that (3.5.1) has a Hamiltonian structure and leads to a definition of *formal* stability.

2.4.2 Formal stability

Before proceeding with the specifics of the formal stability analysis of the fKdV equation it is worth reminding the reader of the definitions of *variation* and *variational derivatives* as defined for a functional $\mathcal{H}[\eta(x)]$ (see, for example Dreizler & Engel, 2011; Gelfand & Fomin, 1963). The *total variation* is defined as

$$\Delta\mathcal{H} \equiv \mathcal{H}[\eta + \varepsilon\zeta] - \mathcal{H}[\eta] \equiv \varepsilon \left.\frac{\mathrm{d}}{\mathrm{d}\varepsilon}\right|_{\varepsilon=0} \mathcal{H}[\eta + \varepsilon\zeta] + \frac{1}{2}\varepsilon^2 \left.\frac{\mathrm{d}^2}{\mathrm{d}\varepsilon^2}\right|_{\varepsilon=0} \mathcal{H}[\eta + \varepsilon\zeta] + \cdots \tag{2.4.5}$$

for $\varepsilon \ll 1$ and the function $\zeta(x,t)$ which decays in the far field of the domain (so that integration by parts can simplify the resulting expressions). The n^{th} *variation* is defined by

$$\delta^n \mathcal{H}[\eta] \equiv \frac{\mathrm{d}^n}{\mathrm{d}\varepsilon^n} \mathcal{H}(\eta + \varepsilon\zeta)\bigg|_{\varepsilon=0} \tag{2.4.6}$$

and the n^{th} *variational derivative*, $\delta^n\mathcal{H}/\delta\eta^n$, is defined implicitly by

$$\delta^n \mathcal{H}[\eta] \equiv \int_{-\infty}^{\infty}\int_{-\infty}^{\infty}\cdots\int_{-\infty}^{\infty} \frac{\delta^n \mathcal{H}}{\delta\eta(x_1)\delta\eta(x_1)\cdots\delta\eta(x_n)} \zeta(x_1,t)\zeta(x_2,t)\cdots\zeta(x_n,t)\,\mathrm{d}x_1\mathrm{d}x_2\cdots\mathrm{d}x_n. \tag{2.4.7}$$

Now the fKdV equation is examined. As noted by Camassa & Wu (1991), the fKdV equation, (2.1.41), can be written in the form of

$$\eta_t = -\frac{1}{6}\frac{\partial}{\partial x}\frac{\delta \mathcal{H}}{\delta \eta}[\eta] \tag{2.4.8}$$

where the Hamiltonian $\mathcal{H}$ is written as

$$\mathcal{H}[\eta] = \frac{1}{2}\int_{-\infty}^{\infty} [6(F-1)\eta^2 - 3\eta^3 + \eta_x^2 - 6\sigma\eta]\,\mathrm{d}x. \tag{2.4.9}$$

Steady solutions, for which $\eta_t = 0$, exist as an extremum of the Hamiltonian; namely

$$\frac{\delta \mathcal{H}}{\delta \eta} = 0 \tag{2.4.10}$$

The stability algorithm of Holm *et al.* (1985) is now followed. The fKdV equation, (2.4.8), in Hamiltonian form is linearised about a steady solution η_s by writing $\eta = \eta_s(x) + \varepsilon\zeta(x,t)$ with $\varepsilon \ll 1$. The methodology is analogous to that of linearising an ODE around an equilibrium point. For an ODE of the form $\dot{\mathbf{u}}(\mathbf{x}) = f(\mathbf{u}(\mathbf{x}))$, writing $\mathbf{u} = \mathbf{u}^* + \varepsilon\mathbf{v}$, where $\mathbf{u}^*$ is an equilibrium point, $\mathbf{v}(x)$ is a perturbation and $\varepsilon \ll 1$, results in the linearised equation, $\dot{\mathbf{v}} = \mathbf{J}(\mathbf{u}^*)\mathbf{v}$ where $\mathbf{J}$ is the Jacobian defined by the matrix entries $J_{ij} = \frac{\partial f_i}{\partial x_j}$. The equation (2.4.8) is linearised about a steady solution η_s so an evolution equation for the perturbation, ζ, can be derived in the form $\zeta_t = f(\zeta)$. Therefore to proceed, the variational derivative, $\frac{\delta\mathcal{H}}{\delta\eta}$, in (2.4.8) is expanded using a Taylor series about $\eta = \eta_s$. Using Taylor's theorem about $\varepsilon = 0$

$$\frac{\delta \mathcal{H}}{\delta \eta}[\eta] = \frac{\delta \mathcal{H}}{\delta \eta}[\eta_s] + \varepsilon\frac{\mathrm{d}}{\mathrm{d}\varepsilon}\left(\frac{\delta \mathcal{H}}{\delta \eta}[\eta_s + \varepsilon\zeta]\right)\bigg|_{\varepsilon=0} + O(\varepsilon^2). \tag{2.4.11}$$

The second term on the right hand side of (2.4.11) is re-written using the second variation. Using (2.4.7) the second variation is defined as

$$\delta^2\mathcal{H}[\eta_s] = \int_{-\infty}^{\infty}\int_{-\infty}^{\infty} \frac{\delta}{\delta\eta(y)}\left(\frac{\delta\mathcal{H}}{\delta\eta(x)}\right)\zeta(x)\zeta(y)\,\mathrm{d}x\,\mathrm{d}y. \tag{2.4.12}$$

The second variation $\delta^2\mathcal{H}$ is now taken to be a functional with argument ζ, i.e.

$$\delta^2\mathcal{H}[\eta_s] = J[\zeta] \tag{2.4.13}$$

A variation of $\delta^2\mathcal{H}$ is now taken with respect to ζ. The variation is written as $\zeta(x) \to \zeta + h\hat{\zeta}(x,t)$ where h is small and $\hat{\zeta}$ is a perturbation that vanishes in the far-field. Therefore $\delta J[\zeta] = \delta(\delta^2\mathcal{H}[\eta_s])$. Performing this variation on (2.4.12) gives

$$\delta(\delta^2\mathcal{H}[\eta_s]) = \frac{\mathrm{d}}{\mathrm{d}h}\left[\int_{-\infty}^{\infty}\int_{-\infty}^{\infty} \frac{\delta}{\delta\eta(y)}\left(\frac{\delta\mathcal{H}}{\delta\eta(x)}\right)(\zeta(x)+h\hat{\zeta}(x))(\zeta(y)+h\hat{\zeta}(y))\,\mathrm{d}x\,\mathrm{d}y\right]\Bigg|_{h=0}. \tag{2.4.14}$$

Noting the order of integration is free to change this becomes:

$$\delta(\delta^2\mathcal{H}[\eta_s]) = 2\int_{-\infty}^{\infty}\int_{-\infty}^{\infty} \frac{\delta}{\delta\eta(y)}\left(\frac{\delta\mathcal{H}}{\delta\eta(x)}\right)\zeta(x)\hat{\zeta}(y)\,\mathrm{d}x\,\mathrm{d}y. \tag{2.4.15}$$

Using the definition of the variational derivative in (2.4.7), the form of (2.4.15) implies

$$\frac{1}{2}\frac{\delta}{\delta\zeta}(\delta^2\mathcal{H}[\eta_s]) = \int_{-\infty}^{\infty}\frac{\delta}{\delta\eta}\frac{\delta\mathcal{H}}{\delta\eta}\zeta\,dx. \tag{2.4.16}$$

Finally by using (2.4.6) and (2.4.7)

$$\frac{1}{2}\frac{\delta}{\delta\zeta}(\delta^2\mathcal{H}[\eta_s]) = \frac{\mathrm{d}}{\mathrm{d}\varepsilon}\bigg|_{\varepsilon=0}\frac{\delta\mathcal{H}}{\delta\eta}. \tag{2.4.17}$$

Therefore the expression in (2.4.11) can be written as

$$\frac{\delta\mathcal{H}}{\delta\eta} = \frac{\delta\mathcal{H}}{\delta\eta_s} + \frac{1}{2}\varepsilon\frac{\delta}{\delta\zeta}\delta^2\mathcal{H}[\eta_s]. \tag{2.4.18}$$

Now (2.4.18) and $\eta = \eta_s + \varepsilon\zeta$ are substituted into (2.4.8) to obtain an evolution equation for the perturbation ζ

$$\frac{\partial\zeta}{\partial t} = -\frac{1}{12}\frac{\partial}{\partial x}\frac{\delta}{\delta\zeta}\delta^2\mathcal{H}[\eta_s]. \tag{2.4.19}$$

If this is compared to the Hamiltonian form of the fKdV equation, (2.4.8) then it is clear that (2.4.19) is also Hamiltonian and the Hamiltonian for equation (2.4.19), denoted by $\mathcal{H}_\zeta$ is

$$\mathcal{H}_\zeta \equiv \delta^2\mathcal{H}[\eta_s]. \tag{2.4.20}$$

It is noted that due to Noether's theorem it can be shown that the Hamiltonian is a conserved quantity of the system (see, for example Gelfand & Fomin, 1963). It is also observed that $\mathcal{H}$ will depend on η and ζ in general. An initial condition can be thought of as a particular choice of steady solution η_s and perturbation ζ. Note that the constant of motion $\mathcal{H}$ may change for different initial conditions as it depends on η_s. However for a given ζ in (2.4.19) the Hamiltonian, $\mathcal{H}_\zeta$ will also be constant for all $t \geq 0$. The second variation is constant in argument of η_s so the value $\mathcal{H}_\zeta$ takes for all t will depend on the particular choice of perturbation ζ. Let the space of all permissible perturbations be denoted by V_ζ. Let p be a mapping such that

$$p : V_\zeta \to \mathbb{R}, \tag{2.4.21a}$$

$$p(\zeta) = \delta^2\mathcal{H}[\eta_s]. \tag{2.4.21b}$$

If $\delta^2\mathcal{H} \geq 0$ then it can be shown that the mapping p satisfies the requirements of a norm (*positive definiteness, the triangle inequality, absolutely homogeneous* and *point-separating*). The Lyapunov stability condition states that for every $\epsilon > 0$, there exists a $\delta > 0$ (not to be confused with the notation above) such that if $\|\zeta(x,0)\| < \delta$ then for all $t \geq 0$, $\|\zeta(x,t)\| < \epsilon$ for a suitable norm (see, for example Holm *et al.*, 1985). Therefore for equation (2.4.19) the mapping p defined above is a suitable norm provided

$$\delta^2\mathcal{H} \geq 0. \tag{2.4.22}$$

If this condition is satisfied then the Lyapunov condition is satisfied for (2.4.19) and the steady solution η_s, is said to be *formally stable*. Formal stability implies linear stability, although the converse is not necessarily true (see Holm *et al.*, 1985). Linear instability can therefore be ruled out if $\delta^2\mathcal{H}$ is definite. As an alternative to (2.4.26), the second variation can also be written in terms of the operator $\mathcal{K}$ in the form

$$\delta^2\mathcal{H} = \frac{1}{3}\left[\langle\zeta, \mathcal{K}\zeta\rangle + 6(F-1)\langle\zeta,\zeta\rangle\right]. \tag{2.4.23}$$

Now, $\mathcal{K}$ is a self-adjoint Schrödinger operator, and the determination of its eigenvalue spectrum constitutes a singular Sturm-Louiville problem on the real line (see, for example Coddington & Levinson, 1955; Titchmarsh, 1962) and is a well-studied problem in quantum mechanics and inverse scattering theory (see, for example Drazin & Johnson, 1989; Landau & Lifshitz, 1977). The admissible perturbations ζ are restricted to the class of $L_2(-\infty,\infty)$ square-integrable functions. Each discrete eigenvalue of $\mathcal{K}$ satisfies

$$\mathcal{K}\phi_n = \nu\phi_n, \tag{2.4.24}$$

for L^2 eigenfunction ϕ_n, and it is straightforward to show that ν is real. By taking an inner product of (2.4.24) with ϕ_n it follows that

$$\langle \phi_n, \mathcal{K}\phi_n \rangle \geq \nu_0 \langle \phi_n, \phi_n \rangle, \tag{2.4.25}$$

where ν_0 is the minimum eigenvalue and the angled brackets represent the usual inner product. The exact form of the second variation for the fKdV equation can be written as

$$\delta^2 \mathcal{H} = \frac{1}{2} \int_{-\infty}^{\infty} \zeta_x^2 - 9\eta_s \zeta^2 + 6(F-1)\zeta^2 \, \mathrm{d}x. \tag{2.4.26}$$

Using the definition for $\mathcal{K}$, equation (2.4.24) can be manipulated to obtain the following formula for ν,

$$\nu = \frac{\langle \phi_n', \phi_n' \rangle - 9\langle \eta_s \phi_n, \phi_n \rangle}{6\langle \phi_n, \phi_n \rangle}. \tag{2.4.27}$$

where a prime indicates differentiation with respect to x. For a general steady solution η_s, the eigenvalues ν may be positive or negative. However, if η_s is negative definite, it is clear from (2.4.27) that the eigenvalues will be strictly positive and therefore for $F > 1$, (2.4.23) will be definite and hence η_s will be formally and hence linearly stable.

Assuming that the set of discrete and continuous eigenfunctions are complete, a general L^2 perturbation can be represented as a combination of these. Making use of (2.4.25) and the linearity of the operator $\mathcal{K}$, a lower bound for the second variation may be constructed as

$$\delta^2 \mathcal{H} \geq \frac{1}{3} \left[\nu_0 \langle \zeta, \zeta \rangle + 6(F-1)\langle \zeta, \zeta \rangle \right]. \tag{2.4.28}$$

For a sech^2 forcing, Camassa & Wu (1991) were able to establish that a negative-definite solution is nonlinearly stable for super-critical flow; the issue of nonlinear stability is not pursued here.

2.4.3 Time-dependent simulations

In this section the time-dependent behaviour of the steady solution types I–V is now described. The numerical method is described in the next section. In all the simulations the steady solution η_s is perturbed by a small amount and this is the initial condition. The initial condition can be stated as

$$\eta(x, 0) = \eta_s + \delta\zeta(x)$$

where δ is small and ζ is a perturbation. If the steady solution had a purely imaginary spectrum of $\mathcal{M}$ then the perturbation ζ was chosen to be η_s. If the spectrum of $\mathcal{M}$

had an unstable eigenvalue then ζ was chosen to be

$$\zeta = \frac{1}{2}(g + g^*)$$

where $g(x)$ is the eigenfunction associated with the unstable eigenvalue and the star denotes complex conjugation. In figure 2.4.1 typical results are displayed for all of the five types of super-critical solutions. Note that these calculations have already been analysed in Camassa & Wu (1991); Chardard *et al.* (2011); Wade *et al.* (2014) but provide a useful method of validation for the numerical code.

For super-critical flow, as expected, the type V solutions are stable as they are negative definite and the formal stability ensures linear stability. Furthermore, for a positive bump the type I solution is also stable. The solution types II, III and IV all display similar behaviour. After a set amount of time, they all 'shed' solitary waves upstream and eventually evolve to the stable steady state of types I and V (for positive and negative topography respectively).

The case of critical flow where the solutions exhibit exponential decay has been analysed thoroughly by Wu (1987) and Camassa & Wu (1991). In general solutions are unstable. In particular, if the steady solution has an unstable eigenvalue of $\mathcal{M}$, a stable solution is not approached in large t, unlike the case of super-critical flow where the stable solution is approached as $t \to \infty$. The critical flow solutions that decay algebraically have not been analysed in the literature and provide an interesting area of investigation which is discussed more thoroughly in chapter 3.

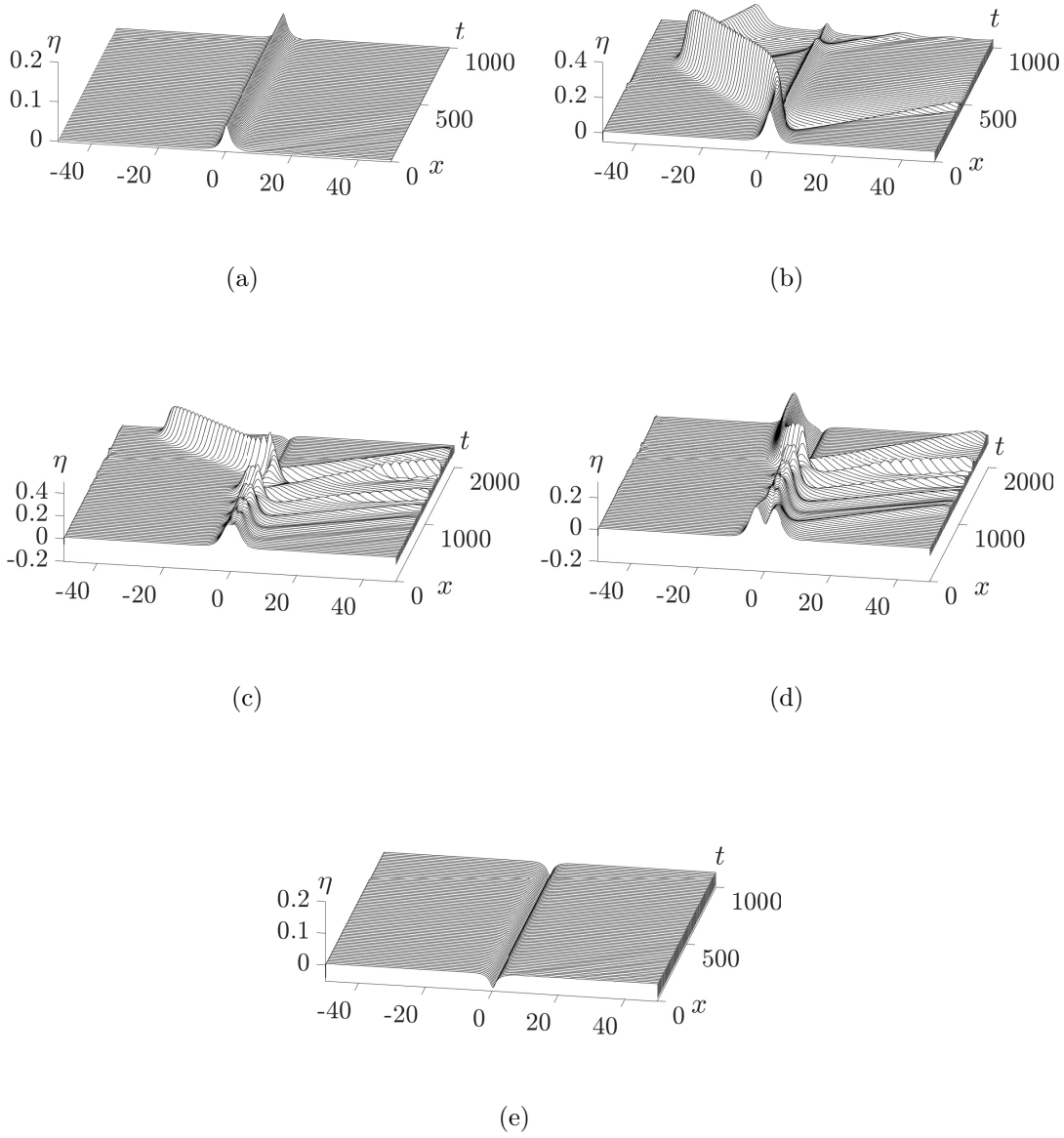

Figure 2.4.1: Super-critical time-dependent simulations. In all figures $\delta = 0.05$, $F = 1$ and $\hat{\beta} = 2.8$ (a) Type I, $\hat{\alpha} = 0.03$. (b) Type II, $\hat{\alpha} = 0.030$. (c) Type III, $\hat{\alpha} = -0.03$. (d) Type IV, $\hat{\alpha} = -0.03$. (e) Type V, $\hat{\alpha} = -0.03$.

2.4.4 Numerical method

The numerical methods used in the time-dependent simulations is now described. The fKdV equation was discretised spatially using a pseudo-spectral approach and then a Runge-Kutta 4 algorithm was employed for the time-stepping. This method is similar to that demonstrated in Chardard *et al.* (2011) and Wade *et al.* (2014). Starting from the fKdV equation, (2.1.41) it is first convenient to transform the spatial variable x by

$$x \mapsto \frac{2\pi x}{L}, \tag{2.4.29}$$

to change the spatial domain limits to $x \in [-\pi, \pi]$. Equation (2.1.41) can then be written as:

$$\eta_t + (F-1)S\eta_x - \frac{3}{2}S\eta\eta_x - \frac{1}{6}S^3\eta_{xxx} = \frac{1}{2}\sigma_x, \tag{2.4.30}$$

where $S = 2\pi/L$. The spatial domain is divided into N equally spaced meshpoints. The values of x and η at the j^{th} spatial grid point are denoted by x_j and $\eta(x_j)$. The spatial derivatives in (2.4.30) are discretised using a pseudo-spectral Fourier scheme. This method assumes that η is periodic on the x domain. This is a reasonable approximation given that η and η_x are required to vanish far upstream and downstream. To implement this scheme the discrete Fourier transform is applied to the $\eta(x_j)$ node values. The Fourier modes are discretised by

$$k_i = [-N/2+1, -N/2, \cdots, 0, 1, 2, \cdots N/2, N/2-1],$$

and the discrete Fourier transform is defined as

$$\hat{\eta}(k_i, t) = \mathcal{F}[\eta(x_j, t)] \equiv \sum_{j=0}^{N} \eta(x_j, t)\mathrm{e}^{-\mathrm{i}k_i x_j}, \tag{2.4.31}$$

where $\hat{\eta}(k_i, t)$ is the nodal value of $\hat{\eta}$ at k_i in Fourier space. This is achieved using the fast Fourier transform (FFT) of Cooley & Tukey (1965). Using the inverse FFT defined as

$$\eta(x_i, t) \equiv \mathcal{F}^{-1}[\hat{\eta}(k_i, t)] \equiv \frac{1}{N}\sum_{j=0}^{N} \hat{\eta}(k_j, t)\mathrm{e}^{\mathrm{i}k_j x_i}, \tag{2.4.32}$$

the discretised derivatives of η in the fKdV equation can be written as

$$\eta_x(x_i) = \mathcal{F}^{-1}[-\mathrm{i}k_i\eta(k_i, t)], \tag{2.4.33a}$$

$$\eta_{xxx}(x_i) = \mathcal{F}^{-1}[\mathrm{i}k_i^3\eta(k_i, t)]. \tag{2.4.33b}$$

To advance the solution forward in time, a Runge-Kutta 4 technique is used on the now discretised form of the fKdV equation

$$\frac{\mathrm{d}}{\mathrm{d}t}(\eta_i) = (F-1)(\eta_x)_i + \frac{3}{2}\eta_i S(\eta_x)_i - \frac{1}{6}S^3(\eta_{xxx})_i + \frac{1}{2}S(\sigma_x)_i. \tag{2.4.34}$$

Since periodicity is assumed in the computations, any disturbance leaving the domain will appear at the opposite end, and such behaviour is clearly nonphysical. To prevent this in the computations a so-called sponge layer is introduced (see, for example, Alias, 2014; Boyd, 2000; Grimshaw & Maleewong, 2016) and in fact the equation

$$\eta_t + (F-1)\eta_x - \frac{3}{2}\eta\eta_x - \frac{1}{6}\eta_{xxx} + A(x)\eta = \frac{1}{2}f_x, \tag{2.4.35}$$

is solved, where

$$A(x) = D\left\{1 + \tanh\left(b_0\left[x - b_1\right]\right)\right\} \tag{2.4.36}$$

for positive parameters D, b_0 and b_1. Note that the function $A(x)$ is zero over most of the computational domain; choosing b_1 to be close to L, then A is non-zero over a narrow region at the left-hand end of the domain. This has the effect of preventing disturbances leaving the upstream end from entering the downstream end (due to the assumed periodicity) and vice versa. In practice, choosing $D = 1.0$, $b_0 = 12/L$ and $b_1 = 0.95L$ had the desired effect in the sponge-layer without compromising the solution in the remainder of the domain. Via numerical experimentation it was confirmed that the same results in the main part of the domain are obtained for sensible deviations from these values. It is worth commenting, however, that choosing b_0 to be larger to achieve a more rapid transition into the sponge-layer has the undesirable effect of reflecting waves back into the domain, and so in practice a moderate value is preferable (Boyd, 2000).

2.5 Steady fully nonlinear formulation

The fKdV equation is an asymptotic description of the fully nonlinear water-wave equations when the free-surface elevation of the free-surface and the topography are not too small. Solutions to the fKdV equation will be comparable to solutions of the fully nonlinear water-wave equations. However, in general the solution space of the fKdV equation and the solution space of the water-wave equations will not necessarily be the same quantitatively and qualitatively. With this in mind, in this section the fully nonlinear problem is re-formulated as a set of boundary integral equations that can be solved numerically to compare with the weakly nonlinear fKdV model.

This problem can be approached in a number of different ways. The Euler equations and boundary conditions are transformed through a series of conformal maps to a boundary integral which can be used to obtain the free-surface from a prescribed bottom topography. A number of authors (Binder *et al.*, 2014; Binder & Vanden-Broeck, 2006; Binder *et al.*, 2005; Chapman & Vanden-Broeck, 2006; Dias & Vanden-Broeck, 2002*b*; Forbes, 1988; Lustri *et al.*, 2006; Page *et al.*, 2014; Tam *et al.*, 2015; Wade *et al.*, 2014) have all employed a similar method to re-phrase the problem in this context. Dias & Vanden-Broeck (2002*b*) compared this method to the weakly nonlinear

solutions of the fKdV equation, Lustri *et al.* (2006) and Chapman & Vanden-Broeck (2006) analysed the case of when $F \approx 0$ and used exponential asymptotics to show that the disturbance of the free surface occurred 'beyond all orders' and that the asymptotic power series for the velocity potential would diverge unless it was truncated optimally. Solutions had to be considered in each case near the vicinity of the singularities in the conformal plane and the corresponding Stokes' lines were discussed. Alternatively Wade *et al.* (2014) analysed the case when $F \approx F_{max}$ where F_{max} is the limiting value of the Froude number for which Stoke stagnation points occur (these shall be discussed later). A scheme was developed where a graded mesh and exact implementation of the far-field conditions was required to accurately compute the Stokes' limiting waves (see also Hunter & Vanden-Broeck, 1983; Longuet-Higgins & Fox, 1977). Vanden-Broeck (1997) created an integro-differential system to be solved to find the flow velocity over a sluice gate which Binder *et al.* (2005) extended to flow over a topography. The boundary integral was parameterised by the velocity potential Φ and the bottom topography was prescribed in Φ. Therefore the exact shape of the topography in physical space is not prescribed. The shape of the free-surface was found as a function of Φ. The recent work of Tam *et al.* (2015) extended this further by prescribing the bottom topography as a function of x so that the topography is exactly known in physical space. This is the approach followed here and the derivation outlined below is well-known.

The water wave equations derived in the hatted coordinates, (2.1.5), (2.1.7a) and (2.1.7b) are transformed into the same coordinates as the fKdV equation so a direct comparison can be made. Using table 2.1 the $\hat{x}, \hat{y}, \hat{\eta}$ and $\hat{\sigma}$ are scaled with the channel width H and the potential, $\hat{\Phi}$ is scaled by $H\sqrt{gH}$. In the flow domain Laplace's equation holds

$$\nabla^2\Phi = 0 \qquad \text{in} \quad -\infty < x < \infty, \quad \sigma(x) < y < 1 + \eta(x). \tag{2.5.1}$$

On the free-surface the dynamic and kinematic boundary conditions need to be satisfied,

$$\left.\begin{aligned} &\frac{1}{2}|\nabla\Phi|^2 + \frac{1}{F^2}y = \frac{1}{2} + \frac{1}{F^2} \\ &\eta_x\Phi_x = \Phi_y \end{aligned}\right\} \quad \text{on} \quad y = 1 + \eta(x), \tag{2.5.2}$$

along with the no-penetration condition on the bottom,

$$\sigma_x\Phi_x = \Phi_y \quad \text{on} \quad y = \sigma(x). \tag{2.5.3}$$

The physical situation is now transformed by introducing the complex coordinate $z = x + \mathrm{i}y$. As the flow is irrotational, the flow can be represented using the complex potential given as

$$w = \Phi + \mathrm{i}\Psi, \tag{2.5.4}$$

where Ψ is the stream function and Φ and Ψ are both functions of z. Note that these

two quantities satisfy the Cauchy-Riemann equations for complex differentiation by design. The velocities of the flow (u, v) are recovered by:

$$\frac{\mathrm{d}w}{\mathrm{d}z} = u - \mathrm{i}v. \tag{2.5.5}$$

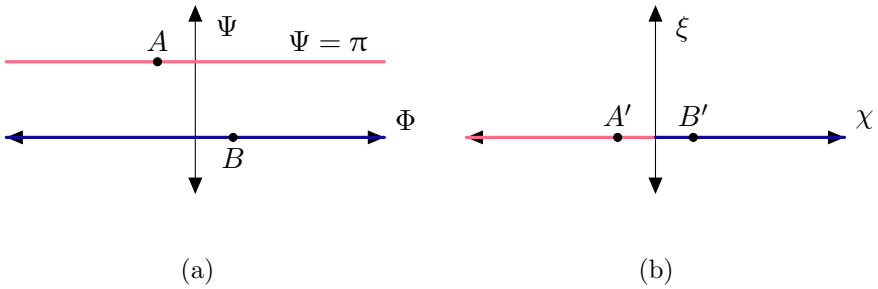

(a) (b)

Figure 2.5.1: Diagrams showing the conformal mappings ζ in the (a) w plane and (b) ζ plane

The problem in the z plane is mapped to the complex potential plane, w. In the z plane the free surface is at $y = 1 + \eta$ and the bottom topography is at $y = 0 + \sigma$ as shown in figure 2.1.1. The stream-function Ψ can be chosen freely on the free-surface and is set as $\Psi = 1$ and therefore on the bottom topography $\Psi = 0$. Therefore any z on the free surface gets mapped to the line in the w-plane as the line $\Psi = 1$ and the bottom topography is mapped to the real φ axis. A further conformal mapping maps the w plane onto the ζ plane via the transformation:

$$\zeta = \chi + \mathrm{i}\xi = \mathrm{e}^{\pi w}. \tag{2.5.6}$$

This elegant transformation transforms the line $\varphi = 1$ into the negative real χ axis and the line $\varphi = 0$ gets mapped to the positive χ axis. Via these two mappings the free-surface and the bottom topography get mapped to the real χ axis. The inverse of (2.5.6) is:

$$w = \frac{1}{\pi}\log(\zeta). \tag{2.5.7}$$

Note that due to this mapping the kinematic condition, the first equation in (2.1.7a) and the 'no-flux' condition (2.1.7b) are automatically satisfied as they effectively state that the stream-function, Ψ is constant on the free-surface and topography; the mapping automatically ensures this. These mappings are shown in figure 2.5.1. All that remains is to satisfy Bernoulli's equation, the second equation in (2.1.7a). To formulate the boundary integral an analytic function is introduced for the flow speed q and the angle of the flow θ. This can be written as:

$$\frac{\mathrm{d}w}{\mathrm{d}z} = q\mathrm{e}^{-\mathrm{i}\theta}$$

Calling $\mathrm{e}^{\tau} = q$ the analytic function $\tau - \mathrm{i}\theta$ is introduced

$$\frac{\mathrm{d}w}{\mathrm{d}z} = \mathrm{e}^{\tau - \mathrm{i}\theta}. \tag{2.5.8}$$

This is an analytic function of z in the the w plane and thus:

$$f(\zeta) = \tau(\zeta) - \mathrm{i}\theta(\zeta) \tag{2.5.9}$$

is an analytic function of ζ. The boundary integral is formed using Cauchy's Integration formula (see, for example Ablowitz & Fokas, 2003) for a general function $f(z)$, this is stated as

$$f(\zeta) = \frac{1}{2\pi\mathrm{i}} \oint_C \frac{f(\zeta)}{\zeta_0 - \zeta}\,\mathrm{d}\zeta_0, \tag{2.5.10}$$

where C is a contour defined going anti-clockwise and the point ζ_0 is in the interior of the contour. The contour C is chosen so that ζ_0 is not in the interior, hence there are no singularities inside (see figure 2.5.2) and by the residue theorem

$$\frac{1}{2\pi\mathrm{i}} \oint_C \frac{f(\zeta)}{\zeta_0 - \zeta}\,\mathrm{d}\zeta_0 = 0. \tag{2.5.11}$$

The contour C is shown in figure 2.5.2 and consists of four parts. Therefore (2.5.11) can be written as

$$\int_{C_1} \frac{\tau(\zeta) - \mathrm{i}\theta(\zeta)}{\zeta_0 - \zeta}\,\mathrm{d}\zeta_0 + \int_{C_2} \frac{\tau(\zeta) - \mathrm{i}\theta(\zeta)}{\zeta_0 - \zeta}\,\mathrm{d}\zeta_0 + \fint_{-R}^{R} \frac{\tau(\chi) - \mathrm{i}\theta(\chi)}{\chi_0 - \chi}\,\mathrm{d}\chi_0, = 0 \tag{2.5.12}$$

where C_1 is the large semi-circular path in blue in figure 2.5.2 (the limit as $R \to \infty$ will be taken at the end) and C_2 is the small semi-circular path in red in figure 2.5.2 around $\chi = \chi_0$ (this integral will be taken in the limit as $\varepsilon \to 0$ where ε is the radius). The third integral on the right hand side is a Cauchy Principal Type integral as there is a singularity on the real axis, the path of integration.

The path C_1 is taken in the limit as $R \to \infty$ and vanishes (see Wade, 2015, for a proof). The integral around C_2 as $\varepsilon \to 0$ becomes $-\pi\mathrm{i}[\tau(\chi_0) - \mathrm{i}\theta(\chi_0)]$ (via the change of variables $\xi_0 = \xi - \varepsilon\mathrm{e}^{\mathrm{i}t}$) and hence as $R \to \infty$ (2.5.11) becomes

$$\pi\mathrm{i}[\tau(\chi_0) - \mathrm{i}\theta(\chi_0)] = \fint_{-\infty}^{\infty} \frac{\tau(\chi) - \mathrm{i}\theta(\chi)}{\chi_0 - \chi}\,\mathrm{d}\chi_0. \tag{2.5.13}$$

Taking real parts gives:

$$\tau(\chi) = -\frac{1}{\pi}\fint_{-\infty}^{\infty} \frac{\theta(\chi)}{\chi_0 - \chi}\,\mathrm{d}\chi_0. \tag{2.5.14}$$

The function τ can be formulated by evaluating the integral in (2.5.14). The values of θ will vary along the integration path depending on the shape of the bottom topography and free surface. Let θ_b be the values on the bottom topography and θ_f be the values on the free surface. For the free-surface, χ is negative. By writing $\chi = -\mathrm{e}^{\pi\Phi}$ in both

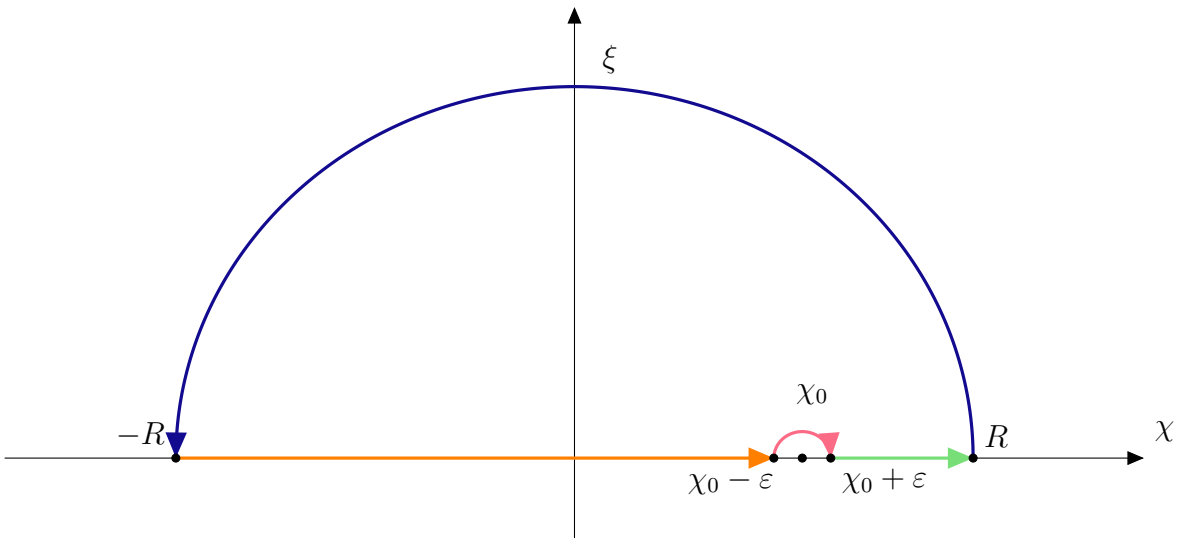

Figure 2.5.2: The contour C in the ζ plane

of the integrals and writing $\chi_0 = -\mathrm{e}^{\pi\Phi_0}$ in the first and $\chi_0 = \mathrm{e}^{\pi\Phi_0}$ in the second (for convenience) an expression for the value of τ on the free-surface can be written

$$\tau_f(\Phi) = \int_{-\infty}^{\infty} \frac{\theta_f(\Phi_0)\mathrm{e}^{\pi\Phi_0}}{\mathrm{e}^{\pi\Phi_0} - \mathrm{e}^{\pi\Phi}}\,\mathrm{d}\Phi_0 - \int_{-\infty}^{\infty} \frac{\theta_b(\Phi_0)\mathrm{e}^{\pi\Phi_0}}{\mathrm{e}^{\pi\Phi_0} + \mathrm{e}^{\pi\Phi}}\,\mathrm{d}\Phi_0. \tag{2.5.15}$$

For the bottom topography, χ is positive. By writing $\chi = \mathrm{e}^{\pi\Phi}$ a similar expression can be found for the value of τ on the bottom:

$$\tau_b(\Phi) = \int_{-\infty}^{\infty} \frac{\theta_f(\Phi_0)\mathrm{e}^{\pi\Phi_0}}{\mathrm{e}^{\pi\Phi_0} + \mathrm{e}^{\pi\Phi}}\,\mathrm{d}\Phi_0 - \int_{-\infty}^{\infty} \frac{\theta_b(\Phi_0)\mathrm{e}^{\pi\Phi_0}}{\mathrm{e}^{\pi\Phi_0} - \mathrm{e}^{\pi\Phi}}\,\mathrm{d}\Phi_0. \tag{2.5.16}$$

Together with Bernoulli's condition,

$$\frac{1}{2}q_f^2(\Phi) + \frac{1}{F^2}y(\Phi) = \frac{1}{2} + \frac{1}{F^2}. \tag{2.5.17}$$

these form a system of integro-differential equations for the unknowns $q_f(\Phi)$ and $\theta_f(\Phi)$ on the free surface. These quantities are functions of the velocity potential Φ and not the physical coordinate system. To find the actual shape of the free surface it is possible to make use of the identity (2.5.5) and state that:

$$\frac{\mathrm{d}z}{\mathrm{d}w} = \frac{1}{u - \mathrm{i}v}. \tag{2.5.18}$$

Recalling that $\mathrm{e}^{\tau} = q$ and integrating this expression along the free surface will yield a parametric representation of the free-surface:

$$\int \frac{\mathrm{d}z}{\mathrm{d}w}\,\mathrm{d}w = \int \frac{1}{u - \mathrm{i}v}\,\mathrm{d}w. \tag{2.5.19}$$

This becomes:

$$z = \int q^{-1} \mathrm{e}^{\mathrm{i}\theta} \, \mathrm{d}w, \tag{2.5.20}$$

And hence:

$$x(\Phi) = x(\infty) + \int_{\infty}^{\Phi} \mathrm{e}^{-\tau_f} \cos\theta_f \, \mathrm{d}\Phi, \tag{2.5.21}$$

$$y(\Phi) = 1 + \int_{\infty}^{\Phi} \mathrm{e}^{-\tau_f} \sin\theta_f \, \mathrm{d}\Phi. \tag{2.5.22}$$

Finally the values of θ_b are required for the formulation and hence in addition to the equations above

$$\tan\theta_b = \frac{\mathrm{d}\sigma}{\mathrm{d}x_b} \tag{2.5.23}$$

is required to close the system. To summarise, a system of integro-differential equations have been derived for the unknowns θ_f and θ_b. The boundary integrals are written as

$$\tau_f(\Phi) = \int_{-\infty}^{\infty} \frac{\theta_f(\Phi_0)\mathrm{e}^{\pi\Phi_0}}{\mathrm{e}^{\pi\Phi_0} - \mathrm{e}^{\pi\Phi}} \, \mathrm{d}\Phi_0 - \int_{-\infty}^{\infty} \frac{\theta_b(\Phi_0)\mathrm{e}^{\pi\Phi_0}}{\mathrm{e}^{\pi\Phi_0} + \mathrm{e}^{\pi\Phi}} \, \mathrm{d}\Phi_0, \tag{2.5.24a}$$

$$\tau_b(\Phi) = \int_{-\infty}^{\infty} \frac{\theta_f(\Phi_0)\mathrm{e}^{\pi\Phi_0}}{\mathrm{e}^{\pi\Phi_0} + \mathrm{e}^{\pi\Phi}} \, \mathrm{d}\Phi_0 - \int_{-\infty}^{\infty} \frac{\theta_b(\Phi_0)\mathrm{e}^{\pi\Phi_0}}{\mathrm{e}^{\pi\Phi_0} - \mathrm{e}^{\pi\Phi}} \, \mathrm{d}\Phi_0. \tag{2.5.24b}$$

The shape of the free-surface and bottom topography can be found by integrating

$$\frac{\mathrm{d}x_f}{\mathrm{d}\Phi} = \mathrm{e}^{-\tau_f} \cos\theta_f, \tag{2.5.25a}$$

$$\frac{\mathrm{d}y_f}{\mathrm{d}\Phi} = \mathrm{e}^{-\tau_f} \sin\theta_f, \tag{2.5.25b}$$

$$\frac{\mathrm{d}x_b}{\mathrm{d}\Phi} = \mathrm{e}^{-\tau_b} \cos\theta_b, \tag{2.5.25c}$$

$$\frac{\mathrm{d}y_b}{\mathrm{d}\Phi} = \mathrm{e}^{-\tau_b} \sin\theta_b. \tag{2.5.25d}$$

Finally Bernoulli's condition on the free-surface, (2.5.2) and the condition for θ_b are

$$e^{-2\tau_f} + \frac{1}{F^2} y_f = \frac{1}{2} + \frac{1}{F^2}, \tag{2.5.26a}$$

$$\tan\theta_b = \frac{\mathrm{d}\sigma}{\mathrm{d}x_b}. \tag{2.5.26b}$$

2.5.1 Numerical method

The algorithm to solving the system of equations (2.5.24), (2.5.25) and (2.5.26) is a standard technique and is explained in more detail in Tam *et al.* (2015). Briefly it is as follows:

1. Discretise Φ_i in N regularly spaced points in the interval $[\Phi_{-\infty}, \Phi_{\infty}]$

2. Use the fKdV solution as an initial guess for $\theta_s(\Phi_i)$, $i = 1, 2, \cdots N$. Use the known $\sigma(x)$ to get an initial guess for $\theta_b(\Phi_i)$, $i = 1, 2, \cdots N$. There are $2N$ unknowns

3. Using the $N-1$ midpoints of Φ_i, the N points $\theta_f(\Phi_i)$ and $\theta_f(\Phi_i)$, calculate $\tau_f(\Phi_{i+1/2})$ and $\tau_b(\Phi_{i+1/2})$ using the trapezoid rule in (2.5.24)

4. Integrate (2.5.25a) and (2.5.25b) using the conditions $y_f(\Phi_N) = 1$, $x_f(\Phi_N) = \Phi_N$ for the free-surface

5. Integrate (2.5.25c) and (2.5.25d) using the conditions $y_b(\Phi_N) = 0$, $x_b(\Phi_N) = \Phi_N$ for the bottom topography

6. Solve for $N-1$ equations given by the first equation in (2.5.26a)

7. Solve for N equations given by (2.5.26b)

8. Solve for 1 equation given by $y_s(\Phi_1) = 1$

9. Newton solve until norm of error is less than 10^{-11}

To continue the solutions in a chosen parameter space Keller's pseudo arclength algorithm is used. Note that this method is suitable for super-critical forcing where it is known from Stokes' result (see, for example Hunter & Vanden-Broeck, 1983)) that the free-surface decays exponentially in the far-field.

2.6 Remarks

The fKdV equation has been derived by an asymptotic expansion of the fully nonlinear water wave problem. For a delta function forcing the solution space is well known and has been described thoroughly using a phase plane analysis. The stability of the solutions for $F > 1$ has also been analysed with recourse to a formal stability argument that utilises the Hamiltonian nature of the fKdV equation. Finally a method for calculating the fully nonlinear solutions has been described so that a comparison can be made.

As discussed in the introduction and in this chapter solutions at $F = 1$ have been less studied and warrant further investigation. In the next chapter steady solutions over a smooth Gaussian forcing are investigated when $F = 1$. The solution space will be described as well as a detailed asymptotic analysis that describes the solution structure. These will be compared with numerical solutions of the fully nonlinear equations. Additionally the stability of these solutions will also be investigated using the formal stability analysis described in this chapter.

Ful

Chapter 3

Critical Free Surface Flow over a Depression Topography

3.1 Weakly nonlinear steady flow

The steady fKdV equation, (2.2.1), is restated for the reader as

$$\eta_{xx} + \frac{9}{2}\eta^2 - 6(F-1)\eta = -3\sigma(x) \tag{3.1.1}$$

A necessary condition for the existence of a steady solution for critical flow ($F = 1$) can be found by integrating (once) the steady form of (3.1.1) and applying the boundary conditions on η in (2.2.2) to obtain

$$\int_{-\infty}^{\infty} \sigma(x)\,\mathrm{d}x \leq 0. \tag{3.1.2}$$

This shows that there are no steady solutions for non-trivial topography which is everywhere non-negative with $\sigma(x) \geq 0$ for all x. However, steady solutions for η may exist when prescribing a dip, or negative bump topography, with $\sigma(x) \leq 0$ (see, for example, figure 2.1.1a) or for any topography satisfying (3.1.2). Following a similar integration procedure but first multiplying the steady form of (2.1.41) by η, the constraint

$$\int_{-\infty}^{\infty} \eta\sigma_x\,\mathrm{d}x = 0 \tag{3.1.3}$$

can be derived. In the remainder of the chapter the topographic forcing $\sigma(x)$ is assumed to be even in x, in which case (3.1.3) holds trivially for any even steady solution $\eta(x)$.

It is assumed that the forcing decays in the far-field, and is represented in the form

$$\sigma(x) = a\,f(bx), \tag{3.1.4}$$

where $f(x)$ is everywhere non-negative and $a < 0$ and $b > 0$ are depth and width

parameters respectively. Setting $F = 1$, the steady fKdV equation is then

$$\eta_{xx} + \frac{9}{2}\eta^2 = -3af(bx). \tag{3.1.5}$$

It is worthwhile repeating that unforced solutions to this equation decay algebraically as shown by (2.2.14). It is mathematically convenient to rewrite the problem in terms of a single parameter by making the change of variables $\eta = \frac{2}{9}b^2u$, $\xi = xb$ and $f = s$ to obtain

$$u_{\xi\xi} + u^2 = \alpha s(\xi), \tag{3.1.6}$$

where $\alpha = -27a/(2b^4)$. The boundary conditions are $u \to 0$ and $s \to 0$ as $|\xi| \to \infty$. From now on it is convenient to work with (3.1.6), but the physical discussion will be aided by making reference to the width and depth parameters a and b.

The analysis is as follows. Initially flow over a wide trench is analysed using a phase-plane analysis. Next the solution space for a wide dip, or negative Gaussian topography is explored by an asymptotic analysis and the solution space is compared to the case of a wide trench. Non-uniqueness is discovered in the forward problem of critical flow; a previously unknown result. These results are augmented by steady fully nonlinear solutions.

3.1.1 Flow over a rectangular trench

Flow over a rectangular trench of width $1/b$ and depth a is considered. The topography is defined as $f(x) = H(x - 1/2b) - H(x + 1/2b)$, where $H(x)$ is the Heaviside function. Solutions are sought for which the free surface is flat far upstream and downstream of the trench. The single-parameter form of the forcing appropriate to (3.1.6) is given by

$$s(\xi) = H(\xi - 1/2) - H(\xi + 1/2). \tag{3.1.7}$$

When $|\xi| > 1/2$, $s = 0$ and (3.1.6) can be integrated once to obtain

$$u_\xi^2 = -\frac{2}{3}u^3 + B, \tag{3.1.8}$$

where B is a constant of integration. This equation describes trajectories in the (u, u_ξ) phase plane which are shown as the solid black curves in figure 3.1.1. There is a single degenerate critical point at the origin which trajectories approach in the limit $|x| \to \infty$ in such a way that $u \to 0$ algebraically. For $|\xi| \leq \frac{1}{2}$ it is convenient to introduce the new variable $v = u_\xi$ and to rewrite (3.1.6) as the dynamical system

$$u_\xi = v, \qquad v_\xi = \alpha - u^2. \tag{3.1.9}$$

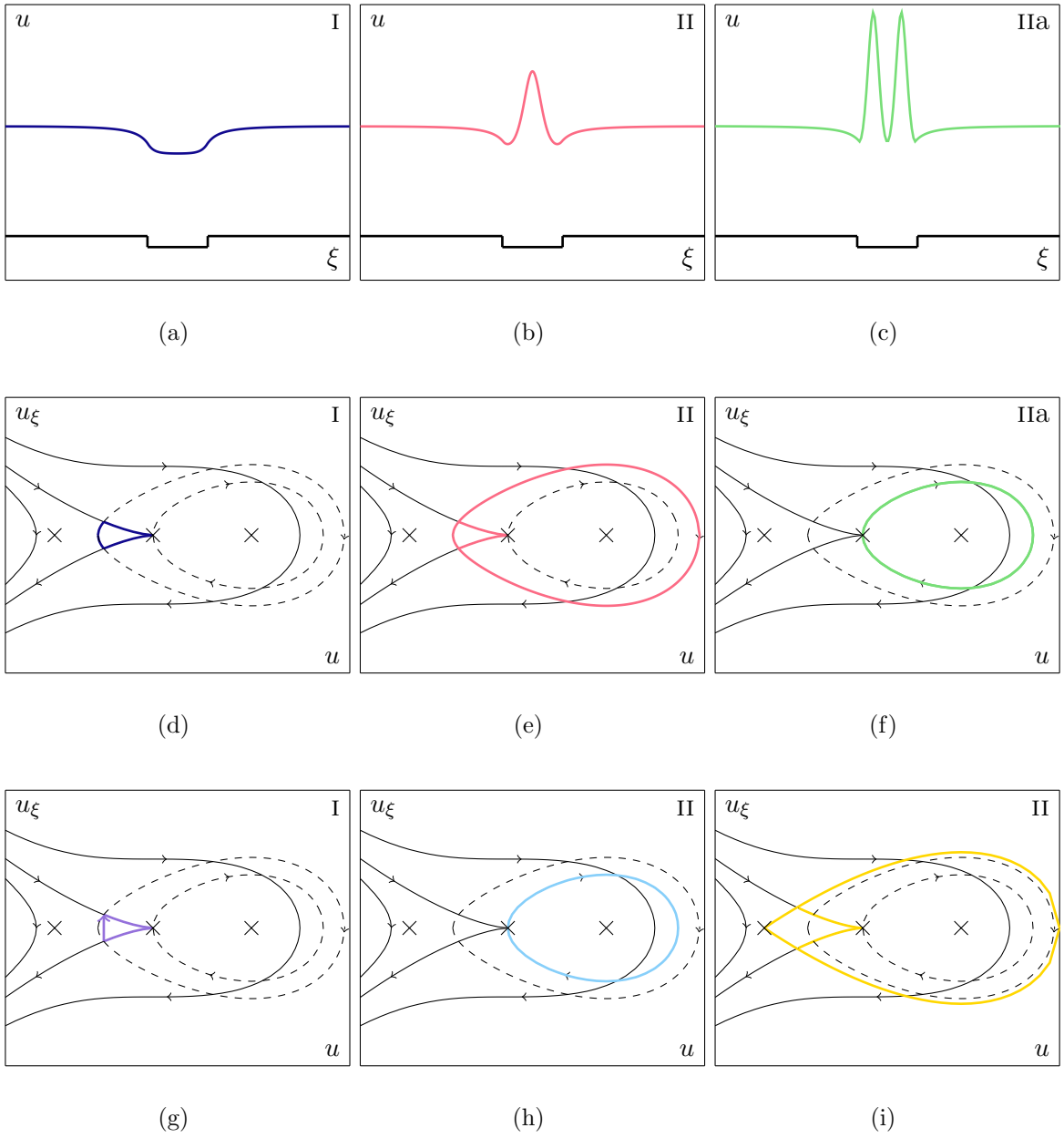

Figure 3.1.1: Sketch of solutions and phase plane analysis for flow past a trench. The dashed curves in the phase plane are for the forced region whilst the solid black curves are for the unforced region. The crosses in the phase plane are for $(\eta, \eta_x) = (\pm\alpha^{1/2}, 0)$ and $(0, 0)$. (a) Type I solution. (b) Type II solution (c) Type IIa solution. (d) Phase plane for Type I solution. (e) Phase plane for Type II solution. (f) Phase plane for limiting Type IIa solution. (g) Phase plane for Type I solution with Gaussian jump condition. (h) Phase plane for limiting type II solutions with amplitude $\sqrt{\alpha}$. (i) Phase plane for limiting type II solutions with amplitude $2\sqrt{\alpha}$.

Critical points occur at the values

$$u_{\pm} = \pm\sqrt{\alpha}, \tag{3.1.10}$$

and straightforward analysis reveals that u_+ is a centre and u_- is a saddle point. The first integral of (3.1.6),

$$u_\xi^2 = 2\alpha u - \frac{2}{3}u^3 + C, \tag{3.1.11}$$

describes different trajectories in the phase plane for different values of the constant C. These trajectories are shown as dashed black curves in figure 3.1.1, where they are overlaid with the solid black curves depicting the unforced phase plane. A solution to (3.1.6) that satisfies the boundary conditions $u \to 0$ as $|\xi| \to \infty$ may be constructed using parts of the unforced phase plane (the solid black curves in figure 3.1.1) and parts of the forced phase plane (the dashed black curves), with a switch made from one to the other where these lines intersect. Since there is more than one way in which this construction can be made for a particular α, there is non-uniqueness of solution.

The first type of solution, hereinafter referred to as type I, represents a depression wave. Examples follow the trajectories highlighted in blue in figures 3.1.1(a) and (d). The distinguishing feature of a type I solution is as follows. A solution exits the origin along a trajectory in the unforced phase plane; it then latches onto and traverses a section of a homoclinic orbit around the centre at $(\sqrt{\alpha}, 0)$ in the forced phase plane, before reattaching to a trajectory in the unforced phase plane and returning to the origin. In passing, note the similarity between this description and the steady solution obtained for a delta function point forcing with $s(\xi) = \delta(\xi)$, which has been considered for critical flow by Binder *et al.* (2014). In this case, the delta function provokes an instantaneous vertical jump upwards in the unforced phase plane, similar to what is shown in figure 3.1.1(g). For a given value of α, the type I solutions follow the path described, but are constrained to lie within the homoclinic orbit which connects the saddle point at $(\sqrt{\alpha}, 0)$ to itself. Thus, in the extreme case a trajectory can come infinitesimally close to the homoclinic orbit, as shown in figure 3.1.1(d). Note also no type I trajectory can enter the right half phase plane. Therefore the minimum elevation for type I solutions occurs at $x = 0$ and must lie in the interval $-\sqrt{\alpha} < u(0) \leq 0$.

Type II solutions correspond to a trajectory which starts at the origin, continues into the left half of the unforced phase plane and then latches onto to a periodic orbit in the forced phase plane, which it must traverse exactly once before reconnecting to the trajectory which returns to the origin in the unforced plane. This is illustrated in figures 3.1.1(b),(e). The closed loop corresponds to a cnoidal wave solution (Whitham, 1974). Alternatively the solution may jump directly from the origin of the unforced phase plane onto a cnoidal loop as in figure 3.1.1(f). The wave profile corresponding to two cnoidal wave periods is shown in figure 3.1.1(c) corresponding to the phase plane in figure 3.1.1(f). In the extreme case, the solution departs from the origin and proceeds

into the left-half unforced plane to latch onto the homoclinic orbit connecting the point $(-\sqrt{\alpha}, 0)$ to itself in the forced plane as in figure 3.1.2(i).

The construction of type II solutions as described places a constraint on the values of α for which such solutions exist. Since the trajectory must execute an integer number of orbits of a cnoidal loop (e.g. figure 3.1.1(h)), there is a minimum value of α, corresponding to a minimum trench width, which supports such solutions. This minimum width is equal to the period of the cnoidal wave whose orbit intersects the origin, as shown in figure 3.1.1(h). This orbit corresponds to taking $C = 0$ in (3.1.11). The solution can be found in closed form and is given by (see, for example Billingham & King, 2000; Whitham, 1974)

$$u(\xi) = \sqrt{3\alpha}\,\mathrm{cn}^2\left(\Delta^{1/4}\xi; \frac{1}{2}\right), \tag{3.1.12}$$

where cn is a Jacobi elliptic function and $\Delta = \frac{\alpha}{3}$. Therefore $u(0) = \sqrt{3\alpha}$. The spatial period of this cnoidal wave is given by

$$\frac{2K(1/\sqrt{2})}{\Delta^{1/4}}, \tag{3.1.13}$$

where K is the complete elliptical integral of the first kind. Therefore type II solutions co-exist with type I solutions, and non-uniqueness is established when

$$\alpha \geq 48K^4(1/\sqrt{2}) \approx 567.0. \tag{3.1.14}$$

The maximum elevation for the type II solutions, which occurs at $\xi = 0$, is constrained by the amplitude of the homoclinic orbit in the forced plane. This orbit corresponds to the value $C = \frac{4}{3}\alpha^{3/2}$ in (3.1.11). For this trajectory, equation (3.1.11) may be integrated to yield the explicit expression for the wave profile,

$$u(\xi) = -\alpha^{1/2} + 3\alpha^{1/2}\,\mathrm{sech}^2\left(\frac{\sqrt{2}}{2}\xi\right) \tag{3.1.15}$$

Hence the maximum elevation is $u(0) = 2\sqrt{\alpha}$. In summary type II solutions have the property $\sqrt{\alpha} < u(0) \leq 2\sqrt{\alpha}$.

Figure 3.1.2 shows part of the solution space for a rectangular trench, characterised by the physical mid-stream elevation $\eta(0)$ for type I and type II solutions for a range of α values. In addition to the type II solution branch shown in figure 3.1.2 there exists an infinitude of solutions of similar character whose trajectories traverse the cnoidal orbit n times for integer $n > 1$. For each n a new solution branch begins at

$$\alpha = 48n^4K^4(1/\sqrt{2}) \tag{3.1.16}$$

The solutions on these extra branches are confirmed numerically for a few values of n

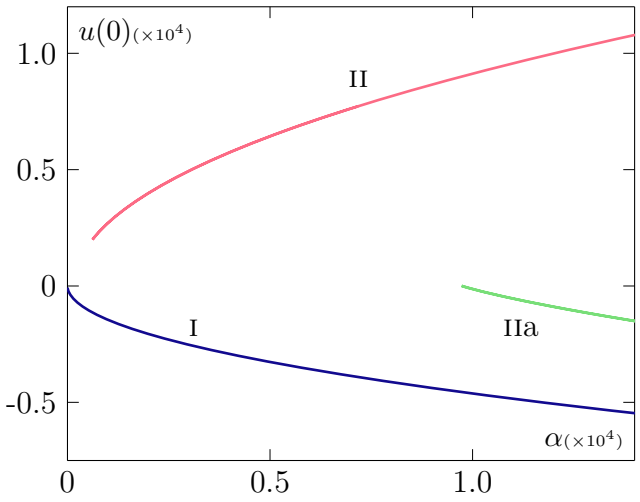

Figure 3.1.2: Solution space in terms of α and $u(0)$.

(see figure 3.1.2).

It is worth emphasising that all of the solutions constructed in this section for a rectangular trench can be written down in closed form. The solution for a general cnoidal loop in the forced plane is available in, for example, Whitham (1974) and Billingham & King (2000). The solution along the trajectory in the unforced plane which connects to the origin can be be found in a straightforward manner to be

$$u(\xi) = -\frac{6}{(D-\xi)^2}, \tag{3.1.17}$$

where the constant D depends on the particular construction of the solution following the prescriptions described above.

Figure 3.1.3 shows numerical solutions calculated for the different types of solution. Note that these were calculated using (3.1.5) with a smooth topography of the form

$$\sigma(x) = \frac{a}{2}[\tanh(\lambda(x+b)) - \tanh(\lambda(x-b))];$$

where λ was chosen to be large to make the walls of the 'trench' as steep as possible. This also means the limit points of the type II solutions will be slightly different, although the behaviour is similar. In the next section the analysis is extended to the case of a smooth topography and the particular example of a Gaussian dip is considered.

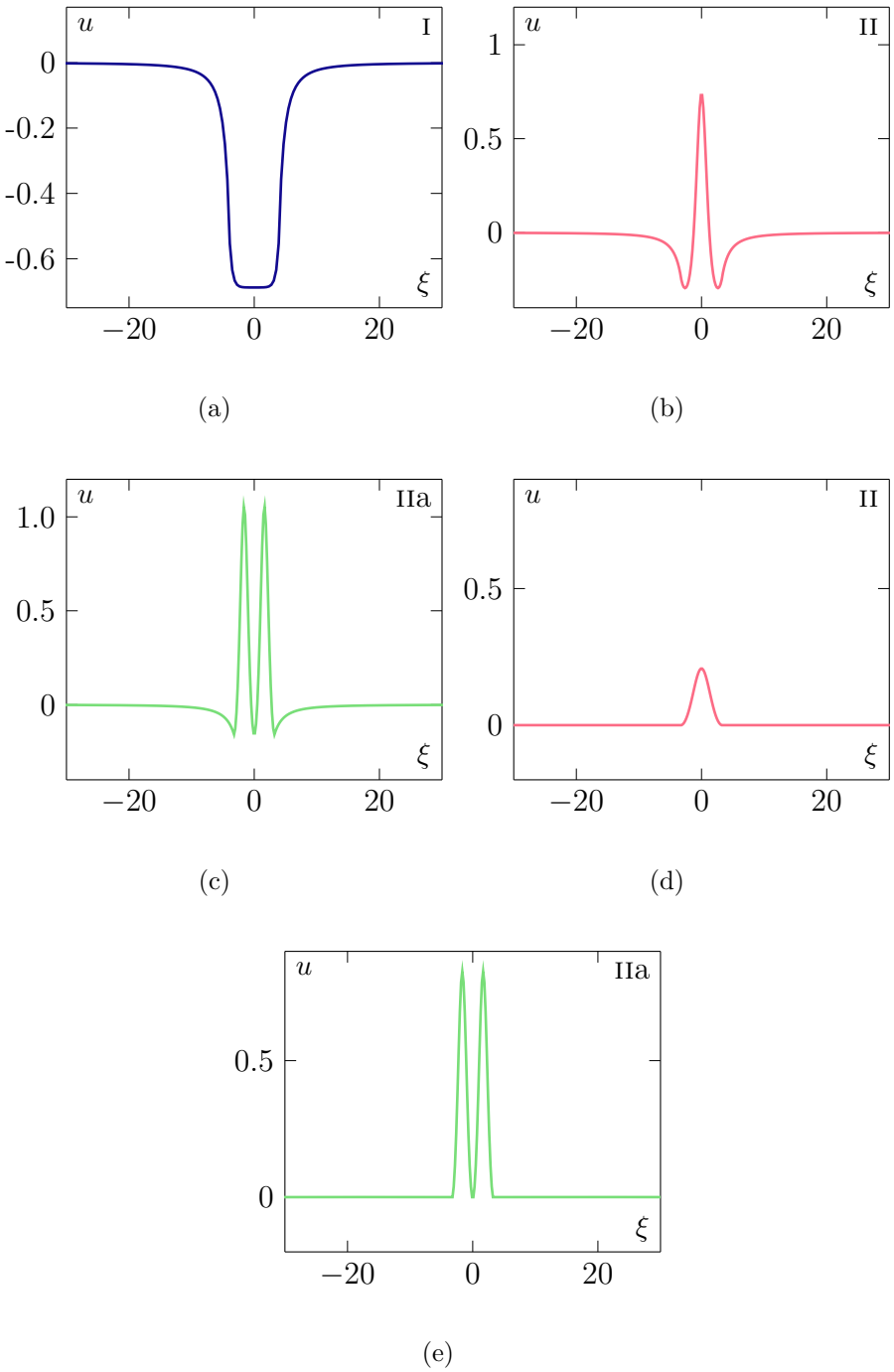

Figure 3.1.3: Numerical Solutions for $\eta(x)$. (a) Type I, $\alpha = 20618.0$, $(a = -0.7143, b = 0.3)$. (b) Type II, $\alpha = 6205.0$ $(a = -0.2152, b = 0.3)$. (c) Type IIa, $\alpha = 13584.0$ $(a = -0.4805, b = 0.3)$. (d) Limiting Type II, $\alpha = 617.0$, $(a = -0.0214, b = 0.1471)$. (e) Limiting Type IIa, $\alpha = 9719$, $(a = -0.3371, b = 0.1471.)$

3.2 Flow over a Gaussian dip

In this section the topographic forcing is prescribed as

$$s(\xi) = \mathrm{e}^{-\xi^2} \tag{3.2.1}$$

in the steady fKdV equation (3.1.6). This corresponds to the choice $\sigma(x) = a\exp(-b^2x^2)$ in (3.1.5), and note that in the limit as $b \to \infty$ with $a = bc/\sqrt{\pi}$, for constant c, then $\sigma \to c\,\delta(\xi)$ so that a delta function forcing is recovered. In this case, type I solutions have already been shown to be possible. In the limit $b \to 0$ corresponding to a wide dip, type II solutions are expected to exist, as in the rectangular trench case studied in section 3.1.1.

In the remainder of this section equation (3.1.6) is studied subject to the non-autonomous forcing (3.2.1). The solution space for different values of $\alpha > 0$ (recall that solutions are not possible for $\alpha < 0$) is also sought. Initially, the extreme cases $\alpha \ll 1$ and $\alpha \gg 1$ are scrutinised separately. It is more convenient to work on the half-domain $\xi \geq 0$ which is consistent with seeking solutions with even symmetry. Therefore the boundary conditions

$$u_\xi(0) = 0, \qquad \lim_{\xi\to\infty} u = 0 \tag{3.2.2}$$

are to be satisfied. For each limit the solution is found to be decomposed into two or more asymptotic regions which must be matched together. In the limit $\alpha \ll 1$ the matching is accomplished between two distinct regions. For $\alpha \gg 1$ the situation is more complex, and four distinct asymptotic zones are required.

3.2.1 Small α asymptotics

For small α an appropriate asymptotic expansion for the asymptotic solution to (3.1.6) is of the form:

$$u(\xi) = \alpha^{2/3}u_0(\xi) + \alpha u_1(\xi) + \alpha^{4/3}u_2(\xi) + \cdots \tag{3.2.3}$$

This form is motivated by analysis of $s(\xi) = \delta(\xi)$ the delta function. A jump condition for the aforementioned forcing can be found by integrating the steady fKdV equation (3.1.6) across $\xi = 0$. It is straightforward to show that the jump condition is

$$u_\xi(0+) - u_\xi(0-) = \alpha. \tag{3.2.4}$$

This upwards jump corresponds to the upwards arrow in figure 3.1.1(g). For a symmetric solution the jump must start at $u_\xi = -\frac{1}{2}\alpha$ and finish at $u_\xi = \frac{1}{2}\alpha$. The trajectory entering the origin is given by $u_\xi = \sqrt{2/3}\,(-u)^{3/2}$. At the end of the jump, where $u_\xi = \frac{1}{2}\alpha$, $u \sim O(\alpha^{2/3})$ and this motivates the form of the asymptotic expansion above. Substituting (3.2.3) into (3.1.6) and solving at successive orders of approximation using

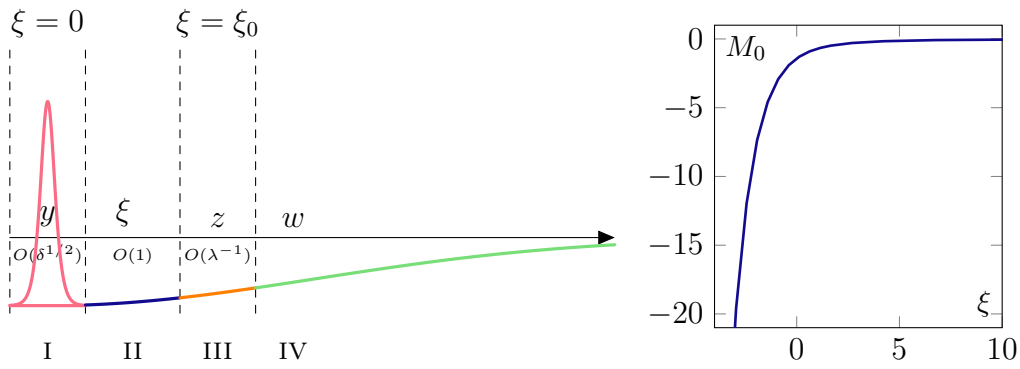

(a) (b)

Figure 3.2.1: (a) Sketch of the four regions used in the matched asymptotics for large α. (b): Numerical solution to the region III problem equation (3.2.26) subject to (3.2.27) with the minus sign.

the first of the conditions in (3.2.2),

$$u_0(\xi) = \overline{u}_0, \qquad u_1(\xi) = \int_0^\xi \mu(\tau)\,\mathrm{d}\tau + \overline{u}_1, \qquad u_2(\xi) = -\frac{1}{2}\overline{u}_0^2\xi^2 + \overline{u}_2, \tag{3.2.5}$$

where the $\overline{u}_i$ are constants of integration, and $\mu(\xi) = \int_0^\xi \exp(-\tau^2)\,\mathrm{d}\tau$. In the far-field

$$u(\xi) \sim \alpha^{2/3}\overline{u}_0 + \alpha\left(\frac{\sqrt{\pi}}{2}\,\xi + \overline{u}_1 - \frac{1}{2}\right) + O(\alpha^{4/3}) \tag{3.2.6}$$

as $\xi \to \infty$, which indicates that the expansion will fail when $\xi \sim O(\alpha^{-1/3})$. Accordingly an outer region is introduced for the new variable $\zeta = \alpha^{1/3}\xi = O(1)$ together with an expansion $u = \alpha^{2/3}\tilde{u}_0(\zeta) + \cdots$ inside this outer region. Substituting into (3.1.6), at leading order and at first order,

$$\tilde{u}_{0\zeta\zeta} + \tilde{u}_0^2 = 0, \qquad \tilde{u}_{1\zeta\zeta} + 2\tilde{u}_0\tilde{u}_1 = 0. \tag{3.2.7}$$

The solutions which satisfy the second condition in (3.2.2) are

$$\tilde{u}_0(\zeta) = -\frac{6}{(\zeta + d_1)^2}, \qquad \tilde{u}_1(\zeta) = \frac{d_2}{(\zeta + d_1)^3}, \tag{3.2.8}$$

where d_1, d_2 are constants of integration. Matching to the inner region determines the constants as

$$\overline{u}_0 = -\frac{6}{d_1^2}, \qquad d_1 = 2\left(\frac{3}{\sqrt{\pi}}\right)^{1/3}, \tag{3.2.9}$$

as well as $d_2 = 0$ and $\overline{u}_1 = 1/2$. In conclusion, for small α, there exists a solution with negative elevation at the point of symmetry with $u(0) < 0$.

3.2.2 Large α asymptotics

Solutions are discussed when $\alpha \gg 1$. It will be convenient to rescale the problem by introducing the new dependent variable $u = \alpha^{1/2}U$ so that (3.1.6) with (3.2.1) takes the form

$$\delta U_{\xi\xi} + U^2 = \mathrm{e}^{-\xi^2} \tag{3.2.10}$$

where $\delta = \alpha^{-1/2}$ and $\delta \ll 1$. Referring to figure 3.2.1(a) the asymptotic solution for small δ has four distinct regions. In the core region, labelled region II in the figure, the solution is expanded by writing

$$U = U_0 + \delta U_1 + \delta^2 U_2 + \delta^3 U_3 + \cdots \tag{3.2.11}$$

Substituting into (3.2.10) algebraic equations are obtained for the U_i at successive orders of approximation which are solved easily. At leading order

$$U_0 = \pm \mathrm{e}^{-\xi^2/2}. \tag{3.2.12}$$

Discussion of the choice of the sign in (3.2.12) will be given below. At $O(\delta)$

$$U_1 = -\frac{U_{0\xi\xi}}{2U_0} = \frac{1}{2}(1 - \xi^2), \tag{3.2.13}$$

which is valid regardless of the sign taken for U_0 in (3.2.12). From the next two orders, the forms are determined as

$$U_2 = \pm\frac{1}{8}(\xi^4 - 2\xi^2 - 3)\mathrm{e}^{\xi^2/2}, \qquad U_3 = \frac{5}{8}(\xi^4 - 1)\mathrm{e}^{\xi^2}. \tag{3.2.14}$$

Although each of the U_i in (3.2.11) satisfies the symmetry condition $U_{i\xi}(0) = 0$ required by (3.2.2), the expansion must nonetheless break down as $\xi \to 0$ since the first term on the left hand side of (3.2.10) will become comparable to the second in this limit. Moreover, (3.2.11) evidently breaks down as ξ increases since successive terms in the expansion grow to become comparable in size to their predecessors. The first of these issues is addressed first, and the solution is considered in the boundary layer at $\xi = 0$, namely region I in figure 3.2.1.

In region I, the boundary-layer variable $y = \delta^{-1/2}\xi$ is introduced and the solution is expanded by writing

$$U = \tilde{U}_0(y) + \delta\tilde{U}_1(y) + \delta^2\tilde{U}_2(y) + \cdots . \tag{3.2.15}$$

Substituting into (3.2.10), at leading order

$$\tilde{U}_{0yy} + \tilde{U}_0^2 = 1 \tag{3.2.16}$$

subject to the symmetry condition $\tilde{U}_{0y}(0) = 0$ and the condition that $\tilde{U}_0 \sim \pm 1$ as $y \to \infty$ to match with region II, the choice of sign in the latter condition being dictated by the choice of sign taken in (3.2.12). This problem has three possible solutions given by

$$(i) \quad \tilde{U}_0 = 1, \qquad (ii) \quad \tilde{U}_0 = -1, \qquad (iii) \quad \tilde{U}_0 = -1 + 3\,\mathrm{sech}^2(y/\sqrt{2}). \tag{3.2.17}$$

Referring to the $(\tilde{U}_0, \tilde{U}_{0y})$ phase plane, these correspond respectively to fixed points at $\tilde{U}_0 = \pm 1$, and a homoclinic orbit encircling $\tilde{U}_0 = 1$ which connects $\tilde{U}_0 = -1$ to itself.

The cases (i) and (ii) are examined first. At $O(\delta)$

$$\tilde{U}_{1yy} \pm 2\tilde{U}_1 = -y^2. \tag{3.2.18}$$

The solution which satisfies $\tilde{U}_{1y}(0) = 0$, and which does not grow exponentially as $y \to \infty$, is given by

$$\tilde{U}_1 = \frac{1}{2}(1 \mp y^2). \tag{3.2.19}$$

Since the expressions in (3.2.19) are forced directly by the solution in the core region II, the matching with that region is immediate. For case (iii),

$$\tilde{U}_{1yy} + 2\Big(3\,\mathrm{sech}^2(y/\sqrt{2}) - 1\Big)\tilde{U}_1 = -y^2. \tag{3.2.20}$$

By making the change of variables $t = \tanh(y/\sqrt{2})$, this can be transformed into the associated Legendre equation

$$\frac{\mathrm{d}}{\mathrm{d}t}\left((1-t^2)\frac{\mathrm{d}\tilde{U}_1}{\mathrm{d}t}\right) + \left(12 - \frac{4}{1-t^2}\right)\tilde{U}_1 = -\frac{4\,\mathrm{arctanh}^2\, t}{1-t^2}. \tag{3.2.21}$$

The solution which satisfies the required symmetry condition $\tilde{U}_{1t}(0) = 0$ is given by

$$\begin{aligned}\tilde{U}_1(t) = \frac{1}{4}p_1(t)\Big[\int_0^t \frac{\mathrm{arctanh}^2\, s}{s^2-1}\,p_2(s)\,\mathrm{d}s - \frac{15}{2}\pi^2\Big] + \frac{1}{32}\,p_2(t)\Big[4\log(1-t^2) \\ - \log\left(\frac{1+t}{1-t}\right)\Big\{(1-t^2)\log\left(\frac{1+t}{1-t}\right) - 4t\Big\} - 8\log 2\Big],\end{aligned} \tag{3.2.22}$$

where

$$p_1(t) = t(t^2-1), \qquad p_2(t) = 15t(t^2-1)\log\left(\frac{1+t}{1-t}\right) + \frac{50t^2 - 30t^4 - 16}{t^2-1} \tag{3.2.23}$$

are the homogeneous solutions to (3.2.21). Note that $\tilde{U}_1(t) \sim \mathrm{arctanh}^2\, t$ as $t \to 1$ and so $\tilde{U}_1 \sim y^2/2$ ensuring a match with region II.

Attention is now turned to region III. Scrutinising the terms U_0 and U_1 in (3.2.12) and (3.2.13), the expansion (3.2.11) in region II breaks down when $\exp(-\xi^2/2) \sim$

$\frac{1}{2}\delta(\xi^2-1)$. This occurs when $\xi \sim \xi_0(\delta)$, where

$$\xi_0 = \lambda - \lambda^{-1}\log\left(\lambda^2/2\right) + \cdots, \tag{3.2.24}$$

with $\lambda = (-2\log\delta)^{1/2}$. Inside this narrow region, the internal layer variable $z = \lambda(\xi - \xi_0)$ is introduced, and the solution is expanded by writing

$$U = \delta\lambda^2 M_0(z) + \delta M_1(z) + \cdots \tag{3.2.25}$$

Substituting this into equation (3.2.10), at leading order,

$$M_{0zz} + M_0^2 = \mathrm{e}^{-2z}. \tag{3.2.26}$$

The boundary conditions are

$$\lim_{z\to-\infty} M_0 = \pm\infty, \qquad \lim_{z\to\infty} M_0 = 0. \tag{3.2.27}$$

Here the $+/-$ sign is required to match to the solution in region II, namely (3.2.12) with the $+/-$ sign selected respectively. It is possible to compute a solution to this problem numerically for either choice of sign; however, great care is needed when attempting to match the solution with region II, as will be discussed below. First the case of the minus sign in (3.2.27) is discussed. Figure 3.2.1(b) shows the result of a calculation using fourth order Runge-Kutta integration to solve the problem (3.2.26) with the minus sign chosen in the boundary condition (3.2.27). An analysis for large negative z reveals that the solution takes the form

$$M_0(z) = -\mathrm{e}^{-z} - \frac{1}{2} + \frac{1}{8}\mathrm{e}^{z} + c_1 K_2\left(2\sqrt{2}\,\mathrm{e}^{-z/2}\right) + \cdots \tag{3.2.28}$$

as $z \to -\infty$, where K_2 is a modified Bessel function of the second kind, and c_1 is a constant which must be determined globally but is not required here. Since it is known that $K_2(w) \sim \sqrt{\pi/2z}\exp(-2z)\cdots$ (e.g. Abramowitz & Stegun, 1964), the final term in (3.2.28) decays super-exponentially and matching to region II is possible. For large positive z, the forcing term on the right hand side of (3.2.26) becomes negligible and the dominant balance of the two terms on the left hand side requires the behaviour $M_0 \sim 6/(z+c_2)^2$, for constant c_2, as $z \to \infty$. In region IV, the expansion proceeds as

$$U(\xi) = \delta\hat{U}_0(w) + \cdots \tag{3.2.29}$$

where $w = \xi - \xi_0 = O(1)$. At leading order $\hat{U}_{0ww} + U_0^2 = 0$ and the solution satisfying the far-field condition in (3.2.2), namely $\hat{U}_0 \to 0$ as $w \to \infty$, is

$$\hat{U}_0 = -\frac{6}{(w+c_3)^2}, \tag{3.2.30}$$

for constant c_3 which can in principle be found by matching to region III.

As noted above, it is possible to numerically compute a solution to the problem (3.2.26) subject to (3.2.27) with the plus sign selected in the boundary condition. However, the numerical solution exhibits small decaying oscillations for large negative z. Indeed, in the limit $z \to -\infty$ it can be shown that

$$M_0(z) \sim \mathrm{e}^{-z} - \frac{1}{2} - \frac{1}{8}\mathrm{e}^{z} + \alpha_1 J_2\left(2\sqrt{2}\mathrm{e}^{-z/2}\right) + \alpha_2 Y_2\left(2\sqrt{2}\mathrm{e}^{-z/2}\right) + \cdots, \qquad (3.2.31)$$

for constants α_1, α_2, where J_2 and Y_2 are Bessel functions of the first and second kind respectively. As $\xi \to \infty$, $J_2(\xi) \sim \sqrt{2/\pi\xi}\cos(\xi - 5\pi/4) + \cdots$ and $Y_2(\xi) \sim \sqrt{2/\pi\xi}\sin(\xi - 5\pi/4) + \cdots$ (Abramowitz & Stegun, 1964) and so M_0 has decaying oscillations as $z \to -\infty$ in agreement with the numerical solution. Since the solution in region II is non-oscillatory, it is not possible to complete a match between regions II and III, and on this basis the choice of the plus sign in (3.2.12) must be rejected since it does not lead to a consistent asymptotic solution.

In conclusion, consistent asymptotic solutions may be constructed for cases (*ii*) and (*iii*) in (3.2.17), but not for case (*i*). This means that there is one asymptotic solution consistent with the choice of a minus sign in (3.2.12), namely case (*ii*), and one solution consistent with the choice of a plus sign in (3.2.12), namely case (*iii*).

3.2.3 Numerical results

In summary, in section 3.2.2 it was found to be possible to construct a consistent asymptotic solution using boundary-layer theory for cases (*ii*) and (*iii*) in (3.2.17), but not for case (*i*). This together with the results of the small α asymptotic analysis in section 3.2.1 suggests that there exist at least two distinct branches of steady solutions. To carry out a full investigation of the solution space, the steady problem (3.1.6) is solved with s given by (3.2.1) numerically by employing a shooting technique based on the 4th order Runge-Kutta method. The problem was first reformulated as a first order system in the form $\mathbf{x}_\xi = \mathbf{F}(\mathbf{x})$, where $\mathbf{x} = (u, u_\xi)^T$ and $\mathbf{F} = (u_\xi, \alpha s - u^2)^T$. Following the assumed symmetry of the solution, the system was integrated forward from the starting point $\mathbf{x}(\xi = 0) = (u_0, 0)^T$ for a chosen u_0. The correct value of u_0 was determined iteratively until the trajectory of the solution in the (u, u_ξ) phase plane approaches the origin. Formally this should happen in infinite time as $\xi \to \infty$ but in computational practice the value of u_0 was refined so that an increasingly large value of ξ was required to reach the origin. There are two qualitatively different ways in which this can happen as follows:

$$\text{(a)} \quad \frac{u_\xi}{u} \sim -\frac{2}{\xi} \qquad \text{or} \qquad \text{(b)} \quad \frac{u_\xi}{u} \sim -2\xi \qquad (3.2.32)$$

as $\xi \to \infty$. Option (a) represents a balance between the two terms on the left hand side of (3.1.6) and constitutes algebraic decay of the solution as $-6\xi^{-2}$ for large ξ. In this case the slope of the trajectory tends to $0-$ as the origin is approached. Option (b) represents a balance between the first term on the left hand side of (3.1.6) and the topographic forcing term on the right hand side. In this case the trajectory enters the origin from below with an infinitely negative slope. The computed solution was checked against an independent calculation in which the boundary value problem was solved using a finite difference method on a uniform grid over the truncated domain $[-L, L]$ with L taken to be suitably large. Approximating the second derivative in (3.1.6) with a centred-difference furnishes a set of nonlinear algebraic equations at each grid point, which were solved using Newton's method.

Figures 3.2.2(a) and (b) show the two numerically-computed solutions whose existence was suggested by the asymptotic analysis. Following the terminology employed for a rectangular trench in section 3.1.1, the depression wave in figure 3.2.2(a) is referred as a type I solution and the elevation wave in figure 3.2.2(b) as a type II solution. The solution space, characterised by the value $u(0)$, is shown in figure 3.2.3. The predictions of the asymptotic analysis are included in figures 3.2.3(a) and (b). Numerically, the far-field behaviour (a) in (3.2.32) is obtained on the lower branch of type I solutions and also on almost all of the upper branch except at the point $\alpha \approx 35.14$, where this branch terminates and the behaviour (b) in (3.2.32) is found. It can be shown analytically (King, 2018) that the branch does indeed terminate in this way and that the solution branch enters the termination point with finite slope. It is also noted that the termination of the type II solution branch is similar to the behaviour found for a rectangular trench in section 3.1.1, where the trajectory in phase space corresponding to the limiting cnoidal wave solution approaches the origin with infinite slope.

Further experimentation with the value of u_0 discussed in the previous paragraph revealed the existence of a seemingly infinite sequence of new solutions which are not predicted by the asymptotic analysis. These solutions all have ripples on the free surface around the origin. An increasing number of ripples are present for each subsequent branch in the sequence IIa,b,c,d and so on as shown in figures 3.2.2(c)-(f). It appears that this sequence of solution branches continues indefinitely, as was seen to occur for the rectangular trench topography discussed in section 3.1.1. Moreover there is a striking broad similarity between the solution spaces found for the two different topographies as shown in figure 3.2.3.

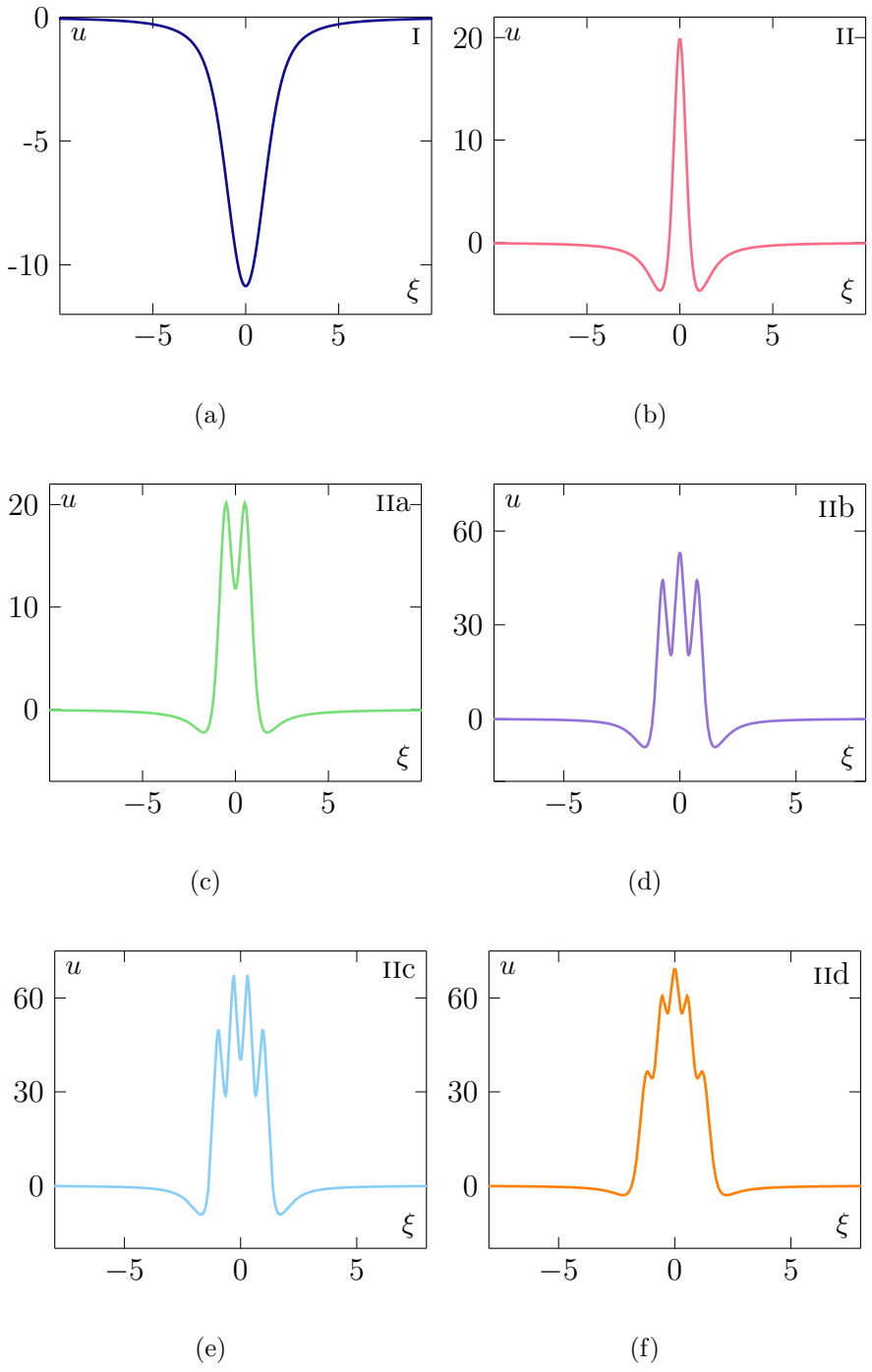

Figure 3.2.2: Numerical solutions for critical flow past a Gaussian dip. The horizontal axis is ξ and vertical axis is u (a) Type I solution, $\alpha = 128.4$. (b) Type II solution, $\alpha = 129.5$. (c) Type IIa solution, $\alpha = 281.5$. (d) Type IIb solution, $\alpha = 1500.0$. (c) Type IIc solution, $\alpha = 3000.0$. (c) Type IId solution, $\alpha = 4000.0$.

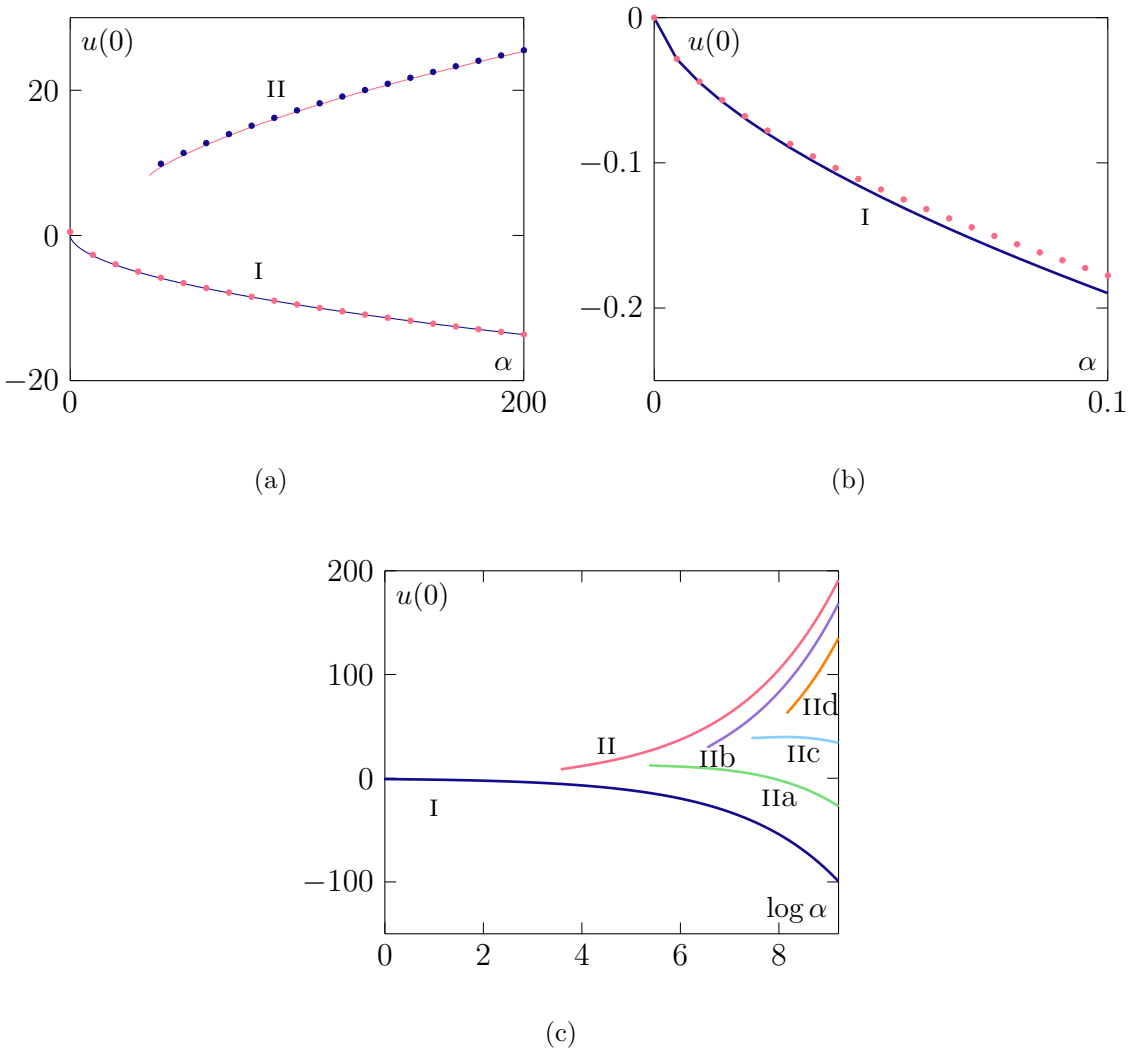

Figure 3.2.3: Solution space (solid lines). (a) The large α asymptotic approximations $u(0) \sim -\alpha^{1/2} + 1/2$, which corresponds to case (ii) in (3.2.17), is shown with a red markers on the lower branch. The blue markers curve on the upper branch illustrates the large α asymptotic behaviour for the type II solution $u(0) \sim 2\alpha^{1/2} - 4\log(2)$ which corresponds to case (iii) in (3.2.17). The type II solution terminates at $\alpha \approx 35.14$. (b) The behaviour for small α of the type I solution. The red markers illustrates the small α asymptotic behaviour $u(0) \sim -(6/d_1^2)\alpha^{2/3} + (1/2)\alpha$, with d_1 as given in (3.2.9). (c) Extended view of the solution space showing a wider range of α than panel (a) and including type IIa, b, c and d solutions. The latter solutions terminate at $\alpha \approx 214.0$, 699.1, 1709.0 and 3508.0 respectively.

3.3 The Kuzmak approximation

The existence of solutions with additional waves around the origin, the IIa,b,c,d,etc,for the fKdV equation is now justified asymptotically. On this point it is illuminating to highlight the similarity between the presently considered problem and the celebrated Carrier problem discussed at length in, for example, Bender & Orszag (1999) (p. 464), wherein an increasing number of interior oscillations appear in the solution as the pertinent dimensionless parameter approaches zero. These solutions are not fully captured by a traditional boundary-layer analysis as described in the previous section. The Kuzmak method; a multi-scales expansion with a slowly varying phase function is now used to reveal the asymptotic structure of these extra solutions. For a detailed explanation of the method see Kuzmak (1959), Bourland & Haberman (1988), King *et al.* (2003) and Chapman & Farrell (2017).

The motivation for using this method comes from the WKBJ method for linear ODE. The model second order equation,

$$y''(t) + Q(\varepsilon t)y(t) = 0,$$

$\varepsilon \ll 1$, where Q is a function, is used to illustrate this. By assuming a solution of the form $y = \exp(S(t))$ and then writing $S(t)$ as an asymptotic expansion with leading order term $O(\varepsilon^{-1})$, the solution can be written as

$$y(t) = \exp\left[\frac{1}{\varepsilon}S_0(t) + S_1(t) + O(\varepsilon)\right], \tag{3.3.1}$$

$$= [Q(\tau)]^{-1/4}\exp\left[\pm\frac{\mathrm{i}}{\varepsilon}\int^{\tau} Q(s)\,\mathrm{d}s + \cdots\right], \tag{3.3.2}$$

where $\tau = \varepsilon t$. The function $S(t) = \varepsilon^{-1}S_0(t) + S_1(t) + O(\varepsilon)$, is called the phase function. As noted by Bender & Orszag (1999), this asymptotic form can also be derived by a multiple-scales analysis. A slowly varying independent variable $T = f(t)$, is introduced where *a priori* $f(t)$ is unknown. After the chain rule has been used to transform the ODE an asymptotic expansion of the form

$$y = Y_0(T, \tau) + \varepsilon Y_1(T, \tau) + \cdots$$

is substituted into the ODE. It can be shown that $f(t) = (-\mathrm{i}/\varepsilon)S_0(t)$ (see Bender & Orszag, 1999, p.556 for this specific example) and the original WKBJ solution is recovered. The multiple-scales approach explicitly assumes the behaviour of the solution to depend on two different scales; a fast scale τ and a slow variable T which is a function depending on t. The type IIa,b,c,d,... solutions also appear to have different behaviours at different length scales and it seems sensible to follow the approach described above. However, the WKBJ method is only valid for linear equations and to proceed a multiple-scales approach using the method of Kuzmak shall be performed.

This can be considered as a nonlinear analogy to the WKBJ theory of linear ODE.

Proceeding in the spirit of the above approach, instead of introducing a boundary layer variable $y = \delta^{-1/2}\xi$ as before, for the type II solutions, the short variable, y, is now written in terms of $\phi(\xi)$; a slowly varying phase function operating at $O(\delta^{-1/2})$, and $\mu(\xi)$; a phase function operating at $O(1)$. Both of these functions are written in terms of the long variable, ξ and are *a priori* unknown. Explicitly,

$$y = \frac{\phi(\xi)}{\delta^{1/2}} + \mu(\xi). \tag{3.3.3}$$

For an important remark on the notation to be used please see [1]. A multiple-scales expansion is to be found in the form, $U(\xi, y)$ for the equation for large α, (or small $\delta = \alpha^{-1/2}$) given in (3.2.10), but repeated here for the reader's convenience

$$\delta U'' + U^2 = \mathrm{e}^{-\xi^2}. \tag{3.3.4}$$

From the chain rule

$$\begin{aligned} U' &= \frac{\partial U}{\partial \xi} + \left(\frac{\phi'}{\delta^{1/2}} + \mu'\right)\frac{\partial U}{\partial y} \\ U'' &= \frac{\partial^2 U}{\partial \xi^2} + 2\left(\frac{\phi'}{\delta^{1/2}} + \mu'\right)\frac{\partial^2 U}{\partial \xi \partial y} + \left(\frac{\phi''}{\delta^{1/2}} + \mu''\right)\frac{\partial U}{\partial y} + \left(\frac{\phi'}{\delta^{1/2}} + \mu'\right)^2 \frac{\partial^2 U}{\partial y^2}, \end{aligned}$$

These expressions are substituted into (3.3.4) to get

$$\delta\left(\frac{\partial^2 U}{\partial \xi^2} + 2\left(\frac{\phi'}{\delta^{1/2}} + \mu'\right)\frac{\partial^2 U}{\partial \xi \partial y} + \left(\frac{\phi''}{\delta^{1/2}} + \mu''\right)\frac{\partial U}{\partial y} + \left(\frac{\phi'}{\delta^{1/2}} + \mu'\right)^2 \frac{\partial^2 U}{\partial y^2}\right) + U^2 = \mathrm{e}^{-\xi^2},$$

which becomes

$$(\phi')^2\frac{\partial^2 U}{\partial y^2} + U^2 + \delta^{1/2}\left(2\phi'\frac{\partial^2 U}{\partial \xi \partial y} + \phi''\frac{\partial U}{\partial y} + 2\phi'\mu'\frac{\partial^2 U}{\partial y^2}\right) + \delta\left(\frac{\partial^2 U}{\partial \xi^2} + 2\mu'\frac{\partial^2 U}{\partial \xi \partial y} + \mu''\frac{\partial U}{\partial y} + (\mu')^2\frac{\partial^2 U}{\partial y^2}\right) = \mathrm{e}^{-\xi^2}. \tag{3.3.5}$$

A multiple-scales expansion of the form

$$U(\xi, y) = U_0(\xi, y) + \delta^{1/2}U_1(\xi, y) + \delta U_2(\xi, y) + \cdots$$

[1] All total derivatives with respect to ξ will be denoted with a prime. Partial derivatives will be written using curly ∂ notation but subscripts will be used when it improves the readability of the argument. It will be stated clearly when this occurs.

is substituted into (3.3.5). At leading order

$$(\phi')^2 \frac{\partial^2 U_0}{\partial y^2} + U_0^2 = \mathrm{e}^{-\xi^2}. \tag{3.3.6}$$

This equation can be solved for $U_0(y)$. Multiplying (3.3.6) by $\frac{\partial U_0}{\partial y}$ and an integration (with respect to y) yields

$$(\phi')^2 \left(\frac{\partial U_0}{\partial y}\right)^2 = 2\mathrm{e}^{-\xi^2} U_0 + A - \frac{2}{3} U_0^3, \tag{3.3.7}$$

where A is a function of integration to be determined. Separating the variables gives

$$\pm\phi' \int_{U^*}^{U_0} (c(\xi, A, t))^{-1/2} \, \mathrm{d}t = y, \tag{3.3.8}$$

$$c(\xi, A, t) = A + 2t\mathrm{e}^{-\xi^2} - \frac{2}{3} t^3, \tag{3.3.9}$$

where U^* is an arbitrary lower limit and t is a dummy variable. The solutions are set to be periodic in y with period 1 (the period of oscillations in the boundary layer variable y is free to be set as ϕ is unknown). For a real, bounded solution there has to be three real roots of the cubic polynomial, $c(\xi, A, U_0)$, say $U_- < U_m < U_+$ (see figure 3.3.1(a)). The cubic is positive for $U_m < U_0 < U_+$. Therefore the leading order solution, U_0 must oscillate between these two roots. U_0 is 1-periodic in y, so as U_0 varies from U_m to U_+ then y must vary by $1/2$. As U_0 traverses back to U_m then y must vary by another $1/2$. Therefore an expression for ϕ' can be established,

$$\phi' = \left(2 \int_{U_m}^{U_+} \left(2\mathrm{e}^{-\xi^2} t + A - \frac{2}{3} t^3\right)^{-1/2} \, \mathrm{d}t\right)^{-1}. \tag{3.3.10}$$

This is a first order equation for $\phi(\xi)$ and an initial condition is required. Therefore to solve (3.3.10), $\phi(0) = 0$ is chosen as a condition w.l.o.g and $\phi(\xi)$ can be determined fully. The solution, (3.3.9) can be re-written as two integrals; one going from $U_m \to U_+$ and the other $U_+ \to U_-$. Overall the period must be 1 and therefore

$$\Phi \int_{U_m}^{U_0} c(\xi, A, t)^{-1/2} \, \mathrm{d}t = y, \quad 0 < y < \frac{1}{2}, \tag{3.3.11}$$

$$\frac{1}{2} + \Phi \int_{U_0}^{U_+} c(\xi, A, t)^{-1/2} \, \mathrm{d}t = y, \quad \frac{1}{2} < y < 1, \tag{3.3.12}$$

where

$$c(\xi, A, t) = A + 2t\mathrm{e}^{-\xi^2} - \frac{2}{3} t^3, \tag{3.3.13}$$

$$\Phi(\xi, A, t) = \phi', \tag{3.3.14}$$

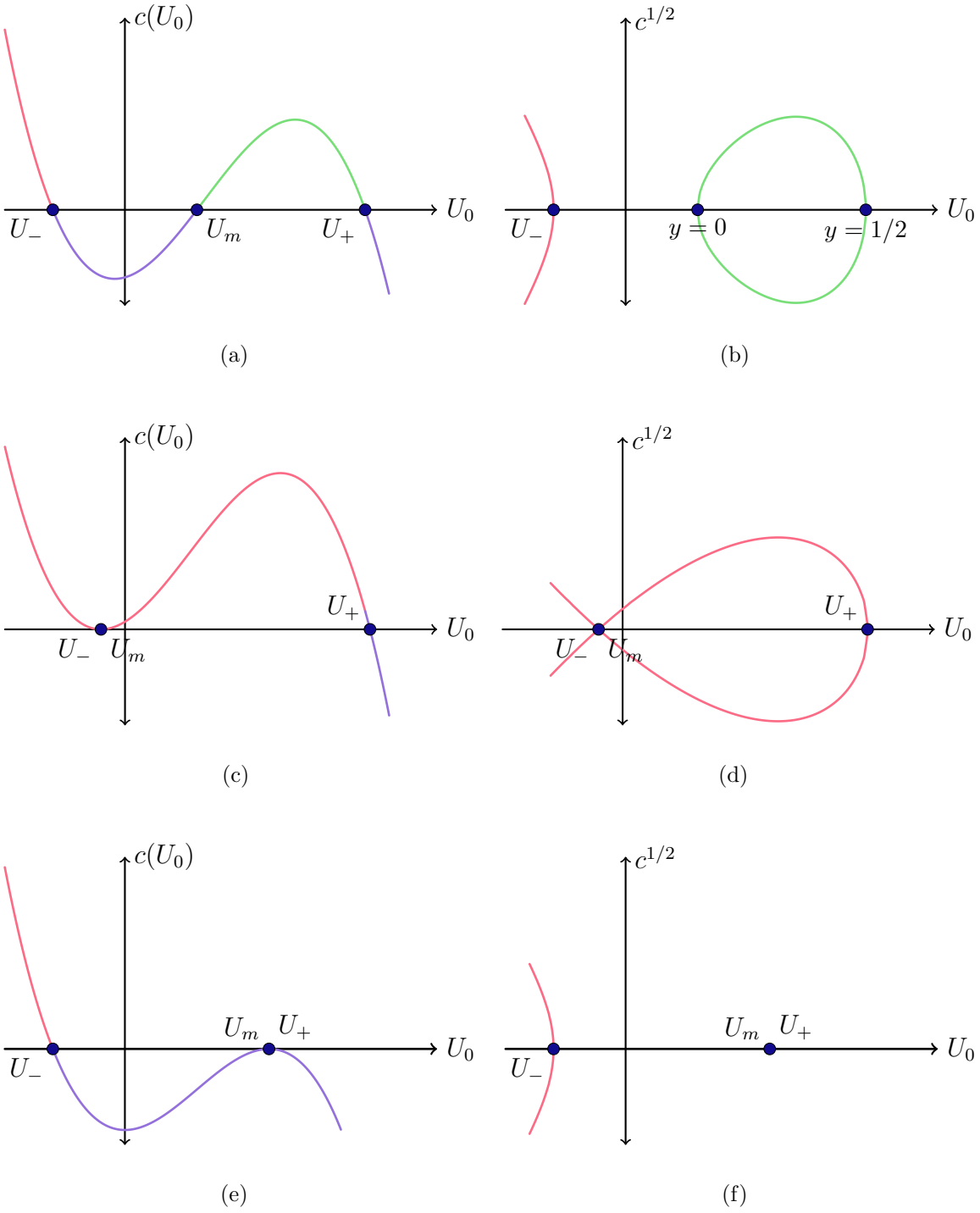

Figure 3.3.1: The panels on the left depict the polynomial $c(\xi, A, t)$ and it's three roots U_-, U_m and U_+. The panels on the right depict the corresponding phase plane for the left panel. (a) The solution U_0 oscillates between U_m and U_+ on the green part of the curve where $0 < k < k_{max}$. (b) The solution is unbounded as $U_m \to U_-$ with $k = 0$. (c) The solution is unbounded and imaginary as $U_m \to U_+$ with $k = k_{max}$.

and $U_0(\xi, Y) = U_0(y, \xi, \Phi(A, \xi), A)$. Note this functions now have a dependence on A as well. The leading order phase function ϕ and the polynomial c are also treated as functions of ξ and A. At this point it is useful to summarise that the leading order solution, U_0 has been obtained (see (3.3.12)) and the leading order phase function, ϕ has also been determined (see (3.3.10)). However the unknown functions A and $\mu(\xi)$ are still to be determined. To do this the equation at $O(\delta^{1/2})$ is required. Equating coefficients of $\delta^{1/2}$ in (3.1.6) yields

$$\Phi^2 \frac{\partial^2 U_1}{\partial y^2} + 2U_0 U_1 = -2\Phi \frac{\partial^2 U_0}{\partial \xi \partial y} - \Phi' \frac{\partial U_0}{\partial y} - 2\Phi\mu' \frac{\partial^2 U_0}{\partial y^2}. \tag{3.3.15}$$

At this point it is useful to notice that U_0 is even-periodic (about $y = \frac{1}{2}$). Therefore

$$\begin{aligned} U_0 &: \text{EVEN - PERIODIC} \\ \frac{\partial U_0}{\partial y} &: \text{ODD - PERIODIC} \\ \frac{\partial^2 U_0}{\partial y^2} &: \text{EVEN - PERIODIC.} \end{aligned} \tag{3.3.16}$$

Therefore (3.3.15) can be written as

$$L(U_1) = R_1 = R_1^O + R_1^E, \tag{3.3.17}$$

where the linear operator L and, odd operator R_1^O and even operator R_1^E are

$$\begin{aligned} L &= \Phi^2 \frac{\partial^2}{\partial y^2} + 2U_0, \\ R_1^O &= -2\Phi \frac{\partial^2 U_0}{\partial \xi \partial y} - \Phi' \frac{\partial U_0}{\partial y}, \\ R_1^E &= -2\Phi\mu' \frac{\partial^2 U_0}{\partial y^2}. \end{aligned} \tag{3.3.18}$$

The superscripts here correspond to even and odd. The homogeneous version of (3.3.17) has a solution

$$U_1^A = \frac{\partial U_0}{\partial y}, \tag{3.3.19}$$

found by differentiating (3.3.6) with respect to y and noting that ϕ doesn't depend on y. Another homogeneous solution can be found by a reduction of order procedure; in particular letting $U_1 = \frac{\partial U_0}{\partial y} v$ and substituting into the homogeneous form of (3.3.17), a further two integration's yields the second homogeneous solution as

$$\begin{aligned} U_1^B &= \frac{\partial U_0}{\partial y} v, \\ v &= \int_0^y \left(\frac{\partial U_0}{\partial y} \right)^{-2} \mathrm{d}s. \end{aligned} \tag{3.3.20}$$

As $\frac{\partial U_0}{\partial y}$ is odd the integrand above is even and can be written as a Fourier series in the form

$$\left(\frac{\partial U_0}{\partial y}\right)^{-2} = a_0 + \sum_{n=1}^{\infty} a_n \cos(2\pi n y),$$

where the a_n are functions of ξ, and hence two homogeneous solutions to (3.3.17) are

$$U_1^A = \frac{\partial U_0}{\partial y}, \tag{3.3.21a}$$

$$U_1^B = y\frac{\partial U_0}{\partial y} + K(\xi, y), \tag{3.3.21b}$$

where $K(\xi, y)$ is an odd-periodic function in y. There is only one periodic homogeneous solution; U_1^A. It is not clear that a particular integral will remain bounded as U_1^B grows like $y\frac{\partial U_0}{\partial y}$ as $y \to \infty$. The Fredholm alternative (see, for example Boyce *et al.*, 1969) states that either $L(f) = 0$ has a non-trivial solution OR $L(f) = R$ has a solution in the class of periodic functions. In the latter case this is guaranteed if U and R are orthogonal, where U satisfies $L(U) = 0$, i.e.

$$\langle U, R\rangle = \int_0^1 UR \,\mathrm{d}y = 0.$$

Therefore the right hand side of (3.3.17) is multiplied by U_1^A (the periodic homogeneous solution) and then integrated over the domain $y \in [0, 1]$. The orthogonality condition can be written as

$$\int_0^1 \left(2\Phi\frac{\partial^2 U_0}{\partial\xi\partial y} + \Phi'\frac{\partial U_0}{\partial y}\right)\frac{\partial U_0}{\partial y}\,\mathrm{d}y + \int_0^1 2\Phi\mu'\frac{\partial^2 U_0}{\partial y^2}\frac{\partial U_0}{\partial y}\,\mathrm{d}y = 0. \tag{3.3.22}$$

This solvability condition, (3.3.22) can be written as

$$\frac{\mathrm{d}}{\mathrm{d}\xi}\left[\phi'\int_0^1 \left(\frac{\partial U_0}{\partial y}\right)^2 \mathrm{d}y\right] + \phi'\mu'\left(\frac{\partial U_0}{\partial y}\right)^2\Bigg|_0^1 = 0 \tag{3.3.23}$$

The second term is zero due to periodicity and integrating once gives

$$\phi'\int_0^1 \left(\frac{\partial U_0}{\partial y}\right)^2 \mathrm{d}y = k \tag{3.3.24}$$

for constant k. The integral in (3.3.24), via a change of variables from y to u, and using (3.3.7), (3.3.24), can be written as

$$2\int_{U_m}^{U_+} c(\xi, A, t)^{1/2}\,\mathrm{d}t = k \tag{3.3.25}$$

for constant k, whose range of possible values is determined later. This equation is an implicit expression for A. By choosing a permissible value of k, the function $A(\xi)$ can

be determined. All that remains now is to determine the first order phase function $\mu(\xi)$. To do this the approach of Bourland & Haberman (1988) is adopted to obtain the full solution to the $O(\delta^{1/2})$ problem. First it is noted that by differentiating the homogeneous version of (3.3.6) with respect to A it becomes

$$L\left(\frac{\partial U_0}{\partial A}\right) = -2\Phi\frac{\partial \Phi}{\partial A}\frac{\partial^2 U_0}{\partial y^2} \tag{3.3.26}$$

Note that here and elsewhere a partial derivative with respect to A is performed with ξ held constant. Additionally it can be seen by direct substitution;

$$L\left(y\frac{\partial U_0}{\partial y}\right) = 2\Phi^2\frac{\partial^2 U_0}{\partial y^2} \tag{3.3.27}$$

and therefore by multiplying both sides of (3.3.26) by Φ and both sides of (3.3.27) by Φ_A gives the second homogeneous solution explicitly as

$$U_1^B = \frac{\partial \Phi}{\partial A}y\frac{\partial U_0}{\partial y} + \Phi\frac{\partial U_0}{\partial A} \tag{3.3.28}$$

The two homogeneous solutions to (3.3.17) have been found explicitly in terms of known functions; see (3.3.21a) and (3.3.28). The second term in (3.3.28) is periodic, as predicted by Floquet theory. The general solution will consist of linear combinations of these two functions and a particular integral, say U_P. A particular integral will contain terms generated from the even and odd parts of R so that $U_P = U_1^E + U_1^O$. For the even terms the following must be satisfied

$$L(U_1^E) = R_1^E = -2\Phi\mu'\frac{\partial^2 U_0}{\partial y^2}, \tag{3.3.29}$$

and this is easily shown using (3.3.27) to be

$$U_1^E = -\frac{\mu'}{\Phi}y\frac{\partial U_0}{\partial y}. \tag{3.3.30}$$

which grows like $y\frac{\partial U_0}{\partial y}$ as $y \to \infty$. The odd part of the integral obtained from

$$L(U_1^O) = R_1^O \tag{3.3.31}$$

will at worst potentially grow like $y\frac{\partial U_0}{\partial y}$ as $y \to \infty$, otherwise it would not be possible to make U_1 periodic which by choosing A such that (3.3.24) holds is guaranteed to be possible by the Fredholm alternative. Therefore a particular integral for (3.3.31) can be written as

$$U_1^O = \gamma y\frac{\partial U_0}{\partial y} + Q,$$

where Q is periodic in y and γ is arbitrary. The unbounded term takes the form of one

of the homogeneous solutions and hence can be absorbed in the multiplying constant of U_1^B. Therefore U_1^O is bounded and can be solved via a variation of parameters procedure and is given by

$$U_1^O = \frac{1}{\Phi} U_1^B \int_0^y R_1^O U_1^A \, \mathrm{d}s - \frac{1}{\Phi} U_1^A \int_0^y R_1^O U_1^B \, \mathrm{d}s. \tag{3.3.32}$$

It is useful to note here that U_1^O is odd itself as can be seen when replacing y by $-y$ in (3.3.32). The complete general solution to (3.3.17) is

$$U_1 = C_1(\xi) U_1^A + D_1(\xi) U_1^B + U_1^E + U_1^O, \tag{3.3.33}$$

where U_1^A is given in (3.3.21a), U_1^B in (3.3.28) and U_1^E and U_1^O given in (3.3.30) and (3.3.32) respectively and C_1 and D_1 are arbitrary functions of ξ. Examining the form of (3.3.28) and ensuring that U_1 remains bounded requires

$$D_1(\xi) = \frac{\mu'}{\Phi \Phi_A}, \tag{3.3.34}$$

where Φ_A is $\frac{\partial \Phi}{\partial A}$. Note that if $\Phi \Phi_A = 0$ the solution will be unbounded, thus contradicting the Fredholm alternative and hence $\Phi \Phi_A \neq 0$. Hence the general solution to the problem is

$$U_1 = C_1(\xi) \frac{\partial U_0}{\partial y} + \frac{\mu'}{\Phi_A} \frac{\partial U_0}{\partial A} + U_1^O. \tag{3.3.35}$$

The usual procedure would now be to establish the equation for U_2 at $O(\delta)$ in the form

$$L(U_2) = R_2^O + R_2^E. \tag{3.3.36}$$

A homogeneous solution of this equation will be $\frac{\partial U_0}{\partial y}$ and as this is periodic, a solvability condition can be obtained by multiplying the right hand side of (3.3.36) by $\frac{\partial U_0}{\partial y}$, integrating between 0 and 1, and insisting this integral vanishes. This is an equation that determines μ, the remaining unknown. However the different (but equivalent as shown by Whitham (1970) and Whitham (1974)) approach of Bourland & Haberman (1988) and King *et al.* (2003) is followed. Instead of examining the problem at each order the full, exact equation, (3.3.5), is multiplied by $\frac{\partial U}{\partial y}$ and then integrated between $y = 0$ and 1 to obtain an exact solvability condition at all orders. Proceeding this way and using the asymptotic expansion for U, (3.3.5) becomes

$$\begin{aligned} &\frac{\mathrm{d}}{\mathrm{d}\xi} \left[(\Phi + \delta^{1/2} \mu') \int_0^1 \left(\frac{\partial U_0}{\partial y} \right)^2 \mathrm{d}y \right] \\ &\qquad + \delta^{1/2} \left(\mu' \int_0^1 \left(\frac{\partial U_0}{\partial y} \right)^2 \mathrm{d}y + 2\Phi \int_0^1 \frac{\partial U_0}{\partial y} \frac{\partial U_1}{\partial y} \, \mathrm{d}y \right) + O(\delta) = 0. \end{aligned} \tag{3.3.37}$$

To leading order (3.3.37) becomes

$$\frac{\mathrm{d}}{\mathrm{d}\xi}\left[\Phi\int_0^1\left(\frac{\partial U_0}{\partial y}\right)^2\,\mathrm{d}y\right]=0, \tag{3.3.38}$$

which is equivalent to the equation that defines A, namely (3.3.24), obtained from the secularity condition at order $O(\delta^{1/2})$. At next order, (3.3.37) is

$$\frac{\mathrm{d}}{\mathrm{d}\xi}\left[2\Phi\int_0^1\frac{\partial U_0}{\partial y}\frac{\partial U_1}{\partial y}\,\mathrm{d}y+\mu'\int_0^1\left(\frac{\partial U_0}{\partial y}\right)^2\,\mathrm{d}y\right]=0. \tag{3.3.39}$$

By substituting (3.3.35) into (3.3.39) another condition is obtained for the remaining unknown μ. Amazingly, because of periodicity in y and the fact that a lot of the terms are perfect derivatives equation (3.3.39) becomes a second order ODE that determines the final unknown; μ:

$$\frac{\mathrm{d}}{\mathrm{d}\xi}\left[\frac{\mu'}{\Phi_A}\left[\frac{\mathrm{d}}{\mathrm{d}A}\left(\Phi\int_0^1\left(\frac{\partial U_0}{\partial y}\right)^2\,\mathrm{d}y\right)\right]\right]=0. \tag{3.3.40}$$

(note that $U_{0,y}$ denotes the partial derivative of U_0 with respect to y) which can be written using (3.3.24) as

$$\frac{\mathrm{d}}{\mathrm{d}\xi}\left[\frac{\mu' k_A}{\Phi_A}\right]=0 \tag{3.3.41}$$

This is a second order equation for $\mu(\xi)$ and therefore two conditions at $\xi=0$ (w.l.o.g) are required. As symmetric solutions are sought the conditions on u are that

$$U|_{\xi=0}=\beta,\qquad \left.\frac{\mathrm{d}U}{\mathrm{d}\xi}\right|_{\xi=0}=0. \tag{3.3.42}$$

The unknown β can be written as an asymptotic sequence in the form

$$\beta=\beta_0+\delta^{1/2}\beta_1+\delta^2\beta_2+\cdots$$

Therefore at leading order, the initial conditions become

$$U_0(0,y(0))=\beta_0,\qquad \Phi(0,A(0))\frac{\partial U_0}{\partial y}(0,y(0))=0. \tag{3.3.43}$$

Now as $\Phi(0,A(0))\neq 0$ then

$$\frac{\partial U_0}{\partial y}(0,y(0))=0. \tag{3.3.44}$$

The function $\frac{\partial U_0}{\partial y}$ is periodic in y which means that $\frac{\partial U_0}{\partial y}(0,y(0))=0$ only if $y(0)=0,1/2,1,...$etc. Also because $\phi(0)=0$ then $y(0)=\mu(0)$ and therefore

$$\mu(0)=0,\ 1/2,\ 1,\cdots \tag{3.3.45}$$

As the equation for μ, (3.3.41), is second order, another condition is required. At next order the boundary conditions in (3.3.42) are

$$U_1(0, y(0)) = \beta_1, \tag{3.3.46a}$$

$$\mu'(0)\frac{\partial U_0}{\partial y}(0, y(0)) + \Phi(0, A(0))\frac{\partial U_1}{\partial y}(0, y(0)) + \frac{\partial U_0}{\partial \xi}(0, y(0)) = 0. \tag{3.3.46b}$$

This is a system of linear equations for $\mu'(0)$ and $C_1(0)$. As $\frac{\partial U_0}{\partial y}(0, y(0)) = 0$, the condition in (3.3.46b) can be re-written as

$$\Phi(0)\frac{\partial U_1}{\partial y}(0, y(0)) = -\frac{\partial U_0}{\partial \xi}(0, y(0)). \tag{3.3.47}$$

The expression for $U_{1,y}$ in (3.3.35) is substituted into (3.3.47). After the cancellation of all terms involving odd functions in y evaluated at $y = \mu = 0, 1/2, ...$, (3.3.46) becomes

$$\frac{\mu'(0)}{\Phi_A(0, A(0))}\frac{\partial U_0}{\partial A}(0, y(0)) = \beta_1, \tag{3.3.48a}$$

$$C_1(0)\frac{\partial^2 U_0}{\partial y^2}(0, y(0)) + \frac{F\mu'(0)}{\Phi(0, A(0))\Phi_A(0, A(0))} = \frac{1}{\Phi}\frac{\partial U_0}{\partial \xi}, \tag{3.3.48b}$$

where

$$F = \Phi_A(0, A(0))\mu(0)\frac{\partial^2 U_0}{\partial y^2}(0, y(0)) + \Phi(0, A(0))\frac{\partial^2 U_0}{\partial y \partial A}(0, y(0)).$$

These equations are trivially solved to find

$$\mu'(0) = \frac{\Phi_A(0)\beta_1}{U_{0,A}(0, y(0))}, \tag{3.3.49a}$$

$$C_1(0) = \frac{1}{U_{0,yy}(0, y(0))\Phi(0)}\left(\frac{\partial U_0}{\partial \xi} - F\beta_1\right). \tag{3.3.49b}$$

Using the Leibnitz integration formula it can be shown that from the definition of k that $k_A = \frac{1}{2}\Phi^{-1}$ and hence (3.3.41) can be solved to obtain

$$\mu'(\xi) = 2B_1\Phi\Phi_A, \tag{3.3.50}$$

where B_1 is a constant of integration. Applying the condition (3.3.49a) means B_1 in (3.3.50) can be explictlly determined so that

$$\mu'(\xi) = \frac{\beta_1\Phi(\xi)\Phi_A(\xi)}{U_{0,A}(0, y(0))\Phi(0)}. \tag{3.3.51}$$

The determination of the constant β_1 will be discussed later. In summary therefore, three expressions have been derived for the three unknown functions; $\phi(\xi)$, $\mu(\xi)$ and A

(equations (3.3.10), (3.3.24) and (3.3.51) respectively):

$$\phi' = \left(2\int_{U_m}^{U_+} c(\xi, A, t)^{-1/2}\,\mathrm{d}t\right)^{-1}, \qquad \phi(0) = 0 \tag{3.3.52a}$$

$$k = 2\int_{U_m}^{U_+} c(\xi, A, t)^{1/2}\,\mathrm{d}t, \tag{3.3.52b}$$

$$\mu'(\xi) = \frac{\beta_1 \Phi(\xi)\Phi_A(\xi)}{U_{0,A}(0, y(0))\Phi(0)}, \qquad \mu(0) = 0,\ 1/2,\ 1, ..., \tag{3.3.52c}$$

where k is a constant. The first equation is an expression that determines ϕ, the second equation is an implicit solution for A whilst the last equation is an equation for μ.

It is also noted that (3.3.52b) is often referred to as the *principle of adiabatic invariance* (see Chapman & Farrell, 2017; Whitham, 1974) which states that the *action integral*;

$$k = 2\int_{U_m}^{U_+} c(\xi, A, t)^{1/2}\,\mathrm{d}t \tag{3.3.53}$$

is a conserved quantity. The analysis up to now is subtle and requiring lots of details. At this point it is also worth summarising the analysis to help the reader have an overview:

1. The $O(\delta^0)$ problem was solved for U_0.
2. At this order $\phi(\xi)$ can be determined with the conditions that U_0 is periodic in y and $\phi(0) = 0$.
3. The $O(\delta^{1/2})$ problem can be solved for U_1. One constant D_2 can be determined by ensuring boundedness of U_1 but the other constant C_1 is left undetermined.
4. A secularity condition can be obtained by multiplying the $O(\delta^{1/2})$ equation by the periodic-homogeneous solution of U_1 and an implicit equation for A can be obtained.
5. To find μ the full equation was multiplied by $\frac{\partial U}{\partial y}$ and by examining the $O(\delta)$ equation and imposing symmetry then μ could be determined.

The next analysis now looks in more detail at the specific forms of A, $\phi(\xi)$ and μ so approximations to the solutions found in the previous section can be constructed.

3.3.1 Explicit Forms

For the definition of ϕ the integral

$$I = \int_{U_m}^{U_+} c(t, \xi)^{-1/2}\,\mathrm{d}t \tag{3.3.54}$$

has to be evaluated. This can be written in closed form. To see this the integral in (3.3.54) can be written in the form

$$I = \left(\frac{3}{2}\right)^{1/2} \int_{U_m}^{U_+} [(t - U_-)(t - U_m)(U_+ - t)]^{-1/2} \, \mathrm{d}t, \tag{3.3.55}$$

where U_-, U_m, U_+ are the roots of c as discussed earlier. Now let $U_- = U_+\hat{U}_-$,$U_m = U_+\hat{U}_m$ and $t = U_+\hat{t}$. The integral above becomes

$$I = \left(\frac{3}{2U_+}\right)^{1/2} \int_{\hat{U}_m}^{1} \left[(\hat{t} - \hat{U}_-)(\hat{t} - \hat{U}_m)(1 - \hat{t})\right]^{-1/2} \, \mathrm{d}\hat{t}. \tag{3.3.56}$$

Now write $\hat{t} = 1 - (1 - \hat{U}_m)\sin^2 M$. This substitution transforms (3.3.56) to

$$I = \left(\frac{6}{U_+}\right)^{1/2} \int_0^{\pi/2} (1 - \hat{U}_-)^{-1/2} \left(1 - \frac{1 - \hat{U}_m}{1 - \hat{U}_-} \sin^2 M\right)^{-1/2} \mathrm{d}M. \tag{3.3.57}$$

By transforming back to the original variables it can be shown that the exact form for I is

$$I = \left(\frac{6}{2U_+ + U_m}\right)^{1/2} K(\Omega); \qquad \Omega = \left(\frac{U_+ - U_m}{2U_+ + U_m}\right)^{1/2} \tag{3.3.58}$$

where $K(\Omega)$ is the complete elliptic integral of the first kind defined by

$$K(\Omega) = \int_0^{\pi/2} (1 - \Omega^2 \sin^2 M)^{-1/2} \, \mathrm{d}M. \tag{3.3.59}$$

Therefore using the definition for ϕ' in (3.3.52a) the function $\phi' = \Phi$ can be written as

$$\Phi = \left(\frac{2U_+ + U_m}{6}\right)^{1/2} \frac{1}{2K(\Omega)}. \tag{3.3.60}$$

By performing the exact same transformations in a similar way the function k as given by (3.3.52b) can be written as

$$k = \frac{2^{5/2}}{3^{1/2}} (2U_+ + U_m)^{1/2} (U_+ - U_m)^2 P(\xi), \tag{3.3.61}$$

where $P(\xi)$ can be written in terms of the complete elliptic integral of the first and second kinds, $K(k)$ and $E(k)$ respectively, as

$$P(\xi) = \int_0^{\pi/2} (1 - \Omega \sin^2 M)^{1/2} \cos^2 M \sin^2 M \, \mathrm{d}M. \tag{3.3.62}$$

$$= \frac{\sqrt{1 - \Omega^2}}{15\Omega^4} \left[(\Omega^2 - 2)K\left(\frac{\Omega^2}{\Omega^2 - 1}\right) + 2(\Omega^4 - \Omega^2 + 1)E\left(\frac{\Omega^2}{\Omega^2 - 1}\right)\right]. \tag{3.3.63}$$

The exact forms of Φ and k have been found. A key observation is that when two of the roots of the polynomial c coalesce the expressions in (3.3.60) and (3.3.61) will have to be treated with care. In the next section the exact expressions for Φ and k are analysed in the extreme cases of when the upper two roots coalesce and when the lower two roots coalesce. As will be seen, the former case gives rise to *turning points* and these shall be explained in detail in the next section.

3.3.2 Coalescing Roots

In analogy with the WKBJ method the boundary layer approximation will cease to be valid when $\phi' = 0$ (when this happens the second derivative in (3.3.6) disappears). The Kuzmak approximation will therefore cease to be valid when $\phi'(\xi) = \Phi(\xi) = 0$. Looking at the form of ϕ', in (3.3.60) this will occur when I becomes infinite. This means when the complete elliptic integral of the first kind becomes infinite. If there are three distinct roots of $c(t)$ then the integral will be finite and hence the two cases when the roots coalesce are considered; i.e. when $U_m \to U_1$ and $U_m \to U_+$. In both of these cases U_m is a double root of $c(t)$ and $c'(t)$ where in this case the prime means differentiation with respect to t . Hence the double roots satisfy

$$c = A + 2\mathrm{e}^{-\xi^2} t - \frac{2}{3}t^3 = 0, \tag{3.3.64a}$$

$$\frac{\mathrm{d}c}{\mathrm{d}t} = 2\mathrm{e}^{-\xi^2} - 2t^2 = 0. \tag{3.3.64b}$$

From (3.3.64b), the double roots occur at

$$t = \pm \mathrm{e}^{-\xi^2/2} \tag{3.3.65}$$

and substituting back into (3.3.64a)

$$A_0(\xi) = -\frac{4}{3}\mathrm{e}^{-3\xi^2/2}, \qquad A_\infty(\xi) = \frac{4}{3}\mathrm{e}^{-3\xi^2/2}. \tag{3.3.66}$$

gives expressions for A in the cases of coalescing roots. These curves are shown in green and blue respectively in figure 3.3.2. Also shown in the figures are curves A_k for different k (in red). It is clear from the figure that the red curves A_k intersect the blue curve, at some value which will depend on k and which is denoted by $\xi_1(k)$, and a formula in terms of k will be provided below. In analogy with the WKBJ method the value of $\xi = \xi_1$ that this occurs will called a *turning point* and is the location where the Kuzmak approximation ceases to be valid. When $A(\xi_1) = A_\infty(\xi_1)$ the roots are $U_- = U_m = -\mathrm{e}^{-\xi_1^2/2}$ and $U_+ = 2\mathrm{e}^{-\xi_1^2/2}$, i.e. the lower roots have coalesced. It will be demonstrated that when this occurs $\phi' = 0$ and hence the analogy with the WKBJ method is established. When the two lower roots have coalesced, $U_m = -\mathrm{e}^{-\xi^2/2}$ and

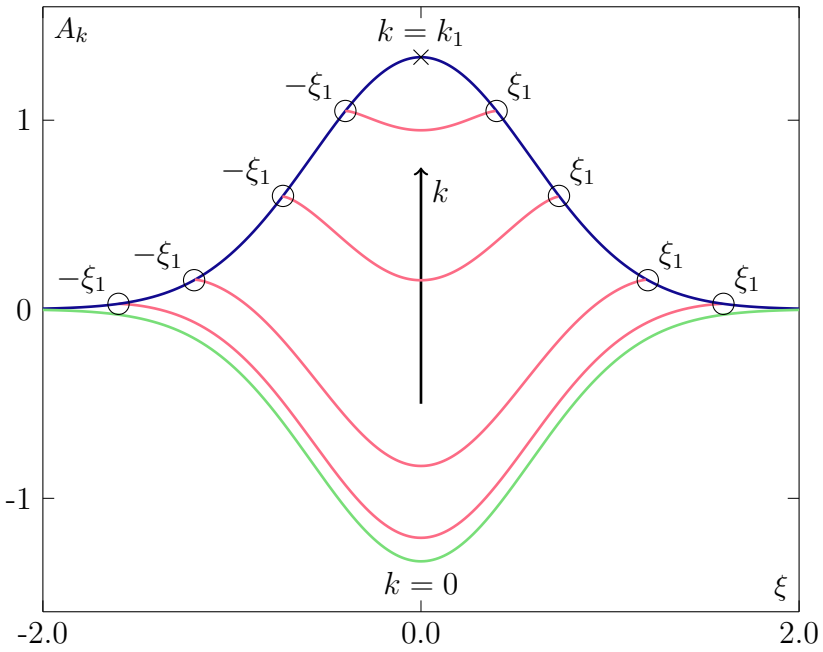

Figure 3.3.2: (a): The red curves are for $\xi_1 = 1.6, 1.2, 0.73, 0.4$ going from bottom to top. The green curve is $A_0(\xi)$ and the blue curve is $A_\infty(\xi)$.

$U_+ = 2\mathrm{e}^{-\xi^2/2}$ and therefore $\Omega = 1$. This means that

$$I = \lim_{\Omega \to 1} 2^{1/2} \mathrm{e}^{\xi_1^2/4} K(\Omega). \tag{3.3.67}$$

As $\Omega \to 1$, the leading order behaviour of I can be determined using the standard results of complete elliptic integrals as

$$I \sim -2^{-1/2} \mathrm{e}^{\xi_1^2/4} \log(1 - \Omega), \tag{3.3.68}$$

and therefore $I \to \infty$ and $\phi' \to 0$ with behaviour

$$\Phi \sim -\frac{2^{1/2} \mathrm{e}^{-\xi_1^2/4}}{\log(1 - \Omega)}. \tag{3.3.69}$$

as $\Omega \to 1$. This behaviour can be written in terms of ξ_1. The roots will in general be a function of ξ and A. At a turning point the roots are solely a function of ξ. By expanding U_m and U_+ as a Taylor series about $\xi = \xi_1$ means that as $\xi \to \xi_1$

$$1 - \Omega \sim a(\xi - \xi_1), \tag{3.3.70}$$

where a is a constant. The behaviour of Φ in (3.3.69) as a turning point is approached can be written as

$$\Phi \sim \frac{a^*}{\log|\xi - \xi_1|}, \tag{3.3.71}$$

where a^* is a constant. Using integration by parts the behaviour of ϕ near the turning points can also be established as

$$\phi \sim \Lambda + \frac{a^*|\xi - \xi_1|}{\log|\xi - \xi_1|}, \tag{3.3.72}$$

where Λ is a constant determined by the condition $\phi(0) = 0$. Note that $\phi \sim \Lambda$ as the turning point is approached. Also note that as $\xi_1 \to 0$ then $\Lambda \to 0$ to satisfy $\phi(0) = 0$. This means that as the Kuzmak region narrows the function ϕ will approach a straight horizontal line, i.e $\phi \sim 0$.

It is possible to get a formula connecting the turning point ξ_1 and k. As $\Omega \to 1$, the exact value of k can be found using (3.3.61). When $\Omega = 1$ the integral in (3.3.63) can be trivially solved and is $2/15$. As the values of U_m and U_+ at the turning points are known the formula in (3.3.61) (at a turning point) reduces to

$$k = \frac{24\sqrt{2}}{5}\mathrm{e}^{-5\xi_1^2/4} \tag{3.3.73}$$

Note that from (3.3.73) there is a one to one correspondence between k, and ξ_1; the location where $\phi' = 0$. Therefore for $\xi_1 > 0$, k is a monotonically decreasing function of ξ_1 and therefore a maximum value of k is

$$k = k_1 = \frac{24\sqrt{2}}{5} \approx 6.78823. \tag{3.3.74}$$

Note the same value was obtained numerically in Chapman & Farrell (2017). When the two upper roots have coalesced, $U_m = U_+ = \mathrm{e}^{-\xi^2/2}$. From (3.3.52b), as $U_m \to U_+$, then $k \to 0$ (as the range of integration becomes zero). A lower permissible bound for k is therefore $k = 0$ and the permissible values of k for $A_k(\xi)$ are;

$$0 < k < k_1, \tag{3.3.75}$$

where k_1 was stated earlier. Additionally as the two upper roots coalesce $\Omega = 0$. This means that using the definition of $K(\Omega)$

$$I = 2^{1/2}\mathrm{e}^{\xi^2/4}K(0) = 2^{-1/2}\mathrm{e}^{\xi^2/4}\pi, \tag{3.3.76}$$

which is finite and hence a turning point does not exist when the two upper roots coalesce. The value of Φ is given by

$$\Phi(\xi) = 2^{-1/2}\mathrm{e}^{-\xi^2/4}\pi^{-1}, \tag{3.3.77}$$

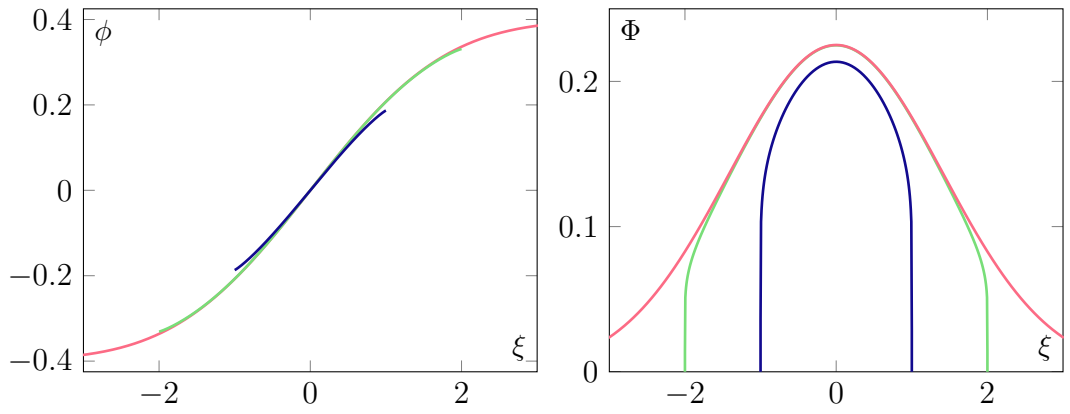

Figure 3.3.3: (a) $\phi(\xi)$ and (b) $\Phi(\xi)$ for different ξ_1. The red curves are $\phi = (2\pi)^{-1}\mathrm{erf}(\xi/2)$ and $\Phi = 2^{-1/2}\pi^{-1}\mathrm{e}^{-\xi^2/4}$ which correspond to $\xi_1 \to \infty$. The green curves are numerical calculations for ϕ and Φ when $\xi_1 = 2$ and similarly the blue curves correspond to $\xi_1 = 1$

and hence

$$\phi(\xi) = 2^{-1/2}\pi^{-1}\int_0^{\xi} \mathrm{e}^{-t^2/4}\,\mathrm{d}t \tag{3.3.78}$$

$$= \frac{1}{\sqrt{2\pi}}\mathrm{erf}(\xi/2). \tag{3.3.79}$$

It is clear from figure 3.3.2 that as $k \to 0$ then $\xi_1 \to \infty$. Using the rules of Gaussian integrals yields

$$\lim_{k\to 0}\phi(\xi_1) = \frac{1}{\sqrt{2\pi}} \approx 0.399, \tag{3.3.80}$$

which will be referred to later when discussing the solution space. The behaviour of the function ϕ has been established in the limit as $\xi_1 \to 0$ and $\xi_1 \to \infty$. In figure 3.3.3 the function (3.3.79) is plotted along with ϕ when $\xi_1 = 1, 2$. Note that this figure demonstrates that as $\xi_1 \to 0$ then ϕ approaches a straight line with an ever vanishing slope.

In summary the functions A_k have been established to be bounded by A_0 and A_∞ (see figure 3.3.2 for numerically computed A_k. For a given k, the leading order solution, U_0 is valid up to the point $\xi = \xi_1$, where $A_k(\xi_1) = A_\infty(\xi_1)$. At this point the Kuzmak approximation ceases to be valid. The values of k and ξ_1 can be calculated using (3.3.73) and permissible values of k are given by (3.3.75). The form of ϕ has been determined near the turning points and exact forms of ϕ can be found in the limits as $\xi_1 \to 0$ and $\xi_1 \to \infty$ (or equivalently, $k \to 24\sqrt{2}/5$ and $k \to 0$ respectively).

3.3.3 A note on the graphical representation

In the preceding analysis *exact* forms of Φ and k were obtained in terms of complete elliptic integrals. Although these are exact, they depend on the roots of the cubic $c(t)$. There is a general formula for a cubic equation and therefore these roots could be written down explictlly in terms of A and ξ. However the expressions in (3.3.60) and (3.3.63) quickly become laborious to write down and hence to show these functions a numerical method was used instead.

To calculate $A_k(\xi)$, the long variable ξ was discretised between $[-\xi_1, \xi_1]$, where ξ_1, the turning point, is a set constant. Using (3.3.73), this meant that k is set constant also. The function A was found by solving (3.3.52b) using Newton's method. The roots of the polynomial were evaluated as functions of ξ using a CAS (in particular MATLAB's symbolic maths toolkit). Once this function was found, Φ was found by evaluating the integral in (3.3.52a) using a sinh-tanh quadrature rule to deal with the square-root singularities at the end-points of the integration (see appendix A for details). Another numerical integration of (3.3.52a) gave a numerical description of ϕ. This procedure was numerically continued as k was varied from ≈ 0.04 to k_1 (note that it was numerically difficult to proceed further than a turning point at $\xi \approx \pm 2$). A selection of different $A_k(\xi)$ are shown in red in figure 3.3.2 for different k.

3.3.4 Solution construction

The construction of solutions from this formulation is discussed. The (leading order) Kuzmak solution can be written down explicitly. Starting from (3.3.7) the equation can be written down as

$$(\phi')^2 \left(\frac{\partial U_0}{\partial y}\right)^2 = \frac{2}{3}(U_0 - U_-)(U_0 - U_m)(U_+ - U_0). \tag{3.3.81}$$

By making the substitutions; $U_0 = U_+\hat{U}_0$, $U_- = U_+\hat{U}_-$ and $U_m = U_+\hat{U}_m$ (3.3.81) becomes

$$(\phi')^2 \left(\frac{\partial \hat{U}_0}{\partial y}\right)^2 = \frac{2}{3}U_+(\hat{U}_0 - \hat{U}_-)(\hat{U}_0 - \hat{U}_m)(1 - \hat{U}_0). \tag{3.3.82}$$

Next a substitution, $\hat{U} = 1 + (\hat{U}_m - 1)\sin^2 M$, transforms (3.3.82) to

$$(\phi')^2 \left(\frac{\partial M}{\partial y}\right)^2 = l(1 - \Omega^2 \sin^2 M), \tag{3.3.83}$$

where

$$l = \frac{1}{6}(2U_+ + U_m), \tag{3.3.84}$$

$$\Omega^2 = \frac{2U_+ + U_m}{U_+ - U_-}. \tag{3.3.85}$$

This can be written as a Jacobi Elliptical Integral;

$$\frac{\sqrt{l}}{\phi'}(y-1/2) = \int_0^M \frac{1}{(1-\Omega^2\sin^2 s)^{1/2}}\,\mathrm{d}s. \tag{3.3.86}$$

The phase shift of $1/2$ modulo 1 is required so that the periodic function U_0 has a minimum when $y = 0$ and a maximum when $y = 1/2$ (all modulo 1), as per the formulation in the previous section. Transforming back to the original pre-transformed variables and taking advantage of the Jacobi Elliptical function identities, a closed form expression can be established for U_0:

$$U_0(\xi, y) = U_m(\xi) + (U_+(\xi) - U_m(\xi))\,\mathrm{cn}^2\left(\frac{\sqrt{l(\xi)}}{\phi'(\xi)}(y-1/2), \Omega^2\right). \tag{3.3.87}$$

where cn denotes the *cnoidal* Jacobi Elliptical function which obeys the identity

$$\mathrm{cn}^2\left(\frac{\sqrt{l(\xi)}}{\phi'(\xi)}(y-1/2), \Omega^2\right) = 1 - \mathrm{sn}^2\left(\frac{\sqrt{l(\xi)}}{\phi'(\xi)}(y-1/2), \Omega^2\right) = 1 - \sin^2 M. \tag{3.3.88}$$

These are plotted as a function of y in the range $y \in [0, 1]$ (for different ξ) in figure 3.3.4(b) for when $k = 0.04$. In the previous section the boundary layer analysis revealed a boundary layer around $\xi = 0$ where the leading order expression for the II solution can be stated using (3.2.17) as

$$U_{0,BL} = -1 + 3\,\mathrm{sech}^2(y/\sqrt{2}). \tag{3.3.89}$$

The expression in (3.2.17) matches with the boundary layer solution in the limit as $\xi_1 \to 0$. In this limit the constant Λ in (3.3.72) is set to zero due to the condition $\phi(0) = 0$.

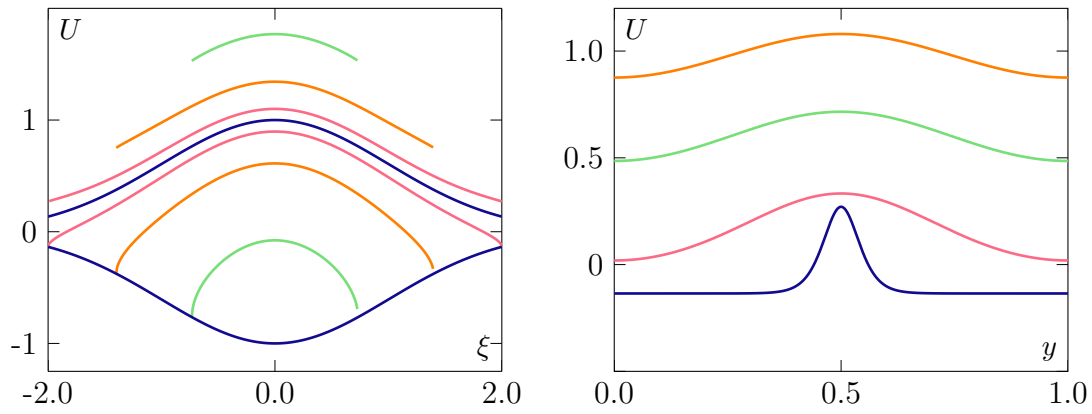

(a) (b)

Figure 3.3.4: (a) The blue curves are the roots of $c(u) = \pm e^{-\xi^2/2}$ for when there is a repeated root. The bottom and top red curves are the roots U_m and U_+ for $\xi_1 = 2$ respectively. The orange curves are for $\xi_1 = 1.4$ and the green curves are for $\xi = 0.8$. (b) The function $U(y)$ when for $\xi = 2$ (blue), $\xi = 1.8$ (red), $\xi = 1.0$ (green) and $\xi = 0.2$ (orange) for $k = 0.046$.

Therefore in this limit

$$\phi \sim \frac{a^*|\xi - \xi_1|}{\log|\xi - \xi_1|}. \tag{3.3.90}$$

In this situation the Kuzmak region matches to the region I of the previous analysis. To explicitly see the match between (3.3.87) and (3.3.89) it is noted that as $\xi \to \xi_1$ (3.3.87) becomes

$$U_0(\xi, y) \sim -e^{-\xi_1^2/2} + 3e^{-\xi_1^2/2}\,\mathrm{cn}^2\left(\frac{e^{-\xi_1^2/4}}{\sqrt{2}}\log|\xi - \xi_1|\left(\frac{|\xi - \xi_1|}{\delta^{1/2}\log|\xi - \xi_1|} - \frac{1}{2} + \mu(0)\right), 1\right). \tag{3.3.91}$$

The Jacobi Elliptic function cn $\to$ sech as the modulus $\Omega \to 1$. Note that as $\xi_1 \to 0$ then as $\xi < \xi_1$, $\xi \to 0$ also. The boundary layer solution has a maximum at $\xi = 0$ and hence the next section shall reveal that $\mu = 1/2$, modulo 1. Additionally as $\delta \to 0$, $\xi_1 \to 0$ (this will become apparant later) and this expression becomes

$$U_0(\xi, y) \sim -1 + 3\,\mathrm{sech}^2\left(\frac{1}{\sqrt{2}}\frac{|\xi - \xi_1|}{\delta^{1/2}}\right). \tag{3.3.92}$$

The variable y^* is defined by $\xi = \xi_1 + \delta^{1/2}y^*$. Therefore the Kuzmak solution can be written as

$$U_0(y^*) \sim -1 + 3\,\mathrm{sech}^2\left(y^*/\sqrt{2}\right). \tag{3.3.93}$$

Note that this expression is exactly the same as the leading order solution in (3.3.89) in the limit as $\xi_1 \to 0$ and the type II solutions of the previous section can be recovered.

3.3.5 Determining μ

The expression for μ' from (3.3.51) is given by

$$\mu'(\xi) = \frac{\beta_1 \Phi(\xi)\Phi_A(\xi)}{U_{0,A}(0, y(0))\Phi(0)}. \tag{3.3.94}$$

The constant β_1 can be determined by ensuring that the Kuzmak solution U_0 matches with the 'outer' solution at the turning points $\xi = \xi_1$. The expression on the right hand side of (3.3.51) is well-behaved for all $|\xi| < \xi_1$ and diverges at the turning points, $|\xi| = \xi_1$. This reason for the divergence at the turning points is that a term of the form $K'(\Omega)$ will be feature in the exact expression for Φ_A. As a turning point is approached $K'(1) \to \infty$ algebraically and hence $\mu' \to \infty$ also. A full analysis of the behaviour of μ' near the turning points will require a detailed boundary layer analysis near $\xi = \xi_1$ to obtain connection formulae. However the numerical evidence suggests that away from the turning points Φ is small, see figure 3.3.3(b). For a fixed k, the maximum value of Φ will occur at $\xi = 0$ as seen in figure 3.3.3(b). The maximum value of $\Phi(0)$ as k varies occurs when $k \to 0$, or equivalently when $\xi_1 \to \infty$. From (3.3.79) this maximum is

$$\Phi_{max}(0) = 2^{-1/2}\pi^{-1}. \tag{3.3.95}$$

The value of $A(0)$ in this limit is $A(0) = -4/3$. As $\xi_1 \to 0$, $\Phi(0) \to 0$ and $A(0) = 4/3$. Therefore the average value of Φ_A at $\xi = 0$ as k varies is

$$\bar{\Phi}_A = \frac{3}{2^{3/2}\pi} \approx 0.2251,$$

which is small. Hence the product of $\Phi\Phi_A$ as a rough approximation is expected to be small away from the turning points. Applying this rough approximation to the definition of μ' in (3.3.94) gives

$$\mu' \approx 0. \tag{3.3.96}$$

Note that same approximation was applied by Billingham (2006) when applying the Kuzmak method to a problem. The conditions in (3.3.45) can be imposed so that (3.3.94) can be solved to find $\mu(\xi)$ and hence

$$\mu \approx 0, 1/2, 1, ... \tag{3.3.97}$$

Note that strictly speaking this approximation only applies away from the turning points.

3.3.6 Matching

For $\xi > |\xi_1|$ the asymptotic description of the previous section will apply. Recall that in region II the solution takes the form (from (3.2.12))

$$U = -\mathrm{e}^{-\xi^2/2} + \frac{1}{2}\delta(1-\xi^2) + \cdots \tag{3.3.98}$$

For this solution to match to the solution in the Kuzmak region, $|\xi| < \xi_1$, continuity has to be established in U and U' at the turning point. At a turning point there a pair of repeated roots at $U_m = -\mathrm{e}^{-\xi_1^2/2}$ and a root at $U_+ = 2\mathrm{e}^{-\xi_1^2/2}$. To match with (3.3.98), $U_0 = U_m$. Therefore because U_0 is at the lower root of c then at the turning point

$$y(\pm\xi_1) \equiv 0 \qquad \text{modulo } 1. \tag{3.3.99}$$

It should be noted that to match the Kuzmak solution to the region II solution at later orders will require knowledge of the unknown constant $C_1(\xi)$ and a detailed boundary layer analysis near to $\xi = \xi_1$. These details are beyond the scope of this analysis and are not pursued here. As y has to take integer values at turning point this means

$$\begin{aligned} y(\xi_1) &= \frac{\phi(\xi_1)}{\delta^{1/2}} + \mu = l, \\ y(-\xi_1) &= \frac{\phi(-\xi_1)}{\delta^{1/2}} + \mu = m, \end{aligned} \tag{3.3.100}$$

for integers l, m. Subtracting these equations (and using the fact that ϕ is odd in ξ) gives

$$\frac{2\phi(\xi_1)}{\delta^{1/2}} = l - m \tag{3.3.101}$$

For solutions with a minimum at $\xi = 0$ there will be a even number of periods in y in the Kuzmak region. Solutions with a maximum at $\xi = 0$ will have an odd number of periods hence either

$$(i) \quad \frac{\phi(\xi_1)}{\delta^{1/2}} = n - 1/2, \tag{3.3.102}$$

for solutions with a maximum at $\xi = 0$, or

$$(ii) \quad \frac{\phi(\xi_1)}{\delta^{1/2}} = n, \tag{3.3.103}$$

for solutions with a minimum at $\xi = 0$. Adding the two equations in (3.3.100) gives a value of y at exactly in between l and m:

$$2\mu = (l + m). \tag{3.3.104}$$

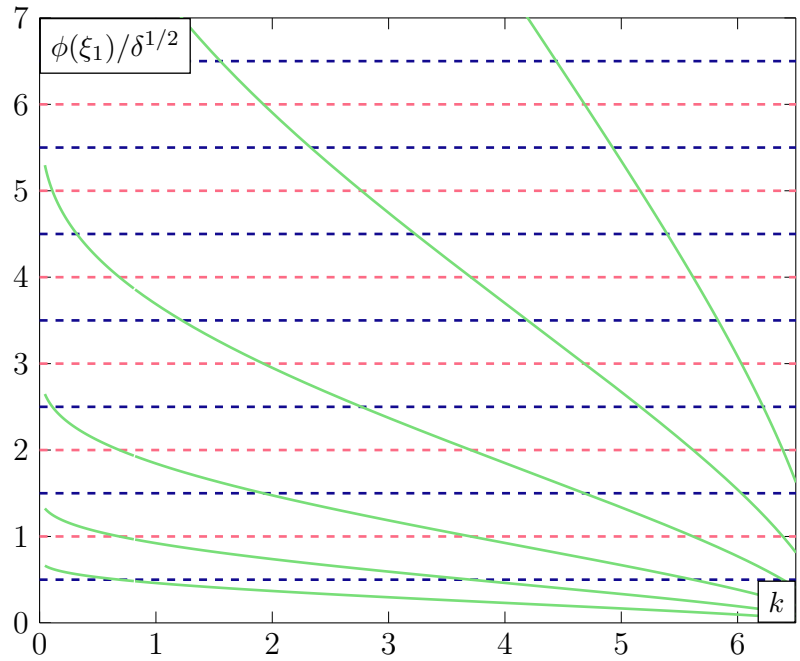

Figure 3.3.5: The green curves are $\phi(\xi_1)/\delta^{1/2}$ for $\delta_i^{1/2} = 2^{-i}$ from $i = 1$ (bottom curve) to $i = 6$ (top curve). Where the green curves and the blue and black lines intersect represent solutions to the problem. Note that only a small example of curves are shown for a discrete set of δ which is a continuous quantity.

For case (i), equation (3.3.104) must yield $\mu = 1/2$ (modulo 1) and for case (ii), it must yield $\mu = 0$ (modulo 1). Therefore as k varies, solutions exist when

$$\frac{\phi(\xi_1)}{\delta^{1/2}} = n, \quad \text{or} \quad n - 1/2 \tag{3.3.105}$$

where n is an integer. The green curves in figure 3.3.5 are $\phi(\xi_1)/\delta^{1/2}$ for different δ. The dotted blue and red lines correspond to the integers and half-integers. At the points of intersection (of the green curves and red/blue lines) a solution can be constructed. As the green curve intersects a particular horizontal line; n^* say, the Kuzmak region ($\xi < |\xi_1|$) will contain $2n^*$ modulated oscillations in y. Additionally, the solution, U_0, will be bounded between the two roots, $U_m(\xi)$ and $U_+(\xi)$, of $c(\xi, A_k(\xi), u)$. The comparison with the numerical solutions are shown in figure 3.3.6 and as expected the agreement is good as δ decreases (note these have been scaled by $\alpha^{1/2}$ so they can be compared to the u solution). Next the approximate locations of the limit points in the $(\alpha, u(0))$ solution space are discussed. Before discussing the solution space the procedure for constructing solutions is now summarised for clarity:

1. Choose a value of $k \in [0, k_1]$. Note this automatically determines ξ_1 uniquely from (3.3.73).

2. Calculate $A(\xi)$ using (3.3.52b).

3. The roots $U_m(\xi, A)$ and $U_+(\xi, A)$ can be determined by solving $c(\xi, A) = 0$.

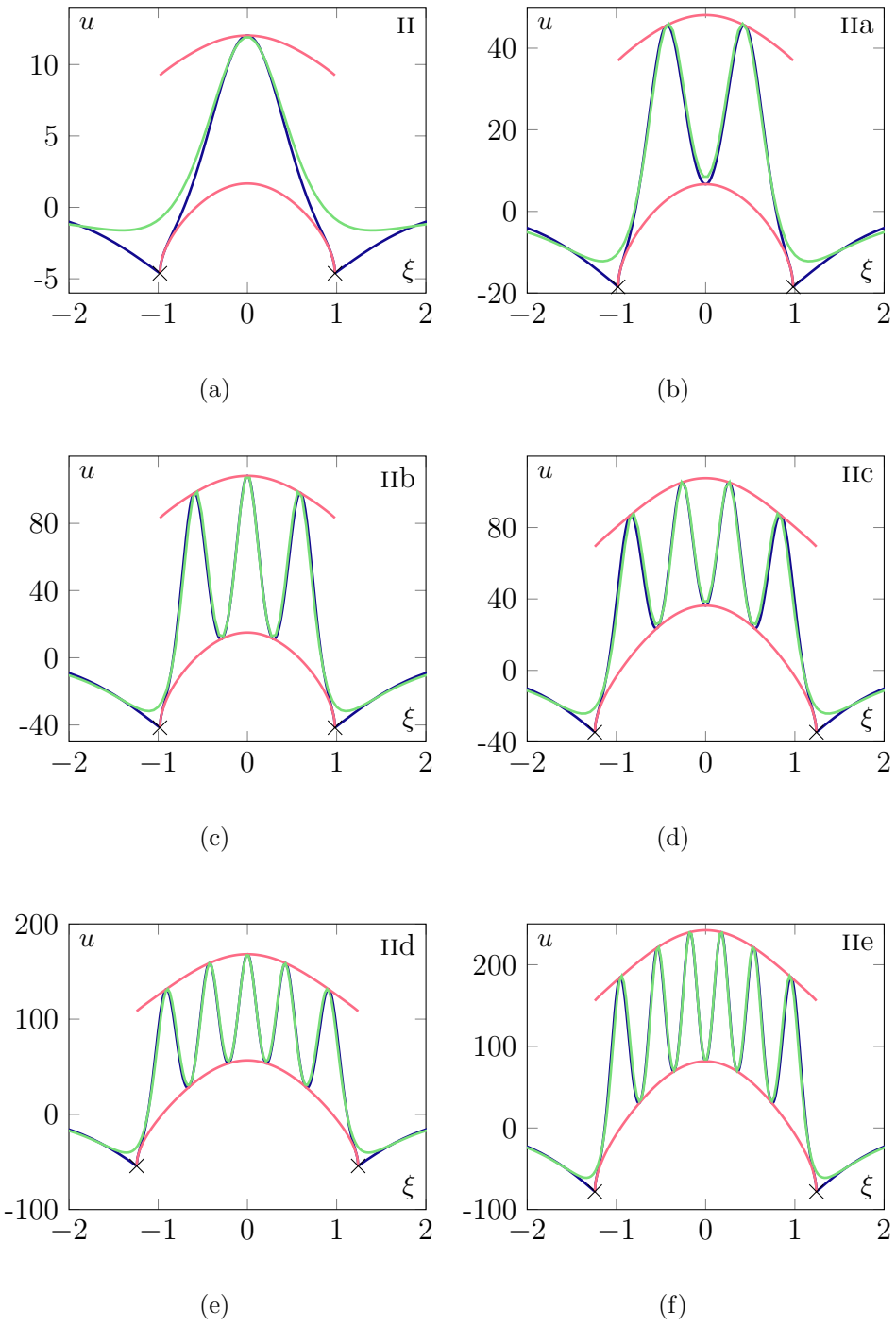

Figure 3.3.6: The comparison between the leading order Kuzmak approximation $\alpha^{1/2}U_0$ and the numerical solution u over a section of the domain close to the origin. The Kuzmak approximation, $\alpha^{1/2}U_0$, is only valid up to the turning point $\xi = \xi_1$ given in the captions and shown as a cross in the diagrams. The blue curve denotes the Kuzmak approximation given by (3.3.87). The green curve is the numerical solution. The two curves are virtually indistinguishable. The upper and lower red curves are the two roots; U_+ and U_- respectively. All values are quoted to 4 significant figures. (a) Type II solution, $\alpha = 55.84$, $\xi_1 = 0.98$. (b) Type IIa solution, $\alpha = 893.0$, $\xi_1 = 0.98$. (c) Type IIb solution, $\alpha = 4523$, $\xi_1 = 0.98$. (d) Type IIc solution, $\alpha = 5605$, $\xi_1 = 1.24$. (e) Type IId solution, $\alpha = 13680$, $\xi_1 = 1.24$. (f) Type IIe solution, $\alpha = 28370$, $\xi_1 = 1.24$.

4. The functions Φ and ϕ can now be determined.

5. To construct a particular solution choose the number of periods $2n^*$ in the Kuzmak region.

6. The value of δ can be calculated by $\phi(\xi_1)/\delta^{1/2} = n^*$.

7. Continuity with solution at $|\xi| = \xi_1$ is guaranteed.

8. In the Kuzmak region the leading order solution will be determined by $u = \alpha^{1/2} U_0(\xi, y)$ where $\alpha = \delta^{-1/2}$ and $U_0(\xi, y)$ is the leading order Kuzmak solution determined in (3.3.87).

3.3.7 Solution space

From figure 3.3.5 it can be seen that $\phi(\xi_1)$ is a monotonically decreasing function of k. Therefore a solution branch will materialise when the green curve in figure 3.3.5 will first intersect a blue or red dotted line. This will occur as $k \to 0$. In particular the value of $\delta^{1/2}$ for which this occurs will be

$$\delta^{1/2} = \left.\frac{\phi(\xi_1)}{n}\right|_{k=0} \tag{3.3.106}$$

When $k \to 0$, $\xi_1 \to \infty$. The roots of $c(t)$ as a function of ξ for varying k are shown in figure 3.3.4(a). The blue curves correspond to the limiting case when $U_m \to U_+$, i.e. $k = 0$. For a given $k \neq 0$ the roots are equally spaced apart from the double root at $U_0 = U_- = U_+$ (see figure 3.3.4(a)). For $k \neq 0$ the solution will oscillate between the two curves representing the two largest distinct roots of $c(y)$. However as $k \to 0$ the two largest roots coalesce and the solution will cease to oscillate and in fact;

$$U_0(\xi) \sim \mathrm{e}^{-\xi^2/2}, \tag{3.3.107}$$

as shown by the upper blue curve in figure 3.3.4(a). Note that this is not a solution to the problem as it decays exponentially from above and this is not permissible far-field behaviour, as the analysis of the previous section revealed. However it does provide an approximate loci of termination points in the $(\alpha, u(0))$ parameter space. From (3.3.107)

$$U_0(0) = 1 \tag{3.3.108}$$

which in the α parameter space is

$$u(0) \sim \alpha^{1/2} + \cdots \tag{3.3.109}$$

A vertical approximation of $u(0)$ for the termination point in the solution space has been discovered and now an attempt to approximate the value of δ for which the

solution branches appear is made.

It can be seen that the first solution on a horizontal line n occurs when the green curves in figure 3.3.5 intersect the horizontal lines at the left-most point. This occurs as $k \to 0$ and hence the value of δ on the green curve where this occurs is horizontal approximation of the termination point in the $(\alpha, u(0))$ solution space. To evaluate this,

$$\lim_{k\to 0} \phi(\xi_1)$$

is required. This has been calculated in (3.3.80) and is repeated here as

$$\lim_{k\to 0} \phi(\xi_1) = \frac{1}{\sqrt{2\pi}} \approx 0.399. \tag{3.3.110}$$

This corresponds to the left most points of the green curves in figure 3.3.5. The approximate values of δ where the solution branches appear can now be approximated using

$$\left.\frac{\phi(\xi_1)}{\delta^{1/2}}\right|_{k=0} = n. \tag{3.3.111}$$

for integer and half-integer n. In the α $(= \delta^{-2})$ solution space and using (3.3.110) the ridiculously simple expression

$$\alpha_n = 4\pi^2 n^4 \tag{3.3.112}$$

gives an approximation to the horizontal position of the termination points for different n. The relative errors compared with the numerical termination points is shown in table 3.1. For large α the approximation is poor but improves gradually as α increases. A possible reason for this is there is the issue of the point ξ_0; the internal boundary layer which facilitates the transition from exponential to algebraic decay. This point has order $\xi_0 \sim (-\log\delta)^{1/2}$ and increases as δ decreases. The turning point at $\xi = \xi_1$ therefore will actually be artificial for moderate values of δ and there will be a artificial turning point when $\xi \sim \xi_0$. From the equation for k this will occur when $k \sim O(\delta^{5/2})$. The above analysis is in the limit as $k \to 0$ so for small, but moderate, δ the 'turning point' will occur when $k = O(\delta^{5/2})$. However despite the limited approximation this gives the analysis does predict a solution space with distinct branches that 'sprout' from nowhere as $\alpha \to \infty$. In fact as a final note, notice the similarity between equation (3.3.112) and the expression for the origin of the branches for the rectangular trench, i.e. equation (3.1.16). In both cases the critical values of α_n are proportional to n^4. In summary the extra branches computed numerically in the previous section have been established (at leading order) using the method of Kuzmak (1959). The positions of the termination points of the branches can be approximated (crudely) using the formulae (3.3.109) and (3.3.112) and in the $(\alpha, u(0))$ parameter space can be written as

$$(\alpha_n, u(0)) \approx (4\pi^2 n^4, 2\pi n^2), \tag{3.3.113}$$

Solution Type	n	Kuzmak α_n	Numerical α_n	Relative Error
II	0.5	2.467	35.14	0.9298
IIa	1	39.48	214.0	0.8155
IIb	1.5	199.9	699.1	0.7141
IIc	2	631.7	1709	0.6304
IId	2.5	1542	3508	0.5604
IIe	3	3198	6042	0.4707
IIf	4	5924	10730	0.4479
IIg	4.5	10110	16870	0.4009

Table 3.1: Relative error of Kuzmak approximation to termination points. The Kuzmak α_n column is calculated using (3.3.112). All values of α correct to 4 significant figures.

a beautifully simple formulae for such a lengthy analysis which although failing to give a good approximation to the turning points, does predict the unusual nature of the solution space diagram with branches terminating at a finite value of α.

3.4 Fully nonlinear steady flow

The results obtained for the weakly-nonlinear model are now compared to those found for the fully non-linear problem. The equations were derived in chapter 2 but are restated here for convenience. In the non-dimensionalised steady water-wave equations the velocity potential $\Phi(x, y)$ satisfies Laplace's equation throughout the flow domain,

$$\nabla^2\Phi = 0 \qquad \text{in} \quad -\infty < x < \infty, \quad \sigma(x) < y < 1 + \eta(x). \tag{3.4.1}$$

On the free-surface the dynamic and kinematic boundary conditions need to be satisfied,

$$\left.\begin{aligned} &\frac{1}{2}|\nabla\Phi|^2 + \frac{1}{F^2}y = \frac{1}{2} + \frac{1}{F^2} \\ &\eta_x\Phi_x = \Phi_y \end{aligned}\right\} \quad \text{on} \quad y = 1 + \eta(x), \tag{3.4.2}$$

along with the no-penetration condition on the bottom,

$$\sigma_x\Phi_x = \Phi_y \quad \text{on} \quad y = \sigma(x). \tag{3.4.3}$$

This system of equations was solved numerically using the boundary integral technique described in chapter 2 for the unknown functions $\Phi(x, y)$ and $\eta(x)$ at $F = 1$ for the Gaussian forcing $\sigma(x) = a\exp(-b^2x^2)$ with the aim of computing solitary wave solu-

tions. Based on the weakly-nonlinear calculations algebraic decay in the far-field may be expected and this may cause numerical difficulties. Such behaviour does indeed occur here for the fully nonlinear problem, and this is established analytically in the next section.

The comparison with the weakly nonlinear solutions for the steady fKdV equation (3.1.5) is shown in figure 3.4.1. The type I solution demonstrates a very good agreement with a small discrepancy at the wave minimum. Note that only a portion of the wave is shown around the origin since the two solutions are visually indistinguishable over the remainder of the range. There is very good agreement on the type I solution branch for small $|a|$ as expected. The fully nonlinear type II solution branch exhibits similar behaviour to the weakly nonlinear prediction but while the latter branch continues indefinitely through negative values of a, the former terminates at a finite value of a. Note that the fully nonlinear branch cannot possibly follow the weakly nonlinear branch for large a since it is clear from the Bernoulli's equation in (2.5.2) that the surface elevation is bounded above with $\eta \leq 1/2$ in the case $F = 1$; equality is obtained at a stagnation-point where the first term in the Bernoulli's equation vanishes. Such an eventuality is expected at the crest of a Stokes limiting-configuration, as is found for unforced solitary waves (e.g. Hunter & Vanden-Broeck, 1983) The point of termination of the branch at the left end is $a \approx -0.066$ (see figure 3.4.2(a). Near to this point the numerical scheme requires a large number of mesh points around the wave crest in order to achieve an accurate solution as the wave does indeed seem to be approaching a Stokes-limiting configuration (e.g. Whitham, 1974) with an interior angle of 120° and a stagnation point at the crest – this corresponds to the limiting value $\theta = \pi/6 \approx 0.52$ in figure 3.4.3. Wade *et al.* (2014) experienced similar numerical difficulties for an imposed distribution of pressure on the free surface and presented an improved numerical scheme with a non-uniform mesh to get closer to the Stokes-limiting configuration. Figure 3.4.1 strongly indicate that the far-field decay in the present case is algebraic like $1/x^2$ as anticipated and in line with the analytical argument presented in the next subsection 3.4.1. This algebraic decay presents an added difficulty in any improvement to the numerical method (in Wade *et al.* (2014) calculations the flow was super-critical, with $F > 1$, in which case the far-field decay is exponential). Note that the same rate of algebraic decay has been demonstrated for gravity-capillary waves in infinite depth by Akylas *et al.* (1998), and for gravity-capillary waves in two-layer flow by Sun (1997), who established the decay rate rigorously using analytical methods. Therefore the numerical method is slightly modified in that instead of setting $y_s(N) = 1$, as for super-critical flow (see chapter 2), the condition now is $y(\Phi_N) = 1 - \tan(\theta_N)\Phi_N/2$. Instead of solving the extra equation $y(\Phi_1) = 1$, the equation $y(\Phi_1) = 1 - \tan(\theta_1)\Phi_1/2$.

As was discussed in section 3.2.3, the weakly nonlinear branch terminates at its right-hand end at a negative value of a, as can be seen in figure 3.4.2(a). Also, the fully nonlinear branch appears to terminate at its right-hand end. Solutions along this fully

nonlinear branch adhere to the far-field behaviour (a) in (3.2.32). This was confirmed by plotting the free surface in (η, η_x) space and checking that in the far-field trajectories in this plane approach the origin in the correct way. It is numerically extremely difficult to identify the shift from algebraic decay to exponential decay (behaviour (b) in (3.2.32)) which anticipate will herald the end of the branch as it does for the weakly-nonlinear theory.

The solution type IIa also exists in the fully nonlinear solution space but there is a large difference between the fKdV and fully nonlinear solution branches (see figures 3.4.2(a),(b) as might be expected since the amplitude a is here rather large. It seems reasonable to suppose that the type IIb,c,... branches are also present in the fully nonlinear regime but since they would likely be quantitatively quite different to their weakly-nonlinear counterparts it may not be straightforward to find them, and have not been explored in this thesis. Also, in common with the weakly-nonlinear theory, the type IIa branch terminates at its right-hand end; however as with the type II solutions it appears also to terminate at its other end, indicating a Stokes' limiting configuration has been approached.

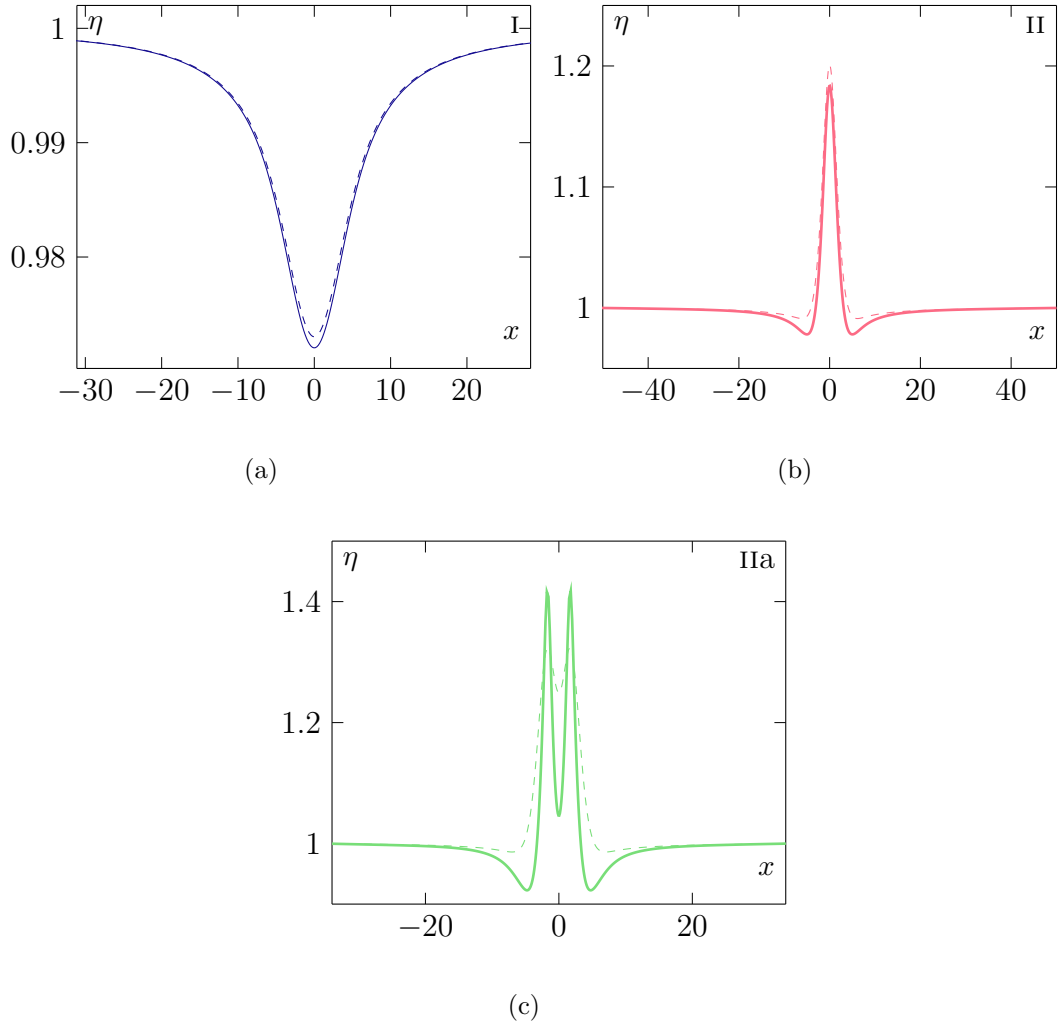

Figure 3.4.1: Fully nonlinear solutions for critical flow past a Gaussian dip. The horizontal axis is x and vertical axis is η. In all panels $b = 0.3$. (a) Type I solution, $a = -0.0017$. (b) Type II solution, $a = -0.039$. (c) Type IIa solution, $a = -0.134$.

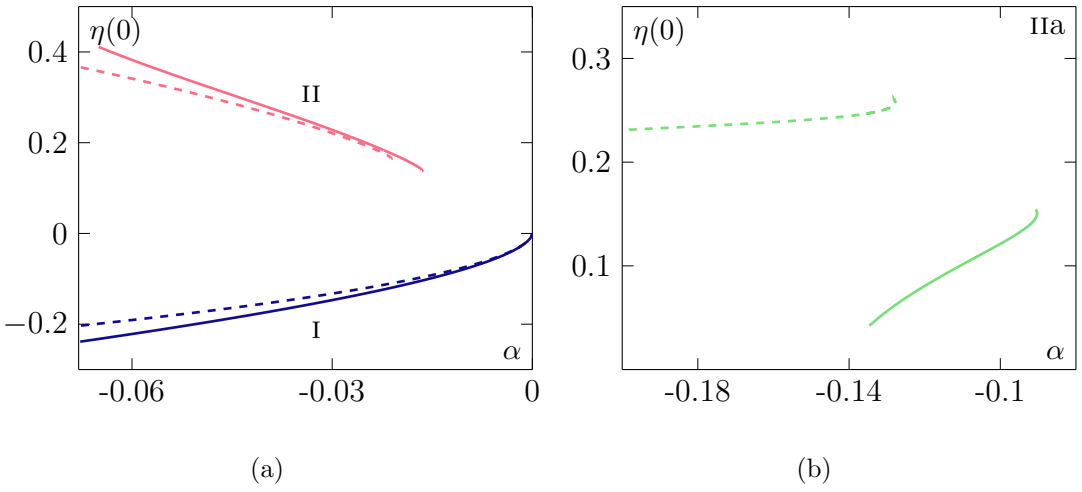

Figure 3.4.2: Fully nonlinear solution space for critical flow past a Gaussian dip. The horizontal axis is α and vertical axis is $\eta(0)$. The dotted lines are the weakly nonlinear results and the solid lines are the fully nonlinear results. (a) Solution space for the type I and II solutions. (b) Solution space for IIa solutions.

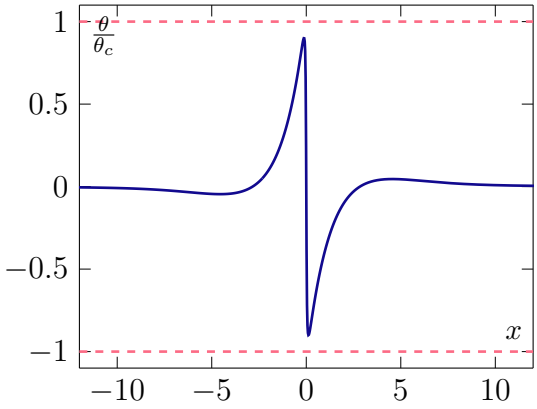

(a)

Figure 3.4.3: Numerical profile for Stokes' limiting configuration. The horizontal axis is a and the vertical axis is θ/θ_c where $\theta_c = \pi/6$. The dotted lines represent $\theta/\theta_c = \pm 1$. The height of the curve appears to approach the dotted lines, indicating a Stokes' limiting configuration is being reached.

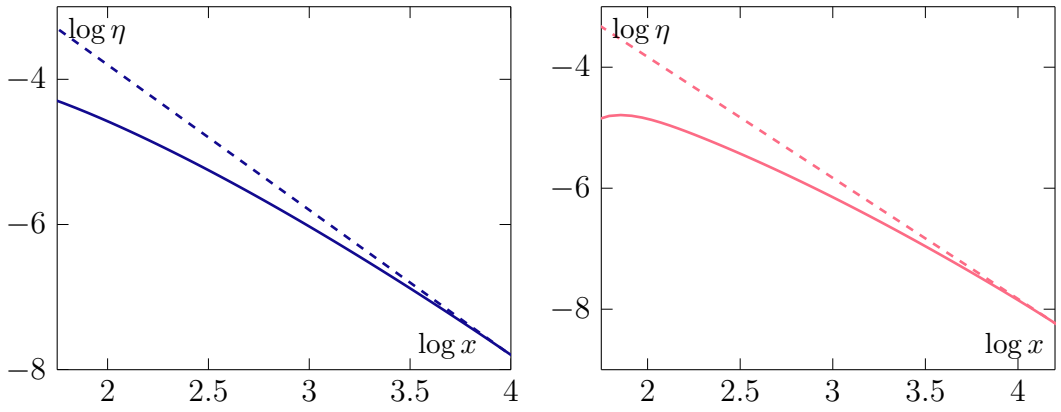

(a) (b)

Figure 3.4.4: Far-field decay for fully nonlinear solutions over a Gaussian dip. The horizontal axis is $\log x$ and the vertical axis is $\log \eta$. The dotted lines have a gradient of -2. (a) Type I solution. (b) Type II solution.

3.4.1 Far-field decay

Now the result that a solitary wave solution for critical flow must decay algebraically in the far-field is presented. Starting from the formulation of the problem (2.5.1)-(2.5.3), it is convenient then to make a conformal transformation $(x, y) \mapsto (\chi, \zeta)$ mapping the physical domain into the infinite strip $-H \leq \zeta \leq 0$ in the mapped plane, where H is a constant to be determined (see figure 3.4.5)

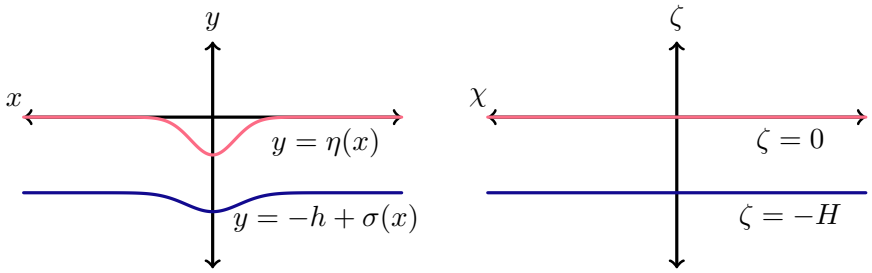

(a) (b)

Figure 3.4.5: A diagram showing the mapping from the (x, y) plane to the (χ, ζ) plane

Working in a manner similar to that adopted by Choi & Camassa (1999) in their discussion of periodic waves, the problem determining the conformal mapping is written down as

$$y_{\chi\chi} + y_{\zeta\zeta} = 0, \quad \text{in } -H \leq \zeta \leq 0, \tag{3.4.4}$$

$$y = 1 + s(\chi) \quad \text{on} \quad \zeta = 0, \tag{3.4.5}$$

$$y = b(\chi) \quad \text{on} \quad \zeta = -H, \tag{3.4.6}$$

where $s(\chi) = \eta[x(\chi)]$ and $b(\chi) = f[(x(\chi)]$ describe the free surface elevation and the bottom topography in the mapped plane respectively. Laplace's equation has to be satisfied if the mapping is analytic (see Ablowitz and Fokas, pg. 346) and the other two conditions describe the mapping of the free-surface and bottom topography onto to the top and bottom boundary in the (χ, ζ) plane. Laplace's equation on a horizontal strip domain can be solved by first taking the Fourier transform with wave number k in the χ variable. The equation

$$-k^2\hat{y} + \hat{y}_{\zeta\zeta} = 0 \tag{3.4.7}$$

has the solution

$$\hat{y} = C_1(k)\cosh k\zeta + C_2(k)\sinh k\zeta. \tag{3.4.8}$$

Applying the boundary conditions gives conditions on C_1 and C_2

$$2\pi\delta(k) + \hat{s} = C_1 + 0, \tag{3.4.9}$$

$$\hat{b} = C_1 \cosh kH - C_2 \sinh kH. \tag{3.4.10}$$

Solving for C_1 and C_2 gives

$$C_1 = 2\pi\delta(k) + \hat{s}, \tag{3.4.11}$$

$$C_2 = \frac{(2\pi\delta(k) + \hat{s})\cosh kH - \hat{b}}{\sinh kH} \tag{3.4.12}$$

$$\tag{3.4.13}$$

and the solution in Fourier space is

$$\hat{y} = -\frac{\sinh k\zeta}{\sinh kH}\hat{b} + \frac{\sinh k(H+\zeta)}{\sinh kH}(2\pi\delta(k) + \hat{s}) \tag{3.4.14}$$

The solution in physical space is found by Fourier inversion to be

$$y = \frac{1}{2\pi}\int_{-\infty}^{\infty}\left((2\pi\delta(k) + \hat{s})\frac{\sinh k(H+\zeta)}{\sinh kH} - \frac{\sinh k\zeta}{\sinh kH}\hat{b}\right)\mathrm{e}^{ik\chi}\,\mathrm{d}k. \tag{3.4.15}$$

Requiring that $s(\chi)$ is real implies

$$s(\chi) = \frac{1}{2\pi}\int_{-\infty}^{\infty}\hat{s}(k)\mathrm{e}^{\mathrm{i}k\chi}\,\mathrm{d}k \tag{3.4.16}$$

must be real. Re-writing the integral

$$s(\chi) = \frac{1}{2\pi}\int_{0}^{\infty}\hat{s}(k)\mathrm{e}^{\mathrm{i}k\chi} + \hat{s}(-k)\mathrm{e}^{-\mathrm{i}k\chi}\,\mathrm{d}k, \tag{3.4.17}$$

then for $s(\chi)$ to be real then $\hat{s}(-k) = \hat{s}^*(k)$. Writing the Taylor series for small positive k and small negative k as

$$\hat{s}(k) \sim a_0 + a_1 k + a_2 k^2 + a_3 k^3 + \cdots, \tag{3.4.18}$$

$$\hat{s}(-k) \sim a_0^* + a_1^* k + a_2 k^2 + a_3^* k^3 + \cdots. \tag{3.4.19}$$

Therefore for continuity at $k = 0$, a_0 must be real and writing $a_n = a_n^r + \mathrm{i}\mathrm{sgn}(k)a_n^i$, with a_n^r and a_n^i both real, for all $n = 1, 2, \ldots$, then the expansion for positive and negative k is of the form

$$\hat{s}(k) \sim a_{00} + \mathrm{i}a_{01}\mathrm{sgn}(k) + a_{10}k + \mathrm{i}a_{11}\mathrm{sgn}(k)k + + a_{20}k^2 + \mathrm{i}a_{21}\mathrm{sgn}(k)k^2 + \cdots \tag{3.4.20}$$

By evaluating

$$\hat{s}(k) = \int_{-\infty}^{\infty} s(\chi)\mathrm{e}^{-k\chi}\,\mathrm{d}\chi$$

at $k = 0$, the constant a_0 can be determined as

$$a_0 = \int_{-\infty}^{\infty} s(\chi)\,\mathrm{d}\chi,$$

the excess mass of the free-surface in the (χ, ζ) plane. Because $\hat{s}(k)$ is infinitely differentiable everywhere expect at $k = 0$, this method will not yield the values of the other coefficients. Using the small k expansions for the expressions involving the hyperbolic functions (3.4.15) can be written as

$$\begin{aligned} y \sim \frac{1}{2\pi}\int_{-\infty}^{\infty} [&(2\pi\delta(k) + a_{00} + \mathrm{i}a_{01}\mathrm{sgn}(k) + a_{10}k + \mathrm{i}a_{11}\mathrm{sgn}(k)k \\ &+ a_{20}k^2 + \mathrm{i}a_{21}\mathrm{sgn}(k)k^2 + \cdots)\left(\frac{\zeta}{H} + 1\right) - \hat{b}\left(\frac{\zeta}{H}\right)\Big]\,\mathrm{e}^{ik\chi}\,\mathrm{d}k. \end{aligned} \tag{3.4.21}$$

This integral can be evaluated using Theorem 18 of Lighthill (1962) and using the fact that

$$\mathcal{F}(x^n) = (-\mathrm{i}k)^{-n}\delta^{(n)}(k), \tag{3.4.22}$$

$$\mathcal{F}(x^{-m}) = -\mathrm{i}\pi\frac{(-\mathrm{i}k)^{m-1}}{(m-1)!}\mathrm{sgn}(k), \tag{3.4.23}$$

for integers n, m, where

$$\mathcal{F}(g(x)) = \int_{-\infty}^{\infty} g(x)\mathrm{e}^{\mathrm{i}kx}\,\mathrm{d}x \tag{3.4.24}$$

and therefore as $\chi \to \infty$ (see also Blyth & Părău, 2016; Viotti *et al.*, 2014)

$$\begin{aligned} y \sim \frac{\zeta}{H} + 1 &+ a_{01}\left(\frac{\zeta}{H} + 1\right)\left(\frac{\mathrm{i}}{\pi}\chi^{-1}\right) + a_{11}\left(\frac{\zeta}{H} + 1\right)\left(-\frac{1}{\pi}\chi^{-2}\right) \\ &+ a_{21}\left(\frac{\zeta}{H} + 1\right)\left(-\frac{2\mathrm{i}}{\pi}\chi^{-3}\right) + a_{31}\left(\frac{\zeta}{H} + 1\right)\left(\frac{6}{\pi}\chi^{-4}\right) \\ &+ a_{41}\left(\frac{\zeta}{H} + 1\right)\left(-\frac{24\mathrm{i}}{\pi}\chi^{-5}\right) + \cdots - \frac{\zeta}{H}b(\chi). \end{aligned} \tag{3.4.25}$$

A similar expansion can be written down for the bottom topography function; since this function is prescribed the precise form of its expansion coefficients are known in

advance. Making use of (3.4.25) and noting that $x_\chi = y_\zeta$

$$\begin{aligned} x_\chi \sim \frac{1}{H} &+ a_{01}\left(\frac{1}{H}\right)\left(\frac{\mathrm{i}}{\pi}\chi^{-1}\right) + a_{11}\left(\frac{1}{H}\right)\left(-\frac{1}{\pi}\chi^{-2}\right) \\ &+ a_{21}\left(\frac{1}{H}\right)\left(-\frac{2\mathrm{i}}{\pi}\chi^{-3}\right) + a_{31}\left(\frac{1}{H}\right)\left(\frac{6}{\pi}\chi^{-4}\right) \\ &+ a_{41}\left(\frac{1}{H}\right)\left(-\frac{24\mathrm{i}}{\pi}\chi^{-5}\right) + \cdots - \frac{1}{H}b(\chi), \end{aligned} \tag{3.4.26}$$

as $\chi \to \infty$. Keeping in mind the application to a Gaussian topographic forcing $\sigma(x)$ in the physical plane, as is considered in the main previous section, it is assumed that $b(\chi)$ decays at least exponentially as $\chi \to \infty$. The analysis up to now has determined x, y and s in terms of ζ by a small k expansion. These expansions will be used when the flow problem is considered in the mapped plane. The flow problem is now formulated in the mapped plane in terms of the mapped stream function $\Psi(\chi, \zeta)$, where $\Psi = \psi(x(\chi, \zeta), y(\chi, \zeta))$, and the stream function in the physical plane ψ is defined in the usual way so that $u = \psi_y$ and $v = -\psi_x$. The problem is

$$\Psi_{\zeta\zeta} + \Psi_{\chi\chi} = 0, \quad \text{in } -H \le \zeta \le 0, \tag{3.4.27}$$

$$\Psi = 1 \quad \text{on} \quad \zeta = 0, \tag{3.4.28}$$

$$\Psi = 0 \quad \text{on} \quad \zeta = -H, \tag{3.4.29}$$

where a unit flux is assumed in the stream wise direction in keeping with the nondimensionalisation introduced in the main part of the chapter. The solution is simply $\Psi = 1 + \zeta/H$. The Cauchy-Riemann equations immediately yield the relation $\Phi_\chi|_{\zeta=0} = 1/H$, where $\Phi(\chi, \zeta)$ is the velocity potential in the mapped plane. At this stage the kinematic conditions on both the bottom topography and on the free surface have been satisfied. The Bernoulli's condition on the free surface in the mapped plane demands that

$$\frac{1}{2J}(\Phi_\chi^2 + \Psi_\chi^2) + \frac{s}{F^2} = \frac{1}{2}, \qquad J = x_\chi^2 + y_\chi^2, \tag{3.4.30}$$

where all terms are evaluated at $\zeta = 0$. Rearranging (3.4.30) for s:

$$s = \frac{1}{2}F^2 - \frac{1}{2}\frac{F^2}{H^2}\frac{1}{J} \tag{3.4.31}$$

Now J is evaluated using the expressions for x_χ and y_χ obtained in (3.4.25) and (3.4.26).

The free-surface s can be expanded in powers of χ^{-1} using the Binomial Theorem;

$$\begin{aligned} s \sim\, & a_{01}F^2\left(\frac{\mathrm{i}}{\pi}\right)\chi^{-1} - \frac{F^2}{2\pi^2}(2\pi a_{11} - 3a_{01}^2)\chi^{-2} \\ & - \frac{F^2}{3\pi^3}(2H^2\pi^2 a_{01} + 6\pi^2 a_{21} - 9\pi a_{01}a_{11} + 6a_{01}^3)\chi^{-3} \\ & + \frac{F^2}{2\pi^4}(4H^2\pi^2 a_{01} - 4H^2\pi^2 a_{21} + 12\pi^3 a_{31} - 12\pi^2 a_{01}a_{21} \\ & - 3\pi^2 a_{11}^2 + 12\pi a_{01}^2 a_{11} - 5a_{01}^4)\chi^{-4} + \cdots, \end{aligned} \tag{3.4.32}$$

as $\chi \to \infty$. The form (3.4.20) implies that

$$s \sim a_{01}\left(\frac{\mathrm{i}}{\pi}\right)\chi^{-1} + a_{11}\left(-\frac{1}{\pi}\right)\chi^{-2} + a_{21}\left(-\frac{2\mathrm{i}}{\pi}\right)\chi^{-3} + a_{31}\left(\frac{6}{\pi}\right)\chi^{-4} + \cdots, \tag{3.4.33}$$

as $\chi \to \infty$. Therefore for consistency between (3.4.32) and (3.4.33) it is required that

$$F = 1, \tag{3.4.34}$$

$$a_{i1} = 0, \qquad i = 0, 2, 4, 6.., \tag{3.4.35}$$

$$a_{11} = \frac{4}{3}H^2\pi. \tag{3.4.36}$$

Note for even i, $a_{i1} = 0$ automatically, as s is required to be real. Note that if $F \neq 1$, as is the case for either sub-critical flow or for super-critical flow, the conclusion must be that $a_{i1} = 0$ for all i; in this case the decay is known to be exponential (see Hunter & Vanden-Broeck, 1983; Longuet-Higgins & Fox, 1977; Wade *et al.*, 2014). Finally it is noted from (3.4.26) that $x = \frac{1}{H}\chi + o(\chi)$ as $\chi \to \infty$ and hence in conclusion,

$$s \sim -\frac{4}{3}x^{-2}, \tag{3.4.37}$$

which is exactly the same rate of decay as the fKdV model as seen in (2.2.14)! It is noted that the same inverse square rate of algebraic decay has been demonstrated for gravity-capillary waves in infinite depth by Akylas *et al.* (1998), and for gravity-capillary waves in two-layer flow by Sun (1997), who established the decay rate rigorously using analytical methods.

3.5 Weakly nonlinear time-dependent flow

3.5.1 Linear stability

As discussed in chapter 2 the aim is to classify the steady solutions that have been computed as being *neutrally*, *spectrally*, *linearly* or *formally* stable (see chapter 2 for a definition of these terms). The initial analysis is repeated here for the convenience of the reader.

The starting point is the time-dependent fKdV equation (2.1.41) at the critical condition $F = 1$, which is repeated here for convenience,

$$\eta_t - \frac{3}{2}\eta\eta_x - \frac{1}{6}\eta_{xxx} = \frac{1}{2}\sigma_x(x). \tag{3.5.1}$$

To investigate the stability of these solutions a perturbation of the form $\eta(x,t) = \eta_s(x) + \varepsilon\zeta(x,t)$ is written, where η_s is a steady solution of (3.5.1) and ζ is a time-dependent perturbation, and where $\varepsilon \ll 1$. The perturbation ζ is demanded to satisfy the same far-field conditions as η, namely equation (2.2.2). Substituting into (3.5.1) and retaining terms at $O(\varepsilon)$

$$\zeta_t = \mathcal{M}\zeta = -\frac{\partial}{\partial x}(\mathcal{K}\zeta), \tag{3.5.2}$$

where the operator $\mathcal{K}$ is defined as

$$\mathcal{K} = -\frac{1}{6}\partial_{xx} - \frac{3}{2}\eta_s. \tag{3.5.3}$$

The general solution to (3.5.2) may be written in the form (e.g. Chang & Demekhin, 2002, section 7.3)

$$\zeta(x,t) = \sum_{k=1}^{N_p} a_k g_k(x)\,\mathrm{e}^{s_k t} + \int_\Gamma a(s)g(x,s)\,\mathrm{e}^{st}\,\mathrm{d}s, \tag{3.5.4}$$

where the a_k and $a(s)$ are expansion coefficients corresponding respectively to the N_p values of s in the point spectrum and to the continuous spectrum of the operator $\mathcal{M}$. These satisfy the relation

$$\mathcal{M}g = sg \tag{3.5.5}$$

(with k subscripts appended in the case of the point spectrum). The integral in the second term in (3.5.4) is taken over the contour Γ which delineates the continuous spectrum in the complex s plane. The eigenfunctions in the point spectrum, $g_k(x)$, reside in $L_2(-\infty,\infty)$. Furthermore, they satisfy the integral constraint,

$$\int_{-\infty}^{\infty} g_k(x)\,\mathrm{d}x = 0 \qquad (s \neq 0), \tag{3.5.6}$$

which is obtained by integrating (3.5.5) over the real line and using the fact that $g_k \to 0$ as $|x| \to \infty$ (Camassa & Wu, 1991). Consequently the eigenfunctions g_k carry zero excess mass. The functions $g(x,s)$ associated with the continuous spectrum Γ are bounded as $|x| \to \infty$. The continuous spectrum itself is determined by examining the behaviour as $|x| \to \infty$ (e.g. Sandstede, 2002). In this limit, the second term in (3.5.3) can be neglected and (3.5.2) reduces to $\zeta_t - (1/6)\zeta_{xxx} = 0$; adopting the form $\zeta = \exp(st)g(x,s)$, the form of g can be found as $g = \exp(\mathrm{i}kx)$ and $s = -\mathrm{i}k^3/6$ for

$k \in \mathbb{R}$ so that the continuous spectrum occupies the imaginary axis: $\Gamma = \{\mathrm{i}q : q \in \mathbb{R}\}$.

In the case of type I steady solutions, which have the property that $\eta_s(x) < 0$ for all x, it can be shown that the point spectrum of the operator $\mathcal{M}$ does not include the origin. Setting $s = 0$ in (3.5.5), integrating once and applying $g_k \to 0$ as $|x| \to \infty$, the equation for g becomes $g_k'' + 9\eta_s g_k = 0$. The eigenfunction g_k is taken to be real without loss of generality. Multiplying this equation by g_k and integrating over the real line and applying the boundary conditions that g_k vanish as $|x| \to \infty$, the condition

$$\int_{-\infty}^{\infty} \eta_s g_k^2 \,\mathrm{d}x = \frac{1}{9}\int_{-\infty}^{\infty} g_k'^2 \,\mathrm{d}x \geq 0 \qquad (s = 0) \tag{3.5.7}$$

is obtained. Since η_s is negative definite (3.5.7) is clearly violated for any non-trivial g_k and, consequently $s = 0$ is not an eigenvalue. In the case of type II steady solutions, numerically computed spectra are found to not include the origin, as will be discussed below.

The spectrum of the $\mathcal{M}$ operator has been computed numerically on a truncated domain $[-L, L]$ with periodic boundary conditions using a spectral method. Sandstede & Scheel (2000) showed that calculations performed on a periodic domain faithfully reproduce the point and continuous spectra provided the size of the domain is large enough. Bridges *et al.* (2002) and Barashenkov & Zemlyanaya (2000) have noted that numerical algorithms for computing eigenvalues in KdV-type problems can lead to spurious eigenvalues leaving/entering the imaginary axis and posing as unstable/stable modes. With this in mind, careful convergence tests have been performed on the results and, furthermore, the results have been confirmed by comparison with time-dependent simulations to be discussed in the next section. For type I solutions the spectrum is found to be contained on the imaginary axis indicating that the flow is spectrally stable in this case. This conclusion will be confirmed via a formal argument to be presented below. In contrast type II solutions are found numerically to be linearly unstable. In all cases computed the operator $\mathcal{M}$ was found to have just one unstable eigenvalue s in the right-half plane (excluding s^*). In fact, this was found to be true for all of the type II and type IIa solutions shown in figure 3.2.2(b) and (c). Tables 3.2 and 3.3 illustrate the convergence of the unstable eigenvalue for sample type II and IIA cases as the discretisation level N and the truncation length of the computational domain L are varied. Evidently convergence is achieved with a rather large number of discretisation points. The spectrum for this case is shown in figures 3.5.1(a) and 3.5.2(a) for type II and IIa solutions respectively. The unstable eigenfunction is shown in figures 3.5.1(b)-(d) and 3.5.2(b)-(d) for the different solutions. The large x behaviour of the eigenfunction is controlled by the balance $(1/6)g_k''' \sim s g_k$ in (3.5.5). Therefore the decay is exponential with $g_k \sim \exp(\mu x)$ as $|x| \to \infty$, where $\mu = (6s)^{1/3} + 2\mathrm{i}k\pi/3$ for $k = 0, 1, 2$. For the unstable eigenvalue given in table 3.2, the dominant decay rate is obtained to be $\mu = 0.73 - 0.41\mathrm{i}$ for $x \to -\infty$ and $\mu = -0.01 + 0.84\mathrm{i}$ as $x \to \infty$. The

N	L	$\mathrm{d}x$	s
1024	100	0.195	$1.9068 \times 10^{-3} + 0.09881\mathrm{i}$
2048	200	0.195	$3.5399 \times 10^{-3} - 0.09955\mathrm{i}$
4096	400	0.195	$3.5612 \times 10^{-3} - 0.09968\mathrm{i}$
8192	800	0.195	$3.5591 \times 10^{-3} - 0.09967\mathrm{i}$
8192	400	0.098	$3.5612 \times 10^{-3} - 0.09968\mathrm{i}$

Table 3.2: Type II solution at $a = -0.1357$, $b = 0.3$ ($\alpha = 226.1$). Convergence of the eigenvalues in the discrete $\mathcal{M}$ spectrum computed on a computational domain $[-L, L]$ with N equally-spaced points. One value of s in the $(s,-s,s^*,-s^*)$ quartet is shown for various N and L (and grid size $\mathrm{d}x = 2L/N$).

N	L	$\mathrm{d}x$	s
1024	100	0.195	$2.9578 \times 10^{-3} + 0.07647\mathrm{i}$
2048	200	0.195	$2.7628 \times 10^{-3} - 0.07729\mathrm{i}$
4096	400	0.195	$2.6624 \times 10^{-3} - 0.07719\mathrm{i}$
8192	800	0.195	$2.6624 \times 10^{-3} - 0.07719\mathrm{i}$
8192	400	0.098	$2.6594 \times 10^{-3} - 0.07719\mathrm{i}$

Table 3.3: Type IIa solution at $a = -0.2$, $b = 0.3$ ($\alpha = 333.3$). Convergence of the eigenvalues in the discrete $\mathcal{M}$ spectrum a computational domain $[-L, L]$ with N equally-spaced points. One value of s in the $(s,-s,s^*,-s^*)$ quartet is shown for various N and L (and grid size $\mathrm{d}x = 2L/N$).

latter value indicates a very slow decay downstream requiring a large computational domain. This explains the large value of L required to achieve numerical convergence (see tables 3.2 and 3.3).

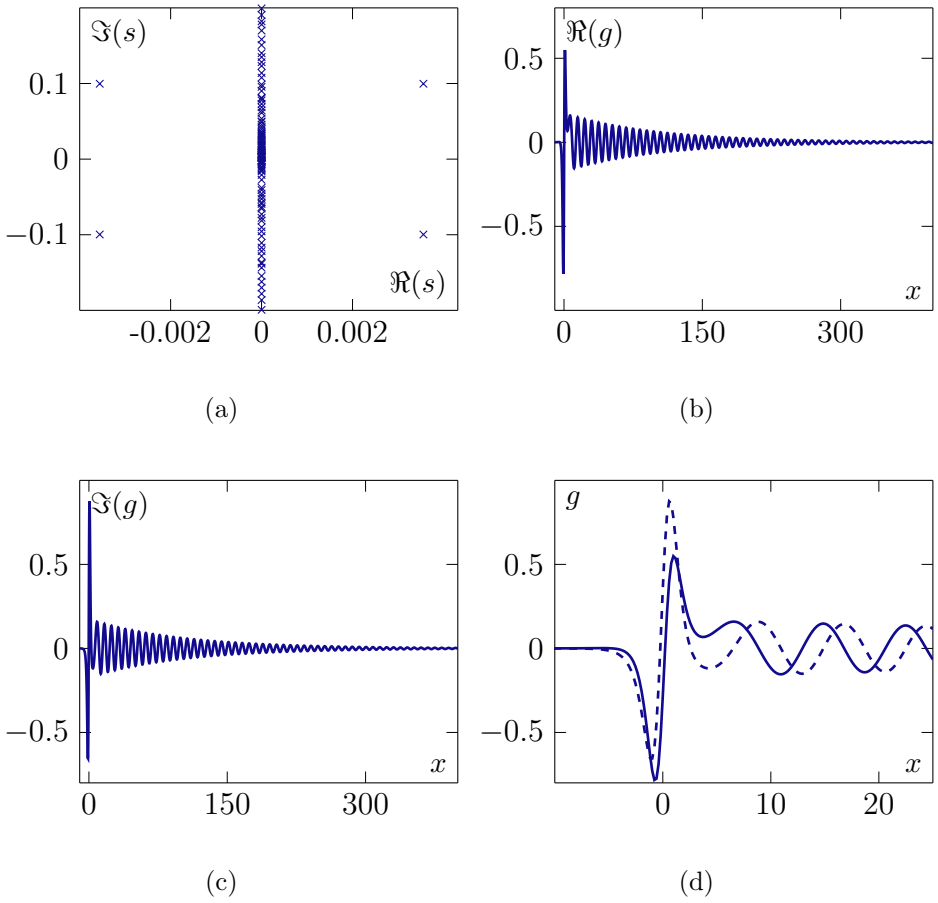

Figure 3.5.1: Stability properties of the type II solution at $a = -0.1357$, $b = 0.3$ ($\alpha = 226.1$): (a) Spectrum of the $\mathcal{M}$ operator and (b) the real and (c) imaginary parts of the unstable eigenfunction for $s = 0.0036 + 0.0997\mathrm{i}$. In (d) the inset shows a close-up of the eigenfunction near to the origin.

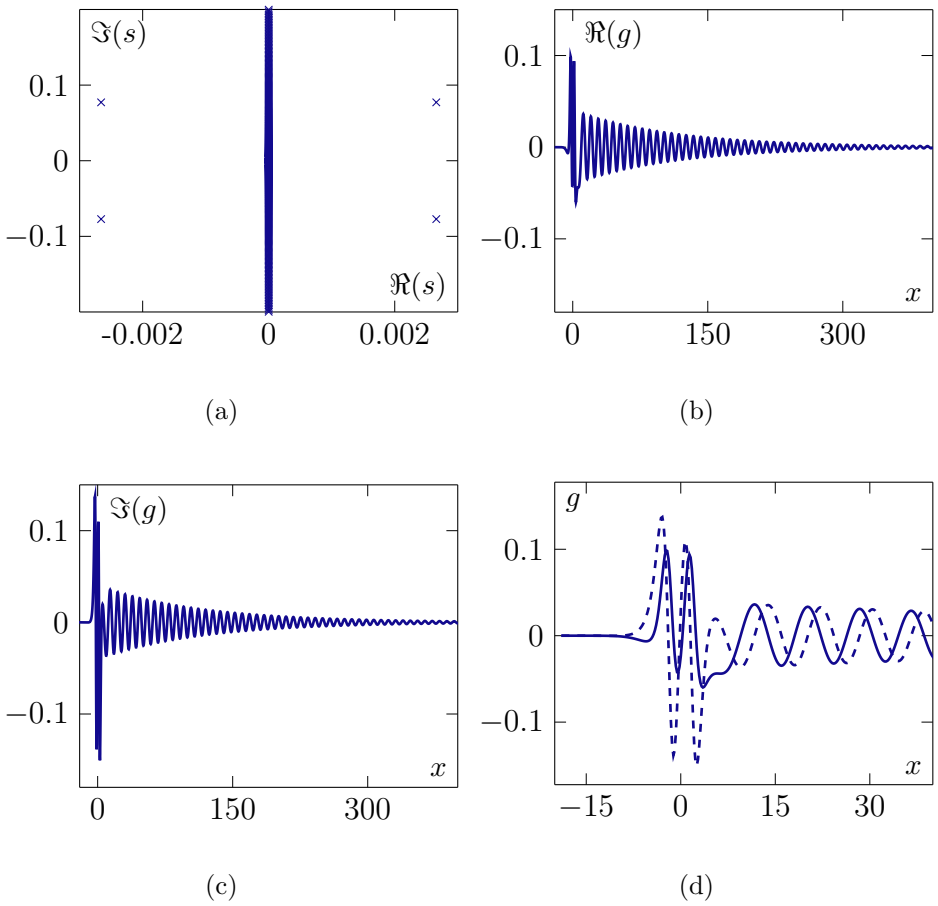

Figure 3.5.2: Stability properties of the type IIa solution at $a = -0.2$, $b = 0.3$ ($\alpha = 333.3$): (a) Spectrum of the $\mathcal{M}$ operator and (b) the real and (c) imaginary parts of the unstable eigenfunction for $s = 0027 - 0.0772\mathrm{i}$. In (d) the inset shows a close-up of the eigenfunction near to the origin.

3.5.2 Formal stability

As discussed in chapter 2 the fKdV equation when $F = 1$ can be written as

$$\eta_t = -\frac{1}{6}\frac{\partial}{\partial x}\left(\frac{\delta \mathcal{H}}{\delta \eta}\right), \tag{3.5.8}$$

where the Hamiltonian is given by

$$\mathcal{H}(\eta, \eta_x) = \frac{1}{2}\int_{-\infty}^{\infty} \eta_x^2 - 3\eta^3 - 6\sigma\eta \, \mathrm{d}x. \tag{3.5.9}$$

If the second variation of the Hamiltonian $\delta^2\mathcal{H}$ (as defined in (2.4.26)) is definite in sign then the steady solution η_s is classified as formally stable. As mentioned in chapter 2 this is equivalent to insisting that the spectrum of $\mathcal{K}$ is definite. Using (2.4.28) the required condition when $F = 1$ is that

$$\delta^2\mathcal{H} \geq \frac{1}{3}\nu_0\langle\zeta, \zeta\rangle.$$

Therefore for critical flow the second variation of the Hamiltonian will be positive definite if $\nu_0 > 0$. By examining (2.4.27) it is clear that $\nu_0 > 0$ if the solution is negative definite. The type I steady solution satisfies this criteria and hence is formally stable as supported by numerical calculations in the previous sub-section.

For the other solution types, which are multi-signed, $\delta^2\mathcal{H}$ is difficult to calculate analytically and instead a numerical pseudo-spectral method was used to determine the $\mathcal{K}$ spectrum and, hence, to calculate ν_0. (It should be emphasised that if for a given solution it is found that $\nu_0 < 0$, so that the solution is formally unstable, this does not imply that it is linearly unstable and further investigation is needed).

The numerical calculations in figure 3.5.3 show the spectrum of ν and the corresponding eigenfunction ϕ. For the type I solution the spectrum is purely continuous and $\nu > 0$ (as expected) and the eigenfunctions are not in the class of L_2 (again, as expected). These calculations confirm the formal stability analysis above.

For the type II and IIa solutions, a discrete part of the spectrum occurs and $\nu_0 < 0$ so that the spectrum of $\mathcal{K}$ is non-definite. The corresponding eigenfunctions ϕ_n are highly localised and reside in class of L_2 (as expected). These solutions are formally unstable but this does not in itself indicate linear instability. It is interesting therefore that the analysis of the operator $\mathcal{M}$ predicts linear instability nevertheless.

In the next section time-dependent simulations of the unsteady fKdV equation are performed with the goals of confirming the stability properties of the type I and II solutions.

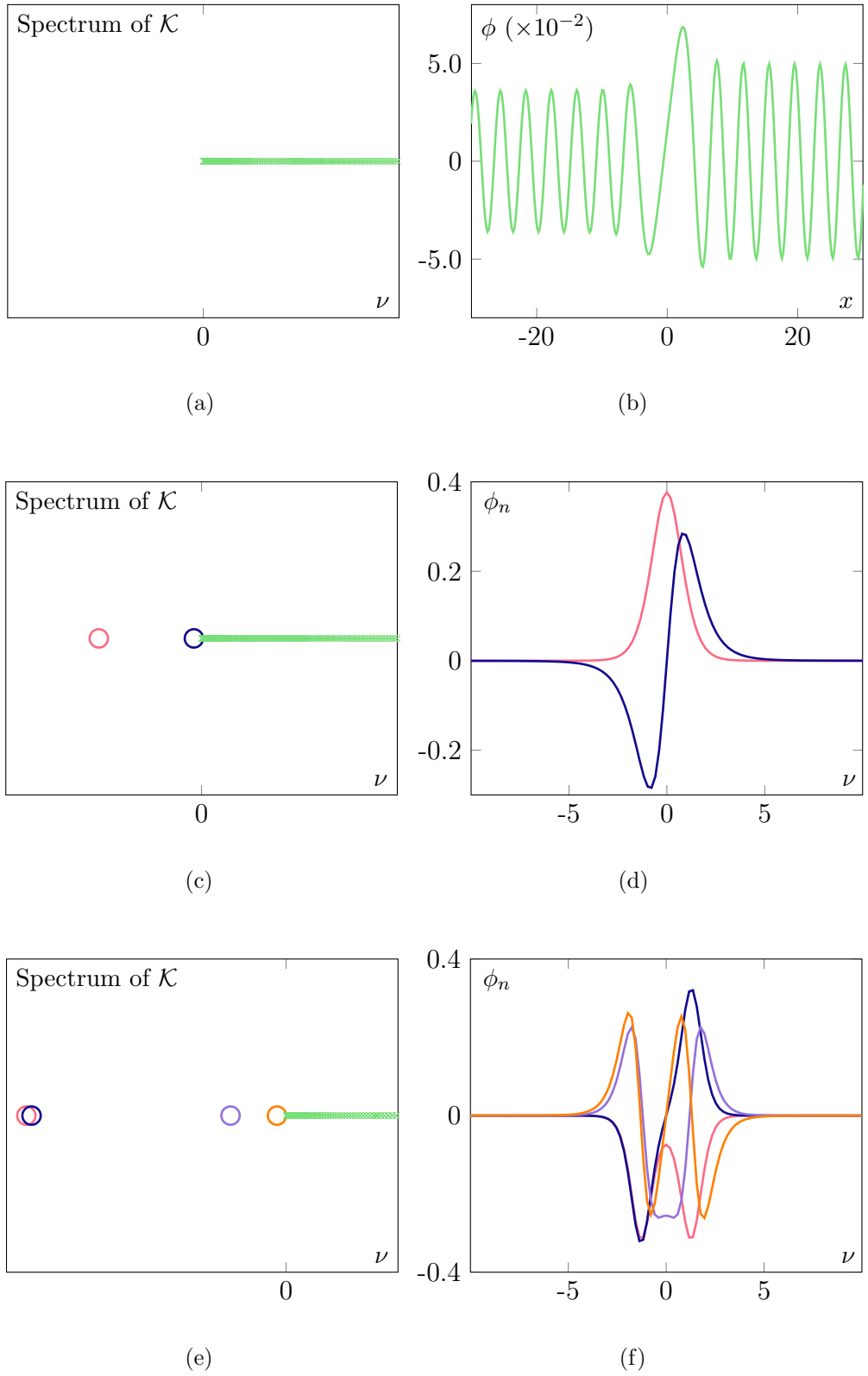

Figure 3.5.3: Spectrum and eigenfunctions of the operator of $\mathcal{K}$. The green markers indicate the continuous spectrum. The circular markers indicate the discrete spectrum. The colours of the eigenfunctions are matched with the same colour marker in the spectrum. (a)-(b) Type I solution ($\alpha = 226.3$). (c)-(d) Type II solution. (e)-(f) Type IIa solution.

3.5.3 Time-dependent simulations

Time-dependent simulations of (2.1.41) on a truncated spatial domain $[-L, L]$, for a specified value of L, assuming periodic boundary conditions and using a method similar to that adopted by Chardard *et al.* (2011) and Wade *et al.* (2014) are discussed in 2.4.4. In numerical practice, solutions may be obtained that satisfy the boundary conditions in the far-field by taking L sufficiently large. In practice taking $\Delta t \sim 10^{-2}$ and 512 Fourier modes was found to be sufficient to ensure the accuracy of the computations.

Multiplying (2.1.41) by η and integrating, after making use of (2.2.2)

$$\frac{\mathrm{d}P}{\mathrm{d}t} = \int_{-\infty}^{\infty} \eta \sigma_x \, \mathrm{d}x \equiv W(\eta), \tag{3.5.10}$$

where the momentum $P = \int_{-\infty}^{\infty} \eta^2 \, \mathrm{d}x$. The expression W is termed the wave resistance coefficient by Camassa & Wu (1991) and is interpreted physically as a measure of the power being supplied by the forcing (see also Wu, 1987).

In the absence of forcing, P is a conserved quantity. In general $P = P(t)$ and so $W \neq 0$; it follows from the integral on the right hand side of (3.5.10) that for a topography which is even in x, as will be assumed in this chapter, $\eta(x, t)$ will have a left-right asymmetry about $x = 0$. In the presence of forcing it is straightforward to show that the excess mass

$$Q = \int_{-\infty}^{\infty} \eta \, \mathrm{d}x \tag{3.5.11}$$

is a conserved quantity. The Hamiltonian (2.4.9) provides a second conserved quantity, and both of these can be used as a check on the fidelity of numerical time-dependent simulations of (2.1.41). A further check can be made by computing W using either of the two alternative expressions given in (3.5.10) and confirming that the same result is obtained in either case. In the numerical results to be discussed in the next section, both Q and $\mathcal{H}$ were performed in the absence of the sponge layer and it was confirmed that they are conserved.

To quantify the size of a perturbation it is convenient to define its L_2 norm as

$$v = \|\varepsilon\zeta\|_2 = \varepsilon \left(\int_{-\infty}^{\infty} \zeta^2 \, \mathrm{d}x \right)^{1/2} = \varepsilon \langle \zeta, \zeta \rangle^{1/2}, \tag{3.5.12}$$

where the inner product is defined as

$$\langle g, h \rangle = \int_{-\infty}^{\infty} g h^* \mathrm{d}x. \tag{3.5.13}$$

Assuming that $v \sim \mathrm{e}^{st}$ for small values of t, then, taking logs of both sides,

$$\log v \sim st. \tag{3.5.14}$$

This formula provides a convenient means of estimating the largest growth rate in the

eigenspectrum in the early stages of a numerical simulation.

In the results to be presented below a time-dependent calculation is started using the initial condition $\eta(x,0) = \eta_s + \varepsilon\hat{\zeta}$ where η_s is a chosen steady solution, $\hat{\zeta}$ is a perturbation and ε is taken to be a small number. In all of the calculations to be presented below, $\varepsilon = 0.025$. If the numerically computed eigenspectrum of the operator $\mathcal{M}$ revealed a positive largest growth rate, the initial perturbation $\hat{\zeta} = (g_k + g_k^*)/2$, with g_k the corresponding eigenfunction, was used. Otherwise if the numerically computed spectrum was found to contain only purely imaginary eigenvalues, the initial perturbation $\hat{\zeta} = \eta_s$ was used. In the early stages of the time evolution, the formula (3.5.14) was used to estimate the largest growth rate and this was then compared with the eigenvalue prediction.

Note that for a given initial condition and a particular choice of the topographic forcing $\sigma(x)$, the solution to the fKdV equation (2.1.41) is known to be unique (Wu, 1987). Also, it is useful to remark that when presenting time simulations of the fKdV equation for topographic forcing similar to that considered here Wu (1987) and Camassa & Wu (1991) both solved the so-called regularised form of the fKdV equation (see Benjamin *et al.*, 1972), whose equivalence is assured only in the limit of long-waves.

Gaussian dip topography

A Gaussian topography of the form $\sigma(x) = a\exp(-b^2x^2)$ is chosen for the simulations. The first goal is to confirm the stability results of sections 3.5.1 and 2.4.2. Figure 3.5.4 shows the results of a numerical simulation starting from a small perturbation of the unique type I steady solution η_s at $\alpha = 141$ ($a = -0.085$, $b = 0.3$). The free-surface profile $\eta(x,t)$ is shown at different times over a portion of the computational domain $[-L, L]$. Note that the solution in the left side of the domain, which is not shown, remains uniformly zero over the duration of the simulation and that no disturbances are observed to propagate upstream. Also shown in the figure are the time signals of the energy E and the wave resistance coefficient W. The initial condition $\eta(x,0) = 1.025\eta_s$ has energy $E(0) = 5.53\times10^{-3}$ which is in excess of the energy of the steady state type I solution energy $E_s = 5.26\times10^{-3}$. The simulation shows that ultimately the system returns to the steady state η_s as time increases. The wave resistance coefficient W approaches zero at large time, which is a necessary condition for the steady state to be recovered. Also W is negative during the simulation and so, according to (3.5.10), the energy E must decrease monotonically. In particular, notice that $E \to E_s$ as $t \to \infty$. A log-log plot of the W signal indicates that $W \sim O(t^{-2})$ for large t, and so E is expected to approach E_s algebraically in time; this explains the very long integration time required to recover the steady state.

It is worth emphasising again that energy cannot be released from the free surface as long as it is symmetric about $x = 0$ since W is zero in this case. Since the initial condition is symmetric, and moreover has a greater energy than the steady state η_s,

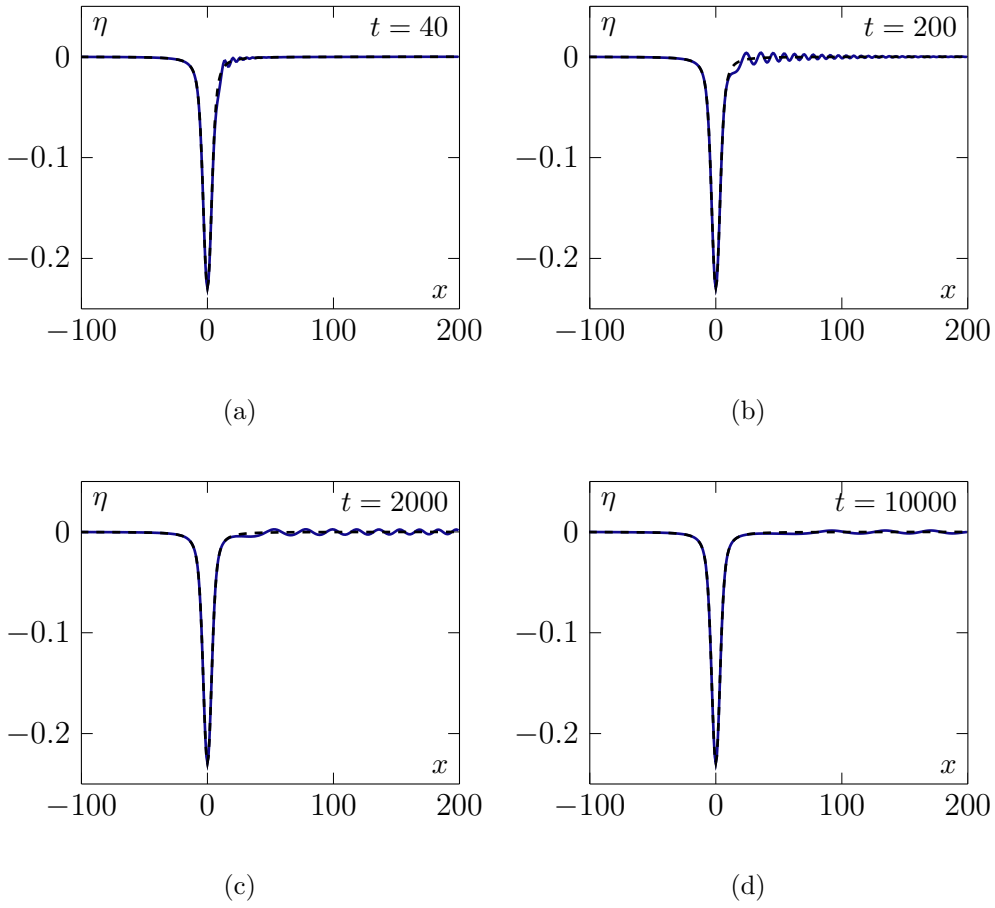

Figure 3.5.4: Numerical simulation of equation (2.4.35) with Gaussian forcing for $\alpha = 141$, $(a = -0.085, b = 0.3)$ with $L = 200$ and $N = 512$. The initial condition is $\eta(0,t) = 1.025\eta_s$, where η_s is the type unique I solution at this α (see figure 3.2.2(a). Panels (a-d) show the solution over a portion of the domain at times $t = 40$, 200, 2000 and 10,000.

it follows that an asymmetric free-surface disturbance must develop in $t > 0$ if the steady state is to be recovered in the long term. As can be seen in figure 3.5.4(a-d), small amplitude waves appear on the leeward side of the free surface. These waves propagate downstream carrying energy with them. Eventually these waves evanesce and the steady state is recovered. Close inspection of these figures reveals that the free surface, shown with a solid line, overlaps with the steady state η_s, shown with a broken line, over an increasingly wide region as time goes on.

Figures 3.5.6 and 3.5.8 shows the results of a numerical simulation starting from a small perturbation of the type II and IIa steady solutions η_s at $\alpha = 226.1$ $(a = -0.1357,\ b = 0.3)$ and $\alpha = 333.3$ $(a = -0.2,\ b = 0.3)$ respectively. The free-surface profile $\eta(x,t)$ is shown at different times over a portion of the computational domain $[-L, L]$. The calculated unstable eigenmode is used as an initial condition for the linearised time-dependent equation (3.5.2) and excellent agreement is found with the calculated unstable eigenvalue when $\log v$ is plotted against time (see figures 3.5.7(b),(c) and3.5.9(b),(c). The agreement for the nonlinear time-dependent equation is also good for small times when the initial condition is given by $\eta(x,0) = \eta_s + \frac{1}{2}\varepsilon(g_k + g_k^*)$, with g

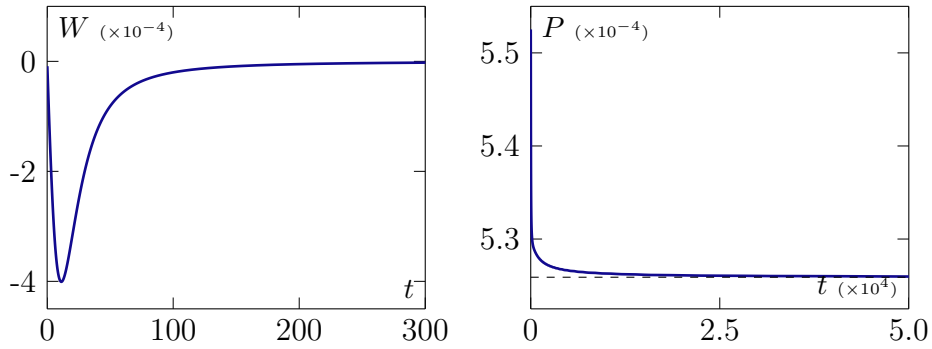

(a) (b)

Figure 3.5.5: Numerical simulation of equation (2.4.35) with Gaussian forcing for $\alpha = 141$, $(a = -0.085, b = 0.3)$ with $L = 200$ and $N = 512$. The initial condition is $\eta(0,t) = 1.025\eta_s$, where η_s is the unique type I solution at this α (see figure 3.2.2(a)). Panels (a) and (b) show the energy W and P respectively against time. The broken line in panel (c) is the energy of the type I steady state, $P = 5.26 \times 10^{-3}$.

the unstable eigenmode (see figures 3.5.7(b),(c) and 3.5.7(b),(c). The initial condition for the calculations in figures 3.5.6 and 3.5.8 is $\eta(x,0) = 1.025\eta_s$ and the different panels show the free-surface profile at different times together with the steady solution, which is shown as a dashed curve. These snapshots show waves travelling downstream in an irregular manner. Additionally, the solution in $x < 0$ does not remain uniformly zero over the duration of the simulation and after a finite interval soliton-like disturbances emerge and propagate upstream. To conserve the excess mass, Q, defined in (3.5.11), the excess mass created by these soliton-like disturbances is balanced by a non- uniform depression region which appears directly downstream of the topography. The time signal of the wave resistance coefficient W is also shown in the figures 3.5.7(a) and 3.5.9(a) and is seen to oscillate with increasing amplitude as time increases. The conclusion is that the solution does not return to the steady state as t increases.

Figure 3.5.10 shows the results of two simulations with the initial condition $\eta(x,0) = 0$. Although a stable steady solution exists in this case, this is not approached at large time. Instead, for a given α, soliton-like waves of different heights are emitted upstream (this is most clearly seen in the movies available in the supplementary material). During a simulation the excess mass (3.5.11) must be conserved, as was noted above, and here the excess mass carried by the solitary waves is balanced by a non-uniform depression which appears immediately downstream of the topography and which lengthens as time increases. Beyond the depression, a train of irregular, cnoidal-like waves propagates downstream. While solitary waves are fired upstream almost immediately at sufficiently small values of α, when this parameter exceeds a threshold there is a delay before the first solitary wave appears (compare panels (a), (b) and (c),(d) in figure 3.5.10). It is interesting to note that the behaviour just described is similar to that observed for critical flow over a positive topography but with some important differences. In

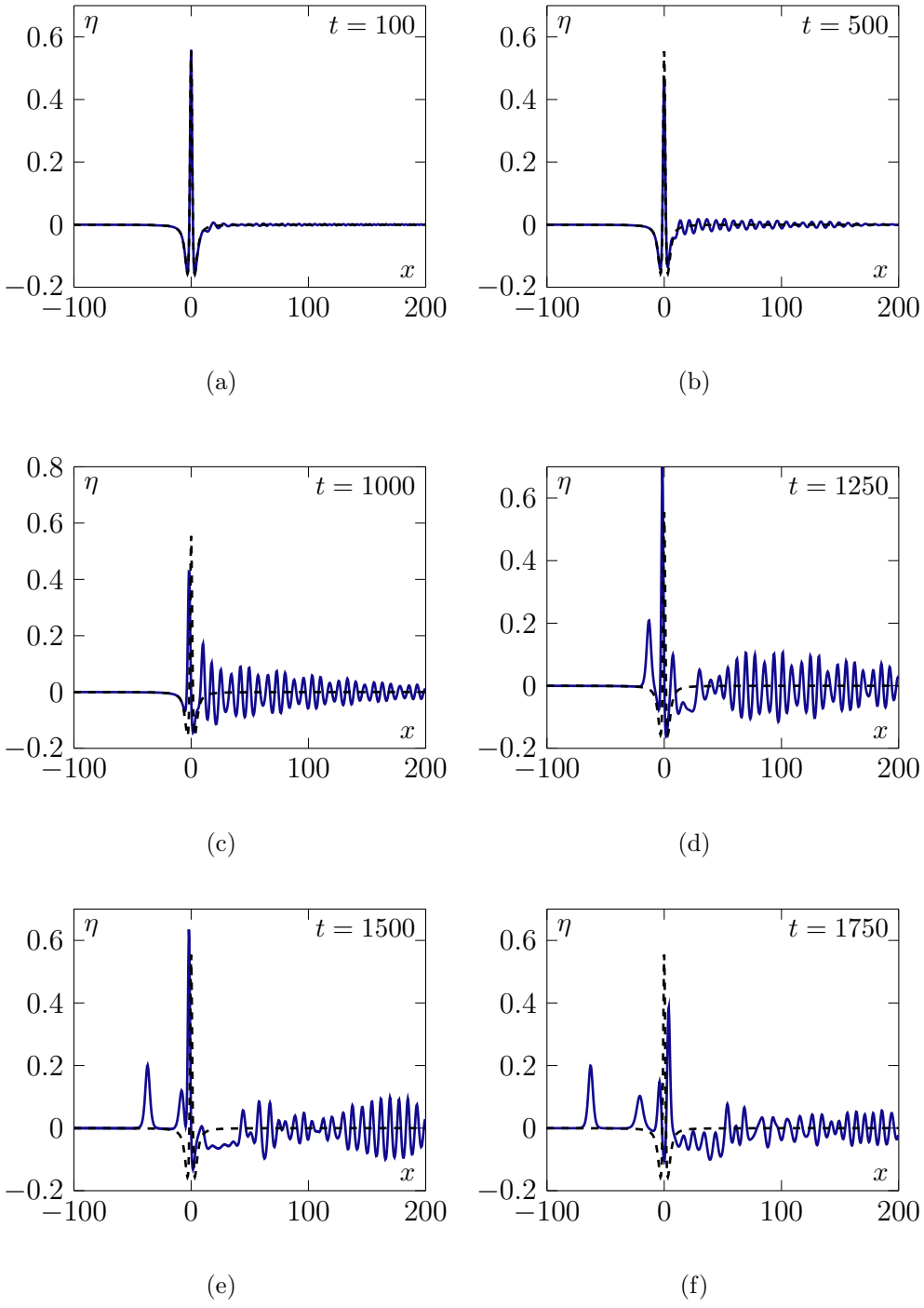

Figure 3.5.6: Numerical simulation of equation (2.4.35) with Gaussian forcing for $\alpha = 226.1$, $(a = -0.1357, b = 0.3)$ with $L = 400$ and $N = 2048$ (note not all of the domain is displayed). The initial condition is $\eta(0,t) = 1.025\eta_s$, where η_s is the type unique II solution at this α (see panel 3.2.2(c)). Panels (a-d) show the solution over a portion of the domain at times $t = 100$, $t = 500$, $t = 1000$, 1100 and 1500. Panel (f) shows W respectively against time. The dotted curve is the steady solution η_s.

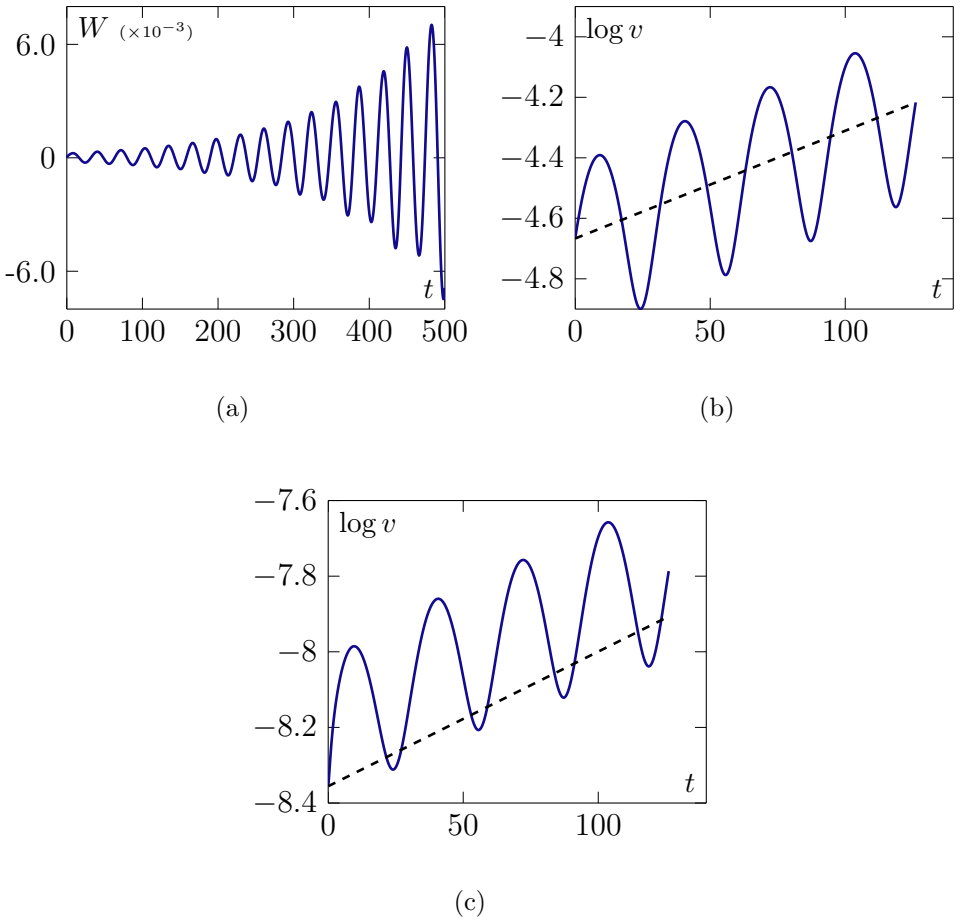

Figure 3.5.7: Time-dependent signals of type II solution. Panel (a) shows W respectively against time.(b) (linear operator) - (c) (nonlinear operator). Evolution of the quantity $\log v$ (solid lines) for $0 \leq t \leq 4\pi/\Im(s)$ of the linearised equation (3.5.2) and equation (2.4.35) with Gaussian forcing. $\alpha = 226.1$, $(a = -0.1357, b = 0.3)$ with $L = 200$ and $N = 2048$. For the linearised equations the initial condition is $\zeta(x,0) = \frac{1}{2}(g_k + g_k^*)$ where g_k is the unstable eigenmode, and for the nonlinear equations $\eta(x,0) = \eta_s + 0.0125(g_k + g_k^*)$. The dotted line in the figures has slope $\Re(s)$, where s is the most unstable eigenvalue.

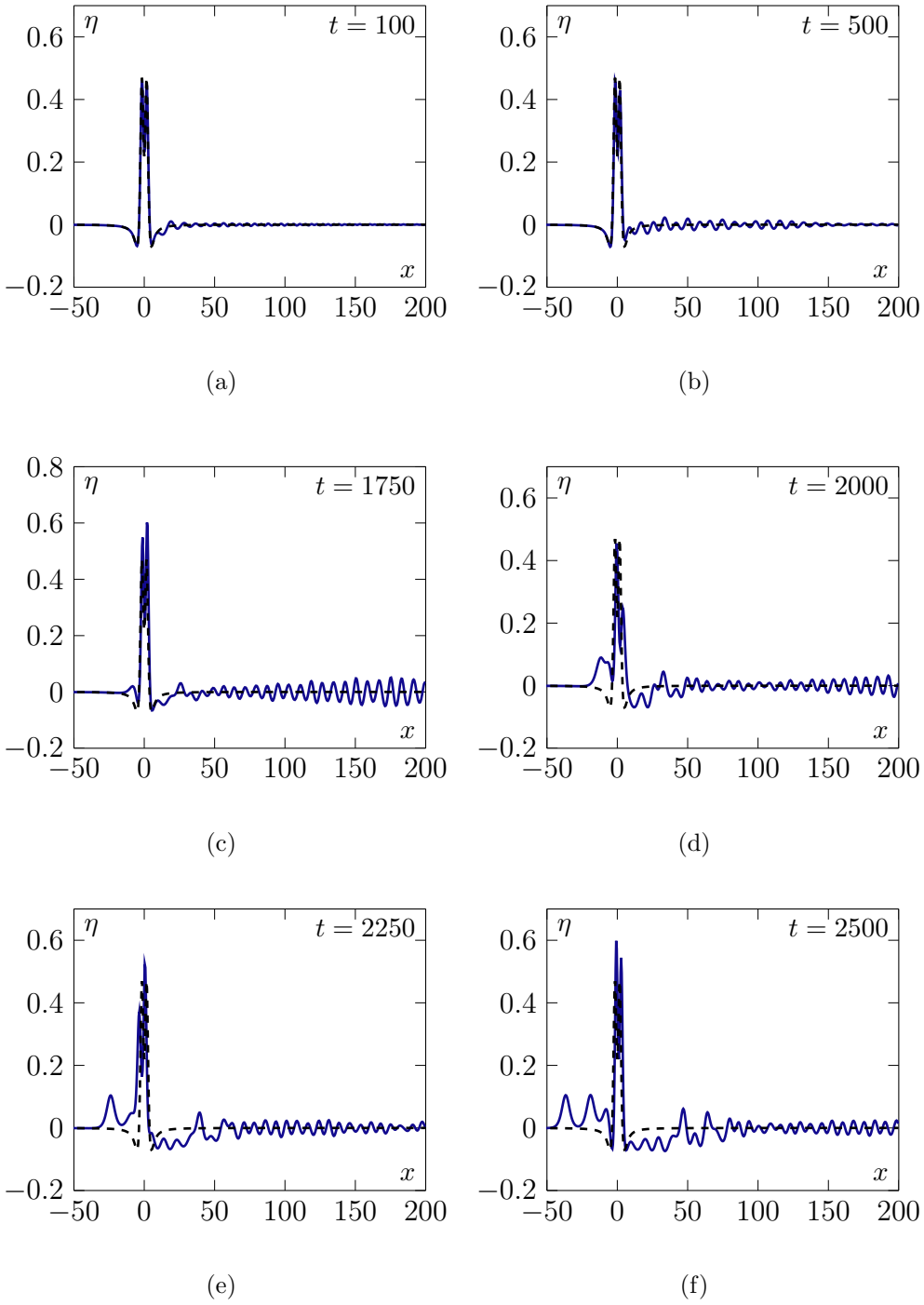

Figure 3.5.8: Numerical simulation of equation (2.4.35) with Gaussian forcing for $\alpha = 333.3$, $(a = -0.2, b = 0.3)$ with $L = 400$ and $N = 4096$ (note not all of the domain is displayed). The initial condition is $\eta(0,t) = 1.025\eta_s$, where η_s is the type unique II solution at this α (see panel 3.2.2(d). Panels (a-d) show the solution over a portion of the domain at times $t = 100$, $t = 500$, $t = 1000$, 1100 and 1500. Panel (f) shows W respectively against time. The dotted curve is the steady solution η_s.

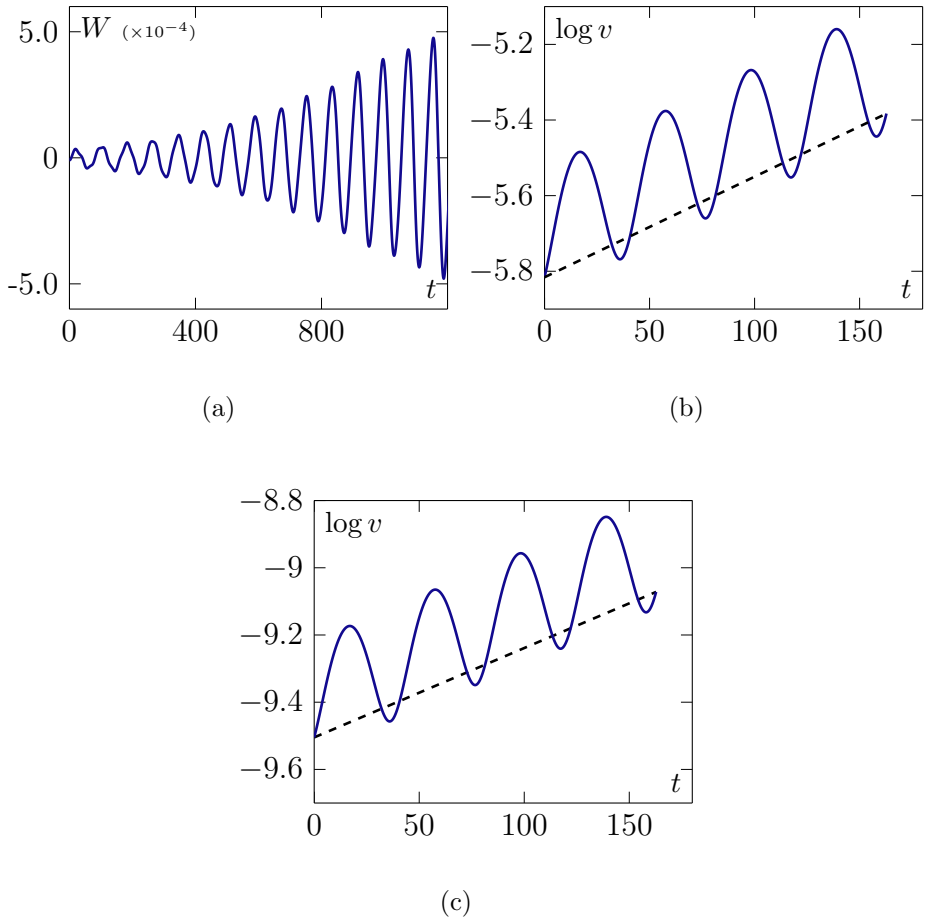

Figure 3.5.9: Time-dependent signals of type IIa solution. Panel (a) shows W respectively against time. (b) (linear operator) - (c) (nonlinear operator). Evolution of the quantity $\log v$ (solid lines) for $0 \leq t \leq 4\pi/\Im(s)$ of the linearised equation (3.5.2) and equation (2.4.35) with Gaussian forcing. $\alpha = 333.3$, $(a = -0.2, b = 0.3)$ with $L = 400$ and $N = 4096$. For the linearised equations the initial condition is $\zeta(x,0) = \frac{1}{2}(g_k + g_k^*)$ where g_k is the unstable eigenmode, and for the nonlinear equations $\eta(x,0) = \eta_s + 0.0125(g_k + g_k^*)$. The dotted line in the figures has slope $\Re(s)$, where s is the most unstable eigenvalue.

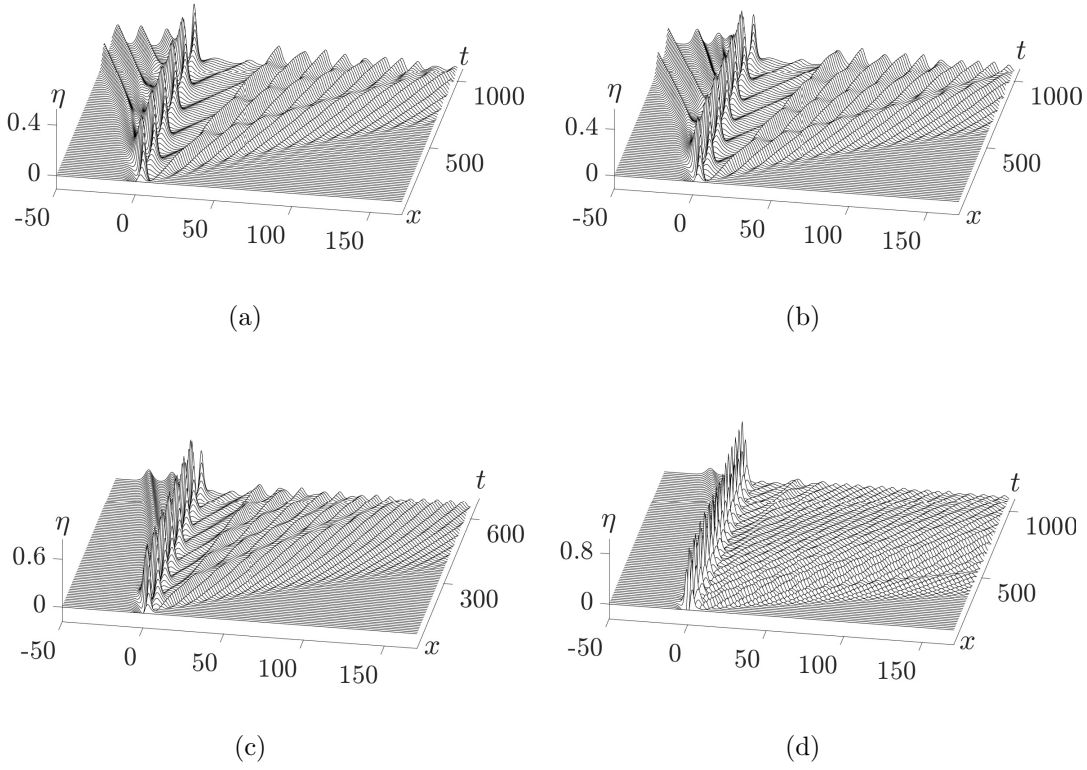

Figure 3.5.10: Time-dependent simulations from a flat initial condition. (a) $\alpha = 40$. (b) $\alpha = 50$. (c) $\alpha = 141$. (d) $\alpha = 226$

the latter case, for a given obstacle, solitary waves of the same height are emitted periodically upstream, and their excess mass is balanced by a depression region of uniform depth (termed an undular bore by some authors) downstream of the obstacle (see the supplementary material for example simulations). The preceding observations are in line with the results obtained by Wu (1987), Camassa & Wu (1991), Grimshaw & Smyth (1986), Grimshaw *et al.* (2007) and Grimshaw (2010).

Inversely found topography

Binder *et al.* (2014) demonstrated non-uniqueness of solution of the steady fKdV equation at $F = 1$ for various topographies using an inverse method. In this section the flow with a Gaussian free-surface,

$$\eta_s = Ae^{-B^2x^2}, \tag{3.5.15}$$

for constants $A > 0$ and B is investigated. The topography corresponding to this solution is found explicitly by substituting (3.5.15) into the steady form of the fKdV equation (2.1.41), and is found to be

$$\sigma(x) = \frac{2}{3}Ae^{-B^2x^2}\Big[B^2(1-2B^2x^2) - \frac{9}{4}Ae^{-B^2x^2}\Big], \tag{3.5.16}$$

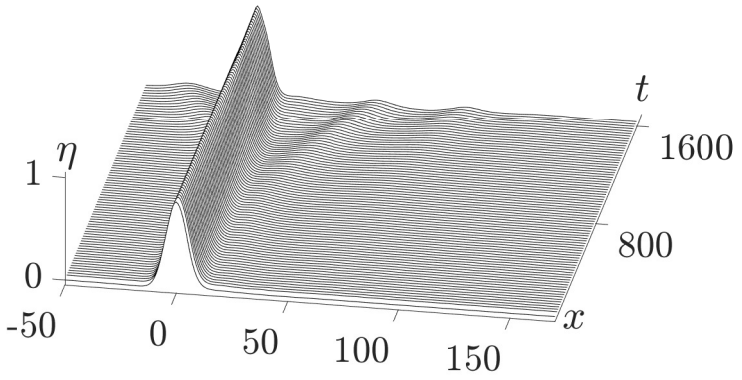

(a)

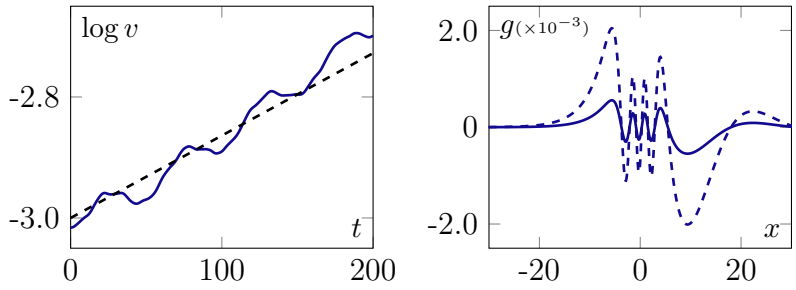

(b) (c)

Figure 3.5.11: Stability of the elevation solution (3.5.15) with $B = 0.3$, $A = 0.84$ with initial condition $\eta(x,0) = \eta_s + \varepsilon(g_k + g_k^*)$. Panel (b) shows the initial growth of the quantity $\log v$ (solid line) as compared with the growth rate corresponding to the unstable eigenvalue (slope of dotted line). Panel (c) shows the real (solid line) and imaginary (dotted line) parts of the unstable eigenfunction near $x = 0$.

Note that σ is either negative-definite, or else is not single-signed depending on the values of A and B. (Note also that this cannot be put in the form of (3.1.4).) Binder *et al.* (2014) showed using a numerical method that a second steady solution coexists with (3.5.15). For $A > 0$, η_s in (3.5.15) is positive-definite and the second steady solution is found to be negative definite. (The possibility of further solutions such as those discussed at length for a Gaussian topography in chapter 5 are not addressed here.) According to the analysis of section 2.4.2, the negative-definite steady solution is linearly stable. This result is confirmed numerically by carrying out time-dependent simulations using as initial condition a small perturbation from the second steady solution (details are not given here).

Next the stability of the positive-definite solution (3.5.15) is discussed. Through a straightforward modification of the argument given in the appendix of Bargmann (1949), it can be shown that the kernel of the $\mathcal{K}$ operator cannot contain an eigenfunction in $L_2(-\infty,\infty)$, so that $\nu = 0$ is not an eigenvalue of $\mathcal{K}$, provided that the

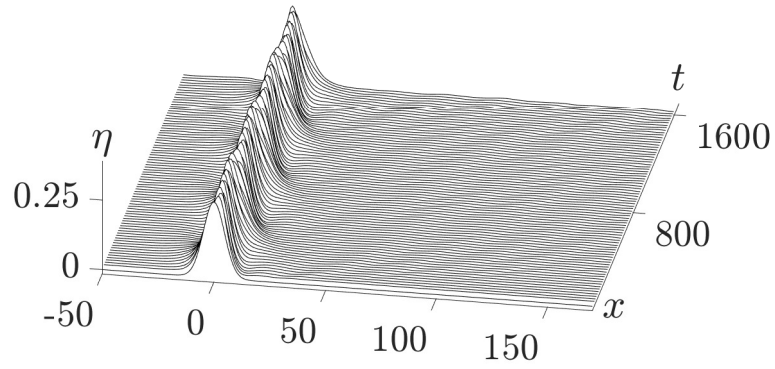

(a)

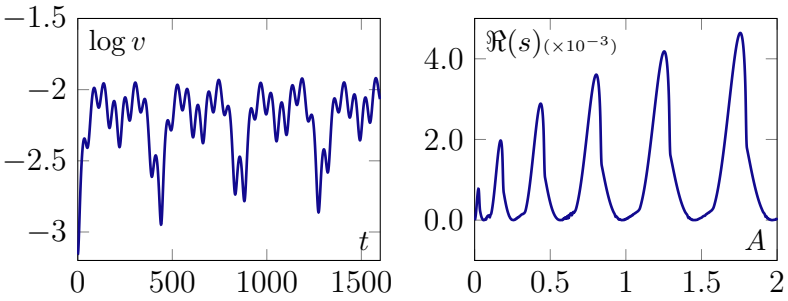

(b) (c)

Figure 3.5.12: Stability of the elevation solution (3.5.15) with $B = 0.3$, $A = 0.26$. Panel (c) shows the real (solid line) and imaginary (dotted line) parts of the unstable eigenfunction near $x = 0$. (a) $A = 0.26$ with initial condition $\eta(x, 0) = (1 + \varepsilon)\eta_s$. In both simulations the computational domain length is $x \in [-100, 300]$ (not all of the domain is displayed) with $N = 512$ and $\varepsilon = 0.025$. Panel (b) shows the initial growth of the quantity $\log v$ (solid line) as compared with the growth rate corresponding to the unstable eigenvalue (slope of dotted line). Panel (f) shows the real part of the leading eigenvalue, s as A varies.

condition $\int_{-\infty}^{\infty} |x||\eta_s|\,\mathrm{d}x < \infty$ holds, which it does in the case of (3.5.15) (note, however, that this condition is violated for the type I, II, IIa,b,... steady solutions since these decay like $1/x^2$ in the far-field). Unfortunately the formal stability analysis of section 2.4.2 is inconclusive in this case since the $\mathcal{K}$ operator always has at least one negative eigenvalue for any $A > 0$ or B. The latter is easy to prove by first writing the eigenvalue problem in variational form and then using the Rayleigh-Ritz method; this is a textbook exercise for demonstrating the existence of bound states for Schrödinger operators in quantum mechanics (e.g. Shankar, 2012, p. 163). For these proofs see appendix B. To determine stability the spectrum of the $\mathcal{M}$ operator is computed using a spectral method as described above for the Gaussian topography in section 3.5.1. Once again careful checks were undertaken to ensure numerical convergence of the eigenvalues in the point spectrum (as for the Gaussian topography the continuous spectrum lies on the imaginary axis.) The stability of the elevation solution is found to depend on A. In contrast to the findings for the type II and IIa solutions for the Gaussian topography, any unstable eigenvalues in the point spectrum are found to be purely real. The corresponding unstable eigenfunctions are strongly localised in space (see for example figure 3.5.11c) and so only a moderate domain size L is required for numerical convergence (contrast figures 3.5.1 and 3.5.2 and tables 3.2 and 3.3). In general the spectrum contains an unstable real eigenvalue in the right half-plane. However, for some special values of A, the free surface is neutrally stable and the $\mathcal{M}$ spectrum is purely imaginary (see figure 3.5.12(c); at $A = 0.26$, for example, there are no unstable eigenvalues).

The results of time-dependent simulations for the unstable case $A = 0.84$ (figure 3.5.11)and the neutrally stable case $A = 0.26$ (figure 3.5.12). The initial condition for $A = 0.84$ was taken to be the steady solution with the perturbation $\hat{\zeta} = \frac{1}{2}\varepsilon(g_k + g_k^*)$ where $g_k(x)$ is the unstable eigenfunction and $\varepsilon = 0.025$. Here the growth in the value of $\log v$ is seen to be in line with the predicted growth rate from the eigenvalue calculation, which is illustrated with a broken line (see figure 3.5.11(b). For the case $A = 0.26$, the initial condition was taken to be the steady solution perturbed by $\hat{\zeta} = \varepsilon\eta_s$. In this case the quantity $\log v$ appears to be bounded (see figure 3.5.12(b). The behaviour observed in simulations started from the flat state $\eta(x, 0) = 0$ is similar to that discussed above in section 3.5.3 with soliton-like waves emitted upstream and a wave train developing downstream of a non-uniform depression region.

Chapter 4

Critical Flow over an Algebraically Decaying Dip

In this chapter steady solutions over an algebraically decaying dip are examined at critical Froude number. When attempting to construct asymptotic solutions to the steady type I,II solutions etc. of chapter 3 it was noted that if a topography of the form $f(\xi) = (1+\xi^2)^{-1}$ is chosen the asymptotic expansion satisfies the boundary conditions at all orders, a property that was not present in the analysis of the Gaussian forcing. However, numerical calculations for this so-called 'Witch of Agnesi' forcing, using a method similar to chapter 3, result in spurious features, including rapidly oscillating behaviour in the profile far upstream and downstream. A careful numerical parameter study to recreate the solution space also displays features that lead to the conclusion that numerical calculations cannot be trusted. The situation is actually a lot more subtle and the issue of existence of asymptotic solutions is discussed in this chapter.

4.1 The Witch of Agnesi

The steady form of the fKdV equation and boundary conditions when $F = 1$ is restated for convenience, namely

$$\delta u'' + u^2 = f(\xi); \qquad u, u_\xi \to 0, \text{ as } |\xi| \to \infty \tag{4.1.1}$$

In chapter 3 it was found that the solution u decays exponentially in a region of $\xi \sim O(1)$ due to the Gaussian forcing decaying exponentially. To facilitate a transition to algebraic decay in the far-field an internal boundary had to be introduced. However, if a topography is chosen to decay algebraically in the far-field, naively it might be expected that asymptotic solutions do not require this internal boundary layer and are easier to construct. To further this claim, the so-called 'Witch of Agnesi' forcing is adopted. This is stated as

$$f(\xi) = \frac{1}{1+\xi^2}. \tag{4.1.2}$$

The boundary layer analysis of the previous chapter can be applied analogously here and the same conclusions are found. Namely for small α there is one negative definite solutions and for large α there are three possible solutions. In the Gaussian case one of these solutions was rejected due to a transition layer. In this case the transition region is not required as the outer solution decays algebraically and there is no reason from the boundary layer analysis to reject this solution. This is investigated in more detail here. First, possible behaviour for large ξ is examined.

4.2 Far-field behaviour

The limit when $|\xi| \gg 1$ is examined first. There are three possible balances of terms which in turn are analysed.

(i) $u^2 \sim 1/(1+\xi^2)$ i.e. $u \sim \pm 1/\xi$.

For convenience δ is chosen to be $\delta = 1$ to simplify the analysis. To analyse this case the solution is linearised around the far-field behaviour

$$u \sim \frac{m}{\xi} + p(\xi), \qquad p \ll 1,$$

for $|\xi| \gg 1$ where p is a small perturbation to be determined and $m = \pm 1$. Substituting into 4.1.1 and neglecting p^2 yields

$$p'' + \frac{2mp}{\xi} = \frac{2m}{\xi^3}, \tag{4.2.1}$$

where $m = \pm 1$. A WKBJ approach can show that the leading order solution for $m = 1$ is $O(\xi^{1/4})$ and for $m = -1$ it is $O(1/\xi^2)$. In particular it can be shown that

$$m = 1: \qquad p \sim C_+ \xi^{1/4} \mathrm{e}^{\pm 2\sqrt{2}\mathrm{i}\xi^{1/2}} + O(1/\xi^3) \quad \text{as} \qquad |\xi| \to \infty, \tag{4.2.2}$$

$$m = -1: \qquad p \sim -C_- \xi^{-2} + \cdots + \xi^{1/4} \mathrm{e}^{\pm 2\sqrt{2}\xi^{1/2}} \quad \text{as} \qquad |\xi| \to \infty, \tag{4.2.3}$$

where $C_\pm$ are constants. Therefore the choice of $m = 1$ is rejected as a possibility because solutions are unbounded due to the $\xi^{1/4}$ multiplier of the oscillating exponential term. For $m = -1$ and $\xi > 0$ the negative sign is chosen in the exponent of the exponential so that the exponential decay cancels out the $\xi^{1/4}$ growth. For $m = -1$ and $\xi < 0$ the positive sign is chosen for identical reasons. Therefore the choice of $m = -1$ is accepted and $u \sim -1/\xi$ is permissible behaviour as $|\xi| \to \infty$. Other possibilities are now explored.

(ii) $\delta u'' \sim 1/(1+\xi^2)$

Again $\delta = 1$ for convenience. In this case two integrations of

$$u'' \sim 1/(1+\xi^2)$$

yields

$$u \sim \xi \arctan(\xi) - \frac{1}{2}\log(1+\xi^2) + C\xi + D$$

for constants C and D. As $\xi \to \infty$, $\arctan(\xi) \to \pi/2$ and so $C = -\pi/2$ is chosen to eliminate linear growth. There is no value D can take to eliminate the logarithmic growth and therefore the minimum possible growth is

$$u \sim -\log(\xi).$$

For large ξ, u does not tend to zero and so this behaviour at large ξ must also be rejected.

(iii) $u'' \sim u^2$

In this case

$$u'' + u^2 \sim 0.$$

Multiplying by u' and integrating,

$$\frac{1}{2}u'^2 + \frac{1}{3}u^3 \sim 0,$$

where the constant of integration has been set to zero using the condition that $u \to 0$ as $\xi \to \infty$. Setting $u = -U$ with $U > 0$, it can be shown that

$$U' = \gamma\, U^{3/2}, \qquad \gamma = \sqrt{\frac{2}{3}}.$$

Integrating,

$$-2U^{-1/2} = \gamma(\xi + c) \quad \to \quad U = \frac{6}{(\xi+c)^2} = -u.$$

for constant c. So $u \sim -6/\xi^2$ and $u' \sim 12/\xi^3$ and so $u'/u \sim -2/\xi$ as $\xi \to \infty$. However, if this is the case then $u'' \sim u^2 \sim 36/\xi^4$ and there is nothing to balance the right hand side in (4.1.1). So the dominant balance of terms considered in this case is invalid. This would work, however, if the right hand side were $O(1/\xi^4)$ as $\xi \to \infty$, for example, $1/(1+\xi^4)$.

Given the above discussion, the only large ξ behaviour possible is the balance (i) with $m = -1$ and $u \sim -1/\xi$ as $|\xi| \to \infty$. So the statement of the problem should be modified to

$$\delta u'' + u^2 = \frac{1}{1+\xi^2}, \qquad u \sim -1/\xi, \ \text{ as } |\xi| \to \infty. \tag{4.2.4}$$

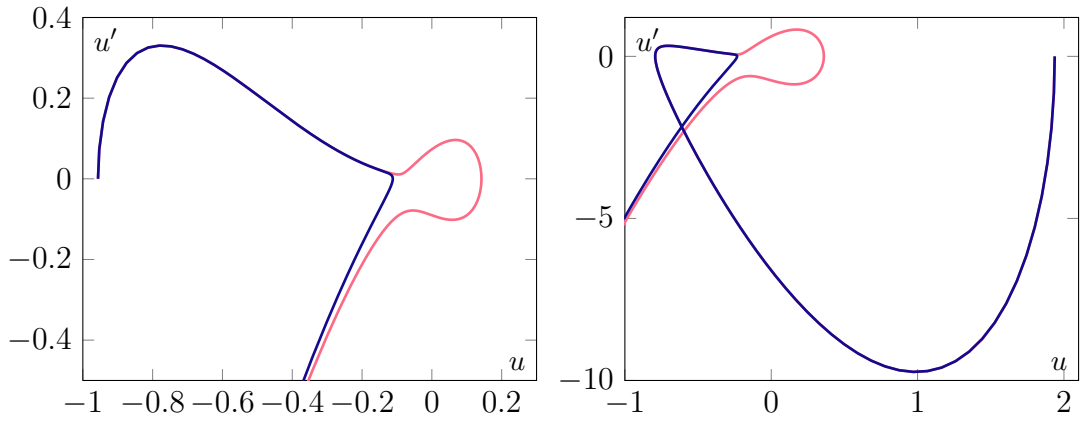

(a) (b)

Figure 4.2.1: Numerical Calculations for the Witch of Agnesi forcing when $\delta = 0.114208$. (a) Trajectories starting near $u(0) \approx -0.956567$. (b) Trajectories starting near $u(0) \approx 1.93689$. These figures demonstrate that there could feasibly exist a value of $u(0)$ such that the trajectory enters the origin in the required way. (a) The lower negative definite solution. (b) The elevated type II solution.

In relation to the boundary layer theory this means that for small δ (large α) there are two solutions; a negative definite solution and an elevation solution in analogy to the solution branches of the Gaussian forcing. Since $u \sim -1/\xi$ and $u' \sim 1/\xi^2$, therefore $u'/u \sim -1/\xi$ as $\xi \to \infty$ and so trajectories in the (u, u') plane must approach the origin from the second quadrant on the parabola $u' = u^2$. However numerical calculations do not display this behaviour. Starting at $\xi = 0$, and specifying $u(0) = a$, where a is constant, and $u_\xi(0) = 0$, Runge-Kutta calculations do not show trajectories entering the origin for any value of a chosen as shown in figure 4.2.1. By appealing to a continuity argument it is reasonable to expect that a trajectory does exist but the correction to the initial condition may be exponentially small and so difficult to find numerically. However the numerics do not rule out the possibility that a solution does not exist. As shown by Chapman *et al.* (2000) the non-existence of solutions to equations can be due to exponentially small terms in an asymptotic expansion of the solution. Therefore the next stage is to construct an asymptotic expansion to (4.2.4) which satisfies the boundary conditions. The analysis of Chapman *et al.* (2000) requires an extension into the complex plane. With this in mind, the independent variable is changed from ξ to z and (4.2.4) is

$$\delta u'' + u^2 = \frac{1}{1+z^2}, \qquad u \sim -1/|z|, \ \text{ as } |z| \to \infty. \tag{4.2.5}$$

In the next section the concepts of optimal truncation of a divergent series are discussed in relation to the equation above.

4.3 Optimal Truncation

The problem is formulated for real z and hence solutions to (4.2.5) are required to be real. Initially a naive expansion of the form

$$u = u_0 + \delta u_1 + \delta^2 u_2 + \cdots \tag{4.3.1}$$

is adopted. After inserting this into (4.2.5) a succession of algebraic equations can be formed at each order:

$$O(1): \qquad u_0^2 = (1+z^2)^{-1}, \tag{4.3.2a}$$

$$O(\delta): \qquad 2u_0u_1 + u_0'' = 0, \tag{4.3.2b}$$

$$O(\delta^2): \qquad 2u_0u_2 + u_1^2 + u_1'' = 0, \tag{4.3.2c}$$

$$\vdots$$

$$O(\delta^n): \qquad u_{n-1}'' + 2u_0u_n + \sum_{k=1}^{n-1} u_k u_{n-k} = 0. \tag{4.3.2d}$$

The first few terms can be calculated as

$$u_0 = -(1+z^2)^{-1/2}, \tag{4.3.3a}$$

$$u_1 = -\frac{1}{2}(2z^2-1)(1+z^2)^{-2}, \tag{4.3.3b}$$

$$u_2 = \frac{5}{8}(-20z^2+4z^4+3)(1+z^2)^{-7/2}. \tag{4.3.3c}$$

The negative sign for the square root is chosen so that the far-field behaviour in (4.2.3) is satisfied. These terms all satisfy the boundary conditions. As stated earlier, by introducing a boundary layer around $\xi = 0$, an additional elevation solution can be discovered. This is exactly analogous to the type II solution of chapter 3. The analysis is easier than for the Gaussian topography because unlike in the Gaussian case the series is uniformly asymptotic for all z and so an internal boundary layer is not required. The problem appears to be solved, however, as will be seen, the issue of consistency is a lot more subtle than first appears and a far deeper analysis is required.

In practice the asymptotic series will be truncated after M terms and the exact solution can be written as

$$u = \sum_{i=0}^{M-1} \delta^i u_i + R_M = u_M + R_M \tag{4.3.4}$$

where R_M is the error term. If the series is truncated after one term, $M = 1$ then the error $\varepsilon_M = |u - u_M|$ is typically large. As more terms are taken then ε_M decreases. For a convergent series $\varepsilon_M \to 0$ as $M \to \infty$ for all z in the radius of convergence. This is not the case in a divergent series as shown in figure 4.3.1. Whilst increasing M will

initially lead to a reduction in the value of ε, eventually as $M \to \infty$, $\varepsilon_M \to \infty$. The value of M where the error, ε_M is the least is called the *optimal truncation* point of the expansion. Typically at this point the error is exponentially small, i.e. $R_M \sim \mathrm{e}^{-1/\delta}$ and 'beyond all orders' of a asymptotic power series (see Boyd, 1999; Segur *et al.*, 1991). In most cases this error term is so small compared to the sum that it can be safely neglected. The value of M for which the error term ceases to decrease is denoted by N. To optimally truncate the value of N needs to be calculated. To do this the late order form of the asymptotic expansion needs to be established, i.e. the form of u_n as $n \to \infty$. Once this has been established the value of N can be found by insisting that successive late-order terms have the same phase and sign (Dingle, 1973). Typically the value of N will depend on z, the independent variable. The issues with this procedure are now discussed.

As mentioned earlier the error term is *usually* exponentially small and can be safely neglected. However, as the independent variable z has been fixed, there could be locations in the complex z plane where additional error terms can become 'switched-on'. The location(s) where this behaviour occurs are called *Stokes' lines*. At these locations the error term R_N *can* cease to be exponentially small and are actually of comparable size to the terms in the asymptotic expansion. These ideas will be expanded upon as the analysis continues.

A brief roadmap of the method (see Chapman *et al.*, 2000) to determine whether this expansion is a valid asymptotic solution to the problem is now presented. The analysis is as follows

1. Find any singularities in the leading order solution
2. Using the fact that the singularities dominate the solution find an expression for late order terms
3. Optimally truncate the asymptotic series (i.e. find when the remainder is smallest)
4. Form an equation for the remainder and solve it, look for Stokes' lines - where the remainder ceases to be exponentially small and get 'switched on'
5. Review this solution in light of the boundary conditions

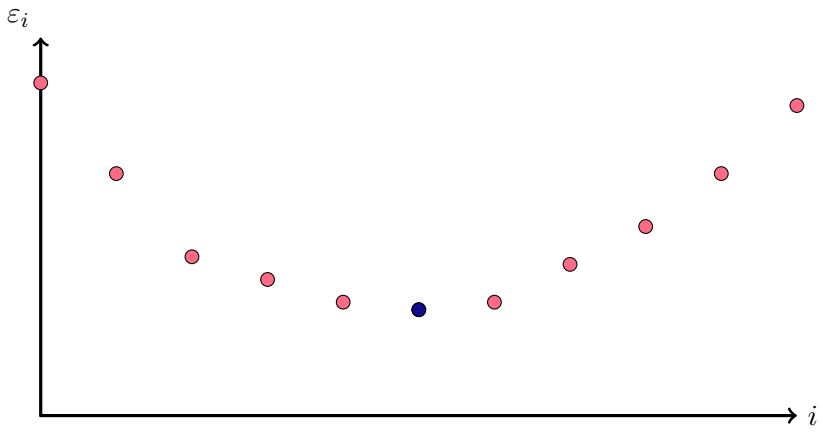

Figure 4.3.1: Optimal Truncation of a asymptotic Series. Eventually the error stops decreasing and starts increasing as more terms are added. The truncation at smallest error is called *optimal truncation* and is denoted by the blue circle.

4.4 Late order Form

An example of divergence is when the expansion is of a 'factorial/power' type. This means that the terms are of order $u_n \sim n!/z^n$. This typically occurs when the leading order term is a rational function of z (for example, $u_0 = z^{-1}$) and the generation of successive terms involves differentiation (for example, $u_{i+1} = u_i'$) (Berry, 1988; Dingle, 1973). The form of (4.3.3) suggests that this criteria is satisfied and it is expected that the terms in (4.3.3) will diverge in a 'factorial/power' manner. This is a consequence of Darboux's theorem (see, for example Segur *et al.*, 1991; Trinh & Chapman, 2015). With this discussion in mind an ansatz for the late order terms of (4.3.2) of the form

$$u_n \sim \frac{\Lambda\Gamma(2n+\gamma+1)}{\phi^{2n+\beta}} \tag{4.4.1}$$

is chosen where the unknowns ϕ, β and γ depend on z but not n. The constant Λ is called the Stokes' multiplier and will be calculated last. The initial goal is to calculate ϕ, β and γ. To achieve this, (4.4.1) is substituted into the recursion relation (4.3.2d), which is repeated here for convenience

$$u_{n-1}'' + 2u_0u_n + \sum_{k=1}^{n-1} u_k u_{n-k} = 0. \tag{4.4.2}$$

The calculations are performed carefully in the limit $n \to \infty$. First the second derivative term; u_{n-1}'' in (4.4.2) is calculated. It can be shown that the leading order term of u_{n-1}'' is $O(n^2)$ as $n \to \infty$ and can be written as

$$u_{n-1}'' \sim \frac{4\Lambda\Gamma(2n+\gamma-1)\phi'^2 n^2}{\phi^{2n+\beta}}. \tag{4.4.3}$$

Primes indicate differentiation with respect to z. By noting from the definition of the Gamma function that $z\Gamma(z) = \Gamma(z+1)$ the leading order term of the $2u_0u_n$ term in (4.4.2) is also $O(n^2)$ and can be written as

$$2u_0u_n \sim \frac{8\Lambda\Gamma(2n+\gamma-1)u_0n^2}{\phi^{2n+\beta}}. \tag{4.4.4}$$

The balance of (4.4.3) and (4.4.4) in (4.4.2) yields an ODE for ϕ;

$$\phi'^2 \sim -2u_0, \tag{4.4.5}$$

as $n \to \infty$. An expression for ϕ in terms of the leading order solution u_0 can be obtained as

$$\phi \sim -\sqrt{2}\int_{\nu}^{z}(1+p^2)^{-1/4}\,\mathrm{d}p \tag{4.4.6}$$

where ν is a point in the complex z plane that is to be determined. Let τ be a singularity of u_0. The terms in the asymptotic expansion will be dominated by behaviour in the vicinity of the singularity. Therefore it is necessary to perform a local analysis around the singularity of the leading order solution $z = \mathrm{i}$. Furthermore looking at the form of (4.4.1) it is clear that around the singularity $u_n = 0$, and for these reasons $\nu = \pm\mathrm{i}$ is the correct choice and hence

$$\phi \sim -\sqrt{2}\int_{\pm\mathrm{i}}^{z}(1+p^2)^{-1/4}\,\mathrm{d}p. \tag{4.4.7}$$

To find the function γ the first order balance in (4.4.2) is examined. It can be shown that the first order terms of (4.4.2) are $O(n\log n)$ and they only originate from the second derivative term. This comes from noting that

$$\Gamma'(2n+\gamma+1) = \Gamma(2n+\gamma+1)\Phi(2n+\gamma+1) \sim \Gamma(2n+\gamma+1)\log n,$$

as $n \to \infty$ where Φ is the digamma function (see, for example Abramowitz & Stegun, 1964). This balance can be written as

$$\frac{-4\Lambda\Gamma(2n+\gamma-1)\frac{\phi'}{\phi}\gamma' n\log n}{\phi^{2n+\beta-2}} \sim 0.$$

As γ is independent of n,

$$\gamma' = 0$$

and γ is therefore constant. Finally the second order balance in (4.4.2) is required so that β can be found. It can be shown that the second order balance is $O(n)$ and there are contributions at this order from the u''_{n-1} and $-2u_0u_n$ terms. This balance can be

written as

$$\frac{\Lambda\Gamma(2n+\gamma-1)n}{\phi^{2n+\beta}}\left(4\beta\left(\frac{\phi'^2}{\phi^2}\right)-2\left(\frac{\phi'}{\phi}\right)'+4\left(\frac{\phi'}{\phi}\right)\beta'\log\phi+\frac{2(4\gamma+6)u_0}{\phi^2}\right)\sim 0.$$

This is an ODE for β which can be written as

$$\beta'+\beta\left(\frac{1}{\log\phi}\frac{\phi'}{\phi}\right)\sim\frac{1}{2}\frac{(\phi'/\phi)'}{(\phi'/\phi)\log\phi}-\frac{1}{2}\frac{(4\gamma+6)u_0\phi}{\phi^2\phi'\log\phi}. \tag{4.4.8}$$

The integrating factor can be shown to be $\log\phi$ and hence equation (4.4.8) becomes

$$(\beta\log\phi)'\sim\frac{1}{2}\frac{(\phi'/\phi)'}{(\phi'/\phi)}-\frac{1}{2}\frac{(4\gamma+6)u_0}{\phi\phi'}.$$

But $u_0=-\frac{1}{2}\phi'^2$ and so

$$(\beta\log\phi)'\sim\frac{1}{2}\frac{(\phi'/\phi)'}{(\phi'/\phi)}-\frac{1}{2}\frac{(2\gamma+3)\phi'}{\phi}.$$

Solving gives

$$\beta\sim\gamma+1+\frac{1}{2}\frac{\log\phi'}{\log\phi}+\frac{C}{\log\phi}, \tag{4.4.9}$$

where C is a constant of integration. To determine C it is noted that when (4.4.9) is substituted in (4.4.1) the term involving C can be written as

$$\phi^{C/\log\phi}=(\mathrm{e}^{\log\phi})^{C/\log\phi}=\mathrm{e}^{C},$$

which is constant. Hence the value of C can be incorporated into the pre multiplier Λ and can be set $C=0$ without loss of generality. At this point β can be found in terms of γ (which is a constant). The constant β is now found. This is independent of z and so an examination of the behaviour near $z=\mathrm{i}$ will reveal the constant. The first few terms of u_i given in (4.3.3) around the singularity at $z=\mathrm{i}$ are given by

$$\begin{aligned}u_0&=-(2\mathrm{i})^{-1/2}(z-\mathrm{i})^{-1/2}\\ u_1&=\frac{3}{2}(2\mathrm{i})^{-2}(z-\mathrm{i})^{-2}\\ u_2&=-\frac{95}{8}(2\mathrm{i})^{-7/2}(z-\mathrm{i})^{-7/2}.\end{aligned} \tag{4.4.10}$$

It is clear that if the u_n has a singularity of strength ρ_n, then u_{n+1} will have a singularity of strength $\rho_{n+1}-\frac{3}{2}$. Therefore the strength of the singularity of u_n is

$$\rho_n=-\frac{3}{2}n-1/2. \tag{4.4.11}$$

Additionally as $z \to \mathrm{i}$ it can be shown that a local expansion of ϕ as stated in (4.4.7) can be stated as

$$\phi = \frac{\mathrm{i}^{7/4}2^{9/4}}{3}(z-\mathrm{i})^{3/4}, \tag{4.4.12}$$

and hence an alternative expression for the strength of the singularity using (4.4.1) is

$$\rho_n = -\frac{3}{4}(2n+\beta). \tag{4.4.13}$$

Equating (4.4.11) and (4.4.13) yields

$$\beta = \frac{2}{3}.$$

Now to find γ the third term on the right hand side of (4.4.9) needs to be calculated. Using the form (4.4.12) means that

$$\frac{\log\phi'}{\log\phi} \sim -\frac{1}{3},$$

as $z \to \mathrm{i}$. Hence the expression in (4.4.9) becomes

$$\beta \sim \gamma + \frac{5}{6},$$

and hence

$$\gamma = -\frac{1}{6}.$$

All that remains is to now find the value of Λ, the Stokes' multiplier. Using (4.4.10) it can be seen that in the neighbourhood of $z = \mathrm{i}$ the n^{th} term of u_n can be written in the form

$$u_n \sim (-1)^{n-1}B_n\left[\mathrm{i}(z-\mathrm{i})\right]^{-\frac{3}{2}n-\frac{1}{2}}, \tag{4.4.14}$$

where B_n is to be determined. Inserting this into (4.3.2d) gives a recursion relation for B_n in the form

$$\begin{aligned} B_n &= \frac{3n(3n-2)B_{n-1}}{2^{5/2}} - 2^{-\frac{1}{2}}\sum_{k=1}^{n-1} B_k B_{n-k}, \\ B_0 &= -2^{-1/2}. \end{aligned} \tag{4.4.15}$$

To proceed it is noted that the late-order form of u_n near $z = \mathrm{i}$ has been established in (4.4.12). Inserting $\beta = \frac{2}{3}, \gamma = -\frac{1}{6}$ and the expression for ϕ, (4.4.12), into

$$u_n = \frac{\Lambda\Gamma(2n+\gamma+1)}{\phi^{2n+\beta}} \tag{4.4.16}$$

gives

$$u_n \sim \frac{\Lambda\Gamma(2n+5/6)2^{-\frac{9}{2}n-\frac{3}{2}}3^{2n+\frac{2}{3}}}{\mathrm{i}^{\frac{7}{2}n+\frac{7}{6}}(z-\mathrm{i})^{\frac{3}{2}n+\frac{1}{2}}}. \tag{4.4.17}$$

Comparing (4.4.17) with (4.4.14) (in the limit, $n \to \infty$) means the Stokes' Multiplier can be evaluated as

$$\Lambda = \frac{2^{3/2}}{3^{2/3}} \lim_{n\to\infty} \left(\frac{B_n 2^{n/2}}{\Gamma(2n+5/6)} \left(\frac{4}{3}\right)^{2n} \right) = \lim_{n\to\infty} \Lambda_n, \tag{4.4.18}$$

The value of Λ can be calculated exactly. As $n \to \infty$ the sum in (4.4.15) is small compared to the linear term. Hence the recursion relation becomes

$$B_n \sim \frac{3}{2^{5/2}} n(3n-2) B_{n-1}, \tag{4.4.19}$$

as $n \to \infty$. This has an exact solution in the form

$$B_n \sim \frac{B_0 3^{2n} n! \Gamma\left(n+\frac{1}{3}\right)}{2^{\frac{5}{2}n} \Gamma\left(\frac{1}{3}\right)}. \tag{4.4.20}$$

Applying Stirling's formula (see, for example Abramowitz & Stegun, 1964) for large n means (4.4.20) can be approximated as

$$B_n \sim \frac{2^{-\frac{5}{2}n+1} 3^{2n} \pi n^{1/3} n^{2n} \mathrm{e}^{-2n} B_0}{\Gamma\left(\frac{1}{3}\right)}. \tag{4.4.21}$$

By applying Stirling's formula again for the Γ function in the denominator of (4.4.18) and then substituting (4.4.21) into (4.4.18) yields an exact value for Λ, i.e.

$$\Lambda = -\frac{2^{7/6}\pi^{1/2}}{3^{2/3}\Gamma\left(\frac{1}{3}\right)} \approx -0.7140572. \tag{4.4.22}$$

Note that this approach applies to other examples where a Stokes' multiplier has to be calculated and is a novel alternative to the numerical approach demonstrated in Chapman *et al.* (2000) for other nonlinear ODE's. Nevertheless this exact value was checked by calculating the value of Λ numerically (by a method similar to Chapman *et al.*, 2000) using (4.4.18) and (4.4.15). The convergence of the expression in brackets in (4.4.18) to the exact value in (4.4.22) as n increases is shown in figure 4.4.1. To summarise this means that the expression in (4.4.1) has been fully determined. The values of β, γ, ϕ and Λ have all been explicitly calculated. The location of the Stokes' lines forms the topic of discussion in the next section.

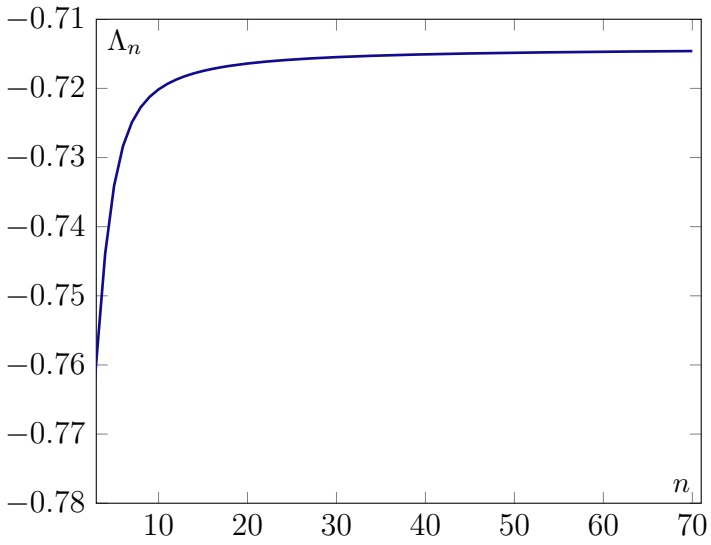

Figure 4.4.1: Convergence of Λ_n in (4.4.18) to Λ as n increases

4.5 Locating the Stokes' lines

There are two equivalent approaches to locating the Stokes' lines. Dingle (1973) states that Stokes' lines appear when successive late order terms have the same phase. Using this approach and equating the phases of successive late-order terms means that

$$\arg\left(\frac{u_{n+1}}{u_n}\right) = 2k\pi, \tag{4.5.1}$$

where arg represents the complex argument. Substituting (4.4.1) into (4.5.1) means that Stokes' lines will appear whenever

$$\arg\left(\frac{1}{\phi^2}\right) = 2k\pi,$$

for $k \in \mathbb{Z}$, which is equivalent to

$$\arg(\phi) = k\pi. \tag{4.5.2}$$

The other method of finding the location of the Stokes' lines is to insist that the *singulant*, in this case ϕ, has zero imaginary part, i.e.

$$\Im(\phi) = 0, \tag{4.5.3}$$

(see, for example Heading, 1962; Segur *et al.*, 1991). Note that the conditions in (4.5.2) and (4.5.3) are equivalent. As ϕ has poles around $z = \pm\mathrm{i}$ then it is expected that Stokes' lines originate from them (Heading, 1962). To find out the direction of the Stokes' lines in the vicinity of a singularity a local expansion for ϕ is required. The local expansion around $z = \mathrm{i}$ has already been stated in (4.4.12). Writing $z - \mathrm{i} = R\mathrm{e}^{i\psi}$ and $\phi = r\mathrm{e}^{\mathrm{i}\theta}$

and substituting them into (4.4.12) yields

$$re^{i\theta} = \frac{e^{7\pi i/8}2^{9/4}}{3}R^{3/4}e^{3\psi i/4}.$$

Using the condition in (4.5.2), by requiring $\theta = k\pi$, means

$$\frac{3\psi}{4} + \frac{7\pi}{8} = k\pi. \tag{4.5.4}$$

This gives Stokes' lines at $\psi = -\frac{7\pi}{6}, \frac{\pi}{6}, \frac{3\pi}{2}, \cdots$. A branch cut needs to be defined that is consistent with taking the negative sign of (4.4.6). There are two branch points at $z = \pm i$ and as the problem is posed on the real line the branch cut cannot cross the real axis. Additionally the problem is symmetric in z and hence the branch-cut is defined going up the imaginary axis from $z = i$ and down the imaginary axis from $z = -i$ (as shown in figure 4.5.1). Locally $-\frac{3\pi}{2} \leq \psi < \frac{\pi}{2}$ and hence the directions of the Stokes' lines about $z = i$ are

$$\psi = -\frac{7\pi}{6}, \ \frac{\pi}{6}.$$

For the singularity at $z = -i$ the local direction of the Stokes' lines can be calculated in a similar way and are found to be

$$\psi = \frac{5\pi}{6}, \ -\frac{\pi}{6}.$$

This analysis is a local one and only gives the initial direction of the Stokes' line as it leaves the singularity. The lines are not guaranteed to continue in a straight line. To investigate this, for large z, ϕ is asymptotic to

$$\phi' \sim -\sqrt{2}z^{-1/2}.$$

Integrating with respect to z gives

$$\phi \sim -\sqrt{2}z^{1/2} + \sqrt{2}(1+i),$$

where the condition that $\phi = 0$ at the singularity at $z = i$ is used to determine the constant of integration. Using the Binomial theorem, writing $z = x + iy$ and assuming $y \ll x$ gives

$$\phi \sim -2\sqrt{2}\left(x^{1/2} + i\frac{y}{2x^{1/2}} + \cdots\right) + \sqrt{2}(1+i).$$

Therefore for large z, the imaginary part of ϕ vanishes when

$$y \sim x^{1/2},$$

and hence the Stokes' lines are curved as $z \to \infty$. This behaviour is shown in figure 4.5.1. Note that if $x \ll y$ or $x = y$ then ϕ cannot become purely real. The problem

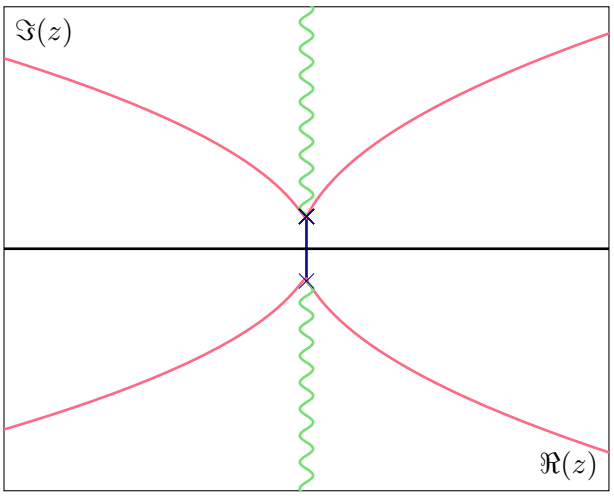

Figure 4.5.1: (a) Global behaviour of the Stokes' lines in the complex plane. The branch cut is given by curly green lines. The red curves are for the case of the negative sign in the leading order solution and the blue line is for the positive sign.

is posed on the real line and as such only Stokes' lines that cross the real axis can potentially affect the 'switching on' of remainder terms.

Additionally if the positive sign was taken in the leading order solution the equation to determine the local arguments of the Stokes' lines becomes

$$\frac{3\psi}{4} + \frac{11\pi}{8} = k\pi. \tag{4.5.5}$$

Defining the branch cut in the same way as before means that there is a single Stokes' line going down the imaginary axis from $z = \mathrm{i}$. Therefore in the case of choosing the positive sign the Stokes' line crosses the real axis and it would be expected that exponentially small terms get 'switched on' which mean that the original expansion (4.3.1) will break down. This strongly suggests that there is no solution of this form. This corroborates the earlier conclusion in (4.2.2) that as $\xi \to \infty$ the far-field behaviour must take the form of (4.2.3) and not (4.2.2). This can be demonstrated analytically as follows. The asymptotic expansion is to be truncated optimally. Therefore the solution is written as

$$u = \sum_{i=0}^{N} \delta^i u_n + R_N, \tag{4.5.6}$$

where R_N is the remainder term that depends on z. The aim is to calculate the value of N such that the remainder is exponentially small. Substituting this into the original ODE, (4.2.5) gives

$$\delta R_N'' + 2R_N u_0 \sim -\delta^N u_{N-1}''. \tag{4.5.7}$$

By taking advantage of the recurrence relation in (4.3.2d) and neglecting terms of $O(R_N^2)$ means that (4.5.7) can be written as

$$\frac{\delta}{(\phi')^2} R_N'' - R_N \sim \delta^N u_N. \tag{4.5.8}$$

The homogeneous form of this equation can be solved by the WKBJ method and hence solutions to (4.5.8) are sought that take the form

$$R_N \sim \frac{A(z)\mathrm{e}^{\pm\phi/\delta^{1/2}}}{(\phi')1/2}, \tag{4.5.9}$$

where $A(z)$ is to be determined. To ensure that the remainder is small as $|z| \to \infty$ the choice of the plus sign is rejected in (4.5.9). It can be shown that substituting (4.5.9) into (4.5.8) yields the following ODE for $A(z)$

$$\frac{-2\delta^{1/2}}{(\phi')^{3/2}}\mathrm{e}^{-\phi/\delta^{1/2}}\frac{\mathrm{d}A}{\mathrm{d}z} \sim \delta^N u_N. \tag{4.5.10}$$

To find N, as mentioned previously, it is required that late-order terms have the same magnitude, i.e.

$$\left|\delta\frac{u_{N+1}}{u_N}\right| \sim 1. \tag{4.5.11}$$

By writing $z - \mathrm{i} = R\mathrm{e}^{\mathrm{i}\psi}$ as before and taking the limit as $N \to \infty$ (with δ fixed) means that

$$N \sim \frac{\hat{c}R^{3/4}}{2\delta^{1/2}}, \tag{4.5.12}$$

where $\hat{c} = \frac{\mathrm{i}^{7/4}2^{9/4}}{3}$. The analysis can be simplified if the independent variable is changed from z to ϕ. Writing $\phi = r\mathrm{e}^{\mathrm{i}\theta}$ means that the optimal truncation will occur when

$$N \sim \frac{r}{2\delta}. \tag{4.5.13}$$

This may not be an integer. Writing

$$N = \frac{r}{2\delta} + \alpha, \tag{4.5.14}$$

where α is a small correction ensures that N is an integer. Now using the chain rule to change the independent variable from z to ϕ means that (4.5.10) can be written as

$$\frac{-2\delta^{1/2}}{(\phi')^{1/2}}\mathrm{e}^{-\phi/\delta^{1/2}}\frac{\mathrm{d}A}{\mathrm{d}\phi} \sim \delta^N u_N. \tag{4.5.15}$$

By substituting $\phi = r\mathrm{e}^{\mathrm{i}\theta}$ and (4.5.14) into (4.5.15), it can be shown using Stirling's formula that

$$-\frac{2\delta^{1/2}\mathrm{i}}{r}\exp(-r\mathrm{e}^{\mathrm{i}\theta}/\delta^{1/2})\frac{\mathrm{d}A}{\mathrm{d}\theta} \sim \frac{\Lambda\sqrt{2\pi}}{r^{1/2}\delta^{1/2(\gamma+1/2)}}\exp\left(-\mathrm{i}\theta\left(r/\delta^{1/2} + 2\alpha + \gamma\right) - r/\delta^{1/2}\right). \tag{4.5.16}$$

Note that the right hand side is exponentially small, and hence $A(z)$ is also exponentially small unless $\theta = 0$ when it is algebraic in r. This corresponds to the Stokes'

line going down the imaginary axis from $z = \mathrm{i}$ and confirms the previous analysis for the location of the Stokes' lines. The Stokes' multiplier does not get discontinuously 'switched on'. As shown by Berry (1988) there is actually a small layer around the Stokes' line where the term gets continuously 'switched on'. To examine an inner region is constructed by writing $\theta = \epsilon\hat{\theta}$. It can be shown that as $|\alpha| \ll 1$ and by using a Taylor expansion for $\mathrm{e}^{\mathrm{i}\theta}$ (4.5.16) becomes

$$-\frac{2\delta^{1/2}\mathrm{i}}{\epsilon r}\frac{\mathrm{d}A}{\mathrm{d}\theta} \sim \frac{\Lambda\sqrt{2\pi}}{r^{1/2}\delta^{1/2(\gamma+1/2)}}\mathrm{e}^{-\frac{1}{2}r\hat{\theta}^2\epsilon^2/\delta^{1/2}}. \tag{4.5.17}$$

Taking the distinguished limit as $\epsilon \sim \delta^{1/4}$ and scaling $A = \delta^{-\frac{1}{2}(\gamma+1)}\hat{A}$ gives

$$\frac{\mathrm{d}\hat{A}}{\mathrm{d}\hat{\theta}} \sim \frac{\mathrm{i}r^{1/2}\Lambda\sqrt{2\pi}}{2}\mathrm{e}^{-r\hat{\theta}^2/2}. \tag{4.5.18}$$

Solving this equation gives

$$\hat{A} \sim a + \frac{\mathrm{i}\Lambda\sqrt{2\pi}}{2}\int_{-\infty}^{\hat{\theta}r^{1/2}} \mathrm{e}^{-t^2/2}\,\mathrm{d}t, \tag{4.5.19}$$

where a is a constant. Thus the Stokes' multiplier gets switched on smoothly in the inner region by an error function. Matching with the outer region means that

$$\hat{A} \to a, \qquad \text{as} \qquad \hat{\theta} \to -\infty, \tag{4.5.20}$$

$$\hat{A} \to a + \mathrm{i}\pi\Lambda, \qquad \text{as} \qquad \hat{\theta} \to +\infty. \tag{4.5.21}$$

Finally it can be seen that the remainder term after it crosses the Stokes' line is given by

$$R_N \sim 2^{-1/4}\hat{C}\Lambda\pi(1+z^2)^{1/8}\mathrm{e}^{\mathrm{i}\pi/4}\delta^{-5/12}\exp\left(\frac{\sqrt{2}\mathrm{i}}{\delta^{1/2}}\int_0^z (1+p^2)^{-1/4}\,\mathrm{d}p\right), \tag{4.5.22}$$

where

$$\hat{C} = \exp\left(-\frac{\sqrt{2}}{\delta^{1/2}}\int_0^1 (1-q^2)^{-1/4}\,\mathrm{d}q\right). \tag{4.5.23}$$

There will be a similar expression for the Stokes' line coming up the imaginary axis from $z = -\mathrm{i}$, namely

$$R_N \sim 2^{-1/4}\hat{C}\Lambda\pi(1+z^2)^{1/8}\mathrm{e}^{-\mathrm{i}\pi/4}\delta^{-5/12}\exp\left(-\frac{\sqrt{2}\mathrm{i}}{\delta^{1/2}}\int_0^z (1+p^2)^{-1/4}\,\mathrm{d}p\right). \tag{4.5.24}$$

This problem is posed on the real line and hence if z is real then for $z > 0$ the terms in (4.5.22) and (4.5.24) will become comparable and hence the remainder term that is

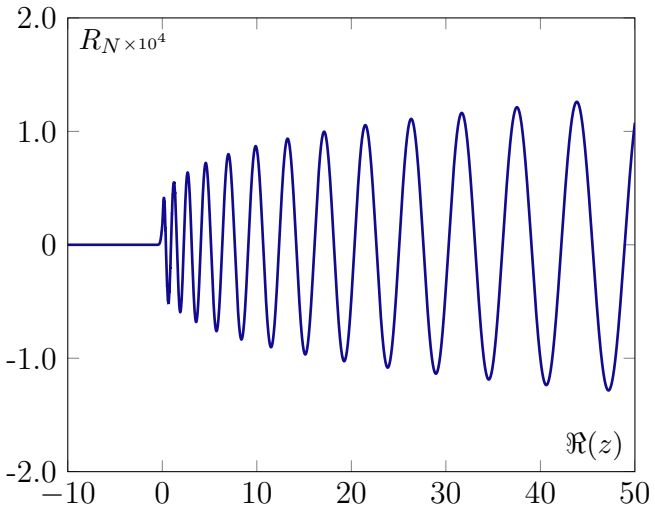

Figure 4.5.2: The remainder term as it goes past the Stokes' line at $z = 0$ on the real line

switched on is of the form

$$R_N \sim 2^{3/4}\hat{C}\mathrm{i}\Lambda\pi(1+z^2)^{1/8}\delta^{-5/12}\cos\left(\frac{\pi}{4} - \frac{\sqrt{2}}{\delta^{1/2}}\int_0^z (1+p^2)^{-1/4}\,\mathrm{d}p\right). \qquad (4.5.25)$$

Note that this agrees exactly with the analysis of the boundary conditions at the beginning of the chapter! For the choice of the positive sign in the leading order solution it was shown that as $\xi \to \infty$ then $u \sim C_+\xi^{1/4}\mathrm{e}^{\pm\mathrm{i}2\sqrt{2},^{1/2}}$. This is precisely what the forms of (4.5.22) and (4.5.24) state in the limit as $|z| \to \infty$ and $\Im(z) = 0$. This behaviour is shown in figure 4.5.2 where R_N becomes oscillatory and growing as the Stokes' line at $z = 0$ is crossed. Therefore the conclusion is that the choice of the positive sign is inconsistent with the asymptotic expansion as the remainder term increases algebraically as a Stokes' line is crossed.

4.6 Remarks

In the case of the negative square root a consistent expansion can be constructed as the Stokes' lines do not cross the real axis. The initial conclusion would be that the remainder term R_N remains exponentially small on the real line and therefore an asymptotic solution could exist that satisfies the boundary conditions. As is indicated by the sketch in figure 4.6.1 a solution to the problem does exist but proves extremely difficult to obtain numerically. Indeed, refining the calculations in this figure to attempt to get the trajectories to enter the origin as required eventually requires adjustments to the initial guess beyond machine precision (on a double precision desktop computer). Nevertheless based on the all of the analysis in this chapter, it is reasonable to conjecture that the solution space will look something like that sketched in figure 4.6.1. Note that in this conjectured sketch the upper branch has a limit point and a fold

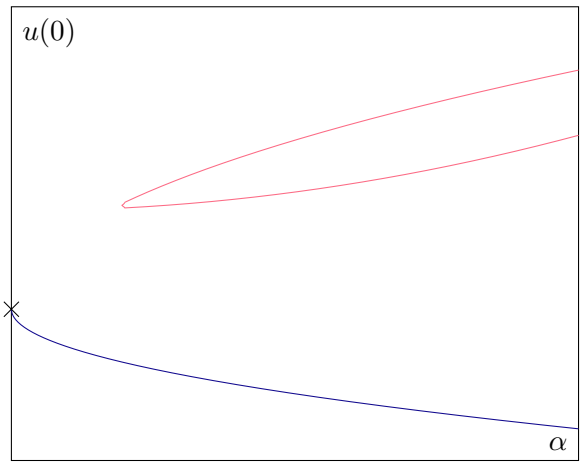

Figure 4.6.1: Conjectured Solution Space for Agnesi Forcing. The cross denotes the origin

instead of a termination point as was found in the Gaussian forcing case. The reason for this is that, as was shown in section 4.2, there is only one possible far-field decay behaviour, namely $u \sim -1/\xi$, and therefore there can be no switch from one type of decay at infinity to another as occurs at the termination point for the Gaussian forcing. Note that since the upper branch has to fold back on itself, this might appear at first glance to contradict the conclusions of our large α boundary layer analysis that there is only one upper branch solution. One possible explanation here is that the lower part of this upper branch corresponds to solutions that cannot be captured by boundary layer theory and for which exponentially small terms need to be taken into account to construct King (2018). This is left as an avenue for future research.

Chapter 5

Free Surface Flow over a Corrugated Topography

This chapter investigates steady flow over a corrugated topography. As shown in chapters 2 and 3 the steady solution space for a delta function exhibits a large range of different solutions. For the weakly nonlinear model, these solutions can be characterised using phase-plane methods. It can also be shown that these solutions also exist in the fully nonlinear solution space (see Dias & Vanden-Broeck, 2002*a*; Vanden-Broeck, 1987; Wade *et al.*, 2014). When the topography is non-localised, phase plane methods as discussed in chapter 2 cannot be applied since the weakly nonlinear system becomes non-autonomous. As defined in Binder *et al.* (2013) and discussed in the introduction in the case of a completely general topography the different taxonomy of flow types can be characterised by the upstream and downstream Froude number. In this work they were able to define eleven different flow types for a general topography. The steady solutions of the delta function; super-critical, sub-critical, critical, generalised hydraulic falls and hydraulic falls, as discussed in chapter 2, can be described using these eleven different flow-types. An example of a non-localised topography is a corrugated topography.

Steady flow over an infinite corrugation, finite corrugation and semi-infinite corrugation will be considered. The first case of infinite corrugation has been studied before by Grimshaw & Tian (1994) and Binder *et al.* (2015). In Grimshaw & Tian (1994) the fKdV equation is modified to include an extra η_x damping term. Using asymptotic methods they were able to show that periodic steady solutions exist and that in general the solutions are chaotic. This was achieved with recourse to a Melnikov method. In Binder *et al.* (2015) the fKdV equation in the form studied in this thesis, (2.1.41) was examined. It is repeated here for convenience

$$\eta_{xx} - 6(F-1)\eta + \frac{9}{2}\eta^2 + A = -3\sigma(x). \tag{5.0.1}$$

By numerical and asymptotic techniques, periodic solutions were constructed when $F > 1$ and σ was chosen to be an infinite corrugation. These results were also aug-

mented by a Melnikov method where chaotic solutions were also constructed.

The second case of finite corrugation has received less attention. It was considered in the case of critical flow, $F = 1$, in Binder *et al.* (2014) by means of an 'inverse' method (see previous chapter) but the focus of their work was on constructing non-unique solutions at critical Froude number. The finite corrugation was exposed as an example of how this was possible; the steady solution space was not explored. The third case of a semi-infinite corrugation has not, to the author's knowledge, been studied previously.

The aim of this chapter is to study the steady solution space in the case of a infinite, finite and semi-infinite corrugated topography. The solutions will be compared to the solutions over a delta function and a comparison will be made on the similarities and differences between the two solution spaces. This chapter starts with an extension of the ideas presented in Binder *et al.* (2015) to provide conditions for when solutions are periodic and when they are quasi-periodic over an infinite corrugation. Finally the cases when the corrugation are finite and semi-infinite are considered and a wide range of solutions are discovered in the weakly nonlinear model and the fully nonlinear model. These are compared to the solution space over a delta function forcing.

5.1 Steady flow over infinite corrugation

As mentioned earlier for the weakly nonlinear model the equation to be solved is

$$\eta_{xx} + \frac{9}{2}\eta^2 - 6(F-1)\eta + A = -3\sigma(x), \tag{5.1.1}$$

as derived from (2.1.41), where A is a constant of integration and the topography is now specified as

$$\sigma(x) = \epsilon \cos(kx).$$

The parameters $k > 0$ and ϵ represent the wave number of the corrugation and amplitude, respectively. Binder *et al.* (2015) argued that A can be set to zero without loss of generality. Consequently, henceforth A is set to zero.

For $F > 1$, periodic solutions can be constructed numerically using a finite difference method with periodicity boundary conditions and are shown in figure 5.1.1 for $\epsilon = 0.1$, $k = 3$ and $F = 1.1$. There are three distinct types of solution for a given $F > 1$; a perturbed uniform flow solution (figure 5.1.1(a)), a perturbed solitary wave solution (figure 5.1.1(b)) and a perturbed cnoidal wave solution (figure 5.1.1(c)). These weakly nonlinear solutions when $F > 1$ were shown in Binder *et al.* (2015) to be periodic. To demonstrate the fact that these solutions are periodic, $\nu_c^2 = 6(F-1)$ is defined and substituted into (5.1.1). As $F > 1$ the value of ν_c is real. Therefore (5.1.1) becomes

$$\eta_{xx} + \frac{9}{2}\eta^2 - \nu_c^2\eta = -3\epsilon \cos(kx). \tag{5.1.2}$$

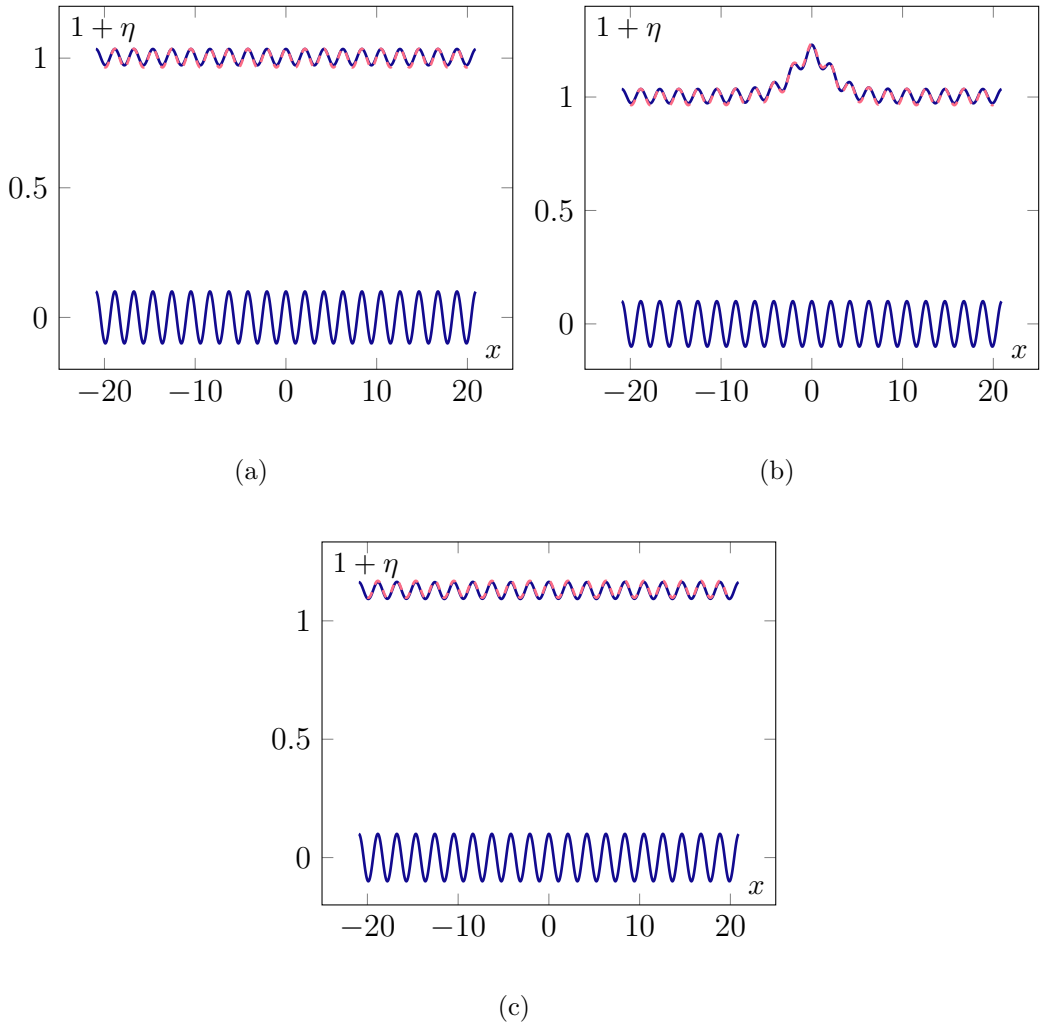

Figure 5.1.1: Weakly Nonlinear Results. The blue curves are the computed free-surfaces whilst the broken red curve is the leading order asymptotic term. In all figures $F = 1.1$, $\epsilon = 0.1$ and $k = 3.0$ and the values of $\eta(0)$ and $\eta_x(0)$ are quoted. (a) The uniform flow solution, $\eta(0) = 0.035, \eta_x(0) = 0$. (b) The solitary wave solution, $\eta(0) = 0.23, \eta_x(0) = 0$ (c) The cnoidal wave solution, $\eta(0) = 0.16, \eta_x(0) = 0$

Following the analysis of Binder *et al.* (2015) an expansion of the form $\eta = \epsilon\eta_1 + \epsilon^2\eta_2 + \cdots$ is substituted into (5.1.2). The leading order solution is given by

$$\eta_1 = A\mathrm{e}^{-\nu_c x} + B\mathrm{e}^{\nu_c x} - \frac{3}{\nu_c^2 - k^2}\cos(kx), \tag{5.1.3}$$

where A and B are arbitrary constants. These are set to zero to ensure the solution is bounded in the far-field. The leading order term of (5.1.2) is

$$\eta = \frac{-3\epsilon}{\nu_c^2 - k^2}\cos(kx) + \cdots, \tag{5.1.4}$$

for the perturbed uniform flow solution. In fact Binder *et al.* (2015) were able to show that provided $\nu_c \neq k$ then higher order terms were also periodic in k. This means that the leading-order expression for the free-surface is in phase with the topography. For the perturbed solitary wave solution an expansion of the form $\eta = \eta_1 + \epsilon\eta_2 + \epsilon^2\eta_3 + \cdots$ gives the solution

$$\eta = 2(F-1)\,\mathrm{sech}^2\left(\sqrt{\frac{3}{2}(F-1)}x\right) - \frac{3\epsilon}{\nu_c^2 - k^2}\cos(kx) + \cdots, \tag{5.1.5}$$

and in this case th first-order solution is in phase with the topography and can be considered as periodic perturbation to the classical solitary wave solution. The final type of solution for $F > 1$, shown in figure 5.1.1, appears to oscillate periodically about $\eta = 4/3(F-1)$. To see this a transformation of the form $N = \eta - \frac{4}{3}(F-1)$ in (5.1.1) yields

$$N_{xx} + \frac{9}{2}N^2 + \nu_c^2 N = -3\epsilon\cos(kx). \tag{5.1.6}$$

The sign of the $\nu_c^2 N$ term is positive and therefore homogeneous solutions will be oscillatory, a key difference to (5.1.2) when they were unbounded at ends of the domain. The expansion $N = \epsilon N_1 + \epsilon^2 N_2 + \cdots$ is substituted into (5.1.6) and the leading order solution can be shown to be

$$N_1 = A_1\cos(\nu_c x) + B_1\sin(\nu_c x) - \frac{3}{\nu_c^2 - k^2}\cos(kx) \tag{5.1.7}$$

where A_1 and B_1 are arbitrary constants and $\nu_c \neq k$. As the corrugation is infinite let the conditions to determine A_1 and B_1 be

$$N(0) = \epsilon\alpha + \cdots, \qquad N'(0) = \epsilon\beta + \cdots. \tag{5.1.8}$$

Without loss of generality β can be set to zero, any non-zero value of β corresponds to a phase-shift in the solution; the periodicity properties are unaffected. Therefore the

leading order solution can be determined as

$$N_1 = \left(\alpha - \frac{3}{k^2 - \nu_c^2}\right)\cos(\nu_c x) + \frac{3}{k - \nu_c^2}\cos(kx). \tag{5.1.9}$$

If ν_c and k are rational then the leading order solution will be periodic with period $2\pi/l$, where $l = \mathrm{lcm}(\nu_c, k)$. If either or both of ν_c or k are irrational then the leading order solution will be quasi-periodic as the $l = \mathrm{lcm}(\nu_c, k)$ does not exist. The equation at first-order is

$$N_{2,xx} + \nu_c^2 N_2 = -\frac{9}{2}N_1^2. \tag{5.1.10}$$

It can be shown that the solution takes the form

$$N_2 = A_2\cos(\nu_c x) + \Omega_1\cos((k-\nu_c)x) + \\ \Omega_2\cos((k+\nu_c)x) + \Omega_3\cos(2\nu_c x) + \Omega_3\cos(2kx), \tag{5.1.11}$$

where A_2 is a constant of integration and Ω_i are constants in terms of α, ν_c and k and are not shown here for brevity. Note that the solution at this order is also bounded, although not necessarily periodic. The equation at $O(\epsilon^3)$ is

$$N_{3,xx} + \nu_c^2 N_3 = -9N_1 N_2. \tag{5.1.12}$$

Expanding the expression on the right hand side means that terms involving $\cos(\nu_c x)$ will appear in the forcing term. A direct consequence is that the solution, N_3, will contain terms proportional to $x\cos(\nu_c x)$ which are unbounded. To ensure the solution is bounded A_1 has to be set to zero. By the exact same argument at the $O(\epsilon^4)$, A_2 has to be set to be zero. This process will continue indefinitely at later orders. Therefore the only terms that appear at each order are proportional to $\cos(kx)$ and the solution will remain bounded and periodic. In terms of the free-surface η the first two terms of the expansion can be written as

$$\eta = \frac{4}{3}(F-1) - \frac{3\epsilon}{\nu_c^2 - k^2}\cos(kx). \tag{5.1.13}$$

The periodic, asymptotic solutions described by (5.1.4), (5.1.5) and (5.1.13) are shown as dotted red curves in figure 5.1.1 and demonstrate excellent agreement with the numerical solutions displayed in blue. However this analysis does not give the complete set of bounded solutions to (5.1.6). The asymptotic expansion for (5.1.6) failed at $O(\epsilon^3)$ in the sense that terms appeared that resonated with the homogeneous solutions. As a result of this the solutions that can be constructed are periodic. It will now be shown using the Poincaré-Lindstedt method (see, for example Drazin, 1992) that solutions can be constructed that are bounded but are quasi-periodic. In fact it will be shown that the periodic solutions of Binder *et al.* (2015) are a sub-set of the complete quasi-periodic solution space.

To proceed with the Poincaré-Lindstedt method it is useful to note there are two dominant frequencies appearing in the solution to (5.1.6); the *natural frequency* of the system, ν_c arising from the wavelength of the homogeneous solutions of the linearised equation and the *forcing frequency*, namely k arising from the wavelength of the forcing. To find bounded solutions the independent variable x is first scaled by the forcing frequency so that $z = kx$ becomes the new independent variable in (5.1.6) and so becomes

$$k^2 N_{zz} + \nu_c^2 N = -3\epsilon \cos(z) - \frac{9}{2} N^2. \tag{5.1.14}$$

As discussed before a naive expansion of the form

$$N = \epsilon N_1 + \epsilon^2 N_2 + \epsilon^3 N_3 + \cdots \tag{5.1.15}$$

will eventually result in secular terms appearing that become unbounded as z increases. Following the example in Drazin (1992)p.184, to alleviate this issue the coefficient of the second derivative, the forcing frequency, is expanded in the form

$$k^2 = k_0^2 + \epsilon k_1 + \epsilon^2 k_2 + \cdots, \tag{5.1.16}$$

where k_0 is a set constant but k_i for $i \neq 0$ are *a priori* unknown constants. The expansions in (5.1.15) and (5.1.16) are substituted into (5.1.14). To $O(\epsilon)$ the system is the same as before and the solution is

$$N_1 = A_1 \cos(\kappa z) + B_1 \sin(\kappa z) + \frac{3}{k_0^2 - \nu_c^2} \cos(z),$$

where A_1 and B_1 are arbitrary constants and $\kappa = \nu_c / k_0$. As the domain of z is the real line and the forcing is infinite conditions on N and N' can to defined at any value of z. For convenience let the conditions be determine A_1 and B_1 be that

$$N(0) = \epsilon\alpha, \qquad N'(0) = \epsilon\beta, \tag{5.1.17}$$

for a given α and β. As before without loss of generality $\beta = 0$ (if β is non zero then this corresponds to a phase-shift; the periodicity characteristics are unaffected). The particular solution at leading order is therefore

$$N_1 = A_1 \cos(\kappa z) + \frac{3}{k_0^2 - \nu_c^2} \cos(z), \tag{5.1.18}$$

where

$$A_1 = \left(\alpha - \frac{3}{k_0^2 - \nu_c^2} \right). \tag{5.1.19}$$

This solution has two dominant frequencies of period $2\pi/\kappa$ and 2π. In general κ will be irrational (unless ν_c is rational) and therefore the solution will be quasi-periodic[1].

[1]It will be assumed that ν_c/k is not rational, in fact this case was studied by Binder *et al.* (2015)

If

$$\alpha = \frac{3}{k_0^2 - \nu_c^2} \tag{5.1.20}$$

then the solution will be periodic and the cnoidal solutions of Binder *et al.* (2015) are recovered. It is assumed that α is not this special value. At next order $O(\epsilon^2)$

$$k_0^2 N_{2,zz} + \nu_c^2 N_2 = -\frac{9}{2} N_1^2 - k_1 N_{0,zz}. \tag{5.1.21}$$

There will be terms proportional to $\cos(z), \sin(z)$ emerging from the $N_{0,zz}$ term on the right hand side which cause secular growth. The choice $k_1 = 0$ eliminates these offending terms. Using (5.1.18) the equation (5.1.21) therefore becomes

$$k_0^2 N_{2,zz} + \nu_c^2 N_2 = -\frac{9}{2} A^2 \cos(\kappa z) - \frac{27A}{k_0^2 - \nu_c^2} \cos(\kappa z)\cos(z) - \frac{9}{k_0^2 - \nu_c^2} \cos^2(z). \tag{5.1.22}$$

The solution to (5.1.22) using (5.1.17) can be written in the form

$$N_2 = A_2 \cos(\kappa z) + \Lambda_1 + \Lambda_2 \cos(2\kappa z) + \Lambda_3 \left(\cos((\kappa - 1)z) + \cos((\kappa + 1)z)\right) + \Lambda_4 \cos(2z),$$

where A_2 is a constant of integration determined from (5.1.17) and Λ_i are determined constants that in the interests of brevity are not included here. This expression is quasi-periodic with frequencies of 2, κ, $\kappa + 1$, $\kappa - 1$ and 2κ arising from each of the terms on the right hand side of (5.1.22). At $O(\epsilon^3)$ the equation for N_3 is

$$k_0^2 N_{3,zz} + \nu_c^2 N_3 = -9 N_1 N_2 - \nu_2 N_{1,zz}. \tag{5.1.23}$$

The right hand side of (5.1.23) will contain a large number of terms. The only terms that need to be considered to ensure the solution remains bounded are the $\cos(\kappa z)$ and $\sin(\kappa z)$ terms emanating from the product $N_1 N_2$ and the $N_{1,zz}$ term. In fact the right hand side of (5.1.23) can be written as

$$k_0^2 N_{3,zz} + \nu_c^2 N_3 = \left[-\frac{9A_1\Lambda_1}{2} - 9A_1\Lambda_2 + A_1 k_2\right] \cos(\kappa z) + \text{Non-resonant terms}. \tag{5.1.24}$$

The choice of

$$k_2 = \frac{9}{2}(\Lambda_2 + 2\Lambda_1)$$

eliminates the offending $\cos(\kappa z)$ term and therefore N_3 is bounded and quasi-periodic. Note that although k_1 and k_2 come as part of the solution the wavelength parameter of the forcing k can still be set freely as k_0 in (5.1.16) can be adjusted for a fixed value of ϵ.

This analysis has demonstrated that asymptotic solutions exist and that in general they are quasi-periodic. The periodic solutions of Binder *et al.* (2015) are obtained

where asymptotic solutions that were periodic were also constructed, this shall not be expanded upon here

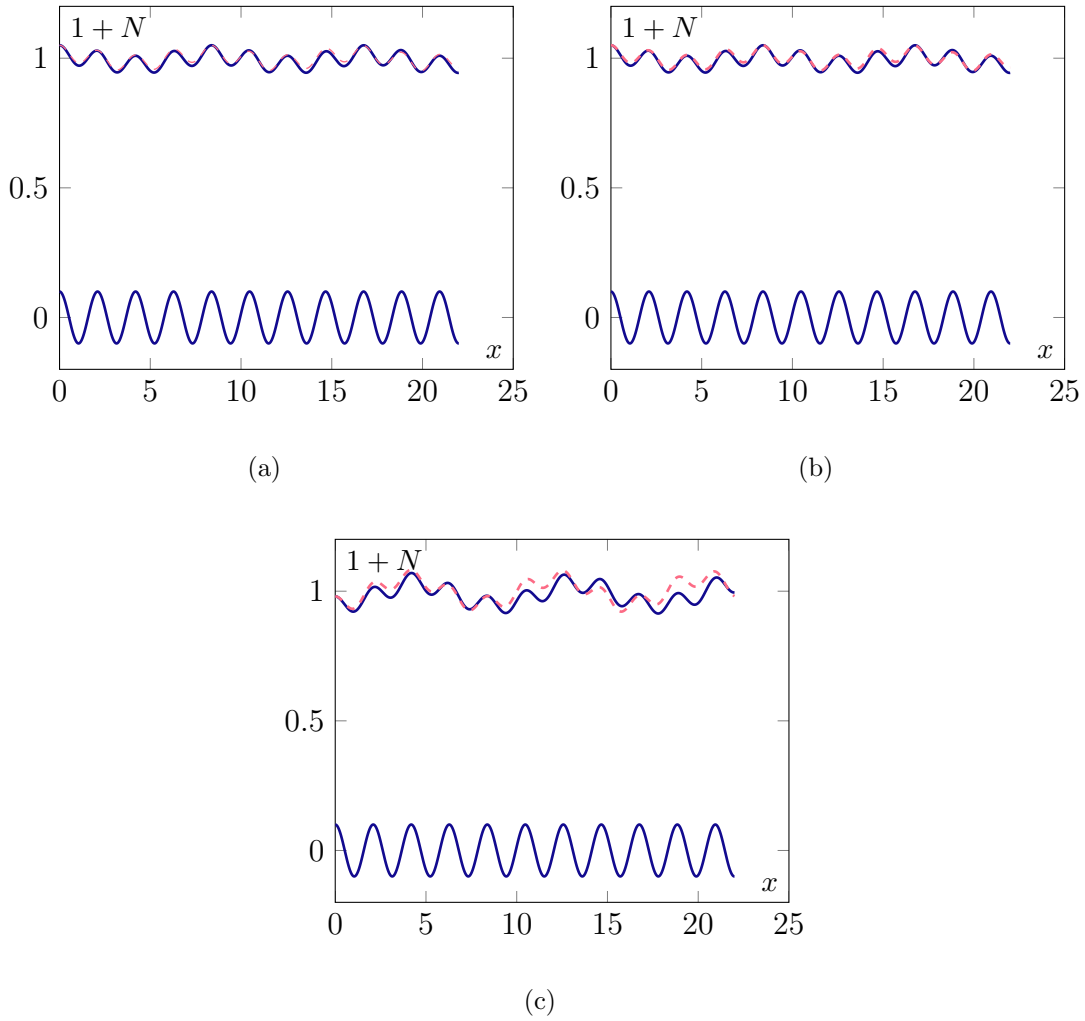

Figure 5.1.2: Quasi-Periodic $F < 1$ steady solutions; $F = 1.1$, $k = 3.0$ and $\epsilon = 0.1$, $N_x(0) = 0$. The blue curves are the computed solutions and the broken red curves are the leading order N_1 term given in (5.1.18). (a) $N(0) = 0.001$, (b) $N(0) = 0.05$, (c) $N(0) = -0.02$

from this analysis by a judicial choice of the initial conditions. This process can be continued for higher orders. Figure 5.1.2 shows numerically computed quasi-periodic solutions in blue and the leading term in (5.1.18) in broken red. In these calculations the free surface was calculated using a Runge-Kutta 4 algorithm with initial conditions given by (5.1.17). Note these solutions are for N in (5.1.6). This analysis completes the asymptotic description of the three types of solutions when $F > 1$ as discussed in Binder *et al.* (2015).

The results from this method also explains the solution structure when $F < 1$. As $\nu_c^2 < 0$, the fKdV equation in (5.1.1) can be written as

$$\eta_{xx} + \frac{9}{2}\eta^2 + \mu_c^2\eta = -3\sigma, \tag{5.1.25}$$

where $\mu_c^2 = -\nu_c^2$. This has exactly the same form as (5.1.6) and hence the Poincare-Lindstedt analysis will be exactly the same as before. In fact the solutions for $F < 1$ have a direct correspondence with the elevated solutions for $F > 1$. This analogy

can be made concrete using the fact that when $F > 1$ (5.1.1) gets transformed by $\eta = \frac{4}{3}(F-1) + N$. This transforms (5.1.1), that has a $-6(F-1)\eta$ term, to (5.1.6), which has a $+6(F-1)$ term. This can be considered as a $F < 1$ solution with Froude number $2 - F$. For example, if $F = 1.1$ then the elevated quasi-peridic solution of (5.1.1) will be the same as the solution to (5.1.1) when $F = 0.9$ modulo a vertical shift of $2/15$. This analysis only applies to an infinite corrugation. This is a unique case as conditions on η and η_x can be chosen anywhere on the real line. For a corrugation that does not extend the full domain this freedom is lost. The next section investigates the case when the corrugation is finite.

5.2 Steady flow over a finite corrugation

As seen in the previous section for an infinite corrugation, quasi-periodic and periodic solutions can be found. If the topography is flat far upstream and downstream then the free-surface must satisfy the vanishing far-field conditions at least either upstream or downstream, i.e.

$$\eta, \eta_x \to 0, \qquad x \to \infty \text{ or } x \to -\infty. \tag{5.2.1}$$

due to the radiation condition. A finite corrugation of the form

$$\sigma = \frac{1}{2}\epsilon\left[\tanh(\lambda(x-\gamma_1)) - \tanh(\lambda(x+\gamma_2))\right]\cos(kx) \tag{5.2.2}$$

is chosen. The parameters ϵ and k define the amplitude and wavelength of the corrugation whilst $\gamma_{1,2}$ control the length of the corrugation. The parameter λ is chosen to ensure a quick transition to the corrugation from the flat part and in these calculations was chosen to be $\lambda = 10$. The solution space is explored for $F > 1$ and $F < 1$. Note that in the case of a bump, as in chapter 2, there are a number of different possible flow configurations and these are repeated for the convenience of the reader. For super-critical flow, $F > 1$, forced solitary waves exist which decay exponentially far upstream and downstream to a zero mean level. For sub-critical flow, $F < 1$, cnoidal-wave solutions exist that are flat at one end of the domain and oscillatory the other end of the domain. Additionally there are generalised hydraulic fall solutions that are flat and uniform at one end, (where $F > 1$) and are oscillatory about a non-zero mean level at the other side of the domain; the change of height at the other side indicates a change in the nature of the Froude number and is sub-critical. If the parameters are chosen carefully then the generalised hydraulic fall solution can become flat at each end. In the case of a finite corrugation the solutions shall also be characterised using this taxonomy. The analysis of the infinite corrugation found solutions to be periodic when the flow was super-critical and quasi-periodic when the flow was sub-critical. The following numerical analysis will seek to understand the free surface behaviour over the corrugation when $F > 1$ and $F < 1$ and establish similarities and differences with the

case of infinite corrugation. Additional comparisons with the steady solution space for a delta forcing will also be discussed. These two cases will be analysed and presented separately.

The weakly nonlinear solution space is complemented with fully nonlinear calculations. Instead of prescribing the topography in x as in the previous chapter the topography is prescribed in terms of the potential ϕ as it is easier to implement numerically. This means that instead of solving the equation

$$\arctan(\theta_b) = \frac{\mathrm{d}\sigma}{\mathrm{d}x},$$

and using the expression (5.2.2) as the prescribed topography, it is more convenient to solve

$$\arctan(\theta_b) = \frac{\mathrm{d}\sigma}{\mathrm{d}\phi},$$

as $x \approx \phi$. This approach however does not prescribe the topography exactly as a function of x, rather the exact form of the bottom topography comes as part of the solution. It was found that there was a minimal wavelength difference between the prescribed topography and the calculated topography and so for numerical convenience this approach was preferred.

5.2.1 $F > 1$

When $F > 1$ there are a large range of solutions that can be constructed. The first type of solutions are periodic over the topography and can be classified as corrugated solitary waves and uniform flow solutions. These are shown in figure 5.2.1. Interestingly as the corrugation is of a finite length more than one solitary wave can be placed in the profile; the number depending on the length of the corrugation. These solutions are analogous to the super-critical forced solitary wave solutions considered in chapter 2. The analysis of the previous section showed that for an infinite corrugation, for $F > 1$, the solitary wave and uniform flow solutions were in phase with the topography. In this case the free-surface is also in phase over the topography. In the taxonomy of Binder *et al.* (2013) these solutions are considered super-critical flow.

The second type of solution is a perturbed 'table-top soliton' (see Chardard *et al.*, 2011, for examples of these type of solutions over a localised bump) as shown in figure 5.2.2(a),(b). The free-surface is flat upstream and downstream but over the topography the profile is elevated above the zero mean and oscillates in a disordered manner. This can be interpreted as the 'joining' together of two generalised hydraulic fall solutions over two different bumps. From the analysis of the previous section when $F > 1$ the elevated solutions were quasi-periodic. Over the corrugation the free-surface is also elevated over the zero mean level. Therefore it is expected that the disordered oscillations of the free-surface in this case are also quasi-periodic. In the taxonomy of Binder *et al.* (2013) these solutions are also considered super-critical flow.

The third type of solution is shown in figures 5.2.2(c),(d) and 5.2.3 and is analogous to a generalised hydraulic fall. In the case of a bump these solutions are characterised by being flat downstream and oscillating around a sub-critical centre far upstream. A number of different configurations are possible. Firstly, a corrugated solitary wave is formed at the start of the corrugation and over the length of the corrugation the profile is periodic. As the corrugation ends the profile oscillates regularly about a non-zero level downstream (see figure 5.2.2(c)). Secondly, the free-surface can remain in phase with the topography as it goes over the corrugation, until it reaches the end of the corrugation and then oscillates regularly, about a non-zero mean level (see figure 5.2.2(c)). In the taxonomy of Binder *et al.* (2013) these solutions are considered generalised hydraulic falls.

Finally, if the height of the free-surface downstream and the amplitude of the topography is allowed to become as part of the solution then the free-surface can become flat downstream (see figures 5.2.2(c) and (d)). The behaviour of these solutions far downstream is analogous to that of a generalised hydraulic fall in the case of a bump.

Alternatively, instead of the solution remaining in phase with the corrugation as it goes over it, the solution can oscillate disorderly around a non-zero mean level, as shown in figure 5.2.3(a)-(d). These oscillations are elevated and can be compared with the quasi-periodic solutions for the infinite corrugation when $F > 1$. These can also be compared to generalised hydraulic fall solutions in the case of a bump topography. Again, as in the previous paragraph, if ϵ and the level of the free-surface are determined as part of the solution the profile can become flat downstream as shown in figure 5.2.3(e),(f). As in the previous paragraph the behaviour of these solutions far downstream can be compared to hydraulic fall solutions over a bump. These are also examples of hydraulic falls according to the categorisation of Binder *et al.* (2013).

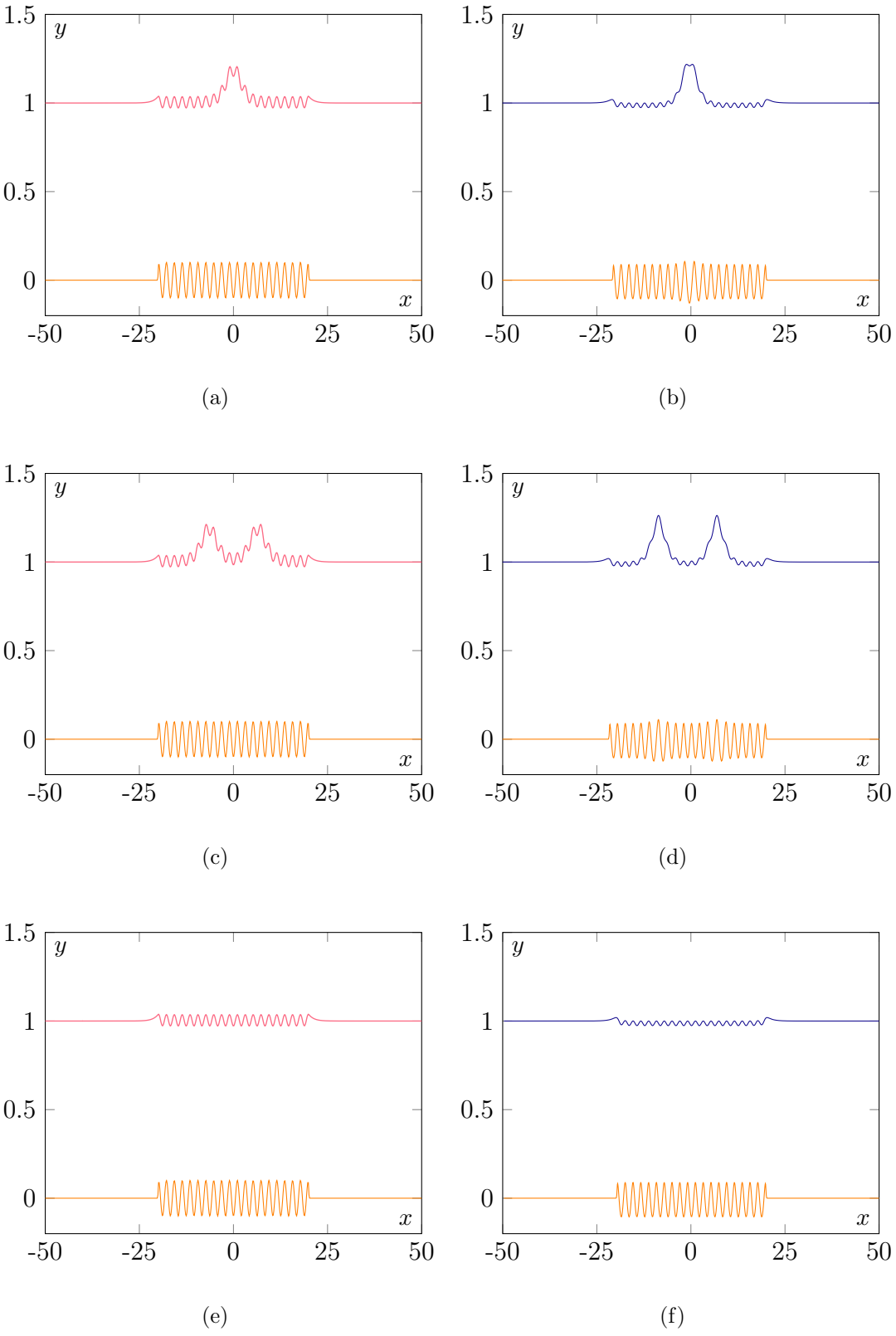

Figure 5.2.1: Corrugated forced solitary waves over a finite corrugation. All figures are for $F = 1.1$ and $k = 3.0$, $\epsilon = 0.1$, $\gamma_1 = 20$, $\gamma_1 = 20$. The red curves are the weakly nonlinear solutions and the blue curves are the fully nonlinear solutions. The dotted black lines in the fully nonlinear plots indicate the topography $y = \sigma(x)$ with the parameters indicated above whilst the orange curves are the actual topography calculated when $y = \sigma(\phi)$.

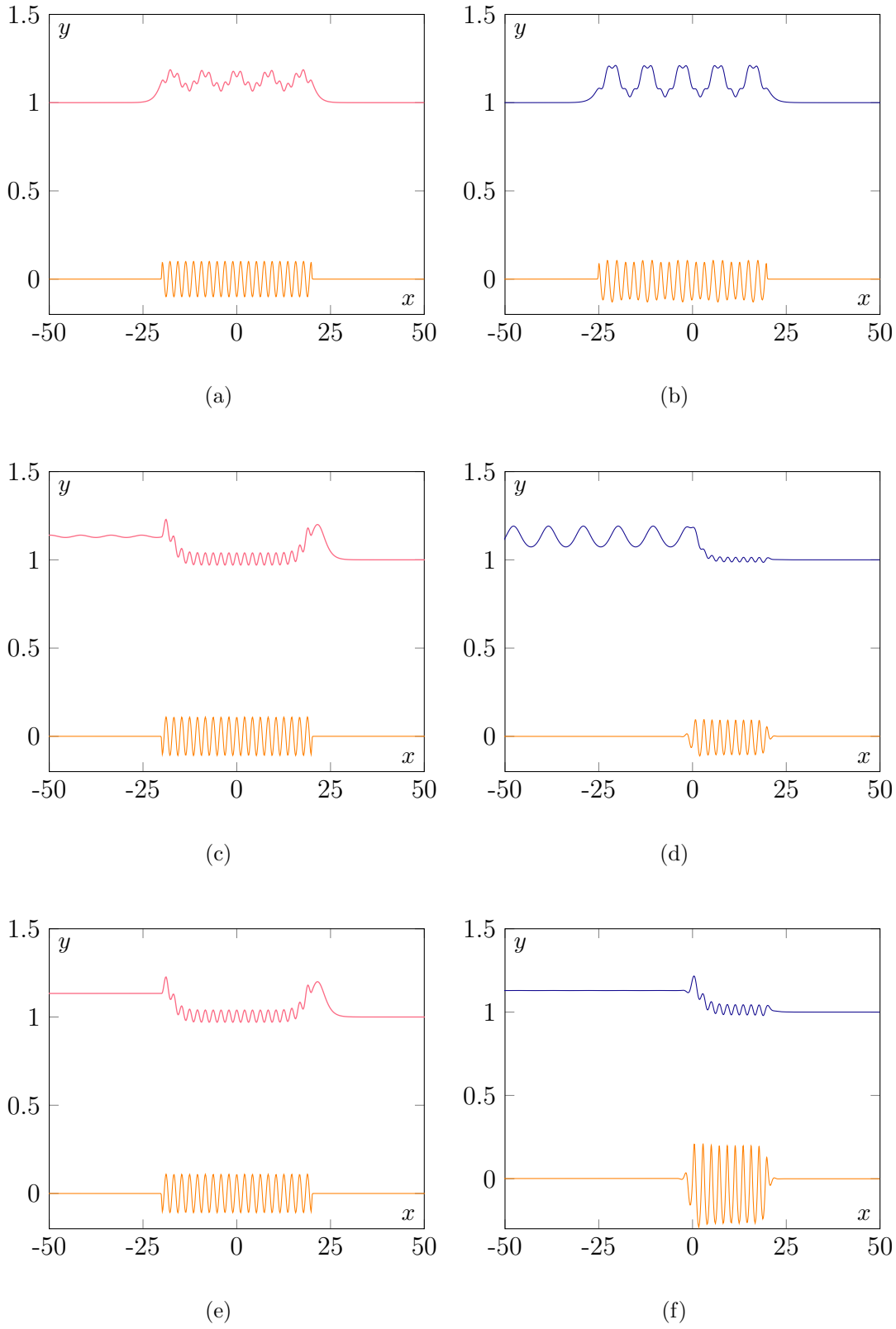

Figure 5.2.2: Corrugated hybrid and table-top solutions over a finite corrugation. Figures (a),(b) are for $F = 1.1$, $\gamma_1 = 20$, $\gamma_2 = 20$, $\epsilon = 0.1$. (c),(e) are for $F = 1.1$ and $k = 3.0$, $\gamma_1 = 20$, $\gamma_2 = 20$, $\epsilon = -0.10877$. (d),(f) $F = 1.1$, $k = 3.0$, $\gamma_1 = 0$, $\gamma_2 = -20$, $\epsilon = -0.1$. (f) $F = 1.1$, $k = 3.0$, $\gamma_1 = 0$, $\gamma_2 = -20$, $\epsilon = -0.26$.

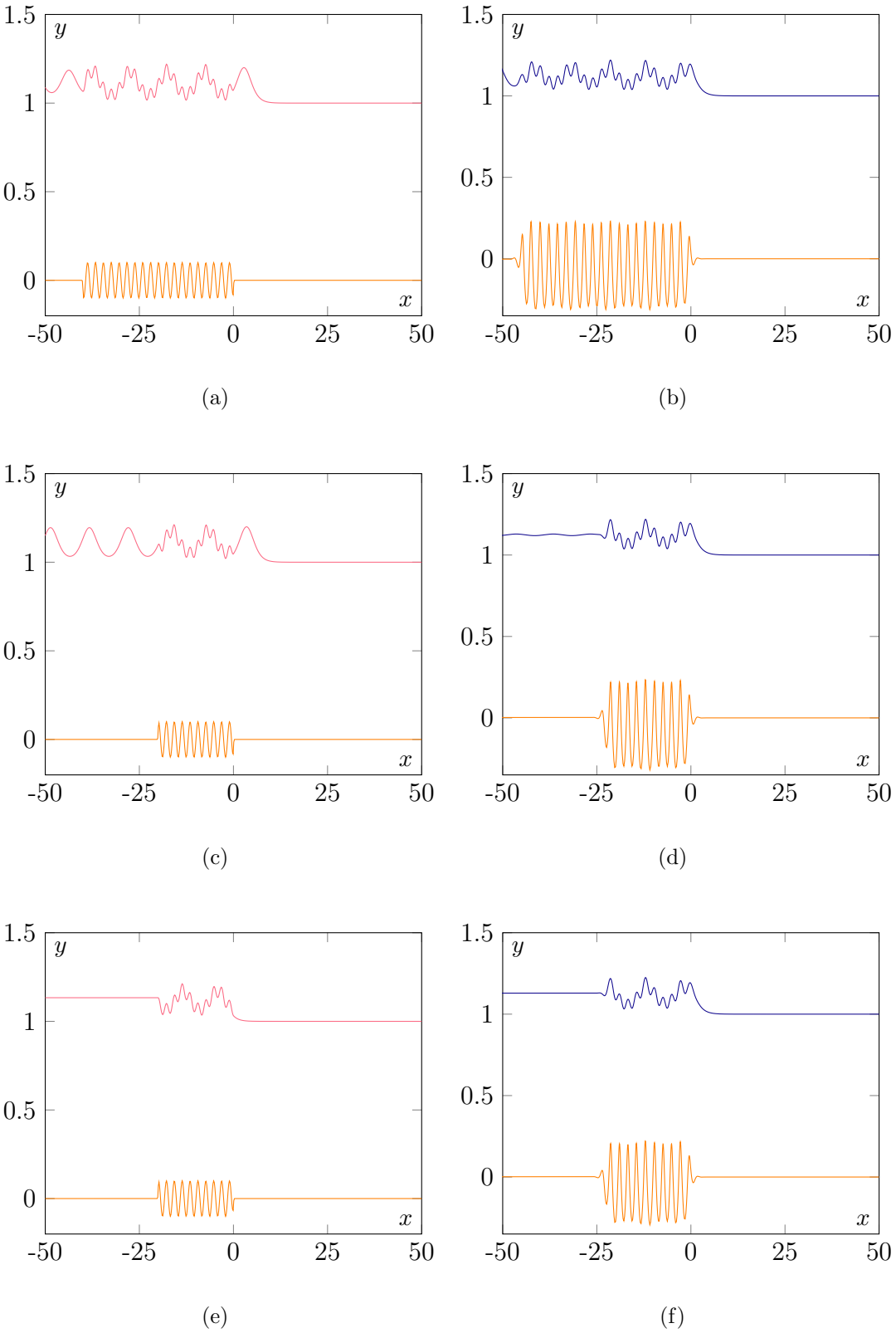

Figure 5.2.3: Corrugated generalised hydraulic fall solutions over a finite corrugation. All figures are for $F = 1.1$ and $k = 3.0$, (a) $\epsilon = 0.1$, $\gamma_1 = 0$, $\gamma_2 = 40$, (b) $\epsilon = -0.2548$, $\gamma_1 = 0$, $\gamma_2 = 40$, (c)-(e) $\epsilon = 0.1092$, $\gamma_1 = 0$, $\gamma_2 = 20$. (d) $\epsilon = -0.2626$, $\gamma_1 = 0$, $\gamma_2 = 20$ (f) $\epsilon = -0.299$, $\gamma_1 = 0$, $\gamma_2 = 20$

5.2.2 $F < 1$

When $F < 1$ the solutions for an infinite corrugation are bounded and in general quasi-periodic (see the analysis of the previous section). In analogy to the general flow-types given in Binder *et al.* (2013) these are examples of sub-critical flow. Some typical profiles are shown in figure 5.2.4. There are some interesting observations. First is that the solution is unique, after a numerical investigation it was found that for a set of parameters only one possible profile is available. The solution is flat upstream, and oscillatory over the topography and downstream. Over the topography the oscillations are disorderly and can be compared to the $F < 1$ solutions in the case of infinite corrugation. Far downstream the oscillation are regular, corresponding to an unforced cnoidal wave.

For a finite topography by letting the height of the corrugation or the length of the corrugation come as part of solution it is not possible to get a wave profile which is flat at both ends unless the topography is symmetrical around $x = 0$. If the topography is symmetrical then profiles that are wave-free upstream and downstream and oscillatory over the topography are possible (see figure 5.2.4(e),(f)) by letting the $\gamma_1 = \gamma_2$ and ϵ come as part of the solution. These are examples of trapped wave solutions for sub-critical flow.

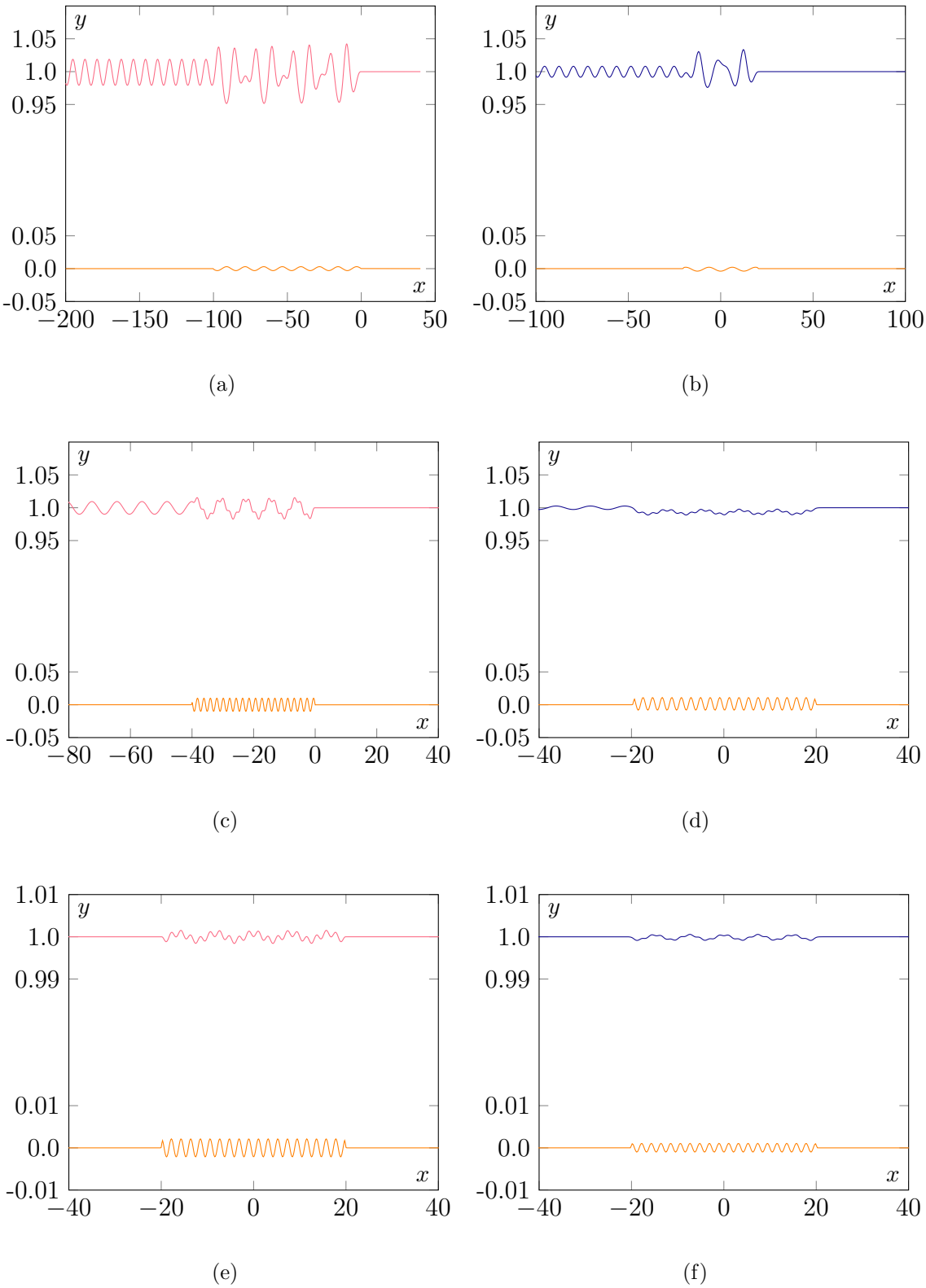

Figure 5.2.4: Corrugated cnoidal and trapped wave solutions over a finite corrugation. Weakly nonlinear solutions are in red, $\lambda = 10$. Fully nonlinear solutions are in blue, $\lambda = 10$. All figures are for $F = 0.9$ (a) $k = 0.5$, $\epsilon = 0.003$, $\gamma_1 = 0$, $\gamma_2 = 100$, (b) $k = 0.5$, $\epsilon = 0.003$, $\gamma_1 = 20.04$, $\gamma_2 = 20.04$, (c) $k = 3.0$, $\epsilon = 0.01$, $\gamma_1 = 0$, $\gamma_2 = 40$, (d) $k = 3.0$, $\epsilon = 0.01$, $\gamma_1 = 19.86$, $\gamma_2 = 19.86$, (e) $k = 3.0$, $\epsilon = 0.00213$, $\gamma_1 = 20$, $\gamma_2 = 20$, (f) $k = 3.0$, $\epsilon = 0.00287$, $\gamma_1 = 20.02$, $\gamma_2 = 20.02$.

5.3 Steady flow over semi-infinite corrugation

The remaining case to investigate is when the topography is semi-infinite. In this case a topography of the form

$$\sigma = \frac{1}{2}\epsilon\left[1 - \tanh(\lambda x)\right]\sin(k(x+\mu)) \tag{5.3.1}$$

is chosen, where ϵ is the amplitude of the forcing, λ is the same 'transition' parameter defined in the previous section, k is the forcing wave number and μ is a phase shift that shall be explained below. As the topography is flat the boundary conditions

$$\eta \to 0, \qquad x \to +\infty, \tag{5.3.2}$$

$$\eta \to A, \qquad x \to -\infty, \tag{5.3.3}$$

where A is a set constant, are imposed on the free-surface. Again the solution space is explored for $F > 1$ and $F < 1$.

5.3.1 $F > 1$

For $F > 1$ the solutions are expected to oscillate regularly over the topography (as per the analysis of the infinite corrugation) and in phase with the topography. Therefore the domain far upstream is truncated at a point such that the topography is at a zero level, i.e. $x = m\pi/k$ where m is an even integer and the value of A in (5.3.3) is chosen to be zero. As in the infinite and finite cases it is possible to get perturbed uniform and solitary wave solutions, as in figure 5.3.1. These are further examples of super-critical flow solutions.

As well as regularly oscillating solutions, discorded oscillatory solutions can also be constructed, see figure 5.3.2. These solutions are characterised by being flat downstream and oscillatory upstream about a non zero mean. As the profile encounters the corrugation it follows the profile of a solitary wave and then becomes disordered upstream. These disordered oscillations are comparable to the quasi-periodic $F > 1$ solutions that are elevated above the zero mean. These solutions are not unique. By altering the parameter A in (5.3.3), different solutions can be constructed. This is akin to a bump topography where it is possible to 'jump' onto different wavelength cnoidal waves orbits around the centre. It is interesting in this case that although this is possible here, the amplitude of the profile does not vary as much as in the case of the bump. The solution downstream behaves in an analogous manner to the generalised hydraulic fall solutions of Binder *et al.* (2013).

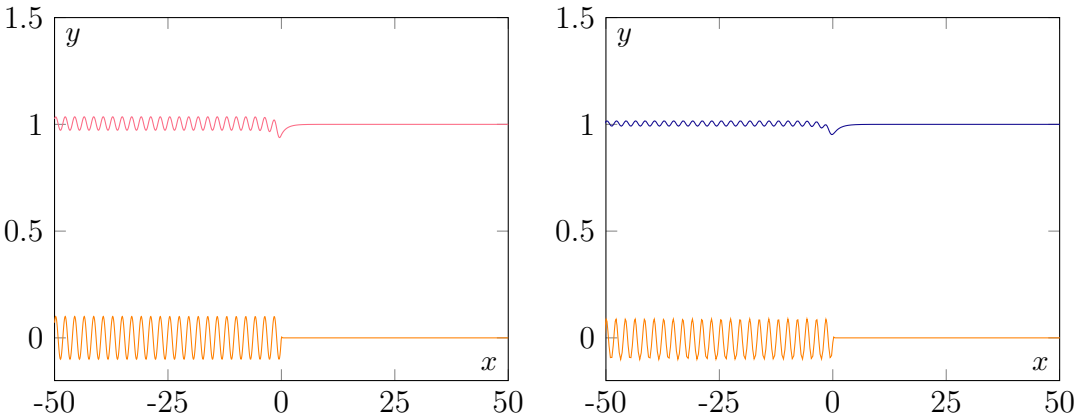

(a)

(b)

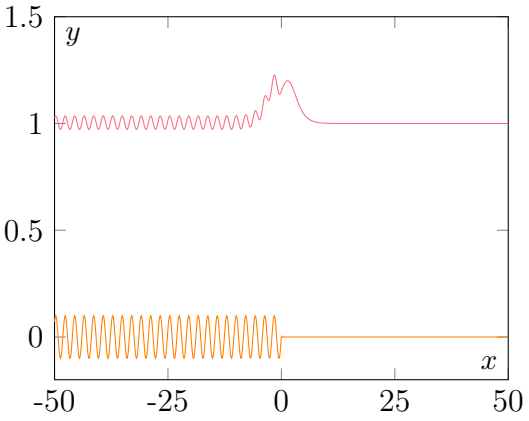

(c)

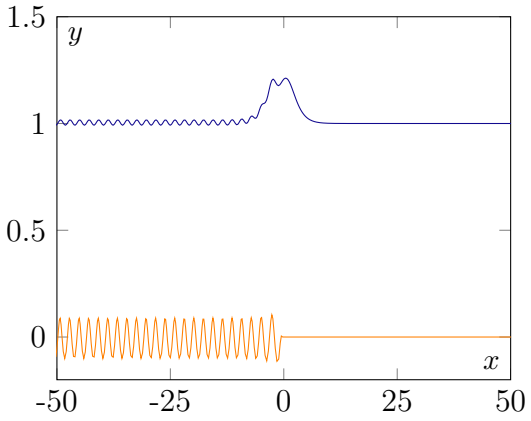

(d)

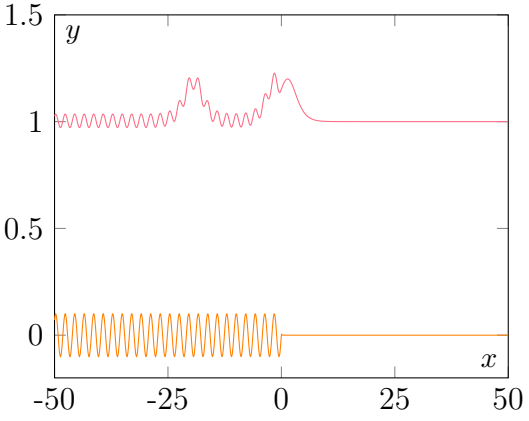

(e)

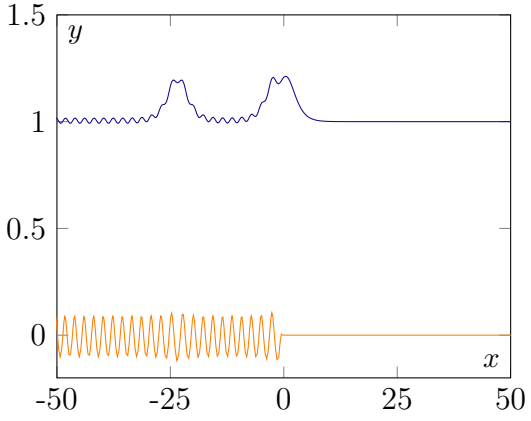

(f)

Figure 5.3.1: Corrugated solitary wave solutions over a semi-infinite corrugation. All figures are for $F = 1.1$ and $k = 3.0$, $\epsilon = 0.1$, $\mu = 0$

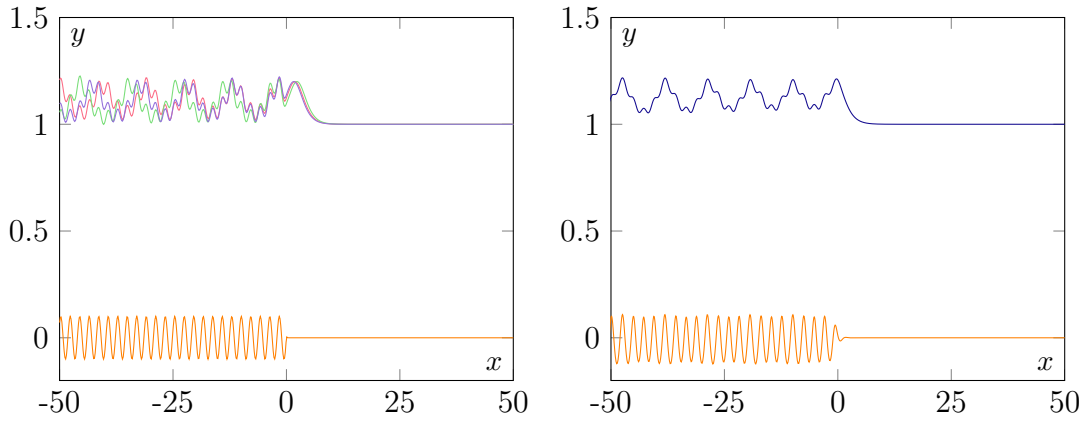

Figure 5.3.2: Corrugated generalised hydraulic fall solutions over a semi-infinite corrugation. Weakly nonlinear solutions are in red, green and purple, $\lambda = 10$. Fully nonlinear solutions are in blue, $\lambda = 1$. All figures are for $F = 1.1$ and $k = 3.0$, $\epsilon = 0.1$ (a) $\mu = 0$, (b) $\mu = -\pi/2k$.

5.3.2 $F < 1$

For $F < 1$ the solutions are expected to be oscillatory over the topography and far upstream and indeed this appears to be the case, see for example figure 5.3.3. These are also examples of sub-critical flow solutions. These are unique in that a solution only exists for a unique value of A. Numerically this value of A will depend on the truncation point upstream. Therefore it is convenient to reformulate the boundary conditions so that

$$\eta, \eta_x \to 0, \qquad \text{as } x \to -\infty. \tag{5.3.4}$$

The advantages of this formulation is that by using a Runge-Kutta 4 algorithm the free-surface can be integrated up to a large value of the domain upstream. Therefore it is possible to analyse the oscillatory behaviour of these solutions by computing a *power spectrum* and a *Poincaré section*. In the Runge-Kutta 4 integration scheme the domain is split into N data points with spacing between two points $\mathrm{d}x$. Let η_i represent the i^{th} data point. The power spectrum $P(\nu)$ is defined by

$$P(\nu) = \left| \sum_{n=1}^{n=N} \mathrm{e}^{-2\pi \mathrm{i} \nu n/N} \eta_n \right|^2 \tag{5.3.5}$$

The quantity $P(\nu)$ will provide information of the highest energy wavelengths present in the wave profile. As seen in the left hand side panels of figure 5.3.4 the power spectrum displays a number of different peaks. There is always a peak in the spectrum when $\nu = k$ (as expected) and also close to $\nu_c = 6\sqrt{1-F}$. This matches the analysis for the infinite case. Additionally other peaks are also visible and these represent the wavelengths present from the $\cos((\kappa \pm 1)z)\cos(kz)$ terms and the $\cos(2^n \kappa z)$ terms from the Poincaré-Lindstedt method described for the infinite corrugation case. The

energy of these are magnitudes of order lower than that of the energy at $\nu = k$ and $\nu = 6\sqrt{1-F}$.

The Poincaré sections are obtained by strobing the solution at the same period as the topography, namely at intervals of $2\pi/k$ starting far downstream, and plotting (η, η_x) at these strobing points, as seen with the right hand panels of figure 5.3.4. There are three possibilities. If when these are plotted there are a finite number of points then the profile is periodic. If the set of points appear to form one (or more) closed curves then the profile is quasi-periodic. If the set of points form a fractal set then the solution is chaotic. As can be seen by figures 5.3.4(b),(d) and (f) the Poincaré sections all appear to form closed curves and hence appear to provide evidence for quasi-periodicity.

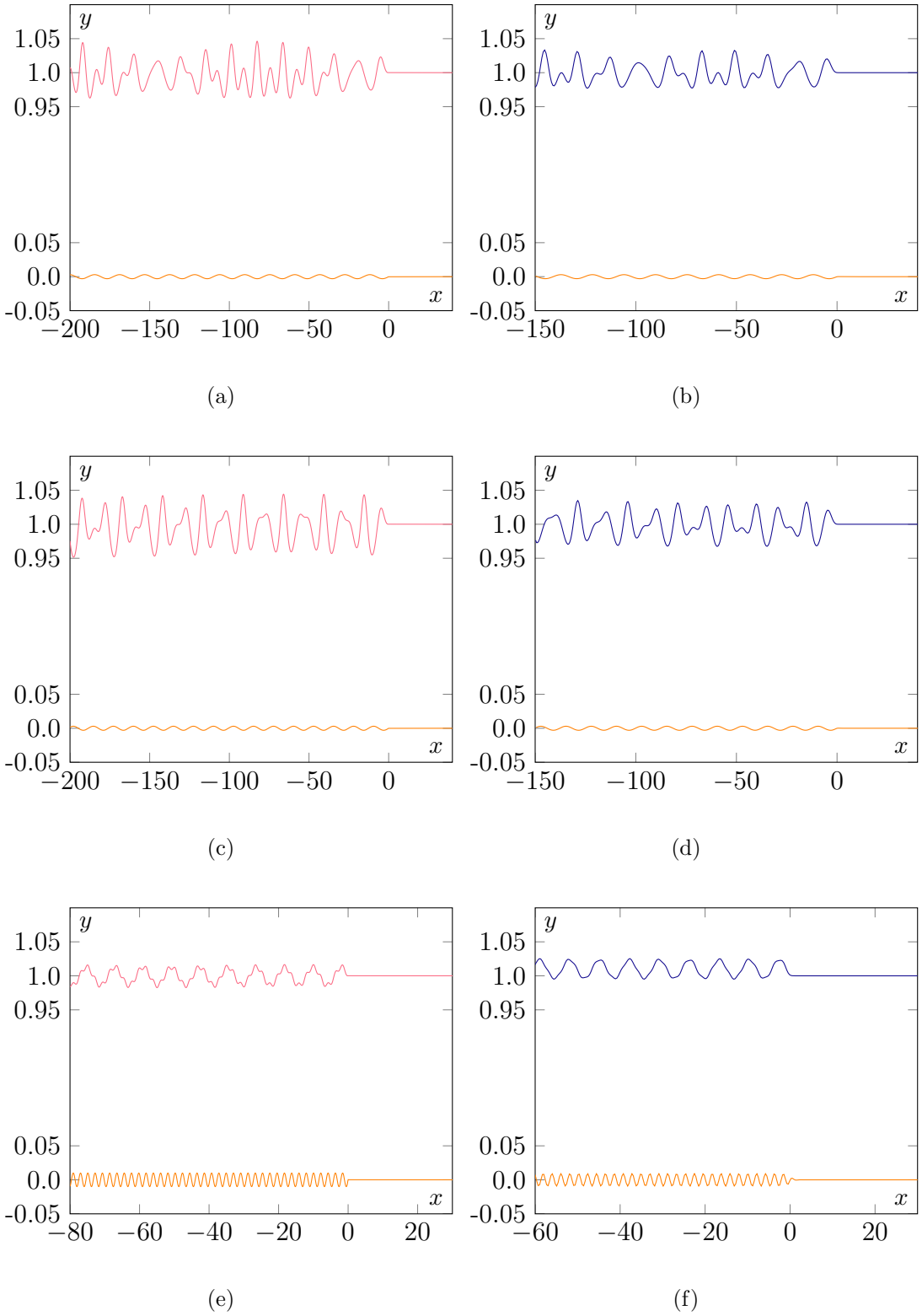

Figure 5.3.3: Corrugated cnoidal wave solutions over a semi-infinite corrugation. Weakly nonlinear solutions are in red, $\lambda = 10$. Fully nonlinear solutions are in blue, $\lambda = 10$. All figures are for $F = 0.9$, $\mu = 0$ (a)-(b) $k = 0.4$, $\epsilon = 0.003$, (c)-(d) $k = 0.5$, $\epsilon = 0.003$, (e)-(f) $k = 3.0$, $\epsilon = 0.01$

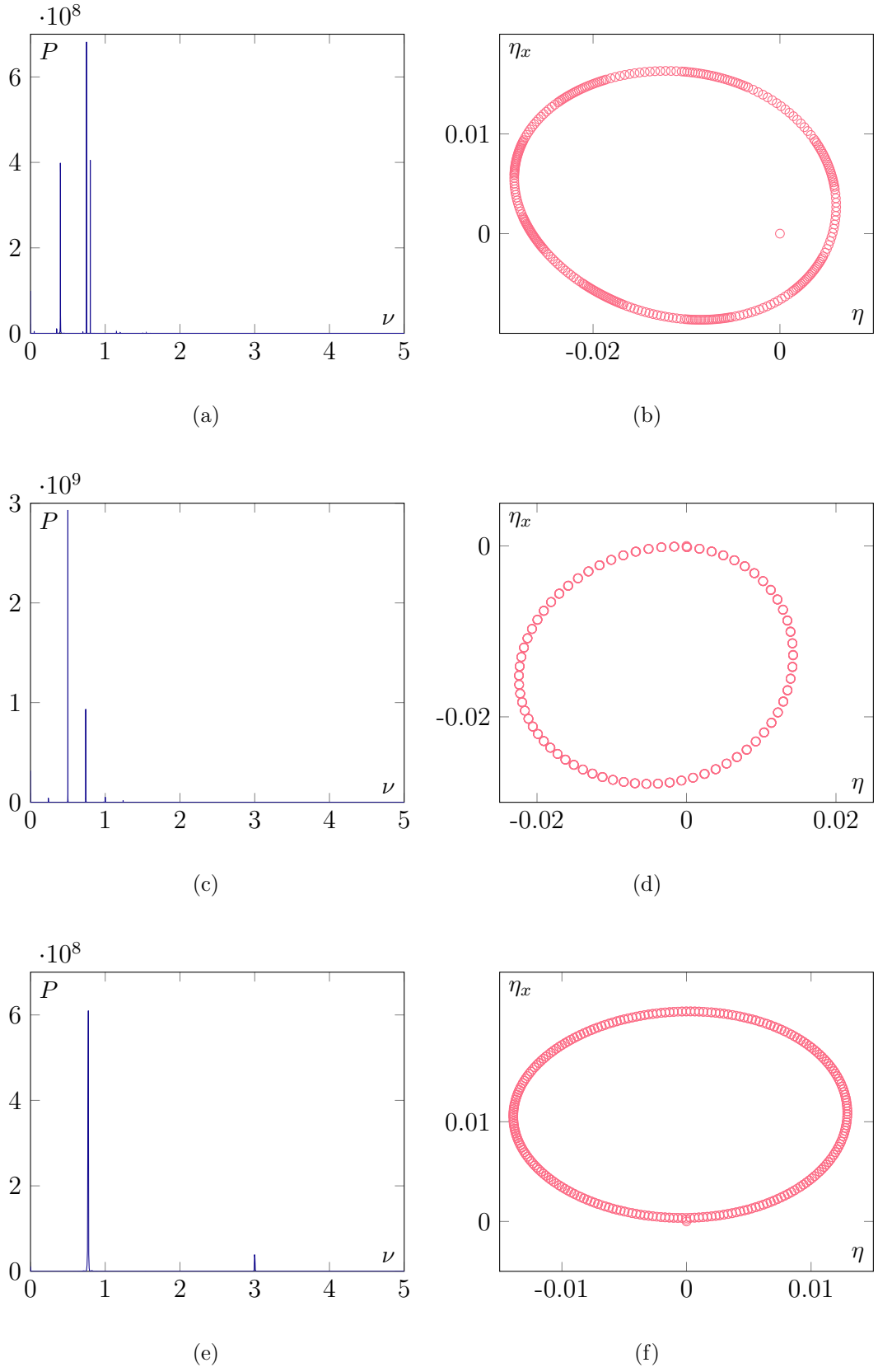

Figure 5.3.4: Poincaré sections and power spectrum's. All figures are for $F = 0.9$ and are integrated from $x = -100$ to $x = 5000$. (a)-(b) $k = 0.4$, $\epsilon = 0.003$, (c)-(d) $k = 0.5$, $\epsilon = 0.003$, (e)-(f) $k = 3.0$, $\epsilon = 0.01$

5.4 Discussion

In this chapter the steady solution space was mapped out when the topography is a corrugated bottom. For an infinite corrugation the work of Binder *et al.* (2015) was extended to demonstrate that for super-critical solutions the solutions were periodic and for sub-critical solutions the solutions were in general quasi-periodic. In the work of Binder *et al.* (2015) only periodic solutions were considered but by implementing a Poincaré Lindstedt analysis quasi-periodic solutions were found when $F < 1$. The periodic solutions of Binder *et al.* (2015) exist when certain, precise conditions can be met, otherwise the profiles are bounded but quasi-periodic. It is noted that the Poincaré-Lindstedt analysis is only valid for the case of the infinite corrugation topography.

The analysis of the infinite case is a useful tool in describing the solutions when the corrugation is not infinite. The numerical calculations suggest this is also the case when the topography is non-infinite. For a finite length of corrugation a number of different solutions were found. In analogy with the solutions for a delta forcing in chapter 2 super-critical solutions exist that are flat at either end of the domain. For sub-critical flow, again in analogy with the delta forcing solution space, solutions exist that are flat at one end but oscillate around the zero level at the other end. A point of difference however is that 'trapped waves' also exist when $F < 1$ which are flat at each end. These are achieved by letting a parameter in the topography come as part of the solution. Finally generalised hydraulic fall solutions exist that are similar to the delta forcing solutions. However there is a large number of possible configurations, resulting from whether the profile remains periodic or quasi-periodic over the topographic forcing resulting in hybrid solutions and so-called 'table-top' solitons.

In the case of a semi-infinite topography the solution space again mirrors that of the delta forcing solution space. For super-critical flow, solutions are flat at one end and then as they go over the topography they oscillate in a regular manner about the zero mean level. These are considered analogous to forced solitary wave solutions. Generalised hydraulic fall solutions also exist that oscillate in a disordered manner about a non-zero level at one end of domain. For sub-critical flow, the semi-infinite corrugation makes the steady fKdV equation amenable to an extended analysis to investigate the periodicity properties. To establish numerically that the solutions were quasi-periodic the system was integrated up to a large value downstream and Poincaré plots and power spectra were computed. The Poincaré plots displayed closed curves in the phase-plane; a numerical indicator of quasi-periodicity. Additionally the power spectra displayed sizeable peaks indicating dominant frequencies predicted by the asymptotic analysis of the infinite corrugation case.

The observant reader will notice that steady solutions at critical flow, $F = 1$ have

not been considered. In the case of an infinite cosine forcing (5.1.2) becomes

$$\eta_{xx} + \frac{9}{2}\eta^2 = -3\epsilon\cos(kx). \tag{5.4.1}$$

Integrating (5.4.1) over one wall period, $L = 2\pi/k$ gives,

$$[\eta_x]_0^L + \frac{9}{2}\int_0^L \eta^2 \,\mathrm{d}x = 0. \tag{5.4.2}$$

Now this means that the first term in (5.4.2) is negative. Therefore

$$\eta_x(L) < \eta_x(0). \tag{5.4.3}$$

Therefore as x varies over a complete period L, the slope of η must decrease. However, following this line of thought means that the slope of the solution will eventually become infinite as $x \to -\infty$. Therefore solutions that are bounded cannot be constructed for an infinite cosine topography when $F = 1$. For a finite corrugation the solutions have already been examined in detail in Binder *et al.* (2014) but for a semi-infinite topography, the argument above means that it is unlikely that converged numerical solutions can be found.

To summarise, a large range of solutions can be found when the corrugation is finite and semi-infinite. When $F > 1$ the free-surface either oscillate regularly around a zero mean over the topography or oscillate in a disordered manner around a non-zero mean over the topography. When $F < 1$ the free-surface oscillates disorderly about the zero mean level. This agrees with the analysis of the infinite corrugation where for $F > 1$ the asymptotic solutions are either periodic or quasi-periodic about a non-zero mean and for $F < 1$ the solutions are quasi-periodic. Additionally a larger number of different free-surface configurations are possible which can be compared to the flow over a bump.

Chapter 6

Future Work

6.1 The Forced KP Equation

This chapter discusses the three dimensional analogue to the fKdV equation,namely the KP equation. A brief sketch of the derivation of the KP equation based on the methodology of chapter 2 is discussed. Additionally, steady solutions that are localised in space are constructed by careful consideration for the topography forcing. Despite there being a wealth of literature for one dimensional flow there is less literature in the case of two dimensional free-surface flow, especially in the context of sub-critical and super-critical flow. In this section the *forced KP* (fKP) equation is analysed (Kadomet-sev & Petviashvili, 1970). The fKP equation can be derived in an analogous manner as the fKdV equation (as in chapter 2) with the addition of an extra spatial dimension. Note that the details are very similar to the analysis of chapter 2 and are left out here for brevity but a full derivation from the three dimensional water-wave equations can be found in Ablowitz & Clarkson (1991); Klein & C.Sparber (1991); Lannes (2013); Lannes & Saut (2013).

For the flat case, $\sigma = 0$, there are two types of KP equation, the KP I and KP II equation which appear in cases of strong surface tension and weak surface tension respectively (Ablowitz & Clarkson, 1991). It is well known that the KP I equation admits localised steady solutions, so-called 'lump' solitons (Groves & Sun, 2008; Min-zoni & Smyth, 1996) that decay algebraically in the far-field. In the absence of surface tension it can be shown that no steady localised solutions exist to the KP equation and water-wave equations (Craig, 2002). However, so-called 'line' solitons exist for which the profile decays in one spatial direction and a large complex pattern of profiles are possible (see, for example Biondini *et al.*, 2009; Kodama, 2010).

Despite there being a number of studies examining the behaviour of the free-surface for the unforced case there has been less work when the system is forced. The fKP equation has been derived in the context of a moving pressure distribution by Katsis & Akylas (1987) and in the case of bottom topography by Lee & Grimshaw (1990). In both of these papers the time-dependent response was considered. In Lu & Liu (2005)

the time-dependent response of solitons in the fKP I equation were investigated. Despite the wealth of literature on steady solutions in the two dimensional fKdV equation there remains, to the author's best knowledge, an opportunity to understand the steady solution space to the to the fKP II equation. In particular there is no three dimensional analogue to the parameter space exploration of chapters 2 and 3. As noted above there is no localised solution to the flat KP II equation but an introduction of a topographic forcing may result in the possibility that localised steady solutions exist. The construction of these steady solutions is discussed in the following analysis.

To start with a third dimension $\hat{z}$ is added to the problem described in chapter 2. This coordinate now represents the vertical height with a typical length scale H. The horizontal dimensions $\hat{x}$ and $\hat{y}$ have typical length scales L as shown in figure 6.1.1.

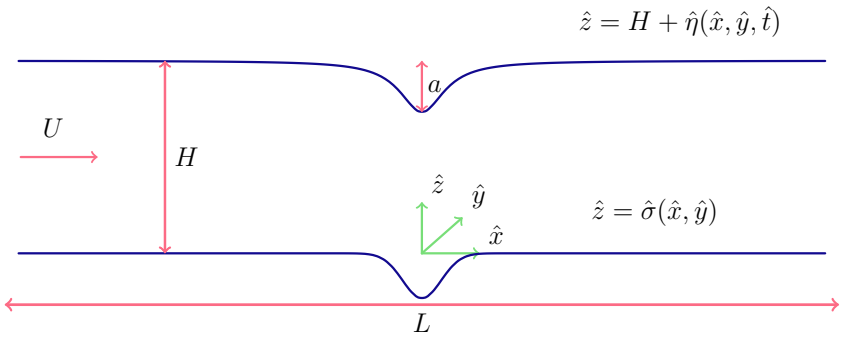

Figure 6.1.1: A diagram showing the physical set up of the problem

The velocity field $(\hat{u}, \hat{v}, \hat{w})$ is assumed to be written in terms of a potential $\hat{\varphi}$ so that the flow is uniform in the $\hat{x}$ direction with speed U, i.e. $(U, 0, 0)$ (this can be done without loss of generality as the $\hat{x}$ direction can be fixed so that it is always in the direction of travel). The bottom topography $\hat{\sigma}(\hat{x}, \hat{y})$ will form a perturbation of the flow

$$\hat{u} = U + \hat{\varphi}_{\hat{x}}, \quad \hat{v} = \hat{\varphi}_{\hat{y}}, \quad \hat{w} = \hat{\varphi}_{\hat{z}}. \tag{6.1.1}$$

In the flow Laplace's equation applies

$$\hat{\varphi}_{\hat{x}\hat{x}} + \hat{\varphi}_{\hat{y}\hat{y}} + \hat{\varphi}_{\hat{z}\hat{z}} = 0 \tag{6.1.2}$$

and the boundary conditions on the free-surface and bottom topography can be written as

$$\left.\begin{aligned} &\hat{\eta}_{\hat{t}} + (U + \hat{\varphi}_{\hat{x}})\hat{\eta}_{\hat{x}} + \hat{\varphi}_{\hat{y}}\hat{\eta}_{\hat{y}} - \hat{\varphi}_{\hat{z}} = 0 \\ &\hat{\varphi}_{\hat{t}} + \tfrac{1}{2}(U + \hat{\varphi}_{\hat{x}})^2 + \tfrac{1}{2}\hat{\varphi}_{\hat{y}}^2 + \tfrac{1}{2}\hat{\varphi}_{\hat{z}}^2 + g\hat{y} = \tfrac{1}{2}U^2 + gH \end{aligned}\right\} \quad \text{on } \hat{z} = H + \hat{\eta}(\hat{x}, \hat{y}, \hat{t}), \tag{6.1.3a}$$

$$-(U + \hat{\varphi}_{\hat{x}})\delta\hat{\sigma}_{\hat{x}} - \delta\hat{\varphi}_{\hat{y}}\hat{\sigma}_{\hat{y}} + \hat{\varphi}_{\hat{z}} = 0 \qquad \text{on } \hat{z} = \delta\hat{\sigma}(\hat{x}, \hat{y}), \tag{6.1.3b}$$

where δ is a small parameter. The hatted set of variables, $(\hat{x}, \hat{y}, \hat{z}, \hat{\eta}, \hat{\varphi}, \hat{\sigma})$, are the

physical variables. The same non-dimensional variables as before are deployed with the exception of $\bar{y} = \hat{y}/L$ and the addition of $\bar{z} = \hat{z}/H$ so that the horizontal coordinates $\hat{x}$ and $\hat{y}$ are both scaled by L and the vertical coordinate $\hat{z}$ is scaled by H. The non-dimensional variables are denoted by a bar, i.e. $(\bar{x}, \bar{y}, \bar{z}, \bar{\eta}, \bar{\varphi}, \bar{\sigma})$. As in chapter 2, F, ϵ and μ are defined in the same way and $\delta = \epsilon$. The non-dimensional water-wave equations therefore can be stated as

$$\mu^2\bar{\varphi}_{\bar{x}\bar{x}} + \mu^2\bar{\varphi}_{\bar{y}\bar{y}} + \bar{\varphi}_{\bar{z}\bar{z}} = 0 \qquad \text{in } \Omega \qquad (6.1.4a)$$

$$\left.\begin{aligned} &\mu\bar{\eta}_{\bar{t}} + (F + \epsilon\mu\bar{\varphi}_{\bar{x}})\mu\bar{\eta}_{\bar{x}} + \epsilon\mu^2\bar{\varphi}_{\bar{y}}\bar{\eta}_{\bar{y}} - \bar{\varphi}_{\bar{z}} = 0 \\ &\epsilon\mu\bar{\varphi}_{\bar{t}} + F\epsilon\mu\bar{\varphi}_{\bar{x}} + \tfrac{1}{2}\epsilon^2(\mu^2\bar{\varphi}_{\bar{x}}^2 + \mu^2\bar{\varphi}_{\bar{y}}^2 + \bar{\varphi}_{\bar{z}}^2) + \epsilon\bar{\eta} = 0 \end{aligned}\right\} \quad \text{on } \bar{z} = 1 + \epsilon\bar{\eta} \qquad (6.1.4b)$$

$$(F + \epsilon\mu\bar{\varphi}_{\bar{x}})\mu\bar{\sigma}_{\bar{x}} + \epsilon\mu^2\bar{\varphi}_{\bar{y}}\bar{\sigma}_{\hat{y}} - \bar{\varphi}_{\bar{z}} = 0 \qquad \text{on } \bar{z} = \epsilon\bar{\sigma}(\bar{x}). \qquad (6.1.4c)$$

where Ω denotes the domain, $-\infty < \bar{x} < \infty$, $-\infty < \bar{y} < \infty$ and $\bar{\sigma} < \bar{z} < 1 + \bar{\eta}$. Note these equations are identical to the two-dimensional case considered in chapter 2 with the addition of $\bar{\eta}$, $\bar{\sigma}$ and $\bar{\varphi}_{\bar{y}}$ terms involving $\bar{y}$ derivatives and the $\bar{y}$ coordinate being replaced by the $\bar{z}$ coordinate. The Froude number F and μ and ϵ are defined as before. The equations in (6.1.4) form the three dimensional water-wave problem. If the flow is weakly three-dimensional, so that $\bar{y}$ is small, then following a similar procedure as described for the two-dimensional case in chapter 2, the forced KP equation can be derived in the long-wave coordinates, $(x, y, z, \eta, \varphi, \sigma)$, in the form

$$\frac{\partial}{\partial x}\left(\eta_t + (F-1)\eta_x - \frac{3}{2}\eta\eta_x - \frac{1}{6}\eta_{xxx} - \frac{1}{2}\sigma_x\right) = \frac{1}{2}\eta_{yy}. \qquad (6.1.5)$$

The long wave variables are defined in a similar same way as the two dimensional case shown in table 2.1. As mentioned before there are two types of KP equation depending on the strength of the surface tension. In this case surface tension is ignored and therefore this is the fKP II equation. When surface tension is included, the fKP I equation can be derived. It can be shown that the coefficient of η_{xxx} changes in the fKP I equation. This difference is not explored here and throughout the following the analysis, reference to the fKP equation is assumed to be a reference to the type II equation with no surface tension.

6.1.1 Steady Solutions

As mentioned above steady solutions are sought for a flat topography that are localised. To be more precise, steady solutions are sought so that η and it's derivative decay in the far-field, i.e.

$$|\eta|, |\eta_x|, |\eta_y| \cdots \to 0, \qquad \text{as} \qquad |x|, |y| \to \infty. \qquad (6.1.6)$$

Initially it is demonstrated that steady solutions exist for the KP II equation that are not localised in both of the x or y directions (Craig, 2002). The time derivative, η_t,

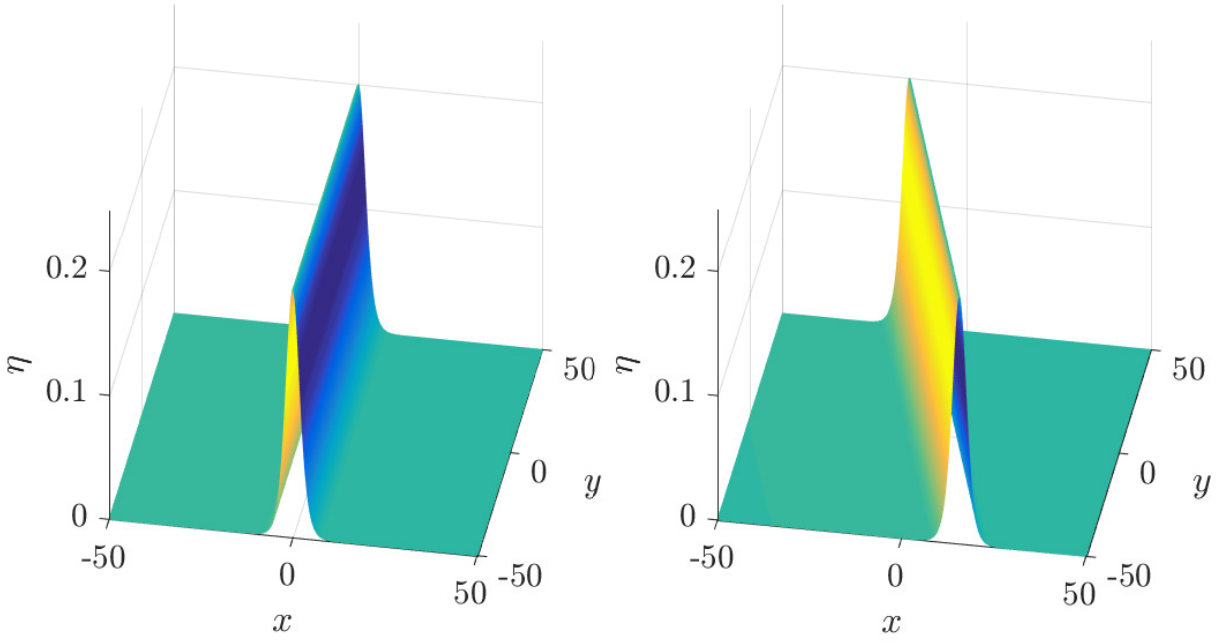

Figure 6.1.2: Flat KP Solutions. Both panels have $A = 0.2$. The left panel has $F = 1.1$ and the right panel has $F = 1.5$.

and the topography, σ are both set to zero in (6.1.5). The KP II equation now becomes

$$\frac{\partial}{\partial x}\left((F-1)\eta_x - \frac{3}{2}\eta\eta_x - \frac{1}{6}\eta_{xxx}\right) = \frac{1}{2}\eta_{yy}. \tag{6.1.7}$$

A solution of the form

$$\eta = A\,\mathrm{sech}^2(Bx + Cy) \tag{6.1.8}$$

is sought, where A is a free parameter, and B and C are constants that can be determined in terms of the amplitude A. By substituting (6.1.8) into (6.1.7) the constants B and C can be determined as

$$B^2 = \frac{3}{4}A, \quad C = \frac{3}{2}(F-1)A - \frac{3}{4}A^2. \tag{6.1.9}$$

If the amplitude is chosen so that $A = 2(F-1)$ the profile is a solitary wave extended uniformly along the y axis as seen in the first panel of figure 6.1.2. For $A \neq 2(F-1)$ the effect is that the solitary wave gets extended uniformly at an angle of θ to the x axis. This angle can be calculated by noting that the maximum of the solitary wave in (6.1.8) occurs when $Bx + Cy = 0$. Therefore $\tan(\theta) = -B/C$, where B and C are in terms of A given in (6.1.9). This is shown in the second panel of figure 6.1.2. These solutions are example of solutions that do not decay in both the x and y directions. As noted by Craig (2002) solutions that are fully localised do not exist for the KP II equation. Therefore can localised solutions be found if the topography is not flat?

The fKP II equation is now considered. Steady solutions are sought by prescribing a free-surface to determine a bottom topography; the so-called 'inverse' approach dis-

cussed in chapter 3. For the fKdV equation if a localised free-surface is prescribed then the corresponding bottom topography is also localised as demonstrated in the latter part of chapter 3 when 'inverse' solutions were constructed. In this case the topography, σ, can explicitly be written in terms of η and η_{xx} which decay in the far-field. However this is not the case in the fKP equation as shall be demonstrated. The steady fKP equation with a bottom topography present can be written as an ODE for σ, the bottom topography. Rearranging the steady version of (6.1.5) gives an ODE for σ:

$$\sigma_{xx} = 2(F-1)\eta_{xx} - 3\eta_x^2 - 3\eta\eta_{xx} - \frac{1}{3}\eta_{xxxx} - \eta_{yy}. \tag{6.1.10}$$

A localised free-surface η can be prescribed as

$$\eta = \alpha x^n \mathrm{e}^{-\beta(x^2+y^2)}, \tag{6.1.11}$$

where α and $\beta > 0$ are constants and n is chosen so that it is an integer. Clearly as η decays in both the x and y directions. A topography is sought that decays in the far-field. Let σ and σ_x decay to zero as $x \to -\infty$. Integrating (6.1.10) once yields an equation for σ_x in the form

$$\sigma_x = 2(F-1)\eta_x - 3\eta\eta_x - \frac{1}{3}\eta_{xxx} - \int_{-\infty}^{x} \eta_{yy}(p,y)\,\mathrm{d}p, \tag{6.1.12}$$

where p is a dummy variable. The behaviour of σ_x is sought as $x \to \infty$. There are two distinct cases. If n is even then in the limit as $x \to \infty$ the integral on the right hand side of (6.1.12) becomes

$$\int_{-\infty}^{\infty} \eta_{yy}(p,y)\,\mathrm{d}p = 2\alpha\beta(1-2\beta y^2)\mathrm{e}^{-\beta y^2} \int_{-\infty}^{\infty} x^n \mathrm{e}^{-\beta^2 x^2}\,\mathrm{d}x, \tag{6.1.13}$$

As n is even, using the standard rules of Gaussian integrals, (see, for example Abramowitz & Stegun, 1964) means that the integral above is well defined and takes a positive value, say $c_1 > 0$. By examining the form of (6.1.12) it is easy to show that $\sigma_x \to -c_1 g(y)$ as $x \to \infty$ where $g(y) = 2\alpha\beta(1-2\beta y^2)\mathrm{e}^{-\beta y^2}$. The implication of this is that by integrating with respect to x once again, σ will be growing linearly as $x \to \infty$ which is an unphysical situation. An example of this is shown in the first panel of figure 6.1.3.

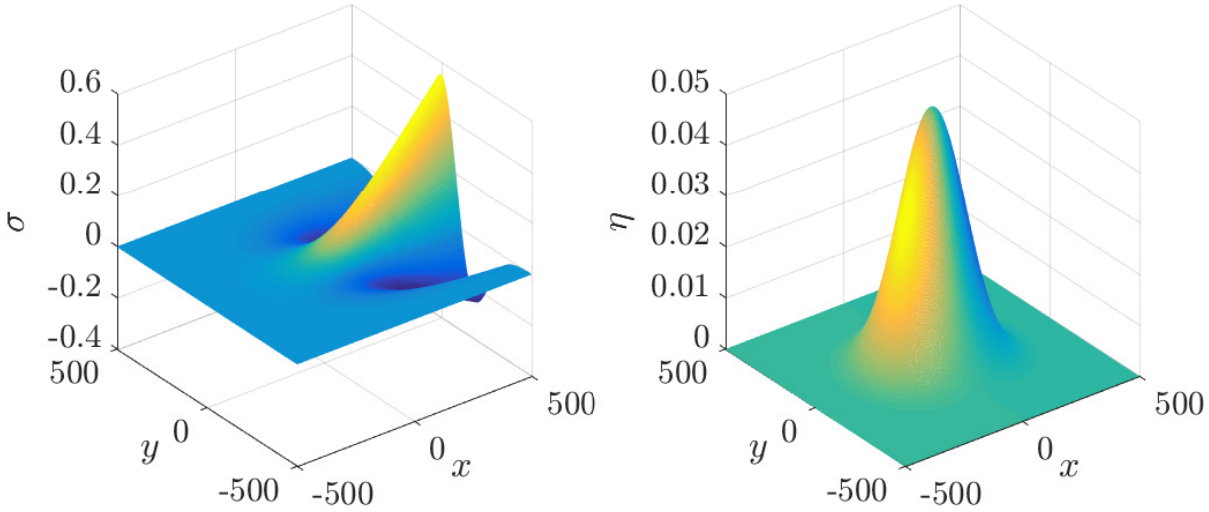

Figure 6.1.3: The free surface η is prescribed by the Gaussian $\eta = \alpha e^{-\beta(x^2+y^2)}$ where $\alpha = 0.05$ and $\beta = 1$ and is shown on the right panel. The topography σ is shown on the left panel.

For odd n the situation is slightly improved because the integral in (6.1.13) will be zero. Hence

$$\sigma_x \to 0, \qquad \text{as} \qquad x \to \infty. \tag{6.1.14}$$

This means that although σ_x approaches zero as $x \to \infty$, σ will approach a constant. The topography is bounded which is physically permissible but does not decay to zero in the far-field and hence is not fully localised. An example is shown in the first panel of figure 6.1.4.

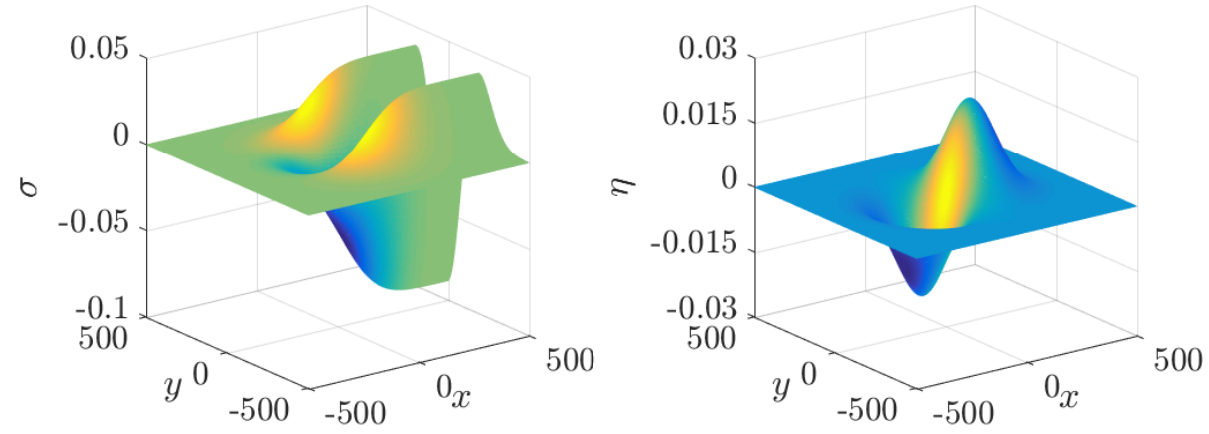

Figure 6.1.4: The free surface η is prescribed by the Gaussian $\eta = \alpha x e^{-\beta(x^2+y^2)}$ where $\alpha = 0.05$ and $\beta = 1$ and is shown on the right panel. The topography σ is shown on the left panel.

Modifying this approach, in an attempt to construct a topography so that $\sigma \to 0$ as $x \to \infty$ a free-surface is now prescribed of the form

$$\eta = \alpha(x-\delta)\mathrm{e}^{-\gamma((x-\delta)^2+y^2)} - \beta(x+\delta)\mathrm{e}^{-\gamma((x+\delta)^2+y^2)}, \tag{6.1.15}$$

where α, β, γ and δ are parameters that can be chosen freely. The integral of η_{yy} can now be integrated exactly. Therefore proceeding in the same way as before, by inspecting the form of (6.1.12) and (6.1.15) and assuming $\sigma_x \to 0$ as $x \to -\infty$, it can be shown that

$$\sigma_x = 2(F-1)\eta_x - 3\eta\eta_x - \frac{1}{3}\eta_{xxx} + \alpha(1-2\gamma y^2)\mathrm{e}^{-\gamma((x-\delta)^2+y^2)} - \beta(1-2\gamma y^2)\mathrm{e}^{-\gamma((x+\delta)^2+y^2)}, \tag{6.1.16}$$

and hence $\sigma_x \to 0$ as $x \to \infty$. Integrating again will mean that as $x \to \infty$, $\sigma \to c_2(y)$, where $c_2(y)$ is a function of y. The function $c_2(y)$ can be shown to be

$$c_2(y) = \mathrm{e}^{-\gamma y^2}(\alpha-\beta)\frac{\sqrt{\pi}}{\gamma}\left(1-2\gamma y^2\right). \tag{6.1.17}$$

So in general the topography does not decay in the far-field which does not constitute an improvement from before. However, if the parameters are chosen so that $\alpha = \beta$ then $c_2(y) = 0$. In this case σ will be localised; it will vanish as $|x|, |y| \to \infty$. This is shown in the first panel of figure 6.1.5 and is an example of a *forced lump soliton*. This approach has demonstrated that it is possible to find localised free-surface profiles when surface tension is absent. The obvious extension of this analysis is to understand the steady solution space when the topography is prescribed instead, so that the free-surface comes as part of the solution, as in the first part of chapter 3. This is an area of further investigation, along with an investigation of the stability properties of these profiles using an pseudo-spectral approach similar in the fKdV in chapter 3.

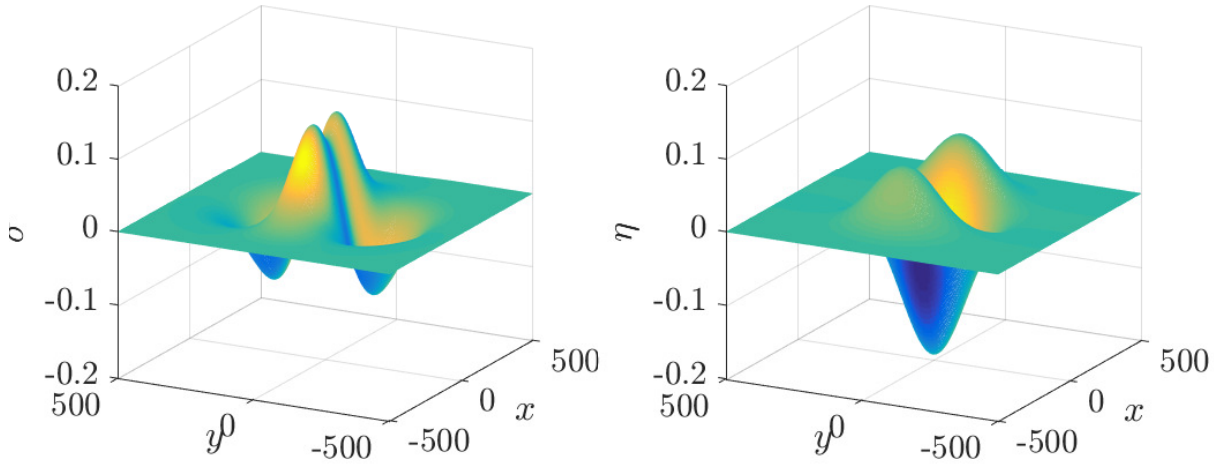

Figure 6.1.5: σ. The free surface η is prescribed by the Gaussian $\eta = \alpha(x-\delta)\mathrm{e}^{-\gamma((x-\delta)^2+y^2)} + \beta(x+\delta)\mathrm{e}^{-\gamma((x+\delta)^2+y^2)}$ where $\alpha = \beta = 0.5$, $\gamma = 1$ and $\delta = 0.2$ and is shown on the right panel. The topography σ is shown on the left panel.

Chapter 7

Conclusion

Critical free-surface flow over a localised bottom topography has been investigated using a weakly-nonlinear forced Korteweg-de Vries model and by way of numerical solutions of the fully nonlinear problem. Critical flow conditions occur when the Froude number is equal to unity both far upstream and far downstream of the localised topography.

In chapter 3 steady solutions were found when the topography takes the form of a rectangular trench or a Gaussian dip (a simple argument dictates that no steady solutions are possible in the case of a positive-definite topography). A phase plane analysis for the rectangular trench revealed that there are two distinct types of solution for the free-surface. The first has a depression profile and the second has an elevation profile. It was demonstrated that additional steady solutions emerge as the width of the trench is increased, and that these solutions feature different numbers of ripples trapped on the free surface immediately over the trench.

A phase plane analysis of this kind is not possible for a smoothly varying topography such as a Gaussian dip. For this topography steady solutions were studied via very carefully conducted numerical calculations. The solution space depends on a single parameter, α. For small α there is a unique steady solution, which is negative-definite and is termed a type I solution. At a critical value of α a second solution, termed type II, appears which is not single-signed. At larger values of α, further branches of steady solutions appear. In general the steady solutions have algebraic decay in the far-field such that the free surface elevation decays as $-(4/3)x^{-2}$ as $x \to \infty$. Similar algebraic decay can occur for gravity-capillary waves in infinite depth (Akylas *et al.*, 1998) and for gravity-capillary waves in two-layer flow (Sun, 1997). To corroborate the numerical solutions, asymptotic solutions were constructed that are valid in the limit of small and large α. For large α an asymptotic solution was constructed which captures the negative-definite type I solution as well as the type II solution.

However, an asymptotic description of the apparently infinite sequence of solution branches, types II a,b,c..., for which an increasing number of ripples are trapped on the free surface around the origin requires a multi-scales Kuzmak approach. By writing

the solution in terms of ξ and $y = \phi(\xi)/\delta^{1/2} + \mu(\xi)$, where ϕ is a slowly-varying phase function, and μ is a phase-shift, the full solution space for flow over a Gaussian bump can be revealed asymptotically. By insisting that the phase function, ϕ, is 1-periodic in y and by looking for symmetric solutions, ϕ can be determined and the leading order solution can be written in closed form with Jacobi Elliptical functions. The comparison with the numerical solutions is excellent and an approximation of the location of the termination points (the points where the solution branch emerges) in the $(\alpha, u(0))$ solution space can be made using this method.

In chapter 3 numerical solutions performed using the boundary integral method confirmed the existence of type I, II and IIa solutions in the fully nonlinear regime. However, these solutions do not extend indefinitely to large α. Rather, as α is increased, the free surface profiles approach a limiting configuration which is locally similar to that found for a classical Stokes wave with an interior angle of 120° at the wave maximum. In the second part of the investigation, the stability of the steady solutions obtained for a Gaussian dip topography was studied; first by computing eigenvalues of the linearised system, and then by numerical computation of the full fKdV initial value problem. For type I solutions all of the eigenvalues were found to lie on the imaginary axis, suggesting linear stability, and this was corroborated by the time-dependent simulations. In fact a simulation initiated with a free-surface which is only a small deviation from a type I solution is seen to slowly relax back to this steady state as time increases; the energy associated with the initial perturbation is leaked downstream in the form of a wave-train which appears on the downstream side of the free-surface shortly after the start of the simulation. The stability calculations for type II and type IIa steady solutions revealed complex eigenvalues which indicate that these solutions are linearly unstable and this was confirmed by time-dependent simulations initiated using an unstable eigenfunction as the form of perturbation. During these simulations, solitary waves are emitted upstream at regular intervals similar to what has been observed by previous workers. Interestingly, a simulation started from a flat free-surface does not approach the stable type I solution but instead behaviour somewhat similar to that found by Wu (1987) for critical flow over a positive obstacle is observed: key differences, however, are that the solitary waves which are emitted upstream have different heights and the depression region which appears downstream of the topography is undular rather than flat. The case of a positive topography has been studied extensively (see, for example Grimshaw, 2010; Grimshaw & Smyth, 1986; Grimshaw *et al.*, 2007; Wu, 1987) and analytic results have been obtained; however, to the author's knowledge no such results are available for a negative topography.

Finally in chapter 3, the stability of some of the steady solutions which were obtained by Binder *et al.* (2014) using an inverse method in which the free surface profile is prescribed and the topography is found directly from the governing equation were examined. In this case it was found that a negative-definite steady solution co-exists

with a prescribed positive-definite Gaussian-shaped free surface. The negative-definite depression solution was found to be linearly stable. The positive-definite solution was found to be in general linearly unstable due to a purely real eigenvalue in the spectrum of the linearised operator. However, by varying the amplitude of the Gaussian, stable positive-definite solutions were also identified.

When reaching these conclusions on the stability properties of the steady solutions for a Gaussian topography/free surface, in addition to numerical eigenvalue calculations and time-dependent simulations, the the Hamiltonian theory of Camassa & Wu (1991) was also applied to show analytically that negative-definite type I solutions are linearly stable. This was done by demonstrating that the $\mathcal{K}$ operator has no negative eigenvalues and hence the second variation of the relevant Hamiltonian is positive-definite. Unfortunately for the type II solutions, which are not single-signed, the results of this analysis are inconclusive. Analytic eigenvalue counts which might be used to deduce stability properties in this case have been discussed at some length in the literature. Notably Pelinovsky (2012) and Kapitula & Stefanov (2014) (see also the earlier work by Chugunova & Pelinovsky, 2010) independently proved a theorem for linearised systems of the form $\partial_x \mathcal{L} u = \lambda u$, which relates the number of potentially unstable eigenvalues λ to the number of negative eigenvalues of the self-adjoint operator $\mathcal{L}$. Chardard *et al.* (2011) used these ideas to infer stability properties of steady, table-top solitary wave solutions for super-critical flow. Unfortunately, the theorem cannot be applied in the present case of critical flow, since it requires that the essential spectrum of the $\mathcal{L}$ operator be bounded away from the origin. Here, $\mathcal{L} = -\mathcal{K} = (1/6)\partial_{xx} + (3/2)\eta_s$ with essential spectrum $[0, \infty)$, which violates this requirement. An eigenvalue count which applies in this case has not been identified in the literature.

In chapter 4 the steady problem when the forcing decays like x^{-2} in the far-field was discussed. Numerical evidence suggests that a solution exists but is difficult to compute. However an asymptotic expansion in this case leads to a solution that is consistent with the boundary conditions at all orders. It was shown that there is a choice of sign for the leading order solution. By constructing an expression for the later order terms in the expansion it was shown that Stokes' lines in the vicinity of the singularities of the leading order term do not cross the real axis with a choice of the negative sign but do cross with the choice of a positive sign. Therefore the asymptotic expansion appears consistent when the negative sign is chosen. A conjectured sketch of the solution space was presented which displayed similarities to the solution space of a Gaussian except for the key difference that the termination point becomes a fold and there is another branch expected.

In chapter 5 the case of steady flow over a corrugated topography was considered. For the infinite topography an asymptotic analysis revealed that for super-critical flow the steady solution is periodic and in phase with the topography. For sub-critical flow the steady solution was found to be quasi-periodic in general but periodic solutions

are possible provided the exact conditions for η and η_x are chosen at $x = 0$. For the case of finite and semi-infinite topography a wide range of steady solutions were found. The solutions were oscillatory over the corrugated part of the topography. For $F > 1$ when the oscillations centered about the zero mean level they appeared regular whilst oscillations about a non-zero mean appeared disorderly. For $F < 1$ the oscillations over the topography were disorderly. The solutions beared striking similarity to the solutions obtained for flow over a bump, in particular perturbed generalised hydraulic falls and perturbed table-top solitons were found. For $F < 1$ and in the case of an semi-infinite topography the periodicity properties were analysed numerically using a power spectrum method and by calculating Poincaré sections and power spectra. The Poincareé plots took the form of closed curves, providing evidence that the solutions were quasi-periodic over the topgraphy. The power spectra corroborated this by displaying peaks where the dominant frequencies predicted from the asymptotic analysis over an infinite corrugation predicted them.

Finally the three-dimensional analogue of the fKdV equation was discussed in chapter 6. For the unforced KP equation with no surface tension no localised solutions exist in which the steady profile decays in all directions. However, by setting the topography carefully fully localised solutions can exist and this was shown with some examples. This work can be extended to find asymptotic solutions to the forced KP equation and also the time-dependent behaviour is yet to be analysed of these steady solutions that decay in all directions.

The work in this thesis has used a variety of asymptotic, numerical and exact methods to describe the wave behaviour in steady and time-dependent flows. The ultimate question that has been answered is 'what do the waves look like if there's something on the bottom?'. The problem is simply stated and understood by the layman, yet the wealth of interesting mathematics that has arisen from considering this simple problem is remarkable. Almost as remarkable is the fact that an ODE as simply stated as

$$\delta u_{\xi\xi} + u^2 - \lambda u = f(\xi)$$

has the vast number of subtleties that have been explored and analysed in this work. It is easy to convince oneself that numerical solutions exist, but to convince oneself that they actually reflect a true solution of the problem is a different task altogether. The small δ expansions in this work have demonstrated that the numerical solutions can be described by asymptotic expansions effectively. However, as has been seen, just because the leading order solution and the numerical solution agree does not mean the story ends there. By probing deeper to higher orders of δ great insight into the structure of the solution space can be found. Numerical solutions are useful but one should always dig deeper. Not only can the numerical solutions be validated, but a plethora of rich and surprising mathematics can be discovered by exploring just a little further below the surface.

Appendix A

Numerical Method for Kuzmak Approximation

Throughout the calculations in chapter 3 the integral I, as stated in (3.3.53), has to be calculated. This has square-root singularities at it's endpoints and a bespoke quadrature rule has to be invoked to alleviate the difficulties these singularities pose. In this section the sinh-tanh quadrature rule is described as a suitable method for such integrals. The basic idea is to transform the integral to the real line so the singularities are transformed are mapped to plus/minus infinity. The integral to be evaluated is in the form

$$I = \int_{U_m(\xi,A(\xi))}^{U_+(\xi,A(\xi))} f(\xi, t, A(\xi))\,\mathrm{d}t, \tag{A.0.1}$$

where $f = c^{-1/2}$ and U_m and U_+ are the roots of the polynomial c. First the interval of integration is converted to $u \in [-1, 1]$ so that (A.0.1) becomes

$$I = \frac{U_+(\xi, A(\xi)) - U_m(\xi, A(\xi))}{2} \int_{-1}^{1} g(\xi, \hat{t}, A(\xi))\,\mathrm{d}\hat{t}, \tag{A.0.2}$$

where

$$\begin{aligned} g(\xi, t, A(\xi)) &= f(\xi, \hat{t}, A(\xi)) \\ t &= \left(\frac{U_+ - U_m}{2}\right)\hat{t} + \frac{U_m + U_+}{2}. \end{aligned}$$

Next the integral in (A.0.2) is transformed to a domain of $u \in [-\infty, \infty]$. This is achieved by the transformation

$$\hat{t} = \tanh\left[\frac{1}{2}\pi \sinh(u)\right]. \tag{A.0.3}$$

The integral in (A.0.2) can be written as

$$I = \int_{-\infty}^{\infty} \frac{1}{2}\pi \frac{\cosh(u)}{\cosh\left[\frac{1}{2}\pi \sinh(u)\right]} f\left(\xi, \tanh\left[\frac{1}{2}\pi \sinh(u)\right], A(\xi)\right) \mathrm{d}u. \tag{A.0.4}$$

To approximate this integral numerically let $u = Mh$ for large $M \in [-(M-1)/2, (M-1)/2]$ and small step-size h. Therefore the integral in (A.0.4) can be approximated as the sum

$$I \approx h \sum_{i=-(M-1)/2}^{i=(M-1)/2} w_i f(\hat{y}_i), \tag{A.0.5}$$

where

$$\hat{y}_i = \tanh\left[\frac{1}{2}\pi \sinh(ih)\right],$$
$$w_i = \frac{1}{2}\pi \frac{\cosh(ih)}{\cosh\left[\frac{1}{2}\pi \sinh(ih)\right]}.$$

It is noted that the integral for ϕ, (3.3.52a), and the equation for k, (3.3.52b), do not have singularities at their endpoints and a standard application of the trapezium rule was implemented to calculate this quantities.

Appendix B

Spectrum of $\mathcal{K}$

In this appendix some of the results regarding the linear operator $\mathcal{K}$ are explained in more detail. In particular the assertion that $\nu = 0$ is not an eigenvalue of $\mathcal{K}$ provided $\int_{-\infty}^{\infty}|x||\eta_s|\,\mathrm{d}x < \infty$. The proof is an adaptation of the proof in the appendix of Bargmann (1949). The second part utilises the Rayleigh-Ritz method to give a condition for a negative discrete eigenvalue of $\mathcal{K}$.

B.1 Condition for empty kernel

The equation to be examined is

$$g'' - \nu g = -\eta_s g, \qquad \lim_{|x|\to\infty} g \to 0, \qquad -\infty < x < \infty. \tag{B.1.1}$$

The problem is transformed to the boundary value problem in the domain $-\infty < x < \infty$

$$f''(\nu,x) - 2\sqrt{\nu}f'(\nu,x) = -\eta_s(x)f(\nu,x), \qquad \lim f(\nu,x) = \begin{cases} 1 & x \to \infty \\ \mathrm{e}^{2\nu x} & x \to -\infty \end{cases}. \tag{B.1.2}$$

by the change of variables $g = \mathrm{e}^{-\sqrt{\nu}x}f$. Equation (B.1.2) is to be written as an integral equation. It can be written as

$$\mathcal{L}f = -\eta_s(x)f(\nu,x), \qquad \mathcal{L} = \frac{\mathrm{d}^2}{\mathrm{d}x^2} - 2\sqrt{\nu}\frac{\mathrm{d}}{\mathrm{d}x}.$$

The theory of Green's functions applies. The Green's function G of $\mathcal{L}$ satisfies

$$G'' - 2\sqrt{\nu}G' = \delta(x-s), \tag{B.1.3}$$

where δ is the Dirac delta function. For $x > s$ the solution is

$$G = A + B\mathrm{e}^{2\sqrt{\nu}x}$$

where A and B are constants. Using the boundary condition, for $x > s$;

$$G = 1.$$

For $x < s$ the solution to (B.1.3) is

$$G = C + D\mathrm{e}^{2\sqrt{\nu}x}.$$

By ensuring continuity at $x = s$ in G the constants C and D must satisfy

$$C + D\mathrm{e}^{2\sqrt{\nu}s} = 1.$$

By integrating (B.1.3) between $[s - \epsilon, s + \epsilon]$ and taking the limit as $\epsilon \to 0$, continuity of G' at $x = s$ means

$$D = \frac{-\mathrm{e}^{-2\sqrt{\nu}s}}{2\sqrt{\nu}}$$

and hence the Green's function can be written as

$$G(s,x) = \begin{cases} 1 + \frac{1-\mathrm{e}^{-2\sqrt{\nu}(s-x)}}{2\sqrt{\nu}}, & x < s < \infty \\ 1, & -\infty < s < x \end{cases}$$

The equation can be written as a Fredholm integral equation in the form

$$f(\nu,x) = -\int_{-\infty}^{\infty} G(s,x)\eta_s(s)f(\nu,s)\,\mathrm{d}s$$

and therefore by adding the homogeneous solutions becomes:

$$f(\nu,x) = C_1 + C_2\mathrm{e}^{2\sqrt{\nu}x} - \int_{-\infty}^{\infty} \eta_s(s)f(\nu,s)\,\mathrm{d}s - \int_{x}^{\infty} D_\nu(s-x)\eta_s(s)f(\nu,s)\,\mathrm{d}s,$$
$$D_\nu(\xi) = \frac{1-\mathrm{e}^{-2\sqrt{\nu}\xi}}{2\sqrt{\nu}}.$$

which by choosing $C_1 = 1 + \int_{-\infty}^{\infty} \eta_s(s)f\,\mathrm{d}x$, $C_2 = 0$ and choosing the normalisation $\int_{-\infty}^{\infty} \eta_s(s)f_\nu(s)\,\mathrm{d}s = 2\nu$ to satisfy the boundary conditions becomes

$$f(\nu,x) = 1 - \int_{x}^{\infty} D_\nu(s-x)\eta_s(s)f(\nu,s)\,\mathrm{d}s. \tag{B.1.4}$$

The next step is to write the solution as a series:

$$f(\nu,x) = \sum_{n=0}^{\infty} f_n(\nu,x); \qquad f_0(\nu,x) = 1. \tag{B.1.5}$$

When substituted into (B.1.4), this form implies

$$f_{n+1} = -\int_x^\infty D_\nu(s-x)\eta_s(s)f_n(\nu,s)\,\mathrm{d}s; \qquad f_0(\nu,x) = 1. \tag{B.1.6}$$

Proposition 1. *If*

$$\Im(\sqrt{\nu}) < 0 \qquad \textit{and} \qquad \int_{-\infty}^{\infty} x|\eta_s(x)|\,dx < \infty,$$

then the series (B.1.5) *converges.*

Proof. Define

$$Y(x) = \int_x^\infty s|\eta_s(s)|\,\mathrm{d}s.$$

Now D_ν remains bounded if $\Im(\nu) \le 0$. Therefore $D_\nu(\xi) = \xi + O(\xi^2)$ and in particular

$$|D_\nu(s-x)| \le s - x \le s.$$

Now using (B.1.6)

$$\begin{aligned}
|f_1| &= \left|\int_x^\infty D_\nu(s-x)\eta_s(s)f_0(s)\,\mathrm{d}s\right| \\
&\le \int_x^\infty |D_\nu(s-x)\eta_s(s)|\,\mathrm{d}s \\
&\le \int_x^\infty s|\eta_s(s)|\,\mathrm{d}s \\
&\le Y(x).
\end{aligned}$$

Furthermore

$$f_2 \le -\int_x^\infty s|\eta_s(s)|Y(x)\,\mathrm{d}s \tag{B.1.7}$$

$$\le -\int_{Y(x)}^0 Y(s)\,\mathrm{d}Y \tag{B.1.8}$$

$$|f_2| \le \frac{(Y(x))^2}{2} \tag{B.1.9}$$

where to get from (B.1.7) to (B.1.8) a change of variables from s to $Y(s)$ has taken place. Let the C_k be the statement

$$C_k: \qquad |f_k| \le \frac{(Y(x))^k}{k!}. \tag{B.1.10}$$

Now using (B.1.6)

$$|f_{k+1}| \leq -\int_x^\infty s|\eta_s(s)|\frac{(Y(x))^k}{k!}\,\mathrm{d}s \tag{B.1.11}$$

$$\leq -\int_{Y(x)}^0 \frac{(Y(s))^k}{k!}\,\mathrm{d}Y \tag{B.1.12}$$

$$\leq \frac{(Y(x))^{k+1}}{(k+1)!}. \tag{B.1.13}$$

and hence if C_k is true then so it C_{k+1}. Hence by induction

$$|f_n| \leq \frac{(Y(x))^n}{n!} \leq \lim_{x\to-\infty}\left[\frac{(Y(x))^n}{n!}\right] < \infty$$

for all n. Therefore by the sandwich proposition the sequence $\{f_n\}$ converges and the proposition is proved. □

The solution $f(\nu, x)$ is therefore uniformly bounded for all ν. Additionally as $g_\nu \to 1$ then g_ν has a finite number of zeros and hence a finite number of discrete eigenvalues (see, for example Couant & Hilbert (1953)). In particular $f(0, \nu)$ is bounded and is a solution of (B.1.2) with $\nu = 0$. By a reduction of order procedure a second linearly independent solution of (B.1.2) is given by

$$f^{(1)}(x) = f(0, x)\int_{x_0}^x \frac{\mathrm{d}s}{[f(0, s)]^2} \tag{B.1.14}$$

for fixed x_0. In the limit as $x \to \infty$, (B.1.14) becomes

$$f^{(1)}(x) \sim \lim_{x\to\infty}\left[f(0, x)\int_{x_0}^x \frac{\mathrm{d}s}{[f(0, x)]^2}\right]$$

$$\sim x.$$

Hence neither $f(0, x)$ nor $f^{(1)}(x)$ are in L_2 (i.e. square integrable) and so neither is $g(\nu, x)$. Furthermore no linear combination of $f(0, x)$ and $f^{(1)}$ will give a square integrable solution and therefore $\nu = 0$ is not part of the point spectrum of (B.1.1). Note the condition in the proposition is a sufficient not necessary condition. Also note that for $\eta_s = A\mathrm{e}^{-Bx^2}$ (as in the inverse solution) then the condition is automatically satisfied but for the type IIa,b,c,... solutions it is not satisfied in the far-field.

B.2 Condition for a negative discrete eigenvalue

Equation (B.1.2) is analysed using the Rayleigh-Ritz method (see, for example Duff & Naylor (1966)). First, (B.1.2) is multiplied by g, integrated over the domain and

rearranged for ν:

$$\nu = \frac{\int_{-\infty}^{\infty} \eta_s g^2 \,\mathrm{d}x - \int_{-\infty}^{\infty} (g')^2 \,\mathrm{d}x}{\int_{-\infty}^{\infty} g^2 \,\mathrm{d}x}.$$

For the steady solution; $\eta_s = A\mathrm{e}^{-B^2x^2}$ this is

$$\nu = \frac{A\int_{-\infty}^{\infty} \mathrm{e}^{-B^2x^2} g^2 \,\mathrm{d}x - \int_{-\infty}^{\infty} (g')^2 \,\mathrm{d}x}{\int_{-\infty}^{\infty} g^2 \,\mathrm{d}x}. \tag{B.2.1}$$

A trial function satisfying the boundary conditions is chosen as

$$g = \left(\frac{C_1}{\pi}\right)^{1/4} \mathrm{e}^{-C_1 x^2/2}.$$

Substituting this into (B.2.1) and using standard results for integrals this becomes

$$\nu_0 \leq A\sqrt{\frac{C_1}{B^2 + C_1}} - 2C_1.$$

The inequality is created due to the fact that the approximate eigenvalue associated with the trial function satisfying the boundary conditions is an upper bound for the lowest eigenvalue (see, for example Duff & Naylor (1966)). Therefore for any B and $A > 0$, C_1 can be chosen so that

$$\nu_0 \leq 0$$

and hence the discrete spectrum contains negative eigenvalues.

Bibliography

Ablowitz, M. J. & Clarkson, P. A. 1991 *Solitons, Nonlinear Evolution Equations and Inverse Scattering*. Cambridge University Press.

Ablowitz, M. J. & Fokas, A. S. 2003 *Complex variables: introduction and applications*. Cambridge University Press.

Abramowitz, M. & Stegun, I. A. 1964 *Handbook of Mathematical Functions with Formulas,Graphs and Mathematical Tables*. US Department of Commerce.

Acheson, D. J. 1990 *Elementary Fluid Mechanics*. Clarendon Press.

Akylas, T. R. 1984 On the excitation of long nonlinear water waves by a moving pressure distribution. *J. Fluid Mech.* **141**, 455–466.

Akylas, T. R., Dias, F. & Grimshaw, R. H. J. 1998 The effect of the induced mean flow on solitary waves in deep water. *J. Fluid Mech.* **355**, 317–328.

Alias, A. B. 2014 Mathematical modelling of nonlinear internal waves in a rotating fluid. PhD thesis, Loughborough University.

Baines, G. B. 1977 Upstream influence and Long's model in stratified flows. *J. Fluid Mech.* **82**, 147–159.

Baines, G. B. 1984 A unifed description of two-layer flow over topography. *J. Fluid Mech.* **146**, 127–167.

Barashenkov, I. V. & Zemlyanaya, E. V. 2000 Oscillatory instabilities of gap solitions: a numerical study. *Comput. Phys. Commun.* **172**, 22–27.

Bargmann, V. 1949 On the connection between phase shifts and scattering potential. *Rev. Mod. Phys.* **21** (3), 488.

Bender, C. M. & Orszag, S. A. 1999 *Advanced Mathematical Methods for Scientists and Engineers I*. Springer-Verlag.

Benjamin, T. B., Bona, J. L. & Mahony, J. J. 1972 Model equations for long waves in nonlinear dispersive systems. *Phil. Trans. R. Soc. Lond.* **272** (1220), 47–78.

Berry, M. V. 1988 Uniform asymptotic smooting of Stokes' discontinuities. *Proc. R. Soc. Lond.* **422**, 7–215.

Billingham, J. 2006 Surface tension-driven flow in a slender wedge. *SIAM J. Appl. Math.* **66** (6), 1949–1977.

Billingham, J. & King, A. C. 2000 *Wave Motion*. Cambridge University Press.

Binder, B. J., Blyth, M. G. & Balasuriya, S. 2014 Non-uniqueness of steady free-surface flow at critical Froude number. *EPL* **105**, 44003.

Binder, B. J., Blyth, M. G. & Balasuriya, S. 2015 Steady free-surface over spatially periodic topography. *J. Fluid Mech. Rapids* **781**, R3.

Binder, B. J., Blyth, M. G. & McCue, S. W. 2013 Free-surface flow past arbitrary topography and an inverse approach to wave-free solutions. *IMA J. Appl. Math.* **78**, 685–696.

Binder, B. J. & Vanden-Broeck, J-M 2006 Steady free-surface flow past an uneven bottom. *Theor. Comput. Fluid Dyn.* **20**, 125 – 144.

Binder, B. J., Vanden-Broeck, J-M. & Dias, F. 2005 Forced solitary waves and fronts past submerged obstacles. *CHAOS* **15**, 1–13.

Biondini, G., Maruno, K-I., Oikawa, M. & Tsuji, H. 2009 Soliton interactions of the kadomtsev–petviashvili equation and generation of large-amplitude water waves. *Stud. Appl. Math.* **122** (4), 377–394.

Blyth, M. G. & Părău, E. I. 2016 The stability of capillary waves on fluid sheets. *J. Fluid Mech.* **806**, 5–34.

Bourland, F. J. & Haberman, R. 1988 The modulated phase shift for strongly nonlinear, slowly varying, and weakly damped oscillators. *SIAM J. Appl. Math.* **48** (4), 737–748.

Boyce, W. E., DiPrima, R. C. & Haines, C. W. 1969 *Elementary differential equations and boundary value problems*, , vol. 9. Wiley New York.

Boyd, J. P. 1999 The devil's invention: asymptotic, superasymptotic and hyperasymptotic series. *Acta Appl. Math.* **56** (1), 1–98.

Boyd, J. P. 2000 *Chebyshev and Fourier Spectral Methods*. Dover Publications.

Bridges, T. J., Derks, G. & Gottwald, G. A. 2002 Stability and instability of solitary waves of the fifth-order KdV equation: A numerical framework. *Physica D* **172**, 190–216.

Burde, G. I. & Sergyeyev, A 2013 Ordering of two small parameters in the shallow water wave problem. *J. Phys. A* **46** (7), 075501.

Camassa, R. & Wu, T. Y-T. 1991 Stability of forced steady solitary waves. *Phil. Trans. R. Soc. Lond.* **10**, 429–466.

Champneys, A 2017 Westward ho! musing on mathematics and mechanics. *Mathematics Today* **53** (4), 180–184.

Chang, H.-H. & Demekhin, E. A. 2002 *Complex Wave Dynamics on Thin Films*. Elsevier.

Chapman, S. J. & Farrell, P. E. 2017 Analysis of carrier's problem. *SIAM J. Appl. Math.* **77** (3), 924–950.

Chapman, S. J., King, J. R. & Adams, K. L. 2000 Exponential asymptotics and Stokes' lines in nonlinear ordinary differential equations. *Proc. R. Soc. Lond.* **454**, 2733–2755.

Chapman, S. J. & Vanden-Broeck, J-M. 2006 Exponential asymptotics and gravity waves. *J. Fluid Mech.* **567**, 299–326.

Chardard, R., Dias, F., Nyguyen, H. Y. & Vanden-Broeck, J-M. 2011 Stability of some stationary soutions to the forced KdV equation with one or two bumps. *J. Eng. Math.* **70**, 175–189.

Choi, J. X., Sun, S. M. & Whang, S. I. 2008 Supercritical surface gravity waves generated by a positive forcing. *Eur. J. Mech. B Fluids* **27**, 750 – 770.

Choi, W. & Camassa, R. 1999 Exact evolution equations for surface waves. *J. Eng. Mech.* **125** (7), 756–760.

Chugunova, M. & Pelinovsky, D. 2010 Count of eigenvalues in the generalized eigenvalue problem. *J. Math. Phys.* **51** (5), 052901.

Coddington, E. A. & Levinson, N. 1955 *Theory of Ordinary Differential Equations*. Tata McGraw-Hill Education.

Cooley, J. W. & Tukey, J. W. 1965 An algorithm for the machine calculation of complex fourier series. *Math Comput* **19** (90), 297–301.

Couant, R. & Hilbert, D. 1953 *Methods of Mathematical Physics, vol. 1*. Wiley-Interscience, New York.

Craig, W. 2002 Non–existence of solitary water waves in three dimensions. *Phil. Trans. R. Soc. Lond.* **360** (1799), 2127–2135.

Dias, F. & Vanden-Broeck, J. M. 2002*a* Generalised critical free-surface flows. *J. Eng. Math.* **42**, 291–302.

Dias, F. & Vanden-Broeck, J-M. 2002*b* Steady two-layer flows over an obstacle. *Phil. Trans. R. Soc. Lond.* **360**, 2137–2153.

Dingle, R. B. 1973 *Asymptotic Expansions: Their Derivation and Interpretation*. Academic Press.

Doedel, E. 2010 Lecture notes on numerical analysis of nonlinear equations. Lecture Notes.

Donahue, A. S. & Shen, S. S. 2010 Stability of hydraulic falls and sub-critical cnoidal waves in water flows over a bump. *J. Eng. Math.* **10**, 1007.

Drazin, P. G. 1992 *Nonlinear systems*, , vol. 10. Cambridge University Press.

Drazin, P. G. & Johnson, R. S. 1989 *Solitons: An Introduction*. Cambridge university press.

Dreizler, R. M. & Engel, E. 2011 *Density Functional Theory: An Advanced Course*. Springer.

Duff, G. F. D. & Naylor, D 1966 *Differential Equations for Applied Mathematics*. J. Wiley and Sons, New York.

Ee, B. K., Grimshaw, R. H. J., Zhang, D.-H. & Chow, K. W. 2010 Steady transcritical flow over a hole: Parametric map of solutions of the forced Korteweg–de Vries equation. *Phys. Fluids* **22**, 056602.

Forbes, L. K. 1988 Critical free-surface flow over a semi-circular obstruction. *J. Eng. Math.* **22**, 3–13.

Gelfand, I. M. & Fomin, S. V. 1963 *Calculus of Variations*. Prentice-Hall, Englewood Cliffs.

Grimshaw, H. J. & Maleewong, M. 2016 Transcritical flow over two obstacles: forced Korteweg–de Vries framework. *J. Fluid Mech.* **809**, 918–940.

Grimshaw, R. 2010 Transcritical flow past an obstacle. *ANZIAM* .

Grimshaw, R. & Maleewong, M. 2013 Stability of steady gravity waves generated by a moving localised pressure disturbance in water of finite depth. *Phys. Fluids* **25**, 076605.

Grimshaw, R. & Smyth, N. 1986 Resonant flow of a stratified fluid over topography. *J. Fluid Mech.* **169**, 429–464.

Grimshaw, R. & Tian, X. 1994 Periodic and chaotic behaviour in a reduction of the perturbed Korteweg–de Vries equation. *Proc. R. Soc. Lond.* **445**, 1–21.

Grimshaw, R. H. J., Zhang, D-H. & Chow, K. W. 2007 Generation of solitary waves by transcritical flow over a step. *J. Fluid Mech.* **537**, 235–254.

Groves, M. D. & Sun, S-M. 2008 Fully localised solitary-wave solutions of the three-dimensional gravity–capillary water-wave problem. *Arch. Rational Mech. Anal.* **188** (1), 1–91.

Heading, J. 1962 *An Introduction to Phase-Integral Methods*. Dover publications.

Holm, D. D., Marsden, J. E., Ratiu, T. & Weinstein, A. 1985 Non-linear stability of fluid and plasma equilibria. *Phys. Rep.* **1** (116).

Hunter, J. K. & Vanden-Broeck, J.-M. 1983 Accurate computations for steep solitary waves. *J. Fluid Mech.* **136**, 63–71.

Iguchi, Tatsuo 2006 A mathematical justification of the forced Korteweg–de Vries equation for capillary-gravity waves. *Kyushu J. Math.* **60** (2), 267–303.

Kadometsev, B. B. & Petviashvili, V. I. 1970 On the stability of solitary waves in weakly dispersive media. *Sov. Phys. - Dok* **15**, 539–541.

Kapitula, T. & Stefanov, A. 2014 A Hamiltonian–Krein (instability) index theory for solitary waves to KdV-like eigenvalue problems. *Stud. Appl. Math.* **132** (3), 183–211.

Katsis, C. & Akylas, T. R. 1987 On the excitation of long nonlinear water waves by a moving pressure distribution. part 2. three-dimensional effects. *J. Fluid Mech.* **177**, 49–65.

Keeler, J. S., Binder, B. J. & Blyth, M. G. 2017 On the critical free surface flow over bottom topography. *J. Fluid Mech.* **832**, 73–96.

King, A. C., Billingham, J. & Otto, S. R. 2003 *Differential Equations: Linear, Nonlinear, Ordinary, Partial*. Cambridge University Press.

King, J. R. 2018 Private communication.

Klein, C. & C.Sparber 1991 Transverse stability of periodic traveling waves in Kadomtsev-Petviashvili equations: A numerical study. *arXiv preprint arXiv:1108.3363* .

Kodama, Y. 2010 KP solitons in shallow water. *J. Phys. A* **43**.

Kuzmak, G. E. 1959 Asymptotic solutions of nonlinear second order differential equations with variable coefficients. *J Appl. Math. Mech.* **23** (3), 730–744.

Landau, L. D. & Lifshitz, E. M. 1977 *Quantum Mechanics - Non-relativistic Theory*. Pergamon Press.

Lannes, D. 2013 *The Water Waves Problem Mathematical Analysis and Asymptotics Mathematical Analysis and Asymptotics*. American Mathematical Society.

Lannes, D. & Saut, J-C 2013 Remarks on the full dispersion Kadometsev and Petviashvli equation. *Kin. Rel. Mod.* **6** (4).

Lee, S-J. & Grimshaw, R. H. J. 1990 Upstream-advancing waves generated by three-dimensional moving disturbances. *Phys. Fluids* **2** (2), 194–201.

Lighthill, M. J. 1962 *Fourier analysis and Generalised Functions*. Cambridge University Press.

Longuet-Higgins, M. S. & Fox, M . J. H. 1977 Theory of the almost-highest wave: the inner solution. *J. Fluid Mech.* **80** (04), 721–741.

Lu, Z. & Liu, Y. 2005 The generation of lump solitions by a bottom topography in a surface-tension dominated flow. *Z. Naturforsch* **60a**, 328–334.

Lustri, C. J., McCue, S. W. & Binder, B. J. 2006 Free-surface flow: A beyond all orders approach. *Eur. J. Mech.* **567**, 685–696.

Malanotte-Rizzoli, P. 1984 Boundary-forced nonlinear planetary radiation. *J. Phys. Ocean.* **14** (6), 1032–1046.

Maleewong, M., Asavanant, J. & Grimshaw, R. 2005 Free surface flow under gravity and surface tension due to an applied pressure distribution: I bond number greater than one-third. *Theor. Comput. Fluid Dyn* **19(4)**, 237–252.

Meur, H. L. 2015 Derivation of a viscous KP equation including surface tension, and related equations. *arXiv preprint arXiv:1506.00456* .

Minzoni, A.A & Smyth, N.F 1996 Evolution of lump solutions for the KP equation. *Wave Motion* **24**, 291–305.

Page, C., Grandison, S. & Parau, E. I. 2014 The influence of surface tension upon trapped waves and hydraulic falls. *Euro. J Mech. B* **43**, 191–201.

Pelinovsky, D. E. 2012 Spectral stability of nonlinear waves in KdV-type evolution equations. *arXiv preprint arXiv:1212.3489* .

Sandstede, B. 2002 Stability of travelling waves. *Handbook of dynamical systems* **2**, 983–1055.

Sandstede, B. & Scheel, A. 2000 Absolute and convective instabilities of waves on unbounded and large bounded domains. *Physica D* **145** (3), 233–277.

Segur, H., Tanveer, S. & Levine, H. J. 1991 *Asymptotics Beyond All Orders*, , vol. 284. Springer Science & Business Media.

Shankar, R. 2012 *Principles of Quantum Mechanics*. Springer Science & Business Media.

Shen, S. S., Manohar, R. P. & L.Gong 1995 Stability of the lower cusped solitary waves. *Phys. of Fluids* **7**, 2507–2509.

Shen, S. S., Moodie, T. B. & Shen, B. 2000 Interpretation of the stability and instability of the solitary waves governed by a forced Korteweg–de Vries equation. *Canad. Appl. Math. Quart.* **8**, 292–303.

Shen, S. S-P. 1995 On the accuracy of the stationary forced Korteweg de Vries equation as a model equation for flows over a bump. *Quart. Appl. Math.* **53** (4), 701–719.

Smyth, N. F. 1988 Dissipative effects on the resonant flow of a stratified fluid over topography. *J. Fluid Mech.* **192**, 287–312.

Sun, S.-M. 1997 Some analytical properties of capillary-gravity waves in two-fluid flows of infinite depth. *Proc. R. Soc. Lond. A* **453**, 1153–1175.

Tam, A. T., Z. Yu, R. M. Kelso & Binder, B. J. 2015 Predicting channel bed topography in hydraulic falls. *Phys. Fluids* **27**, 112–106.

Titchmarsh, E. C. 1962 *Eigenfunction Expansions Associated With Second Order Differential Equations. Part One*. Oxford University Press.

Trinh, P. H. & Chapman, S. J. 2015 Exponential asymptotics with coalescing singularities. *Nonlinearity* **28** (5), 1229.

Vanden-Broeck, J-M. 1987 Free-surface flow over an obstruction in a channel. *Phys. Fluids* **30**, 2315–2317.

Vanden-Broeck, J-M. 1997 Numerical calculations of the free-surface flow under a sluice gate. *J. Fluid Mech.* **330**, 339–347.

Viotti, C., Dutykh, D. & Dias, F. 2014 The conformal-mapping method for surface gravity waves in the presence of variable bathymetry and mean current. *Procedia IUTAM* **11**, 110–118.

Wade, S. 2015 Gravity waves in supercritical flow past compact forcing. PhD thesis, University of Adelaide.

Wade, S. L., Binder, B. J., Mattner, T. W. & Denier, J. P. 2014 On the free surface flow of very steep forced solitary waves. *J. Fluid Mech.* **739**, 1–21.

Whitham, G. B. 1970 Two-timing, variational principles and waves. *J Fluid. Mech.* **44** (02), 373–395.

Whitham, G. B. 1974 *Linear and Non-linear Waves*. J. Wiley and Sons.

Wu, T. Y-T. 1987 Generation of upstream advancing solitons by moving disturbances. *J. Fluid Mech.* **184**, 75–99.

Zhang, Yinglong & Zhu, Songping 1997 Subcritical, transcritical and supercritical flows over a step. *J. Fluid Mech.* **333**, 257–271.